

Spatial Cell Biology:

Dissecting and directing intracellular transport mechanisms

ISBN: 978-90-393-6762-9

The studies described in this thesis were performed at the division of Cell Biology at the Faculty of Science of Utrecht University in Utrecht, the Netherlands.

This work is part of the research programme of the Foundation for Fundamental Research on Matter (FOM), which is part of the Netherlands Organisation for Scientific Research (NWO).

Printed by: Gildeprint, Enschede

Cover: Redrum Bureau

Copyright by M. Adrian, 2017

All rights reserved.

Spatial Cell Biology:

Dissecting and directing intracellular transport mechanisms

Ruimtelijke celbiologie:
Bestuderen en besturen van intracellulaire transportmechanismes
(met een samenvatting in het Nederlands)

Räumliche Zellbiologie:
Intrazelluläre Transportmechanismen erforschen und steuern
(mit einer Zusammenfassung in deutscher Sprache)

Proefschrift

ter verkrijging van de graad van doctor aan de Universiteit Utrecht op gezag van
de rector magnificus, prof. dr. G.J. van der Zwaan, ingevolge het besluit van het
college voor promoties in het openbaar te verdedigen op woensdag 5 juli 2017
des middags te 2.30 uur

door

Maximilian Adrian

geboren op 29 juni 1987

te Aken, Duitsland

Promotor: Prof. dr. C. C. Hoogenraad

Copromotor: Dr. L. C. Kapitein

TABLE OF CONTENTS

Chapter 1 General Introduction	7
Chapter 2 Barriers in the Brain: Resolving Dendritic Spine Morphology and Compartmentalization	29
Chapter 3 Probing the Interplay between Dendritic Spine Morphology and Membrane-Bound Diffusion	53
Chapter 4 Positioning of AMPA Receptor-containing Endosomes Regulates Synapse Architecture	71
Chapter 5 Optogenetic Control of Organelle Transport and Positioning	103
Chapter 6 A Phytochrome-Derived Photoswitch for Intracellular Transport	131
Chapter 7 General Discussion	149
Addendum Summary Nederlandse samenvatting Zusammenfassung in deutscher Sprache Curriculum Vitae List of Publications Acknowledgements	167



General Introduction

Max Adrian

Division of Cell Biology, Faculty of Science, Utrecht University, Utrecht, The Netherlands.

INTRODUCTION

Cells are the basic unit of all life. A human body is made up of around thirty trillion (3×10^{13}) cells that all contribute to the proper functioning of our bodies (1). Divided in the organs of our body, there are more than one hundred cell types characterized, that specialize into different roles to make tissues functional. At the same time each cell is more than a static building block as it carries out complex processes like metabolism and replication. Therefore, the organization of the interior of the cell is not random and the proper spatial organization of the cell's organelles, lipids and proteins is very important for its survival and functionality. We are just beginning to understand this dynamic inner architecture of cells and this thesis aims to provide both new insights into cellular organisation and new technology to study the effects of organelle positioning.

In this introduction, I discuss some of the principles of cellular organisation. Next, I focus on the mechanisms that a cell can utilise to transport proteins and organelles to their destinations. Finally, the last section deals with recent developments in the methods that we can use as cell biologists to study intracellular compartmentalization and transport. This chapter ends with the scope of the thesis to show how the aspects highlighted here are related the research questions addressed.

SPATIAL ORGANIZATION OF THE CELL

Cells are more than mere bags of lipids and proteins. To fulfil their specific function in a tissue, many biochemical processes have to take place that require different enzymes and environments. Cells therefore use a three-fold spatial organisation strategy. First, biochemical processes are assigned to specialized cellular organelles. This division of labour reduces the complexity of reactions within the cell and facilitates different environments to carry out each task (Figure 1A). Second, the positioning of organelles with respect to each other is important to efficiently utilize or redistribute the products of the biochemical reactions. For many processes, different organelles need to interact (Figure 1B) and the importance of organelle contact sites is currently acknowledged by an increasing amount of studies (2). Thirdly, the absolute positioning of proteins and organelles into cellular domains is crucial to integrate cellular processes with the extracellular environment (Figure 1C). For example, secreted proteins are usually stored close to their release site or nutrient uptake and release are mediated by opposite cell membrane domains in polarized gut cells. For many organelles preferred localisations have been documented, but we still do not understand the significance and function of many of them (3).

Cellular organelles

Compartmentalization of proteins into organelles is best known for typical membrane-enclosed organelles as mitochondria, the endoplasmic reticulum, the Golgi apparatus, lysosomes, autophagosomes, endosomes and the nucleus. Each of them has a number of resident proteins and is enclosed with at least one lipid bilayer. This compartmentalization allows for a different chemical environment inside the organelle. Lysosomes, for example, have a lower luminal pH than the cytoplasm, which is required for protein degradation by proteases and prevents their activity elsewhere in the cell. This is achieved by proton pumps

in its membranes, acidifying the lysosomal lumen (4). Mitochondria on the other hand use proton pumps to create a membrane potential that allows for import of resident proteins and for oxidative respiration to generate energy (5).

Classically, the cytoplasm is seen as a general unstructured cellular compartment, but recent reports of phase transitions within the cytoplasm suggest that the cytoplasm is highly heterogeneous and is compartmentalized as well (6–8). Also the plasma membrane is an important cellular organelle. Not only does it form the barrier between cytosol and extracellular matrix, but it contains also many receptor proteins that relay information from the cells surrounding into biochemical signals that let the cell adapt. The model of the fluid mosaic membrane suggests that proteins can freely diffuse in the lipid bilayer, but it has become apparent that again many processes are confined in subdomains or lipid rafts e.g. to facilitate efficient coupling to intracellular signalling or external cues (9, 10). The precise nature of these subdomains and the underlying mechanisms that create them are in many cases still not well defined.

Between these cellular organelles, there is extensive traffic of various cargoes for example through the secretory and endosomal pathways. Membrane-associated and secreted proteins are synthesized in the Endoplasmic Reticulum from where they are transported to the Golgi apparatus after quality control processes. Passing through the Golgi stacks, proteins get sorted, modified and eventually packaged into secretory vesicles to be transported to the cell periphery. Once there, these vesicles can be fused with the plasma membrane to insert or secrete the proteins (11). The endocytic pathway takes up membrane proteins through endocytic vesicles that fuse into early endosomes. From there, proteins are sorted into either a degradation pathway, which ultimately ends in lysosomes, or a recycling pathway, from which proteins can be recovered and re-inserted into the membrane (12). The sorting of cargoes between these endosomal compartments is highly regulated (13), e.g. by stimuli from the environment (14), but for many transitions the sorting mechanisms remain to be uncovered.

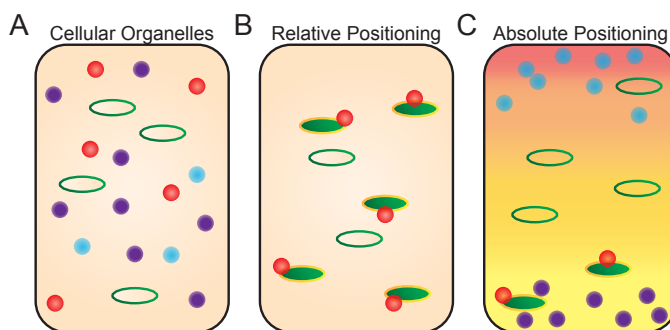


Figure 1 | Spatial compartmentalization in cells

(A) Different cellular organelles compartmentalize different biochemical reactions within a cell. **(B)** Relative positioning: Interactions between organelles convey new functions and allow exchange of proteins and lipids between compartments. **(C)** Absolute positioning: In polarized cells, certain organelles are localized into distinct cellular domains where they can interact with other organelles to carry out site-specific functions.

Each of these compartments is composed of different lipids and surface proteins, e.g. Rab GTPases, to organize their sorting and downstream effector proteins (13).

Moreover, endosomes also play an important role in signal transduction. Signalling endosomes contain activated membrane receptors whose signal is carried with the vesicle into the cytoplasm. Often the receptors revert to their off-state once internalized to limit downstream cascades but other times this signal can remain active and become re-localized within the cell to stimulate alternative signalling pathways (15). Much remains to be learned about the dynamics of membrane trafficking in space and time. While live-cell microscopy enabled us to follow these processes, the tools to manipulate specific organelles or even specific subsets of them have remained the bottleneck and the development of new techniques to study organelle functioning and positioning are needed (3).

Relative positioning of organelles: Organelle contact sites

Next to having specialized organelles that compartmentalize biochemical reactions, cells also coordinate the positioning of organelles and proteins. There are two aspects of organelle positioning: First, relative positioning of organelles towards each other facilitates organelle interactions at membrane contact sites, e.g. to exchange proteins and lipids. Secondly, organelles can have an absolute position with respect to the cell morphology. Especially in polarized cells, there are cellular domains that add another level of compartmentalization. Relative and absolute organelle positioning are explained in more detail in this and the following section, respectively.

Organelle contact sites have recently attracted much interest of the cell biology community. While contact sites have first been described in electron microscopy studies, live-cell imaging has revealed many unexpected dynamics in cell biology over the last couple of years, amongst which are the interactions of organelles (16, 17). An increasing amount of contact sites and mechanisms of interaction are revealed and is often found to be very dynamic in response to the cellular environment (18, 19). In fact many processes as signalling, apoptosis, organelle biogenesis or metabolism rely on crosstalk and interaction of organelles (2). These functions may rely on the exchange of cargoes between these organelles, e.g. fatty acids exchanged between peroxisomes, mitochondria and lipid droplets (20, 21), but also different mechanisms are important for cellular functioning. For example, fission of mitochondria and endosomes is regulated by contact sites with the endoplasmic reticulum (22, 23).

Following more organelles, if not all, with live-cell microscopy is currently a challenge for microscopists. In addition, next to observing organelle interactions, future studies are needed to better understand the context in which these interactions are required and what exact functions they serve in cells. To carry out such studies, sophisticated methods are required to prevent or induce specific contacts with high temporal precision.

Absolute positioning of organelles: Functional positioning of organelles

Polarized cells have different cellular domains. This is an additional form of compartmentalization that aligns cellular processes with the positioning of the cell in a tissue. Epithelial cells have an apical domain facing a lumen and a basolateral domain facing

neighbouring cells and the extracellular matrix. The function, composition and in some cases also the morphology of these membranes is very different and so are the organelles interacting with them (24). In secretory epithelia, for example, secreted proteins need to be collected in the lumen of the collecting duct. Therefore, all cells need to release their secretory vesicles at the apical membrane. The positioning of organelles at specific cellular domains is thus another important aspect of the spatial organization of a cell that influences cellular function (25).

Not only does cell polarization determine the positioning of organelles, but also other factors like nutrient gradients or local signals can attract certain organelles. For example, processes highly dependent on ATP, like release of neurotransmitters from a synapse, require positioning of mitochondria close to the release sites. In this case, mitochondrial positioning is regulated by elevated Ca^{2+} levels at these sites, which are sensed by adaptor and anchoring proteins and result in mitochondrial enrichment (26). In other cases mitochondrial motility has also been observed to follow glucose levels (27) or after injury mitochondria were observed to improve axonal regeneration (28). Moreover, correct positioning of the Golgi apparatus determines cell polarization in secreting and migrating cells (29) and regulated transport is crucial for the multiple functions of lysosomes (30). In some cases it still remains unclear whether organelle positioning is the cause or consequence of polarization. During cell division, positioning of organelles often changes drastically and many organelles temporarily redistribute and simultaneously change their function (31). In mitosis proper positioning of organelles is also crucial for their correct inheritance in daughter cells, especially in asymmetrically dividing stem cells (32). However, since manipulations to study this process have been technically very challenging until recently, we are just beginning to understand the importance of correct and dynamic organelle positioning in cells (3).

COMPARTMENTALIZATION IN NEURONS: DENDRITIC SPINES

Neurons are polarized cells that exhibit a remarkable morphology that underlies their functioning (Figure 2A). In order to build a meaningful network to process information, neurons need to distinguish between incoming and outgoing signals. Therefore neurons have a specialized morphology: The soma contains the nucleus and most of the protein synthesis machinery while the neurites are thin, long and branched protrusions that facilitate contacts with other neurons. Dendrites are the neurites that receive depolarizations as input from upstream neurons through the post-synapses that are positioned along them. Outgoing signals are sent through the axon, a single neurite that converts incoming depolarisations into action potentials and features pre-synapses that can release neurotransmitters onto many downstream neurons (33, 34). The somato-dendritic and axonal compartments are separated through the axon initial segment, a domain at the base of the axon that has important functions in protein sorting and action potential generation (35). At synapses the incoming action potentials are transformed into biochemical signals. The presynaptic terminal of the transmitting neuron and the post-synapse of the receiving neuron are separated by a small synaptic cleft. The electrical signal in the upstream neuron induces neurotransmitter release from the pre-synapse. After diffusing through the cleft, these molecules can bind receptors located in the post-synapse, which results in the generation of a small depolarization of the postsynaptic membrane.

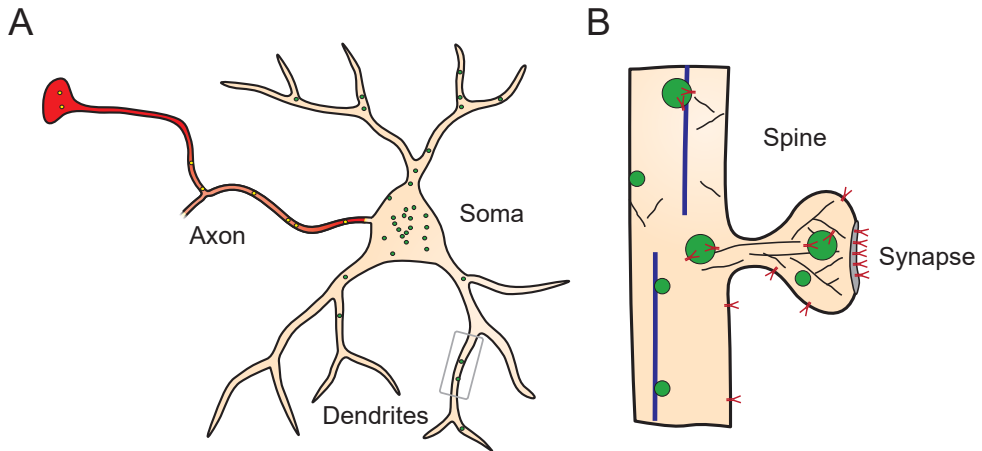


Figure 2 | Compartmentalization in neurons

(A) Schematic overview of the morphology of a neuron. The soma in the centre features several long protrusions called neurites. There is a single axon (red) that sends outgoing signals to downstream cells. All other neurites are dendrites that receive and compute incoming signals. These signals are received through synapses with upstream neurons that are located in dendritic spines. The composition of the axonal and somato-dendritic compartments differ as illustrated by endosomes carrying different cargoes. **(B)** Dendritic spines are small protrusions located along the dendrite containing the post-synapse in their head. Organelles and proteins can reach the synapse either by active transport along the microtubules and actin filaments or by lateral diffusion through the plasma membrane. Green: endosome, blue: microtubule, black: actin filaments, red: glutamate receptor.

Importantly, the excitatory synapses of hippocampal neurons are not formed on the dendritic shaft, but on the head of small protrusion called dendritic spines (Figure 2B). Mature spines have a mushroom-like shape: The spine head contains the glutamate receptors as well as the scaffold and signalling domain called the postsynaptic density and is connected to the dendritic shaft through a thin neck (36). Because of their morphology, dendritic spines form small individual compartments along the dendrite, that are important for regulating synaptic strength (37, 38). This strength depends mostly on the amount of glutamate receptors present in a synapse and is thought to underlie basic cognitive functions as memory formation and learning (39). To regulate synaptic strength on a single spine level two parameters must be controlled locally: First, to increase synaptic strength or to replace receptor turnover, new receptors must be able to reach the synapse. Second, to maintain the synaptic strength mechanisms must be in place to retain receptors and keep their amount stable over prolonged times.

The morphology of dendritic spines limits exchange of cytoplasmic proteins with the dendritic shaft. This allows to compartmentalize their signalling proteins and to maintain their signalling capacity (38, 40–42). Synaptic input can modulate the extent to which this compartmentalization limits protein exchange through the cytoplasm (43). However, glutamate receptors are transmembrane proteins that can reach the synapse in two ways.

Either they diffuse through the plasma membrane into spines where they can get incorporated into the postsynaptic density, or they can be exocytosed locally in spines from recycling endosomes. Whereas both routes have been demonstrated to contribute to glutamate receptor transport to synapses (44), it is still not clear what the relative contribution of each pathway is or if the supply mechanism depends on neuronal activity. Moreover, the dynamics and regulation of endosomal glutamate receptor pools in dendrites and spines have not yet been studied extensively.

INTRACELLULAR TRANSPORT MECHANISMS

To bring organelles and proteins to their site of action, cells can utilize different transport mechanisms. Active transport moves cargoes along the cytoskeleton using chemical energy to power motor proteins resulting in selective and directed long-range transport. Passive transport is less directional and relies on the diffusion of cargo through the cytoplasm or membrane by thermal energy, but is by itself unable to generate asymmetric cargo concentrations or mediate efficient long-distance transport (45).

Passive transport

Diffusion depends on Brownian motion generated by thermal excitation of a protein either in the cytoplasm or in the lipid bi-layer of membranes. Chapters 2 and 3 of this thesis focus on membrane-bound diffusion in dendritic spines and specifically how spine morphology may play a role in retaining glutamate receptors.

Generally, the plasma membrane is classically characterized as a fluid mosaic in which proteins can diffuse more or less freely in a lipid bilayer. While the size of a protein dictates its diffusive speed, the environment also influences it. Crowded environments slow diffusion rates of similar sized particles and the composition of lipids in a membrane can change the diffusion rates of membrane-bound proteins or even capture them within lipid rafts (10). In addition, proteins can encounter other proteins or physical barriers (46, 47).

The diffusion of neurotransmitter receptors along dendrites has been studied for several decades making use of many techniques either measuring bulk diffusion, or movements of single molecules (48–50). Activity regulated retention of diffusive glutamate receptor in hippocampal synapses has become a widely accepted model for regulation of synaptic strength (51, 52). The postsynaptic density, a protein-dense meshwork of adaptor proteins in dendritic spines, is thought to slow diffusion of these receptors through interactions with scaffolding proteins that are regulated by synaptic activity (53–55). Next to direct interactions of receptors and scaffold proteins at synaptic domains (9, 56), retention of glutamate receptors is also influenced by molecular crowding (57), synaptic nanodomains (9), interactions with the cytoskeleton (58) and membrane morphology (59, 60). A further detailed discussion of how dendritic spines compartmentalize the post-synapse is provided in Chapter 2. Recently, theoretical and numerical studies demonstrated that the thin necks of mushroom-like dendritic spines may further impact diffusion speeds of glutamate receptors and their retention at the synapse (61). While earlier studies have shown that stubby spines exchange have faster exchange of membrane-bound probes (60), there have not been any experimental studies to directly test the influence of spine morphology, in particular of the spine neck

diameter, on membrane-bound diffusion.

Active transport

To transport cargoes over wider distances or to specifically target them to a subcellular domain, directed active transport is necessary (45). This form of transport relies on motor proteins that use chemical energy in the form of ATP to move cargo along microtubules and actin filaments.

The cytoskeleton

Motor proteins can transport cargo along two different filaments in cells: microtubules and actin. Microtubules are long fibres, which reach lengths in the order of several microns and are 25nm wide (62). They are made of α - and β -tubulin dimers that assemble head-on into 13 protofilaments, resulting in an overall polarity of the microtubule, exposing a β -tubulin subunit at the plus-end (63, 64). Importantly, microtubules are not static, but they continuously grow and shrink at their ends. The more dynamic plus-end of the microtubule undergoes rapid growth phases and catastrophes, a process called dynamic instability, during which tubulin dimers are added or removed, respectively (65, 66). These dynamics are important for many cellular functions, such as cell migration, formation of the mitotic spindle or cell polarization and organelle positioning (67, 68).

Actin filaments (also called f-actin) are made of actin monomers that assemble into two intertwined strands. Like microtubules, the asymmetry of the monomers imposes an overall polarity on the fibre and we distinguish between the barbed and pointed end. In contrast to microtubules, in which the dynamics are nearly restricted to the plus end, actin filaments undergo treadmilling. Actin monomers are continuously added to the barbed end while the pointed end dissociates. The rates of these two reactions determine whether the filament grows, shrinks or maintains its length. But even in the latter case the individual actin monomers are rapidly exchanged (69, 70).

Actin fibres can be assembled into different types of lattices: Anti-parallel actin fibres allow myosin motors to slide them along each other to induce contractility, for example in muscle cells. Parallel fibres often form protrusions of the cell membrane, as in filopodia or dendritic spines. Lastly, branched actin as often found in lamellipodia can be used to push cells forward (70). These different lattices are the result of an intricate network of actin polymerizing enzymes and their regulators.

The orientation of the cytoskeleton is important for the directionality of motor based transport and this orientation mostly depends on the site of nucleation. In many unpolarised cells, the centrosome nucleates the majority of microtubules. The resulting radial array of microtubules is therefore oriented with their plus-ends towards the cell periphery (71). In dividing cells it has been shown that stabilization of microtubules minus ends at one spindle pole can induce asymmetrical organelle distribution in the daughter cells (72). The cytoskeletal arrangement serves as tracks for all active transport and thus needs to be adapted to cellular functions.

In polarized cells, the microtubule orientation is often regulated differently. For example, in

the epithelium, microtubules are arranged parallel to the cells axis, with minus-ends at the apical side. Such an arrangement allows for efficient transport to and from the apical and basal membranes, facilitating the cell's function to absorb or secrete molecules (24, 73). At the apical membrane, the brush border is made out of many actin rich microvilli, protrusions that highly amplify the surface and therefore allow efficient nutrient uptake (74). The actin-rich terminal web just below the microvilli may furthermore anchor important signalling and recycling compartments at the apical membrane (75).

In neurons, most microtubules are not organized by the centrosome (76). In the axon, microtubules are oriented uniformly with their plus-end towards the growth cone, while dendrites have a mixed microtubule orientation (77, 78). How this particular arrangement of microtubule polarity is set-up or maintained is a topic of ongoing research, but it might explain how cargoes can be trafficked preferably into the axon or dendrites (79, 80). The actin cytoskeleton is important for the plasticity of dendritic spines, the dynamics of the growth cones and the axon initial segment, where it may help in cargo sorting (80–82). Furthermore, recent super-resolution imaging revealed previously unknown actin rings that are thought to stabilize neurite calibre (83). Advances in nanoscopy (see below) now let us understand the architecture of the cytoskeleton. Innovative approaches are currently developed to understand which cargoes chose which cytoskeletal tracks (84). Combined imaging of the cytoskeleton and active transport will further help us decipher the mechanisms that govern the directionality of active transport in cells.

Motor proteins

Along the microtubule and actin fibres, motor proteins can move cargoes forward. There are three major families of motor proteins in mammalian cells: Kinesins and dyneins generally move towards the plus and minus end of microtubules, respectively, while myosins move into different directions on actin fibres (85–87). Usually motor proteins are dimers that have a motor domain that binds to actin or tubulin and a tail domain that binds the cargo either directly or through adapter proteins, linked with coiled-coil stalk that allows for inactivation or regulation by co-factors. By hydrolysing ATP, one of the motor domains can let go of the cytoskeleton and step forward using its power stroke. The step size depends on the length of the neck linker and the structure of the fibre. Kinesins move with 8nm steps from one tubulin monomer to the next in a hand-over-hand fashion (88). Myosins vary in their linker length and rotation angle and have step sizes from 7 to 36 nanometres that can be modified experimentally through molecular engineering (89, 90). The molecular structure of dynein is more complex and requires several adaptors and binding proteins to show processive transport in steps of 8 to 32 nm (91, 92).

Interestingly, although there are 45 mammalian kinesins and 40 myosins known, there are only 2 cytoplasmic dyneins described in the literature (93, 94). The large variety of kinesins allows for different motors with specific characteristics in the speed, processivity or cargo binding abilities to perform different functions. In addition, adapter proteins form another layer of regulation on motor based transport along with many regulatory proteins that can activate the right motor proteins for a given situation. Such regulatory proteins also allow dynein to adjust its speed and processivity. Also, not all members of these superfamilies are constitutive motors carrying cargoes. Some members of the kinesin family have different

functions like regulating the dynamics of microtubule or sliding them along each other (86).

Larger cargoes, e.g. organelles, generally have more than one motor protein attached. Most even bind a variety of motors that have to be coordinated for efficient transport along different types of cytoskeleton the cargo may have to pass. The speed and processivity of this transport depends on the constellation and interaction of these motor proteins (95–97) but also on the available microtubule and actin fibre orientation and crossings (84). While generally being slower motors than kinesins, myosins have also been characterized as tethers, especially in the actin-dense cell cortex (98).

Without going into further molecular detail, it should be apparent that the combination of a large variety of motor proteins together with an organized and regulated cytoskeletal arrangement, equips the cell with the means to transport specific cargoes like proteins, organelles or mRNA to their local site of action. However, for many processes, e.g. the transport of glutamate receptors into dendritic spines, the relative importance of transport along the different cytoskeletal fibres remains unclear.

EMERGING METHODS TO STUDY INTRACELLULAR TRANSPORT

Transport and compartmentalization in cells are dynamic processes. As any dynamic process it is difficult to study its details from static readouts such as microscopy pictures or biochemistry. To comprehensively understand cellular transport, it needs to be studied in living cells with adequate spatial and temporal resolution. In this section, different active-illumination or advanced light-microscopy techniques are briefly introduced that greatly influenced our studies of intracellular transport. Active illumination refers to the use of light in microscopy experiments for other uses than to generate the image. Light can be used to either manipulate the probe that is imaged (i.e. the fluorescent label) or the cellular structure itself. The first option usually allows to deduct dynamic properties of the labelled protein, e.g. its diffusion speed, turnover or migration pattern, whereas the latter allows to induce changes to the system, e.g. by inducing damage with microsurgery or optogenetic stimulation of a certain process.

Here, three methods are discussed that are important to study the biological questions raised above: To follow dynamic pools of organelles or to measure diffusion time scales of glutamate receptors in dendritic spines, active illumination techniques like photobleaching and photoconversion are necessary. Because dendritic spines are very small, conventional light microscopy is insufficient to resolve their exact morphology. Single-molecule localisation microscopy offers the necessary nanoscopic resolution and is compatible with live-cell imaging. Finally, optogenetic methods are introduced as a novel and versatile toolbox to stimulate and manipulate cellular processes.

Measuring protein dynamics in cells

While usually seen as a disadvantage of fluorescence microscopy, photobleaching can also be actively used as an advantage in live-cell imaging. Since we are interested in studying endosomal transport in dendrites, we need to quantify a dynamic process in a region with dense fluorescent signals. Bleaching an area of the dendrite reduces this background signal

and subsequently only the pool of vesicles moving into the bleached area can be followed. While background signal and signal coming from stationary vesicles is bleached, this approach enhances the contrast of the moving vesicles which enables quantification of e.g. vesicle speeds or abundance. The same approach has been used to visualize discrete events of membrane receptor exocytosis that otherwise would have been too dim to distinguish from the membrane-bound pool of the same receptors (99–101).

Fluorescence recovery after photobleaching (FRAP) is one of the most used active illumination techniques. By bleaching the fluorescent label on a given protein in a small area of the cell and following the subsequent recovery of fluorescence intensity, we can follow the timescale at which the bleached proteins are replaced with new, unbleached ones. Plotting fluorescence intensity against time allows for the easy readout of the timescale of replenishment and also shows the size of the immobile fraction. This is the amount of fluorescence loss attributed to non-exchanging proteins (102). As an extension of FRAP, Fluorescence loss in photobleaching (FLIP) was developed as a tool to study the extent of bleached organelle networks. Early applications showed e.g. that the ER is made of a single continuous membrane (103).

Photoconversion is a further development of this technique. Instead of using high intensity illumination to bleach fluorophores, here the emission spectrum of a fluorescent protein is changed, typically by illumination with low intensities of UV light. There is a growing number of photoconvertible or photoswitchable fluorescent proteins available that can be switched between different fluorescent states e.g., from green to red emission peaks or from dark to fluorescent states. These proteins can then be used to highlight proteins, organelles or entire cells to follow their dynamics in crowded environments.

Single-Molecule Localization Microscopy

Photoconvertible fluorescent proteins can also be used for photoactivated localisation microscopy (PALM), a single molecule localization microscopy technique that enables imaging with nanoscopic resolution (104). Diffraction limits the resolution of conventional light microscopy to approximately 200nm, because fluorophores located closer together cannot be resolved as individual objects. Through sparse illumination with UV light, at any time a stochastic subset of proteins will be converted. By imaging only these single molecules, the fluorophores' centroids can be fitted with subpixel resolution. Repeating this process over several thousand frames and plotting all resulting localisations results in a super-resolved reconstruction of the original image (105). For example the morphology of dendritic spines or the actin cytoskeleton within spines has now been shown using these techniques in living cells or *in vivo* (106–109).

Optogenetics

Optogenetics has revolutionized the precision with which neuronal circuits and electrophysiological stimulations can be studied in the brain (110). This advance was mostly driven by the development of light-activated ion-channels, in particular the channelrhodopsins, that can be expressed in neurons and let them generate action potentials in response to illumination. By now, all-optical systems have been set up that allow stimulation and read out of neuronal activity with a fluorescence microscope without the need for any

electrodes (111). But also the fields of cell and developmental biology have profited from advances in light-sensitive stimulation techniques. The main advantage of optogenetic manipulations is the unprecedented spatiotemporal control over cellular functions as laser light can be targeted very precisely. Several photosensitive domains originating from plants or bacteria have been adapted for use in cell biology that react with a conformational change to different wavelengths of light (112). Applications include light-inducible protein secretion, signal cascade activation, enzyme uncaging, protein relocalization and regulation of gene expression amongst others (113–119).

One widely used concept is that of light-induced dimerization. Using two protein domains that dimerize upon illumination, protein-protein interactions can be induced in an area of interest. There are already several optogenetic dimerizers described in the literature, each with its own sensitivity, wavelengths and on/off kinetics that are suited for different applications. Compared to chemical heterodimerization systems (120), which require an exogenous compound to bind two protein domains, the dimerization speed of optogenetic systems is much faster and lies in the range of seconds rather than minutes. They vary in their ability of reverting to their dark non-interacting state, another feature that is not possible with chemical dimerizers (3).

Currently, there are a number of different light-sensitive dimerization modules characterized and used for cell-biological applications. The UV-sensitive UVR8 domains form homodimers in the dark that release upon illumination and have been used to control protein secretion (121). There are a range of blue light-sensitive protein domains derived of two plant flavoprotein families. The plant cryptochrome CRY2 gained much interest as a light-inducible heterodimer with CIB1 (122). However, the bulkiness of these domains and their tendency to oligomerize are disadvantageous in many applications. The light-oxygen-voltage-sensing (LOV) domains are smaller blue light-sensitive domains that change the conformation of a peptide helix upon illumination. This conformational change has been used to create light-sensitive caging domains that block the active site of an actin-polymerizing enzyme or an inositol 5-phosphatase in the absence of light (116, 123). There are also more generic applications of LOV domains for dimerization assays. The VIVID system can be used as blue light-sensitive homodimers (124) or, if further mutated to Magnet domains, as heterodimers (125). The best characterized blue-light system to date are the Tuneable, Light-controlled Interacting Protein tags (TULIPs). In response to illumination with blue light, this series of dimerization domains with different affinities and dissociation kinetics can be used for many diverse applications (118). It exploits the conformational change of the LOV domain to expose a small carboxy-terminal peptide that can interact with an engineered PDZ domain. Recently, this system has been further developed by adding bacterial interacting domains, of which one is caged in the dark condition. Subsequent rational mutagenesis of these iLID domains resulted in an increased range of affinities compared to the TULIPs. (126, 127). Lastly, the class of red light-inducible phytochrome-based dimers have the additional advantage that they are photoswitchable: Illumination with 625nm light allows binding of PhyB with its interaction partner, while 750nm light actively induces rapid dissociation of the domains (128). Recently bacterial phytochromes have been described in the literature with similar photoswitchable characteristics that do no longer require exogenous cofactors (129). Thus, this optogenetic toolbox allows precise spatio-temporal manipulation of cells and can be combined with live-cell imaging or biochemical assays to read out the effects.

To study the effect of organelle positioning, optogenetic dimerization domains could be coupled to the organelle of interest and a motor protein with known directionality to locally and temporally change the position of the organelle. A similar approach has been developed for chemical heterodimerization (79, 98) and recently all kinesins have been screened for their behaviour in this assay (130). Making organelle repositioning light-inducible would extend our abilities in manipulating cellular trafficking and organelle positioning to study their effects on cellular processes. However, it has not yet been shown whether light-inducible dimers can withstand the pulling forces of the motor domains, which light-inducible dimerization domains would perform best and how reversible and controllable the optogenetic stimulations are. Additionally, to study organelle interactions it needs to be established if orthogonal optogenetic dimers can be used in combination with multi-colour fluorescence imaging.

SCOPE OF THIS THESIS

As described above, cells use several mechanisms to make sure that proteins and organelles are transported to their site of action. In this thesis, advanced (live) cell imaging has been used to study these transport processes. First, we studied the compartmentalization of dendritic spines in neuronal cells. **Chapter 2** reviews the literature supporting the concept that dendritic spines are functional compartments, responsible for the local computation of electrical and biochemical signals along a dendrite. Moreover, we discuss the evidence that spines can also compartmentalize pools of glutamate receptors in the plasma membrane – a function that could be important for synaptic plasticity. **Chapter 3** tests one way in which this compartmentalization may be established. We hypothesized that the distinct mushroom-like shape of mature dendritic spines may be an important factor in the ability of a spine to retain membrane proteins at the synapse. Combining super-resolution imaging and photoconversion measurements, we correlated spine morphology and membrane-bound diffusion rates in living dendritic spines. We also used the nanoscopic morphology measurements to run particle simulations on the surface of real spine shapes to compare them to our experiments in order to evaluate the impact of spine morphology on diffusion speeds.

The supply of glutamate receptors to the synapse does not only rely on diffusion through the plasma membrane. They are also transported to dendritic spines in recycling endosomes but the relative importance of these two pathways had been debated in the literature. **Chapter 4** characterizes endosomal recycling routes in dendrites and spines. We investigated the delivery dynamics of endosomes along the cytoskeleton in dendrites and dendritic spines. Using chemically-induced hetero-dimerization to move recycling endosomes out of spines, we investigated whether intracellular pools of glutamate receptors in recycling endosomes have an impact on synaptic architecture and spine morphology.

To manipulate positioning of recycling endosomes locally and reversibly, we established an optogenetic tool to couple organelles to motor proteins in **Chapter 5**. We tested two optogenetic dimerization domains for their ability to relocate recycling endosomes and peroxisomes into spines with high spatiotemporal control. Moreover, we investigated the requirement of local pools of recycling endosomes in growth cones for axonal outgrowth. **Chapter 6** is dedicated to further refine our optogenetic tools to reposition cellular organelles. Using phytochromes instead of LOV domains, made the dimerization of organelle and motor photoswitchable. Illumination with far-red light dissociates the two domains making the system insensitive to illumination used for fluorescence imaging and allowed for even better spatio-temporal control. **Chapter 7** concludes this thesis with a summary of the key results and a discussion of outstanding research questions.

REFERENCES

1. Sender, R., S. Fuchs, and R. Milo. 2016. Revised Estimates for the Number of Human and Bacteria Cells in the Body. *PLOS Biol.* 14: e1002533.
2. Schrader, M., L.F. Godinho, J.L. Costello, and M. Islinger. 2015. The different facets of organelle interplay-an overview of organelle interactions. *Front. cell Dev. Biol.* 3: 56.
3. van Bergeijk, P., C.C. Hoogenraad, and L.C. Kapitein. 2016. Right Time, Right Place: Probing the Functions of Organelle Positioning. *Trends Cell Biol.* 26: 121–34.
4. Mindell, J.A. 2012. Lysosomal acidification mechanisms. *Annu Rev Physiol.* 74: 69–86.
5. Kulawiak, B., J. Höpker, M. Gebert, B. Guiard, N. Wiedemann, and N. Gebert. 2013. The mitochondrial protein import machinery has multiple connections to the respiratory chain. *Biochim. Biophys. Acta - Bioenerg.* 1827: 612–626.
6. Hyman, A.A., C.A. Weber, and F. Jülicher. 2014. Liquid-liquid phase separation in biology. *Annu. Rev. Cell Dev. Biol.* 30: 39–58.
7. Hyman, A.A., and K. Simons. 2012. Cell biology. Beyond oil and water--phase transitions in cells. *Science.* 337: 1047–9.
8. Lee, C.F., C.P. Brangwynne, J. Gharakhani, A.A. Hyman, and F. Jülicher. 2013. Spatial organization of the cell cytoplasm by position-dependent phase separation. *Phys. Rev. Lett.* 111: 88101.
9. MacGillavry, H.D., Y. Song, S. Raghavachari, and T.A. Blanpied. 2013. Nanoscale Scaffolding Domains within the Postsynaptic Density Concentrate Synaptic AMPA Receptors. *Neuron.* 78: 615–622.
10. Ziółkowska, N.E., R. Christiano, and T.C. Walther. 2012. Organized living: Formation mechanisms and functions of plasma membrane domains in yeast. *Trends Cell Biol.* 22: 151–158.
11. Bonifacino, J.S., and B.S. Glick. 2004. The Mechanisms of Vesicle Budding and Fusion. *Cell.* 116: 153–166.
12. Grant, B.D., and J.G. Donaldson. 2009. Pathways and mechanisms of endocytic recycling. *Nat. Rev. Mol. Cell Biol.* 10: 597–608.
13. Stenmark, H. 2009. Rab GTPases as coordinators of vesicle traffic. *Nat. Rev. Mol. Cell Biol.* 10: 513–25.
14. Ehlers, M.D. 2000. Reinsertion or Degradation of AMPA Receptors Determined by Activity-Dependent Endocytic Sorting. *Neuron.* 28: 511–525.
15. Schmiege, N., G. Menendez, G. Schiavo, and M. Terenzio. 2014. Signalling endosomes in axonal transport: travel updates on the molecular highway. *Semin. Cell Dev. Biol.* 27: 32–43.
16. Murley, A., and J. Nunnari. 2016. The Emerging Network of Mitochondria-Organelle Contacts. *Mol. Cell.* 61: 648–653.
17. Shai, N., M. Schuldiner, and E. Zalckvar. 2016. No peroxisome is an island - Peroxisome contact sites. *Biochim. Biophys. Acta - Mol. Cell Res.* 1863: 1061–1069.
18. Poüs, C., and P. Codogno. 2011. Lysosome positioning coordinates mTORC1 activity and autophagy. *Nat. Cell Biol.* 13: 342–344.
19. Korolchuk, V.I., S. Saiki, M. Lichtenberg, F.H. Siddiqi, E.A. Roberts, S. Imarisio, L. Jahreiss, S. Sarkar, M. Futter, F.M. Menzies, C.J. O’Kane, V. Deretic, and D.C. Rubinsztein. 2011. Lysosomal positioning coordinates cellular nutrient responses. *Nat. Cell Biol.* 13: 453–60.
20. Rambold, A.S., S. Cohen, and J. Lippincott-Schwartz. 2015. Fatty acid trafficking in starved cells: Regulation by lipid droplet lipolysis, autophagy, and mitochondrial fusion dynamics. *Dev. Cell.* 32: 678–692.
21. Chu, B.B., Y.C. Liao, W. Qi, C. Xie, X. Du, J. Wang, H. Yang, H.H. Miao, B.L. Li, and B.L. Song. 2015. Cholesterol transport through lysosome-peroxisome membrane contacts. *Cell.* 161: 291–306.
22. Friedman, J.R., L.L. Lackner, M. West, J.R. DiBenedetto, J. Nunnari, and G.K. Voeltz. 2011. ER tubules mark sites of mitochondrial division. *Science.* 334: 358–62.
23. Rowland, A.A., P.J. Chitwood, M.J. Phillips, and G.K. Voeltz. 2014. ER contact sites define the position and timing of endosome fission. *Cell.* 159: 1027–1041.
24. Rodriguez-Boulan, E., G. Kreitzer, and A. Müsch. 2005. Organization of vesicular trafficking in epithelia. *Nat.*

- Rev. Mol. Cell Biol. 6: 233–47.
25. Bornens, M. 2008. Organelle positioning and cell polarity. *Nat. Rev. Mol. Cell Biol.* 9: 874–886.
 26. Wang, X., and T.L. Schwarz. 2009. The Mechanism of Ca²⁺-Dependent Regulation of Kinesin-Mediated Mitochondrial Motility. *Cell.* 136: 163–174.
 27. Pekkurnaz, G., J.C.C. Trinidad, X. Wang, D. Kong, and T.L.L. Schwarz. 2014. Glucose Regulates Mitochondrial Motility via Milton Modification by O-GlcNAc Transferase. *Cell.* 158: 54–68.
 28. Zhou, B., P. Yu, M.Y. Lin, T. Sun, Y. Chen, and Z.H. Sheng. 2016. Facilitation of axon regeneration by enhancing mitochondrial transport and rescuing energy deficits. *J. Cell Biol.* 214: 103–119.
 29. Yadav, S., S. Puri, and A.D. Linstedt. 2009. A primary role for Golgi positioning in directed secretion, cell polarity, and wound healing. *Mol. Biol. Cell.* 20: 1728–36.
 30. Pu, J., C.M. Guardia, T. Keren-Kaplan, and J.S. Bonifacino. 2016. Mechanisms and functions of lysosome positioning. *J. Cell Sci.* 129: 4329–4339.
 31. Jongsma, M.L.M., I. Berlin, and J. Neefjes. 2015. On the move: organelle dynamics during mitosis. *Trends Cell Biol.* 25: 112–24.
 32. Knoblach, B., and R.A. Rachubinski. 2015. Motors, Anchors, and Connectors: Orchestrators of Organelle Inheritance. *Annu. Rev. Cell Dev. Biol.* 31: 55–81.
 33. Dotti, C.G., C.A. Sullivan, and G.A. Banker. 1988. The establishment of polarity by hippocampal neurons in culture. *J. Neurosci.* 8: 1454–68.
 34. Goslin, K., and G. Banker. 1989. Experimental observations on the development of polarity by hippocampal neurons in culture. *J. Cell Biol.* 108: 1507–1516.
 35. Rasband, M.N. 2010. The axon initial segment and the maintenance of neuronal polarity. *Nat. Rev. Neurosci.* 11: 552–562.
 36. Sorra, K.E., and K.M. Harris. 2000. Overview on the structure, composition, function, development, and plasticity of hippocampal dendritic spines. *Hippocampus.* 10: 501–11.
 37. Grunditz, A., N. Holbro, L. Tian, Y. Zuo, and T.G. Oertner. 2008. Spine Neck Plasticity Controls Postsynaptic Calcium Signals through Electrical Compartmentalization. *J. Neurosci.* 28: 13457–13466.
 38. Harvey, C.D., R. Yasuda, H. Zhong, and K. Svoboda. 2008. The spread of Ras activity triggered by activation of a single dendritic spine. *Science.* 321: 136–40.
 39. Huganir, R.L., and R. Nicoll. 2013. AMPARs and Synaptic Plasticity: The Last 25 Years. *Neuron.* 80: 704–17.
 40. Tønnesen, J., G. Katona, B. Rózsa, and U.V. Nägerl. 2014. Spine neck plasticity regulates compartmentalization of synapses. *Nat. Neurosci.* 17: 678–685.
 41. Lee, S.-J.R., Y. Escobedo-Lozoya, E.M. Szatmari, and R. Yasuda. 2009. Activation of CaMKII in single dendritic spines during long-term potentiation. *Nature.* 458: 299–304.
 42. Colgan, L. a, and R. Yasuda. 2014. Plasticity of Dendritic Spines: Subcompartmentalization of Signaling. *Annu. Rev. Physiol.* 76: 365–385.
 43. Bloodgood, B.L., and B.L. Sabatini. 2005. Neuronal activity regulates diffusion across the neck of dendritic spines. *Science.* 310: 866–9.
 44. Opazo, P., and D. Choquet. 2011. A three-step model for the synaptic recruitment of AMPA receptors. *Mol. Cell. Neurosci.* 46: 1–8.
 45. Vale, R.D. 2003. The molecular motor toolbox for intracellular transport. *Cell.* 112: 467–480.
 46. Singer, S.J., and G.L. Nicolson. 1972. The fluid mosaic model of the structure of cell membranes. *Science.* 175: 720–31.
 47. Kusumi, A., C. Nakada, K. Ritchie, K. Murase, K. Suzuki, H. Murakoshi, R.S. Kasai, J. Kondo, and T. Fujiwara. 2005. Paradigm shift of the plasma membrane concept from the two-dimensional continuum fluid to the partitioned fluid: high-speed single-molecule tracking of membrane molecules. *Annu. Rev. Biophys. Biomol. Struct.* 34: 351–378.
 48. Axelrod, D., D.E. Koppel, J. Schlessinger, E. Elson, and W.W. Webb. 1976. Mobility measurement by analysis

- of fluorescence photobleaching recovery kinetics. *Biophys. J.* 16: 1055–1069.
49. Axelrod, D., P. Ravdin, D.E. Koppel, J. Schlessinger, W.W. Webb, E.L. Elson, and T.R. Podleski. 1976. Lateral motion of fluorescently labeled acetylcholine receptors in membranes of developing muscle fibers. *Proc. Natl. Acad. Sci. U. S. A.* 73: 4594–8.
 50. Young, S.H., and M.M. Poo. 1983. Rapid lateral diffusion of extrajunctional acetylcholine receptors in the developing muscle membrane of *Xenopus* tadpole. *J. Neurosci.* 3: 225–31.
 51. Triller, A., and D. Choquet. 2005. Surface trafficking of receptors between synaptic and extrasynaptic membranes: and yet they do move! *Trends Neurosci.* 28: 133–9.
 52. Makino, H., and R. Malinow. 2009. AMPA receptor incorporation into synapses during LTP: the role of lateral movement and exocytosis. *Neuron.* 64: 381–90.
 53. Borgdorff, A.J., and D. Choquet. 2002. Regulation of AMPA receptor lateral movements. *Nature.* 417: 649–53.
 54. Tardin, C., L. Cognet, C. Bats, B. Lounis, and D. Choquet. 2003. Direct imaging of lateral movements of AMPA receptors inside synapses. *EMBO J.* 22: 4656–65.
 55. Ehlers, M.D., M. Heine, L. Groc, M. Lee, and D. Choquet. 2007. Diffusional trapping of GluR1 AMPA receptors by input-specific synaptic activity. *Neuron.* 54: 447–60.
 56. Sheng, M., and C.C. Hoogenraad. 2007. The postsynaptic architecture of excitatory synapses: a more quantitative view. *Annu. Rev. Biochem.* 76: 823–47.
 57. Santamaria, F., J. Gonzalez, G.J. Augustine, and S. Raghavachari. 2010. Quantifying the effects of elastic collisions and non-covalent binding on glutamate receptor trafficking in the post-synaptic density. *PLoS Comput. Biol.* 6: e1000780.
 58. Richards, D. a, V. De Paola, P. Caroni, B.H. Gähwiler, and R. a McKinney. 2004. AMPA-receptor activation regulates the diffusion of a membrane marker in parallel with dendritic spine motility in the mouse hippocampus. *J. Physiol.* 558: 503–12.
 59. Holcman, D., and A. Triller. 2006. Modeling synaptic dynamics driven by receptor lateral diffusion. *Biophys. J.* 91: 2405–15.
 60. Ashby, M.C., S.R. Maier, A. Nishimune, and J.M. Henley. 2006. Lateral diffusion drives constitutive exchange of AMPA receptors at dendritic spines and is regulated by spine morphology. *J. Neurosci.* 26: 7046–55.
 61. Kusters, R., L.C. Kapitein, C.C. Hoogenraad, and C. Storm. 2013. Shape-Induced Asymmetric Diffusion in Dendritic Spines Allows Efficient Synaptic AMPA Receptor Trapping. *Biophys. J.* 105: 2743–2750.
 62. Tilney, L.G., J. Bryan, D.J. Bush, K. Fujiwara, M.S. Mooseker, D.B. Murphy, and D.H. Snyder. 1973. Microtubules: evidence for 13 protofilaments. *J. Cell Biol.* 59: 267–75.
 63. Bryan, J., and L. Wilson. 1971. Are cytoplasmic microtubules heteropolymers? *Proc. Natl. Acad. Sci. U. S. A.* 68: 1762–6.
 64. Ledbetter, M.C., and K.R. Porter. 1964. Morphology of Microtubules of Plant Cell. *Science.* 144: 872–4.
 65. Akhmanova, A., and M.O. Steinmetz. 2008. Microtubule structure and dynamic instability. *Nat. Rev. Mol. Cell Biol.* 9: 309–322.
 66. Mitchison, T., and M. Kirschner. 1984. Dynamic instability of microtubule growth. *Nature.* 312: 237–42.
 67. Fletcher, D.A., and R.D. Mullins. 2010. Cell mechanics and the cytoskeleton. *Nature.* 463: 485–492.
 68. De Forges, H., A. Bouissou, and F. Perez. 2012. Interplay between microtubule dynamics and intracellular organization. *Int. J. Biochem. Cell Biol.* 44: 266–274.
 69. Pollard, T.D., and J.A. Cooper. 2009. Actin, a central player in cell shape and movement. *Science.* 326: 1208–12.
 70. Blanchoin, L., R. Boujemaa-Paterski, C. Sykes, and J. Plastino. 2014. Actin dynamics, architecture, and mechanics in cell motility. *Physiol. Rev.* 94: 235–63.
 71. Schneider, M., W. Lu, S. Neumann, A. Brachner, J. Gotzmann, A.A. Noegel, and I. Karakesisoglou. 2011. Molecular mechanisms of centrosome and cytoskeleton anchorage at the nuclear envelope. *Cell. Mol. Life*

- Sci. 68: 1593–1610.
72. Derivery, E., C. Seum, A. Daeden, S. Loubéry, L. Holtzer, F. Jülicher, and M. Gonzalez-Gaitan. 2015. Polarized endosome dynamics by spindle asymmetry during asymmetric cell division. *Nature*. 528: 280–285.
 73. Bacallao, R., C. Antony, C. Dotti, E. Karsenti, E.H. Stelzer, and K. Simons. 1989. The subcellular organization of Madin-Darby canine kidney cells during the formation of a polarized epithelium. *J. Cell Biol.* 109: 2817–32.
 74. Walton, K.D., A.M. Freddo, S. Wang, and D.L. Gumucio. 2016. Generation of intestinal surface: an absorbing tale. *Development*. 143: 2261–2272.
 75. Goldenring, J.R. 2015. Recycling endosomes. *Curr. Opin. Cell Biol.* 35: 117–122.
 76. Yau, K.W., S.F.B. vanBeuningen, I. Cunha-Ferreira, B.M.C. Cloin, E.Y. vanBattum, L. Will, P. Schätzle, R.P. Tas, J. vanKrugten, E.A. Katrukha, K. Jiang, P.S. Wulf, M. Mikhaylova, M. Harterink, R.J. Pasterkamp, A. Akhmanova, L.C. Kapitein, and C.C. Hoogenraad. 2014. Microtubule minus-end binding protein CAMSAP2 controls axon specification and dendrite development. *Neuron*. 82: 1058–1073.
 77. Yau, K.W., P. Schatzle, E. Tortosa, S. Pages, A. Holtmaat, L.C. Kapitein, and C.C. Hoogenraad. 2016. Dendrites In Vitro and In Vivo Contain Microtubules of Opposite Polarity and Axon Formation Correlates with Uniform Plus-End-Out Microtubule Orientation. *J. Neurosci.* 36: 1071–1085.
 78. Kapitein, L.C., and C.C. Hoogenraad. 2015. Building the Neuronal Microtubule Cytoskeleton. *Neuron*. 87: 492–506.
 79. Kapitein, L.C., M. Schlager, M. Kuijpers, P.S. Wulf, M. van Spronsen, F.C. MacKintosh, and C.C. Hoogenraad. 2010. Mixed microtubules steer dynein-driven cargo transport into dendrites. *Curr. Biol.* 20: 290–9.
 80. Kapitein, L.C., and C.C. Hoogenraad. 2011. Which way to go? Cytoskeletal organization and polarized transport in neurons. *Mol. Cell. Neurosci.* 46: 9–20.
 81. Honkura, N., M. Matsuzaki, J. Noguchi, G.C.R. Ellis-Davies, and H. Kasai. 2008. The subspine organization of actin fibers regulates the structure and plasticity of dendritic spines. *Neuron*. 57: 719–29.
 82. Hotulainen, P., and C.C. Hoogenraad. 2010. Actin in dendritic spines: Connecting dynamics to function. *J. Cell Biol.* 189: 619–629.
 83. Xu, K., G. Zhong, and X. Zhuang. 2013. Actin, spectrin, and associated proteins form a periodic cytoskeletal structure in axons. *Science*. 339: 452–6.
 84. Lakadamyali, M. 2014. Navigating the cell: how motors overcome roadblocks and traffic jams to efficiently transport cargo. *Phys. Chem. Chem. Phys.* 16: 5907–16.
 85. Schroer, T.A., E.R. Steuer, and M.P. Sheetz. 1989. Cytoplasmic dynein is a minus end-directed motor for membranous organelles. *Cell*. 56: 937–946.
 86. Hirokawa, N., Y. Noda, Y. Tanaka, and S. Niwa. 2009. Kinesin superfamily motor proteins and intracellular transport. *Nat. Rev. Mol. Cell Biol.* 10: 682–96.
 87. Hartman, M.A., and J.A. Spudich. 2012. The myosin superfamily at a glance. *J. Cell Sci.* 125: 1627–1632.
 88. Asbury, C.L., A.N. Fehr, and S.M. Block. 2003. Kinesin moves by an asymmetric hand-over-hand mechanism. *Science*. 302: 2130–4.
 89. Kneussel, M., and W. Wagner. 2013. Myosin motors at neuronal synapses: drivers of membrane transport and actin dynamics. *Nat. Rev. Neurosci.* 14: 233–47.
 90. Köhler, D., C. Ruff, E. Meyhöfer, and M. Bähler. 2003. Different degrees of lever arm rotation control myosin step size. *J. Cell Biol.* 161: 237–241.
 91. McKenney, R.J., W. Huynh, M.E. Tanenbaum, G. Bhabha, and R.D. Vale. 2014. Activation of cytoplasmic dynein motility by dynactin-cargo adapter complexes. *Science*. 345: 337–41.
 92. Asai, D.J., P. Michael, and M.P. Koonce. 2001. The dynein heavy chain: Structure, mechanics and evolution. *Trends Cell Biol.* 11: 196–202.
 93. Miki, H., M. Setou, K. Kaneshiro, and N. Hirokawa. 2001. All kinesin superfamily protein, KIF, genes in mouse and human. *Proc. Natl. Acad. Sci. U. S. A.* 98: 7004–11.
 94. Berg, J.S., B.C. Powell, and R.E. Cheney. 2001. A millennial myosin census. *Mol. Biol. Cell.* 12: 780–94.

95. Soppina, V., A.K. Rai, A.J. Ramaiya, P. Barak, and R. Mallik. 2009. Tug-of-war between dissimilar teams of microtubule motors regulates transport and fission of endosomes. *Proc. Natl. Acad. Sci. U. S. A.* 106: 19381–6.
96. Fu, M. meng, and E.L.F. Holzbaur. 2014. Integrated regulation of motor-driven organelle transport by scaffolding proteins. *Trends Cell Biol.* 24: 564–574.
97. Barlan, K., M.J. Rossow, and V.I. Gelfand. 2013. The journey of the organelle: Teamwork and regulation in intracellular transport. *Curr. Opin. Cell Biol.* 25: 483–488.
98. Kapitein, L.C., M. a Schlager, W. a van der Zwan, P.S. Wulf, N. Keijzer, and C.C. Hoogenraad. 2010. Probing intracellular motor protein activity using an inducible cargo trafficking assay. *Biophys. J.* 99: 2143–52.
99. Yudowski, G. a, M. a Puthenveedu, D. Leonoudakis, S. Panicker, K.S. Thorn, E.C. Beattie, and M. von Zastrow. 2007. Real-time imaging of discrete exocytic events mediating surface delivery of AMPA receptors. *J. Neurosci.* 27: 11112–21.
100. González-González, I.M., F. Jaskolski, Y. Goldberg, M.C. Ashby, and J.M. Henley. 2012. Measuring membrane protein dynamics in neurons using fluorescence recovery after photobleach. *Methods Enzymol.* 504: 127–46.
101. Henley, J.M., and K.A. Wilkinson. 2013. AMPA receptor trafficking and the mechanisms underlying synaptic plasticity and cognitive aging. *Dialogues Clin. Neurosci.* 15: 11–27.
102. Reits, E.A.J., and J.J. Neeffjes. 2001. No Title. *Nat. Cell Biol.* 3: E145–E147.
103. Lippincott-schwartz, J., E. Snapp, and A. Kenworthy. 2001. Studying protein dynamics in living cells. *Nat. Rev. Mol. Cell Biol.* 2: 444–56.
104. Chozinski, T.J., L.A. Gagnon, and J.C. Vaughan. 2014. Twinkle, twinkle little star: Photoswitchable fluorophores for super-resolution imaging. *FEBS Lett.* 588: 3603–3612.
105. Huang, B., M. Bates, and X. Zhuang. 2009. Super-Resolution Fluorescence Microscopy. *Annu. Rev. Biochem.* 78: 993–1016.
106. Willig, K.I., H. Steffens, C. Gregor, A. Herholt, M.J. Rossner, and S.W. Hell. 2014. Nanoscopy of filamentous actin in cortical dendrites of a living mouse. *Biophys. J.* 106: L01-3.
107. Giannone, G., E. Hossy, F. Levet, A. Constals, K. Schulze, A.I. Sobolevsky, M.P. Rosconi, E. Gouaux, R. Tampe, D. Choquet, and L. Cognet. 2010. Dynamic superresolution imaging of endogenous proteins on living cells at ultra-high density. *Biophys. J.* 99: 1303–1310.
108. Frost, N. a, H.E. Lu, and T. a Blanpied. 2012. Optimization of cell morphology measurement via single-molecule tracking PALM. *PLoS One.* 7: e36751.
109. Shim, S.-H., C. Xia, G. Zhong, H.P. Babcock, J.C. Vaughan, B. Huang, X. Wang, C. Xu, G.-Q. Bi, and X. Zhuang. 2012. Super-resolution fluorescence imaging of organelles in live cells with photoswitchable membrane probes. *Proc. Natl. Acad. Sci.* 109: 13978–13983.
110. Adamantidis, A., S. Arber, J.S. Bains, E. Bamberg, A. Bonci, G. Buzsáki, J.A. Cardin, R.M. Costa, Y. Dan, Y. Goda, A.M. Graybiel, M. Häusser, P. Hegemann, J.R. Huguenard, T.R. Insel, P.H. Janak, D. Johnston, S.A. Josselyn, C. Koch, A.C. Kreitzer, C. Lüscher, R.C. Malenka, G. Miesenböck, G. Nagel, B. Roska, M.J. Schnitzer, K. V Shenoy, I. Soltesz, S.M. Sternson, R.W. Tsien, R.Y. Tsien, G.G. Turrigiano, K.M. Tye, and R.I. Wilson. 2015. Optogenetics: 10 years after ChR2 in neurons--views from the community. *Nat. Neurosci.* 18: 1202–12.
111. Hochbaum, D.R., Y. Zhao, S.L. Farhi, N. Klapoetke, C. a Werley, V. Kapoor, P. Zou, J.M. Kralj, D. Maclaurin, N. Smedemark-Margulies, J.L. Saulnier, G.L. Boulting, C. Straub, Y.K. Cho, M. Melkonian, G.K.-S. Wong, D.J. Harrison, V.N. Murthy, B.L. Sabatini, E.S. Boyden, R.E. Campbell, and A.E. Cohen. 2014. All-optical electrophysiology in mammalian neurons using engineered microbial rhodopsins. *Nat. Methods.* 11: 825–833.
112. Tischer, D., and O.D. Weiner. 2014. Illuminating cell signalling with optogenetic tools. *Nat. Rev. Mol. Cell Biol.* 15: 551–558.
113. Chen, D., E.S. Gibson, and M.J. Kennedy. 2013. A light-triggered protein secretion system. *J. Cell Biol.* 201:

- 631–40.
114. Toettcher, J.E., D. Gong, W. Lim, and O.D. Weiner. 2011. Light-based feedback for controlling intracellular signaling dynamics. *Nat. Methods*. 8: 837–839.
 115. Toettcher, J.E., O.D. Weiner, and W. a Lim. 2013. Using optogenetics to interrogate the dynamic control of signal transmission by the ras/erk module. *Cell*. 155: 1422–34.
 116. Wu, Y.I., D. Frey, O.I. Lungu, A. Jaehrig, I. Schlichting, B. Kuhlman, and K.M. Hahn. 2009. A genetically encoded photoactivatable Rac controls the motility of living cells. *Nature*. 461: 104–8.
 117. Müller, K., R. Engesser, S. Schulz, T. Steinberg, P. Tomakidi, C.C. Weber, R. Ulm, J. Timmer, M.D. Zurbriggen, and W. Weber. 2013. Multi-chromatic control of mammalian gene expression and signaling. *Nucleic Acids Res*. 41: e124.
 118. Strickland, D., Y. Lin, E. Wagner, C.M. Hope, J. Zayner, C. Antoniou, T.R. Sosnick, E.L. Weiss, and M. Glotzer. 2012. TULIPs: tunable, light-controlled interacting protein tags for cell biology. *Nat. Methods*. 9: 379–84.
 119. Spiltoir, J.I., D. Strickland, M. Glotzer, and C.L. Tucker. 2016. Optical Control of Peroxisomal Trafficking. *ACS Synth. Biol*. 5: 554–560.
 120. Clackson, T., W. Yang, L.W. Rozamus, M. Hatada, J.F. Amara, C.T. Rollins, L.F. Stevenson, S.R. Magari, S.A. Wood, N.L. Courage, X. Lu, F. Cerasoli, M. Gilman, and D.A. Holt. 1998. Redesigning an FKBP-ligand interface to generate chemical dimerizers with novel specificity. *Proc. Natl. Acad. Sci. U. S. A.* 95: 10437–42.
 121. Crefcoeur, R.P., R. Yin, R. Ulm, and T.D. Halazonetis. 2013. Ultraviolet-B-mediated induction of protein-protein interactions in mammalian cells. *Nat. Commun*. 4: 1779.
 122. Kennedy, M.J., R.M. Hughes, L. a Peteya, J.W. Schwartz, M.D. Ehlers, and C.L. Tucker. 2010. Rapid blue-light-mediated induction of protein interactions in living cells. *Nat. Methods*. 7: 973–5.
 123. Idevall-Hagren, O., E.J. Dickson, B. Hille, D.K. Toomre, and P. De Camilli. 2012. Optogenetic control of phosphoinositide metabolism. *Proc. Natl. Acad. Sci. U. S. A.* 109: E2316–23.
 124. Zoltowski, B.D., and B.R. Crane. 2008. Light activation of the LOV protein vivid generates a rapidly exchanging dimer. *Biochemistry*. 47: 7012–9.
 125. Kawano, F., H. Suzuki, A. Furuya, and M. Sato. 2015. Engineered pairs of distinct photoswitches for optogenetic control of cellular proteins. *Nat. Commun*. 6: 6256.
 126. Guntas, G., R. a. Hallett, S.P. Zimmerman, T. Williams, H. Yumerefendi, J.E. Bear, and B. Kuhlman. 2015. Engineering an improved light-induced dimer (iLID) for controlling the localization and activity of signaling proteins. *Proc. Natl. Acad. Sci.* 112: 112–117.
 127. Zimmerman, S.P., R.A. Hallett, A.M. Bourke, J.E. Bear, M.J. Kennedy, and B. Kuhlman. 2016. Tuning the Binding Affinities and Reversion Kinetics of a Light Inducible Dimer Allows Control of Transmembrane Protein Localization. *Biochemistry*. 55: 5264–5271.
 128. Levskaya, A., O.D. Weiner, W. a Lim, and C. a Voigt. 2009. Spatiotemporal control of cell signalling using a light-switchable protein interaction. *Nature*. 461: 997–1001.
 129. Kaberniuk, A.A., A.A. Shemetov, and V. V Verkhusha. 2016. A bacterial phytochrome-based optogenetic system controllable with near-infrared light. *Nat. Methods*. 13: 591–597.
 130. Lipka, J., L.C. Kapitein, J. Jaworski, and C.C. Hoogenraad. 2016. Microtubule-binding protein doublecortin-like kinase 1 (DCLK1) guides kinesin-3-mediated cargo transport to dendrites. *EMBO J*. 35: 302–318.



Barriers in the Brain: Resolving Dendritic Spine Morphology and Compartmentalization

Max Adrian¹, Remy Kusters², Corette J. Wierenga¹, Cornelis Storm^{2,3}, Casper C. Hoogenraad¹ and Lukas C. Kapitein¹

¹ *Division of Cell Biology, Faculty of Science, Utrecht University, Utrecht, The Netherlands,*

² *Department of Applied Physics, Eindhoven University of Technology, Eindhoven, The Netherlands,*

³ *Institute for Complex Molecular Systems, Eindhoven University of Technology, Eindhoven, The Netherlands.*

ABSTRACT

Dendritic spines are micron-sized protrusions that harbor the majority of excitatory synapses in the central nervous system. The head of the spine is connected to the dendritic shaft by a 50-400 nm thin membrane tube, called the spine neck, which has been hypothesized to confine biochemical and electric signals within the spine compartment. Such compartmentalization could minimize interspinal crosstalk and thereby support spine-specific synapse plasticity. However, to what extent compartmentalization is governed by spine morphology, and in particular the diameter of the spine neck, has remained unresolved. Here, we review recent advances in tool development - both experimental and theoretical - that facilitate studying the role of the spine neck in compartmentalization. Special emphasis is given to recent advances in microscopy methods and quantitative modeling applications as we discuss compartmentalization of biochemical signals, membrane receptors and electrical signals in spines. Multidisciplinary approaches should help to answer how dendritic spine architecture affects the cellular and molecular processes required for synapse maintenance and modulation.

INTRODUCTION: DENDRITIC SPINES

The dendritic compartment of a neuron receives input from thousands of upstream neurons via synapses. The majority of excitatory inputs in the central nervous system are located at dendritic spines. Spines are micron-sized protrusions along the dendritic shaft and have first been described about a century ago by Ramón y Cajal (1). They are composed of a spine head and a thin spine neck that connects them to the dendritic shaft. Typical dimensions are $\sim <1 \mu\text{m}$ for the head diameter, and a $\sim 100 \text{ nm}$ wide and $\sim 1 \mu\text{m}$ long spine neck, but notable differences in spine morphology exist (2). Based on electron microscopy, three shape categories have been defined: thin, filopodia-like protrusions ('thin spines'), short spines without a well-defined spine neck ('stubby spines') and spines with a large bulbous head ('mushroom spines') (2). Importantly, spine shape is not static, but can change, even throughout adulthood, reflecting the plastic nature of synaptic connections. For example, neuronal activity *in vitro* and experience *in vivo* can alter spine morphology (3). Changes in spine size are thought to be generally correlated with changes in the strength of the excitatory synapse (4, 5). Such functional and structural changes of spines and synapses are believed to be at the core of learning and memory in the brain (3, 6, 7).

The actin cytoskeleton plays a key role in shaping dendritic spines and is critically important for numerous processes that contribute to the plasticity of synaptic function (8-12). The rapid polymerization and depolymerization of actin filaments produces protrusive forces that can quickly change neuronal morphology (13). For example, during spine enlargement, rapid actin polymerization provides the mechanical force required for pushing out the spine membrane (14). In addition, the actin cytoskeleton provides tracks for myosin-based transport of various cellular materials in and out of spines, including AMPA-type glutamate receptors (15).

The mechanisms through which spine shape affects its function are not yet fully understood. At its minimum, morphological changes associated with synaptic modulation could just be a secondary effect of altered actin dynamics required to more directly modulate synapse functioning or actin-based transport. Nevertheless, modeling studies have often emphasized the interesting effects that shape can have on the diffusion of proteins, calcium

ions and other signaling molecules (16). A small neck should slow diffusion and result in functional compartmentalization by preventing signaling molecules to escape from the spine. In addition, more recent modeling studies report that shape should also affect lateral diffusion of proteins embedded in the plasma membrane (17). Several studies have indeed reported evidence for compartmentalization, but the extent to which this was governed by shape alone could often not be directly assessed because the limited resolution of live-cell light microscopy did not allow to directly correlate diffusion dynamics and spine shape. Recent breakthroughs in fluorescence microscopy allow imaging at resolutions below the diffraction limit, allowing to directly explore how spine shape affects diffusion of cytoplasmic or membrane-embedded molecules (18, 19). In this review, we first discuss existing and emerging technologies to image spine morphology. We then present existing evidence for the compartmentalization of in spines. Finally, we discuss how different aspects of spine shape contribute to compartmentalization, with an emphasis on recent modeling studies exploring the influence of shape on lateral diffusion in the membrane.

IMAGING SPINE MORPHOLOGY

Ramón y Cajal discovered dendritic spines using light microscopy of neurons stained using Golgi impregnation and he suggested these small protrusions to be sites of neuronal signal transmission (20). His hypothesis was confirmed with the development of electron microscopy (EM) during the interwar, which allowed imaging at much higher resolution (21). Subsequent refinements of this technology, especially the careful analysis of series of thin tissue sections in serial-sectioning EM, allowed a full morphological description of dendritic spines and have provided many beautiful insights into spine architecture (2). Serial-sectioning EM directly visualizes all tissue surrounding spines as well as the structure of the postsynaptic specialization and has been used to identify precise morphological changes upon specific stimuli (2). However, the use of EM also has several limitations. First of all, sample preparation procedures and imaging conditions prevent imaging of living tissue. In addition, different preparation procedures can easily introduce artifacts (22) and also the labeling of specific proteins has so far remained challenging and very inefficient. Therefore, to study dynamics of spines or specific proteins associated with spines, live-cell fluorescence microscopy is the method of choice.

Conventional Live Cell Imaging

Both laser-scanning and spinning disk confocal microscopy are standard techniques to study spine dynamics in dissociated neurons. For imaging in tissue, however, these techniques impose several limitations. Visible light penetrates poorly into tissue and is quickly distorted, resulting in a rapid loss of resolution with increased focus depth because the focus size is no longer diffraction-limited. In addition, many focal planes need to be imaged sequentially to reconstruct complete neurons in three dimensions. Because exposure to excitation light is not restricted to the plane in focus, this results in increased phototoxicity and photobleaching, limiting sample life time and signal intensity.

Two-photon microscopy overcomes both of these limitations through the use of a pulsed infrared light source that excites fluorophores by the combined energy of two photons arriving on the sample nearly simultaneously (23, 24). Infrared light is much less distorted

and penetrates deeper into the sample compared to visible light. As two-photon excitation efficiency scales quadratically with excitation intensity, it is largely limited to the focus plane and prevents photobleaching of out-of-focus planes. Two-photon microscopy rapidly became the method of choice for deep tissue imaging and has even enabled intravital brain imaging in mice (25). However, despite its unique advantages, the resolution of two-photon microscopy is still inherently limited by diffraction to 400-500 nm. Therefore, several studies have combined two-photon live imaging with post-hoc serial sectioning electron microscopy to examine the microstructure of spine, for example to directly demonstrate synapse formation associated with the emergence of a new spine during live imaging (22, 26, 27). As this requires fixing the sample, this approach might not detect all morphological changes that occur upon specific stimuli and is prone to morphological artifacts. For this, live-cell imaging beyond the diffraction limit is required.

Live-Cell Imaging Beyond the Diffraction Barrier

The diffraction of light limits the ability of microscopes to resolve the location of two objects that are located closer to each other than approximately half the wavelength of the light used for imaging. For conventional fluorescence microscopy using visible light this limit lays around 200-300 nanometers. Over the last years, different technologies have allowed fluorescence microscopy at a resolution below the diffraction limit (28). Dendritic spines have frequently been used for proof-of-principle applications of these techniques, because of their small size and physiological relevance. Indeed, careful analysis of spine morphologies using superresolution microscopy has demonstrated that conventional light microscopy methods overestimate the amount of stubby spines in acute and organotypical slice cultures (18). Here, we highlight several techniques that have recently contributed to novel insights into spine morphodynamics and synapse architecture.

Stimulated Emission Depletion (STED) microscopy was developed as an extension of confocal microscopy. The conventional excitation beam is complemented with a depletion beam that forms a donut shaped spot surrounding the focus of the excitation beam (28, 29). The wavelength of the depletion beam is chosen within the tail of the emission spectrum of the imaged fluorophore. It brings fluorophores excited by the excitation laser back to their ground-state by inducing stimulated emission at exactly the wavelength of the depletion beam. As a result, fluorescence emission at all other wavelengths of the emission spectrum is restricted to the center of the donut. Importantly, the size of this zone is not limited by diffraction. Therefore, scanning the lasers with very small steps over the sample improves the resolution of the final image up to 50 nm (28, 29).

The first STED images of spines in organotypical slices expressing YFP in a sparse subset of neurons were published in 2008 (30). Neck diameters of spines located at 0-10 μm depth were originally measured to be on average $\sim 40\%$ reduced compared to confocal imaging (30), whereas more recent measurements have found neck diameters as low as 51 nm in organotypic cultures and 59 nm in acute slices (18). Recently, STED microscopy has also been established *in vivo* in mouse brain (31).

The STED principle can also be applied to two-photon microscopy (32). However, the depletion wavelength needs to be within the (visible) emission spectrum and is therefore

prone to distortions. Nevertheless, it has been successfully applied to dendritic spines in organotypical slices, resulting in 60-150 nm lateral resolution at 50-100 μm depths, but without improving the axial resolution (33-35). In addition, two-color detection has been established using spectral unmixing of either pairs of organic dyes (36) or the fluorescent proteins YFP and GFP (34). None of the techniques described here improve the axial resolution. However, development of three-dimensional depletion patterns and compensation of optical distortions through adaptive optics promise improvements in the near future (37, 38).

Inducing stimulated emission requires very high light intensities, which can induce artifacts and phototoxicity in the imaged sample. To circumvent this, a comparable technique reduces the size of the confocal volume using a specifically engineered fluorescent protein that can transition to a non-fluorescent dark state (RESOLFT: reversible saturable/switchable optical transitions) (39). This approach requires orders of magnitude less light intensity and has been demonstrated on living brain slices (40). Novel probes are currently being developed that should allow two-color RESOLFT of dendritic spines (41, 42).

Another set of powerful techniques to achieve resolutions beyond the diffraction barrier uses switchable fluorophores or special imaging conditions to ensure that only a small, random subset of fluorophores in the sample is emitting at any given time (43). Because these fluorophores are then distributed sparsely enough to be clearly separated, their positions can be obtained from their point spread function with 1-10 nm accuracy. Repeating this procedure thousands of times for different subsets of fluorophores in the region of interest eventually allows reconstructing a superresolved image from the calculated positions. This basic concept of repetitive detection of small subsets has been applied in many different ways and these techniques are collectively referred to as single-molecule localization microscopy (SMLM), of which the most prominent variants are known as PALM, STORM and dSTORM (44). These techniques are often used on fixed samples, because the temporal resolution is limited by the repetitive detection and the required excitation intensities are high. Nevertheless, several groups have succeeded in live-imaging of dendritic spines using these techniques: Spine morphology has been probed using labeled antibodies against membrane-bound proteins (45, 46), using genetically encoded fluorophores that either directly label or transiently bind to actin (47, 48), or using a lipophilic cyanine dye that labels the plasma membrane (49). In all cases, live super-resolution microscopy requires some thoughtful compromises between temporal and spatial resolution (50).

DENDRITIC SPINES FORM DYNAMIC COMPARTMENTS

In principle, there may be several advantages of having substructures like dendritic spines containing synapses along the dendrite. First of all, spines might facilitate connectivity by bridging the physical gap between slightly distant axons and dendrites. However, not all neurons have spines (e.g. stellate neurons) and they can receive excitatory input directly on their shafts (51). It is therefore likely that spines have additional functions. Ever since their discovery by Ramón y Cajal, it has been suggested that spines may play a role in the compartmentalization of synaptic signals (20). Such compartmentalization may facilitate spine-specific plasticity and thereby regulate the individual strength of synaptic connections (3, 52-54). Compartmentalization of spines has been reported on three levels that we discuss in detail in this section: (1) From a molecular and cell biological perspective, signaling

cascades elicited by synaptic stimulation may be confined to single spines, making them biochemical signaling compartments that confine structural plasticity to individual spines. (2) Spines may also compartmentalize neurotransmitter receptors, both by opposing their diffusion out of spines and by maintaining spine-selective intracellular storage pools, in order to directly regulate the sensitivity of a synapse to stimulations. (3) Lastly, spines may serve as an electrical compartment, playing a role in the processing of synaptic depolarization from synapses along the dendrite.

Compartmentalization of Biochemical Signaling

The compartmentalization of spines is most easily studied by measuring the extent to which fluorescent dyes, specific proteins or ions exchange between a spine and the parent dendrite. We first discuss studies that examined the cytoplasmic coupling between spines and the dendritic shaft as a general measure of spine head isolation. In addition, we review the evidence for specific biochemical compartmentalization of calcium ions and signaling molecules.

Diffusional Coupling between Spine and Dendrite

Using two-photon fluorescence recovery after photobleaching (FRAP) microscopy on hippocampal neurons filled with fluorescent dyes in cultured slices, early studies found that spines can indeed compartmentalize cytoplasm as fluorescence recovery rates in dendritic spines are significantly lower than in the shaft (23). Repeated activation of a photo-activatable variant of GFP (PA-GFP) in individual spines showed substantial variation in the cytoplasmic coupling of individual spines over time that may be regulated by neuronal activity. In a small population of spines, no exchange of soluble fluorescent proteins between shaft and spine heads could be measured during a period of several minutes.(55). Whereas in these earlier studies the exact relation between spine shape and cytoplasmic coupling could not be resolved, recent experiments have used STED microscopy to correlate spine morphology and cytoplasmic diffusion kinetics (see Section 4.1).

In addition to the exchange of soluble dyes and fluorescent proteins between spines and dendrites, the diffusion of calcium ions has also been studied extensively (56). Calcium ions play a crucial role in initiating downstream signaling during long-term potentiation (LTP) and depression (LTD) and influx of calcium is both necessary and sufficient for structural synaptic plasticity (57-59). Pioneering two-photon microscopy of calcium dynamics in single spines in slices of hippocampal neurons revealed that synaptic stimulation results in accumulation of calcium ions in single spines (53). The extent to which the diffusion kinetics of calcium ions are regulated by spine morphology and neck width in particular is debated in the literature. Importantly, when calcium is bound to buffering proteins like calmodulin, the diffusion of the resulting complex is more sensitive to spatial constraints than single ions because of its larger size (18, 60). In addition to diffusion into the dendritic shaft, calcium can also be removed from spines by absorption into the smooth endoplasmic reticulum located in spines or by Na/Ca exchangers located in the plasma membrane (60). These processes help to confine transient calcium ions to the spine head. Nevertheless, morphology does play a role, as long and thin necks prevent the diffusion of calcium, whereas shorter and thicker necks allow for better diffusional coupling with the dendrite (60-64).

Other factors influencing the local calcium concentrations in spines are the surface to volume ratio of spines and the localization of calcium-permeable ion channels (60). If these ion channels were distributed equally throughout the plasma membrane, one would expect a higher effective concentration of these channels in spines compared to dendrites as the surface-to-volume ratio of the former is higher. This should theoretically lead to a higher influx of calcium in spines than in the surrounding dendrite (60). Such an effect is strengthened by the existence of classes of voltage gated calcium channels that exclusively localize to spines but not dendrites and cooperate with other calcium channels to shape local depolarization and synaptic plasticity (65, 66).

Spatial Restriction of Signaling Domains

Calcium ions in dendritic spines have an important function in activating signaling cascades that underlie and regulate synaptic plasticity (67). Their retention in an individual stimulated spine may thus be important to induce downstream signaling and structural plasticity in a synapse-specific manner. CaMKII is a calcium-activated kinase involved in structural plasticity by remodeling of the postsynaptic density (68), rearrangement of the actin cytoskeleton (69) and maintenance of spine enlargement (54, 70). Downstream of CamKII, Ras and Rho GTPases are important for regulating spine morphology (71, 72) and synaptic strength (73, 74). It is thought that Rho activation causes spine loss and shrinkage by inhibiting actin polymerization, whereas Cdc42 and Rac activation increase the number of spines by promoting actin polymerization. The precise crosstalk and integration is however not completely understood (67).

To explore the activity of signaling molecules, activity sensors can be used in which the amount of Förster Resonance Energy Transfer (FRET) between two fluorophores is different between active and inactive conformations. FRET is the process in which an excited donor molecule transfers energy to an acceptor fluorophore, whose excitation spectrum overlaps with the emission spectrum of the donor. The efficiency of this energy transfer is very sensitive to the distance between both fluorophores, which should be within the 2-5 nm range. Energy transfer can be detected either by the appearance of red-shifted emission from the acceptor, or by a decrease in the excited state life time of the donor. In a series of papers, Yasuda and co-workers have used activity reporters for different signaling molecules and measured their fluorescence lifetimes by two-photon microscopy (2P-FRET-FLIM) in cultured hippocampal slices. Additionally, using photoactivatable protein tags, the diffusion kinetics of the same proteins could be measured in spines. This combination of techniques allowed recording activity patterns for CaMKII (70), Ras (75), RhoA and Cdc42 (76) in dendritic spines following local glutamate uncaging. Intriguingly, these signaling molecules show different activity patterns: while CaMKII and Cdc42 activities are confined to the stimulated dendritic spine (70, 76), Ras and RhoA activities spread along the parent dendrite. Ras activity was shown to invade typically 10-20 neighboring spines in a range of 10 μ m along the dendrite, whereas RhoA activity only spread 5 μ m and rarely invaded neighboring spines (75, 76). Thus, despite all being triggered by NMDA-dependent calcium influx, these molecules have quite different signaling ranges. The spread of their signaling activity depends on three factors: (1) the extent and persistence of the upstream activation event, (2) the diffusion rate of the signaling molecule and (3) its inactivation kinetics, see Figure 1.

Upon single-spine glutamate uncaging, the activation of CaMKII peaked within six seconds and only lasted for a few minutes (70). The diffusional coupling of CaMKII with the dendrite was significantly slower, in the range of several minutes (70), and additional modelling studies have shown that the effective CaMKII diffusion constant depends heavily on binding to synaptic scaffolds and the actin cytoskeleton in spine necks (77). Thus, because inactivation of CaMKII has faster kinetics than CaMKII diffusion, activity of the kinase is restricted to stimulated spines. It should be noted that these results based on single spine stimulations contrast earlier biochemical studies that reported persistent phosphorylation of CaMKII upon more global induction of LTP (78-80).

The activation of Ras measured by FRET-FLIM was dependent on CaMKII activation, peaked later, and recovered to baseline level only after 15 minutes. Its diffusion rate out of the spine was relatively fast, reaching the dendrite within seconds without leaving any immobile fraction in the spine (75). Together, this explains why Ras activity can spread to neighboring synapses.

Both Cdc42 and Rho showed a rapid activity peak 30 seconds after stimulation followed by decay over 5 minutes and a sustained lower activity for more than 30 minutes. Also the diffusion kinetics of both molecules were comparable and similar to Ras diffusion and showed no immobile fraction left in the spine. Nevertheless, Cdc42 activity remained spatially confined, because it had an intrinsic inactivation time constant of 6 seconds and therefore depends on continuous activation by CaMKII (76). In contrast, Rho inactivated 5 times slower and could therefore spread into the dendrite. Thus, the specific combinations of activity life-time and diffusion kinetics can explain why CaMKII and Cdc42 activities are restricted to spine heads whereas Ras and Rho activities spread along the dendrite.

From the examples of CaMKII, Ras and Rho it becomes clear that the interplay between diffusion and activity of the signaling proteins is highly coordinated in dendritic spines. This is crucial because these signaling events are thought to coordinate local processes in

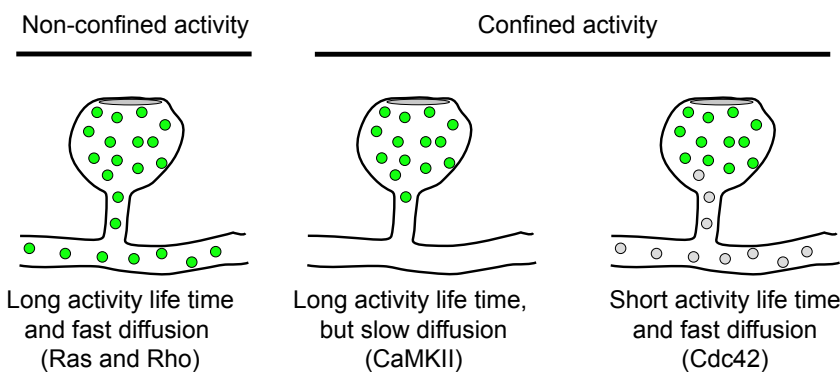


Figure 1 | Diffusion models for signaling molecules in spines.

The spread of active signaling molecules (green) with long activity life-times depends on their diffusion rate. Limiting the activity life time of signaling molecules is an orthogonal approach to confine signaling activity to individual spines.

the stimulated spine. CaMKII-Cdc42-Pak signaling increases spine volume and synaptic strength (76), while Rho signaling leads to local AMPA receptor integration in the dendrite (74). In addition, Rho-Rock and Ras-ERK signaling pathways lower the threshold for LTP in neighboring spines (70, 73, 75, 81). In potentiated spines, the structural rearrangement of spine morphology during LTP slows the diffusional coupling between spines and dendrites even further (18). Taken together, this highly controlled signaling network allows precise spatiotemporal activation and retention of calcium-induced signaling.

Compartmentalization of Membrane-bound Receptors

Another aspect of compartmentalization in individual spines is the distribution of membrane and membrane-bound proteins. Controlled addition and removal of AMPA-type glutamate receptors from the postsynaptic density is believed to underlie the changes in synaptic strength during learning and memory formation (82-85). Whereas reports based on static electron microscopy suggested that glutamate receptors are restricted to synapses (86), live-cell imaging techniques like FRAP and single molecule tracking changed this view radically (87, 88). Lateral diffusion of receptors through the plasma membrane and activity-triggered exocytosis of receptors from internal endosomal compartments have become generally accepted regulation mechanisms for synaptic plasticity, although their respective contributions have remained unresolved (89-101). Here, we focus on the contribution of lateral diffusion of glutamate receptors and its regulation during structural plasticity of dendritic spines.

The study of bulk AMPA receptor mobility has been greatly facilitated by the generation of a pH sensitive GFP variant, called superecliptic pHluorin (SEP) (102, 103), whose fluorescence is quenched in the acidified endosomal compartments, but not in the extracellular environment after incorporation into the plasma membrane. Studying the FRAP dynamics of a fusion of SEP with the AMPA receptor subunit GluA2 (SEP-GluA2) revealed that receptor turnover in spines is slower compared to non-spinal plasma membrane and that recovery in the spine neck and base is particularly slow (90). Furthermore, fluorescently-tagged plasma membrane probes in spines of different morphologies showed a faster recovery rate in stubby than in mushroom-shaped spines (87, 90), indicating that mushroom-shaped spines form a membrane compartment in which diffusion is slowed. Combining SEP-GluA1 photobleaching experiments with glutamate uncaging in organotypic slices revealed that synaptic potentiation of AMPA receptors is achieved by restricting their diffusion out of the synaptic membrane (104). In addition, a live single-molecule localization microscopy study showed reduced diffusion speeds of plasma membrane markers in spine necks (49). Together these data indicate that the spine neck is a general diffusion barrier for membrane-bound proteins which, together with the regulated retention of receptors in the synapse, regulates receptor diffusion in the spine compartment.

Another approach to study receptor dynamics in dendritic spines uses single-molecule tracking. Membrane-bound receptor movements are followed with extracellular probes, e.g. antibodies or derived fragments, coupled to fluorescent reporters (88). The earliest report used latex beads coupled to GluA2 receptors and found that these receptors reversibly stop at synaptic sites. This is modulated by neuronal activity levels that affect calcium transients in the cell. Calcium elevations were shown to generally slow diffusion and locally accumulate AMPA receptors (91). However the large size of the beads (~200nm) precluded a more

detailed analysis of receptor motility in spines and synaptic membrane domains. Fluorescently labelled glutamate receptor antibodies were subsequently used to address diffusion kinetics in synaptic and extrasynaptic regions. A pool of synaptic receptors was shown to be immobile while another synaptic pool and extrasynaptic receptors were rapidly moving. Glutamate stimulation enhances the exchange between these pools and increases overall motility of glutamate receptors (105). Long-term tracking of receptor movements was facilitated by using quantum-dots (QD) as fluorescent probes, which have the advantage of relatively small diameters and good photostability allowing bleaching-free imaging over prolonged times (106). AMPA receptors tagged with QDs were reported to selectively reduce their mobility at active synapse while they freely diffused through non-active synapses (92). The same study observed reduced exchange of single receptor molecules between spines during stimulation. In addition, recent studies have shown that glutamate receptors localize to submicron scale clusters within the synaptic membrane as shown by various techniques ranging from EM to PALM microscopy (92, 107, 108).

How exactly synaptic recruitment and localization of glutamate receptors are regulated is currently under debate. Whereas previously the cytoplasmic tails of GluA receptors have been shown to differentially regulate receptor diffusion and trapping at synapses (93), a recent study suggests that truncated receptors void of any cytoplasmic tail can rescue the depletion of endogenous GluA1-3 (109). Even though the physiological relevance of these experiments has been debated (110), the observed diffusional trapping of truncated receptors in the spine head is interesting as it requires an intrinsic property of the spine to accumulate transmembrane proteins. Based on results from modeling (111) it has been suggested that crowding in the spine head may contribute to this phenomenon (112). In addition, trapping of receptors may be facilitated by the curvature of plasma membrane in spines (17), as discussed in detail below.

Compartmentalization of Electrical Signals

In addition to inducing compartmentalization of biochemical signals and receptors, it has been suggested that dendritic spines may also serve as electrical compartments (113, 114). As small protrusions connected to a large dendrite, spines may be theoretically described as sealed-end cables with an intrinsic asymmetry in conducting electric signals. This means that voltage signals from the dendrite propagate without attenuation into the spines (115-117), but synaptic potentials generated inside the spine head are filtered when they travel to the dendrite (52, 118, 119). In addition, the high input resistance of spines may further facilitate synaptic potentials inside spines compared to equally strong synapses onto the dendritic shaft. However, how much of these effects contribute to the compartmentalization of synaptic potentials in spines is strongly debated, as most of the relevant parameters, such as spine neck resistance, are simply not known and experimentally inaccessible at present times.

Because voltage and calcium imaging at single spine resolution has long been technically challenging, the majority of available literature either discusses theoretical work or indirectly calculated spine neck resistances based on diffusional coupling of cytoplasm (23, 120, 121) and often relies on static morphology data from EM (122, 123). The resulting values for the spine neck resistance have varied over a wide range and are strongly influenced by the methods and theoretical models used. Most recently, STED microscopy on dendritic spines

in organotypic and acute slices suggested that electric compartmentalization is moderate, but not absent, in most spines (18, 19). For the final answer we will probably need to wait until it is possible to directly measure synaptic potentials in spines and nearby dendrites with voltage-sensitive dyes.

Interestingly, induction of plasticity not only results in an increase in spine size (54, 124), but also in changes in spine shape (125), with consequences for compartmentalization. It was shown that reduction of spine neck length after synaptic potentiation mediates enhanced electric coupling of spine and dendrite, thereby increasing the influence of the potentiated spine on the dendritic and somatic membrane potential (18, 52). Interestingly, it was suggested that the reduction in electrical compartmentalization occurs while chemical compartmentalization is preserved, reflecting two separate functions of spines within the dendrite.

In addition to passive amplification of synaptic potentials, spines are thought to be able to actively contribute to local membrane voltage. Voltage-dependent ion channels are present within spines and activation of these channels will result in a change of local membrane potential. Opening of sodium and calcium channels will boost local depolarization (65, 116, 126-128), while opening of potassium channels decrease local input resistance and result in smaller synaptic potentials (129, 130). These active properties of dendritic spines are thought to play an important role in the interactions between multiple synaptic inputs in dendritic computation (119, 128).

SPINEMORPHOLOGY AS COMPARTMENTALIZATION MECHANISM

We have summarized the evidence for spine-based compartmentalization on three levels: biochemical signaling, membrane-bound receptor dynamics and electrical signaling. All of these levels contribute to proper information processing in the dendritic arbor and are interconnected. However, the exact mechanisms through which spines can regulate different aspects of compartmentalization have remained unclear. Do reduced diffusion rates depend on dedicated barriers imposed by specific protein-based structures, similar to the way in which the axon initial segment forms a barrier for axon entry? Or is the shape of spines sufficient to confine both membrane-based and cytoplasmic diffusion? How exactly do these processes depend on spine neck diameter and spine neck length? In addition, the effect of spine neck constriction on vesicle transport through neck has remained largely unexplored. In this section, we first discuss the role of the spine neck in diffusional coupling with the dendrite and then focus on recent studies showing that spine morphology directly influences lateral diffusion of membrane-bound proteins to and from the synapse. Finally, we discuss the effect of spine shape on vesicular transport into spines.

Spine Necks as Barriers

Conventional two-photon microscopy has a limited resolution that prevents accurate description of spine shape. Two pioneering studies have recently used STED microscopy (33-35) to overcome this problem and studied the correlation between spine morphology and diffusional coupling to dendrites by analyzing the recovery of fluorescence after photobleaching of soluble fluorophores in the spine (18, 19), see Figure 2. Both studies suggest that the recovery time scale τ roughly follows what would be expected if diffusion is governed

largely by spine geometry:

$$\tau = \frac{V * L}{D * A}$$

where V denotes the volume of the spine head, D the diffusion coefficient, and L and A the length and cross-sectional area of the neck, respectively. Indeed, both groups find an inverse relation between spine neck diameter d and the recovery time, which appears to follow the predicted inverse quadratic relation ($\tau \propto 1/d^2$). However, whereas the equation suggests a linear increase of the recovery time scale with spine head volume, Takasaki et al. instead find a weak decrease. Similarly, Tonessen et al. report a quadratic dependence on head width w , whereas the model predicts a w^3 dependence (assuming a spherical spine head in which $V \propto w^3$). Interestingly, a fraction of spines strongly deviated from the average trends that were observed (19), suggesting that small local constrictions, local protein accumulations and organelle positioning in the neck may create additional diffusion barriers (5, 113). Nonetheless, these important studies demonstrate that the constriction of the spine neck alone has a major impact on crosstalk between spine and dendrite.

Membrane-bound proteins like glutamate receptors are restricted in their passage through the spine neck, as we discussed in section 3.2. Such restriction has several causes: In addition to the direct influence of the spine morphology on membrane proteins that we will discuss in the next section (17), several cell-biological factors including molecular crowding, corraling and receptor retention in synaptic scaffolds have been studied in recent years. The postsynaptic density is believed to regulate the number of glutamate receptors localized in the synapse and thereby preventing their diffusion out of the spine (97). Additionally, the high density of proteins in the synapse may reduce diffusion rates of all membrane-bound proteins including glutamate receptors due to crowding (131). Cell adhesion complexes have also been identified as diffusion barriers for membrane proteins (132, 133). Lastly, the actin cytoskeleton is

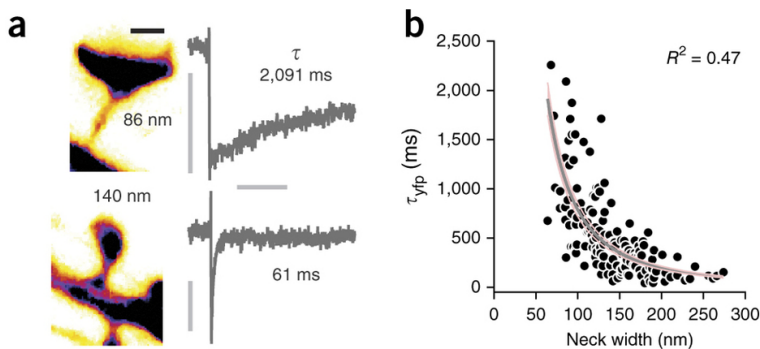


Figure 2 | Correlation of spine morphology and diffusional coupling.

(A) Left: Two dendritic spines filled with soluble fluorophores were imaged with STED microscopy and neck diameters measured with line scans. Scale bar 500nm. Right: The rate of diffusional coupling (τ) of these spines was measured by the recovery of photobleached fluorophores (FRAP). (B) τ plotted as function of neck width. Gray line indicates inverse-square fit with 95% confidence interval in pink. Reprinted by permission from Macmillan Publishers Ltd: Nature Neuroscience (ref 18), copyright 2014.

known to mediate receptor positioning (134) and its depolymerization was shown to reduce glutamate receptor accumulations in spines (135). In the following sections, we discuss the role of spine shape on the passive (diffusive) and active (endosomal) transport of receptors.

The Effect of Spine Shape on Lateral Diffusion

Several experiments have shown that two-dimensional diffusion of membrane markers and AMPA- type glutamate receptors is sensitive to the morphology of the dendritic spine (49, 90). Mushroom shaped spines were found to retain AMPA receptors in the vicinity of the synapse for an increased period of time (90, 92, 97), see Figure 3(A). These observations have been rationalized by several modelling studies, which showed that the typical mushroom-like morphology of dendritic spines strongly alters the lateral diffusion of AMPA receptors, demonstrating a pronounced suppression of the receptor exit rate out of spines with decreasing neck radius as well as increasing neck length (16, 17, 136). More specifically, the characteristic timescale for retention, the mean escape time of receptors through the neck of a typical mushroom-shaped spines follows a power-law dependence on neck radius r ,

$$\tau_{escape} \sim (r_{neck})^{-\lambda}$$

as well as neck length l ,

$$\tau_{escape} \sim (l_{neck})^{\eta}$$

where λ and η are positive constants, whose numerical value depends on the actual shape of the spine (17, 136).

In combination with an exocytic event in the head of the spine, a decreasing neck radius and increasing neck length effectively increase the confinement of receptors at the synapse, as can be seen in Figure 3(B) showing the time-evolution of receptor concentration after the release of 1000 receptors at the top of the spine (17). Mushroom shaped spines with the smallest neck radii are thus significantly more effective at retaining receptors. Moreover, the particular shape of the mushroom-shaped spine in combination with receptor trapping at the synapse further enhances their retention. The timescale for an AMPA receptor reaching the synapse may be up to an order of magnitude faster than the time it takes for a receptor to exit through the neck of the spine. Altogether, this modeling study concluded that mushroom shaped spines with an exocytosis site adjacent to the synapse are privileged over others, because they can rapidly and specifically regulate the synaptic AMPA receptor level (17).

Hydrodynamic interactions of proteins with the plasma membrane and the surrounding liquid significantly reduce their mobility. For flat membranes, Saffman and Delbruck (137) predicted a logarithmic dependence of the diffusion coefficient with the “size” of the membrane, relative to the size of the protein. Recent experimental studies on membrane tubes show that reducing the radius of a membrane tube, which sets the relevant length scale in the Saffman-Delbruck theory, indeed reduced the mobility of both lipids and proteins with a factor of five compared to planar diffusion (138, 139). The thin and slender neck, typical for mushroom spines, is in that same range of radii as in these the experiments by Domanov et al. and could therefore reduce the mobility of glutamate receptors, compared to that on the dendritic shaft.

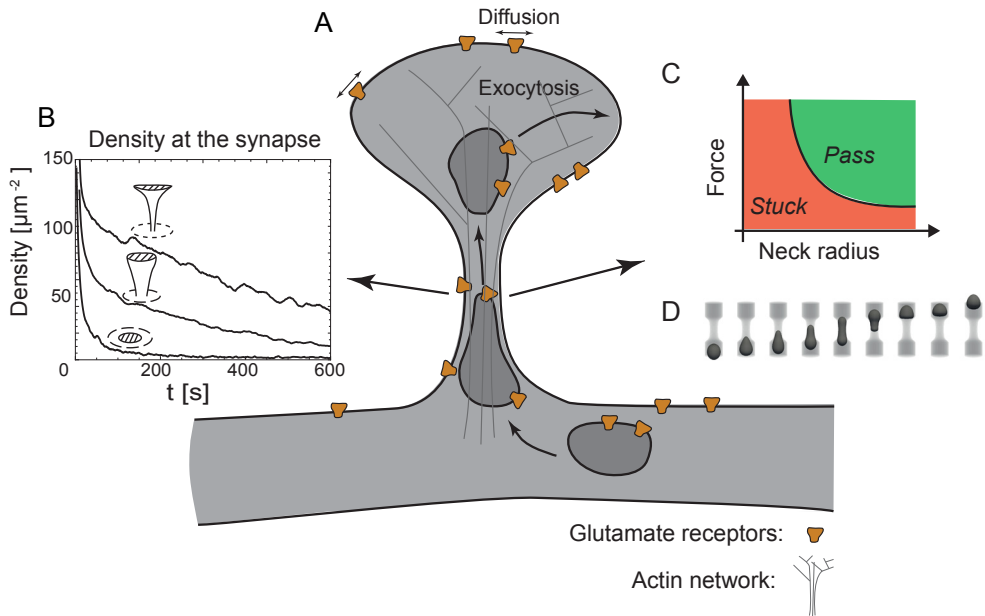


Figure 3 | The dendritic spine as a regulatory system.

(A) Schematic view of a dendritic spine containing recycling endosomes, glutamate receptors and actin cytoskeleton. (B) Decreasing the radius of the neck increases the retention of receptors at the synapse, indicated by the time-evolution of the density at the synapse (dashed area) for a planar, stubby and mushroom shaped spine (ref 17). (C) Phase diagram indicating that decreasing the neck radius increases the force necessary to transport recycling endosomes through the actin rich constriction. (D) Typical sequence of shapes during the translocation of an endosome through the neck, obtained with three-dimensional Lattice-Boltzmann simulations (ref 143).

The concept of a freely diffusive environment for these receptors, as has been presumed in all the previously described studies, is a very crude approximation of reality. The dendritic membranes on which these receptors reside are, similar to other biological membranes, highly crowded structures (140). Crowding itself is known to significantly decrease the in-plane mobility of proteins (131). A recent study on the diffusion of steric repulsive particles confined to a cylinder confirmed that, for dense systems, a tubular geometry effectively limits the diffusion of particles along the long axis of the tube (141). However, how crowding exactly affects the diffusion on highly curved structures remains elusive and will be the focus of future experimental and theoretical studies.

The Effect of Spine Shape on Vesicular Transport

Besides the effect of shape on lateral mobility, the overall shape of a dendritic spine also impacts the active transport of recycling endosomes. These endosomes, necessary for the delivery and the retrieval of receptors, have been found to operate both close to the synapse, within the head of the spine and in the dendritic shaft (94, 142). Endosome-based delivery of receptors

into the head of the dendritic spine does come at a cost: To reach the spine head, they have to cross the actin rich neck, which inevitably causes the endosomes to deform. A recent study that explicitly modeled the translocation of vesicles through narrow constrictions has shown that the force produced by a realistic number of molecular motors is capable of transporting an endosome through constrictions with similar dimensions as spine necks (143). However, this translocation is highly sensitive to the size of the neck and the applied force. This can be shown in a phase diagram indicating whether an endosome passes through the neck or gets stuck in the constriction; see Figure 3(C,D). Although this study did not explicitly model the actin meshwork in the neck, nor the potential deformation of the spine neck itself, it suggests that decreasing the size of the neck, in contrast to its effect on passive diffusion, could hamper the active transport of receptors (143). Further development of this model requires a careful experimental analysis of the deformations of both vesicles and the spine neck during spine entry events.

SUMMARY AND OUTLOOK

In this review we have highlighted existing evidence for a role of spine morphology in the compartmentalization of different important processes, such as receptor trafficking and multiple signaling events. Despite the importance for spine functioning, the exact mechanisms that govern compartmentalization are poorly understood. For example, the extent in which protein diffusion is governed by spine shape alone has remained unclear, because most experiments have so far been unable to directly correlate dynamic readouts with exact spine shape. Importantly, two pioneering studies have recently exploited developments in high-resolution light microscopy to more directly map spine morphology in live experiments and examine its effect on diffusion of free molecules (18, 19). Combined with the mathematical modeling approaches that we described (17), this should allow to dissect the interplay between purely shape-based compartmentalization mechanisms and additional cell-biological mechanisms that confine both signaling and receptor localizations. A better understanding of spine compartmentalization and its implication in plasticity will lead to a deepened and refined model on how synaptic strength is regulated on a molecular level.

ACKNOWLEDGEMENT

This work is part of the research programme of the Foundation for Fundamental Research on Matter (FOM), which is part of the Netherlands Organisation for Scientific Research (NWO). C.J.W was supported by an NWO-VIDI grant.

AUTHOR CONTRIBUTIONS

M.A. designed the outline and wrote the manuscript with advice from L.C.K and C.C.H.. L.C.K. and C.J.W. contributed to sections “Imaging Spine Morphology” and “Compartmentalization of Electrical Signals”, respectively. R.K. and C.S. contributed to the section “Spine Morphology as Compartmentalization Mechanism”.

REFERENCES

1. Ramón y Cajal, S. 1888. Estructura de los centros nerviosos de las aves.
2. Bourne, J. N., and K. M. Harris. 2008. Balancing structure and function at hippocampal dendritic spines.

- Annual review of neuroscience 31:47-67.
3. Holtmaat, A., and K. Svoboda. 2009. Experience-dependent structural synaptic plasticity in the mammalian brain. *Nature reviews. Neuroscience* 10:647-658.
 4. Schikorski, T., and C. F. Stevens. 1999. Quantitative fine-structural analysis of olfactory cortical synapses. *Proceedings of the National Academy of Sciences of the United States of America* 96:4107-4112.
 5. Arellano, J. I., R. Benavides-Piccione, J. Defelipe, and R. Yuste. 2007. Ultrastructure of dendritic spines: correlation between synaptic and spine morphologies. *Front Neurosci* 1:131-143.
 6. Yuste, R., and T. Bonhoeffer. 2001. Morphological changes in dendritic spines associated with long-term synaptic plasticity. *Annual review of neuroscience* 24:1071-1089.
 7. Kasai, H., M. Fukuda, S. Watanabe, A. Hayashi-Takagi, and J. Noguchi. 2010. Structural dynamics of dendritic spines in memory and cognition. *Trends in neurosciences* 33:121-129.
 8. Matus, A. 2000. Actin-based plasticity in dendritic spines. *Science* 290:754-758.
 9. Hering, H., and M. Sheng. 2001. Dendritic spines: structure, dynamics and regulation. *Nature reviews. Neuroscience* 2:880-888.
 10. Luo, L. 2002. Actin cytoskeleton regulation in neuronal morphogenesis and structural plasticity. *Annual review of cell and developmental biology* 18:601-635.
 11. Ethell, I. M., and E. B. Pasquale. 2005. Molecular mechanisms of dendritic spine development and remodeling. *Prog Neurobiol* 75:161-205.
 12. Hotulainen, P., and C. C. Hoogenraad. 2010. Actin in dendritic spines: connecting dynamics to function. *The Journal of cell biology* 189:619-629.
 13. Kessels, M. M., L. Schwintzer, D. Schlobinski, and B. Qualmann. 2011. Controlling actin cytoskeletal organization and dynamics during neuronal morphogenesis. *Eur J Cell Biol* 90:926-933.
 14. Bosch, M., and Y. Hayashi. 2012. Structural plasticity of dendritic spines. *Current opinion in neurobiology* 22:383-388.
 15. Kneussel, M., and W. Wagner. 2013. Myosin motors at neuronal synapses: drivers of membrane transport and actin dynamics. *Nature reviews. Neuroscience* 14:233-247.
 16. Holcman, D., and Z. Schuss. 2011. Diffusion laws in dendritic spines. *J Math Neurosci* 1:10.
 17. Kusters, R., L. C. Kaptein, C. C. Hoogenraad, and C. Storm. 2013. Shape-induced asymmetric diffusion in dendritic spines allows efficient synaptic AMPA receptor trapping. *Biophysical journal* 105:2743-2750.
 18. Tonnesen, J., G. Katona, B. Rozsa, and U. V. Nagerl. 2014. Spine neck plasticity regulates compartmentalization of synapses. *Nature neuroscience* 17:678-685.
 19. Takasaki, K., and B. L. Sabatini. 2014. Super-resolution 2-photon microscopy reveals that the morphology of each dendritic spine correlates with diffusive but not synaptic properties. *Frontiers in neuroanatomy* 8:29.
 20. Ramón y Cajal, S. 1904. *Histology of the Nervous System of Man and Vertebrates - La Textura del Sistema Nerviosa del Hombre y los Vertebrados*.
 21. Gray, E. G. 1959. Axo-somatic and axo-dendritic synapses of the cerebral cortex: an electron microscope study. *J Anat* 93:420-433.
 22. Bourne, J. N., and K. M. Harris. 2012. Nanoscale analysis of structural synaptic plasticity. *Current opinion in neurobiology* 22:372-382.
 23. Svoboda, K., D. W. Tank, and W. Denk. 1996. Direct measurement of coupling between dendritic spines and shafts. *Science* 272:716-719.
 24. Denk, W., J. H. Strickler, and W. W. Webb. 1990. Two-photon laser scanning fluorescence microscopy. *Science* 248:73-76.
 25. Svoboda, K., and R. Yasuda. 2006. Principles of two-photon excitation microscopy and its applications to neuroscience. *Neuron* 50:823-839.
 26. Holtmaat, A., L. Wilbrecht, G. W. Knott, E. Welker, and K. Svoboda. 2006. Experience-dependent and cell-type-specific spine growth in the neocortex. *Nature* 441:979-983.

27. Trachtenberg, J. T., B. E. Chen, G. W. Knott, G. Feng, J. R. Sanes, E. Welker, and K. Svoboda. 2002. Long-term in vivo imaging of experience-dependent synaptic plasticity in adult cortex. *Nature* 420:788-794.
28. Hell, S. W. 2007. Far-field optical nanoscopy. *Science* 316:1153-1158.
29. Klar, T. A., S. Jakobs, M. Dyba, A. Egner, and S. W. Hell. 2000. Fluorescence microscopy with diffraction resolution barrier broken by stimulated emission. *Proceedings of the National Academy of Sciences of the United States of America* 97:8206-8210.
30. Nagerl, U. V., K. I. Willig, B. Hein, S. W. Hell, and T. Bonhoeffer. 2008. Live-cell imaging of dendritic spines by STED microscopy. *Proceedings of the National Academy of Sciences of the United States of America* 105:18982-18987.
31. Berning, S., K. I. Willig, H. Steffens, P. Dibaj, and S. W. Hell. 2012. Nanoscopy in a living mouse brain. *Science* 335:551.
32. Moneron, G., and S. W. Hell. 2009. Two-photon excitation STED microscopy. *Optics express* 17:14567-14573.
33. Ding, J. B., K. T. Takasaki, and B. L. Sabatini. 2009. Supraresolution imaging in brain slices using stimulated-emission depletion two-photon laser scanning microscopy. *Neuron* 63:429-437.
34. Bethge, P., R. Chereau, E. Avignone, G. Marsicano, and U. V. Nagerl. 2013. Two-photon excitation STED microscopy in two colors in acute brain slices. *Biophysical journal* 104:778-785.
35. Takasaki, K. T., J. B. Ding, and B. L. Sabatini. 2013. Live-cell superresolution imaging by pulsed STED two-photon excitation microscopy. *Biophysical journal* 104:770-777.
36. Tonnesen, J., F. Nadrigny, K. I. Willig, R. Wedlich-Soldner, and U. V. Nagerl. 2011. Two-color STED microscopy of living synapses using a single laser-beam pair. *Biophysical journal* 101:2545-2552.
37. Gould, T. J., D. Burke, J. Bewersdorf, and M. J. Booth. 2012. Adaptive optics enables 3D STED microscopy in aberrating specimens. *Optics express* 20:20998-21009.
38. Loew, L. M., and S. W. Hell. 2013. Superresolving dendritic spines. *Biophysical journal* 104:741-743.
39. Grotjohann, T., I. Testa, M. Leutenegger, H. Bock, N. T. Urban, F. Lavoie-Cardinal, K. I. Willig, C. Eggeling, S. Jakobs, and S. W. Hell. 2011. Diffraction-unlimited all-optical imaging and writing with a photochromic GFP. *Nature* 478:204-208.
40. Testa, I., N. T. Urban, S. Jakobs, C. Eggeling, K. I. Willig, and S. W. Hell. 2012. Nanoscopy of living brain slices with low light levels. *Neuron* 75:992-1000.
41. Lavoie-Cardinal, F., N. A. Jensen, V. Westphal, A. C. Stiel, A. Chmyrov, J. Bierwagen, I. Testa, S. Jakobs, and S. W. Hell. 2014. Two-color RESOLFT nanoscopy with green and red fluorescent photochromic proteins. *Chemphyschem : a European journal of chemical physics and physical chemistry* 15:655-663.
42. Shcherbakova, D. M., P. Sengupta, J. Lippincott-Schwartz, and V. V. Verkhusha. 2014. Photocontrollable fluorescent proteins for superresolution imaging. *Annual review of biophysics* 43:303-329.
43. Huang, B., M. Bates, and X. Zhuang. 2009. Super-resolution fluorescence microscopy. *Annu Rev Biochem* 78:993-1016.
44. Huang, B. 2010. Super-resolution optical microscopy: multiple choices. *Curr Opin Chem Biol* 14:10-14.
45. Giannone, G., E. Hossy, F. Levet, A. Constals, K. Schulze, A. I. Sobolevsky, M. P. Rosconi, E. Gouaux, R. Tampe, D. Choquet, and L. Cognet. 2010. Dynamic superresolution imaging of endogenous proteins on living cells at ultra-high density. *Biophysical journal* 99:1303-1310.
46. Ries, J., C. Kaplan, E. Platonova, H. Eghlidi, and H. Ewers. 2012. A simple, versatile method for GFP-based super-resolution microscopy via nanobodies. *Nature methods* 9:582-584.
47. Frost, N. A., H. Shroff, H. Kong, E. Betzig, and T. A. Blanpied. 2010. Single-molecule discrimination of discrete perisynaptic and distributed sites of actin filament assembly within dendritic spines. *Neuron* 67:86-99.
48. Izeddin, I., C. G. Specht, M. Lelek, X. Darzacq, A. Triller, C. Zimmer, and M. Dahan. 2011. Super-resolution dynamic imaging of dendritic spines using a low-affinity photoconvertible actin probe. *PLoS one* 6:e15611.
49. Shim, S. H., C. Xia, G. Zhong, H. P. Babcock, J. C. Vaughan, B. Huang, X. Wang, C. Xu, G. Q. Bi, and X. Zhuang. 2012. Super-resolution fluorescence imaging of organelles in live cells with photoswitchable membrane

- probes. *Proceedings of the National Academy of Sciences of the United States of America* 109:13978-13983.
50. Frost, N. A., H. E. Lu, and T. A. Blanpied. 2012. Optimization of cell morphology measurement via single-molecule tracking PALM. *PLoS one* 7:e36751.
 51. Anderson, J. C., R. J. Douglas, K. A. Martin, and J. C. Nelson. 1994. Map of the synapses formed with the dendrites of spiny stellate neurons of cat visual cortex. *J Comp Neurol* 341:25-38.
 52. Araya, R., T. P. Vogels, and R. Yuste. 2014. Activity-dependent dendritic spine neck changes are correlated with synaptic strength. *Proceedings of the National Academy of Sciences of the United States of America* 111:E2895-2904.
 53. Yuste, R., and W. Denk. 1995. Dendritic spines as basic functional units of neuronal integration. *Nature* 375:682-684.
 54. Matsuzaki, M., N. Honkura, G. C. Ellis-Davies, and H. Kasai. 2004. Structural basis of long-term potentiation in single dendritic spines. *Nature* 429:761-766.
 55. Bloodgood, B. L., and B. L. Sabatini. 2005. Neuronal activity regulates diffusion across the neck of dendritic spines. *Science* 310:866-869.
 56. Bloodgood, B. L., and B. L. Sabatini. 2007. Ca(2+) signaling in dendritic spines. *Current opinion in neurobiology* 17:345-351.
 57. Lledo, P. M., G. O. Hjelmstad, S. Mukherji, T. R. Soderling, R. C. Malenka, and R. A. Nicoll. 1995. Calcium/calmodulin-dependent kinase II and long-term potentiation enhance synaptic transmission by the same mechanism. *Proceedings of the National Academy of Sciences of the United States of America* 92:11175-11179.
 58. Pettit, D. L., S. Perlman, and R. Malinow. 1994. Potentiated transmission and prevention of further LTP by increased CaMKII activity in postsynaptic hippocampal slice neurons. *Science* 266:1881-1885.
 59. Otmakhov, N., J. H. Tao-Cheng, S. Carpenter, B. Asrican, A. Dosemeci, T. S. Reese, and J. Lisman. 2004. Persistent accumulation of calcium/calmodulin-dependent protein kinase II in dendritic spines after induction of NMDA receptor-dependent chemical long-term potentiation. *The Journal of neuroscience : the official journal of the Society for Neuroscience* 24:9324-9331.
 60. Sabatini, B. L., T. G. Oertner, and K. Svoboda. 2002. The life cycle of Ca(2+) ions in dendritic spines. *Neuron* 33:439-452.
 61. Noguchi, J., M. Matsuzaki, G. C. Ellis-Davies, and H. Kasai. 2005. Spine-neck geometry determines NMDA receptor-dependent Ca2+ signaling in dendrites. *Neuron* 46:609-622.
 62. Majewska, A., E. Brown, J. Ross, and R. Yuste. 2000. Mechanisms of calcium decay kinetics in hippocampal spines: role of spine calcium pumps and calcium diffusion through the spine neck in biochemical compartmentalization. *The Journal of neuroscience : the official journal of the Society for Neuroscience* 20:1722-1734.
 63. Holthoff, K., D. Tsay, and R. Yuste. 2002. Calcium dynamics of spines depend on their dendritic location. *Neuron* 33:425-437.
 64. Korkotian, E., D. Holcman, and M. Segal. 2004. Dynamic regulation of spine-dendrite coupling in cultured hippocampal neurons. *The European journal of neuroscience* 20:2649-2663.
 65. Bloodgood, B. L., A. J. Giessel, and B. L. Sabatini. 2009. Biphasic synaptic Ca influx arising from compartmentalized electrical signals in dendritic spines. *PLoS biology* 7:e1000190.
 66. Bloodgood, B. L., and B. L. Sabatini. 2007. Nonlinear regulation of unitary synaptic signals by CaV(2.3) voltage-sensitive calcium channels located in dendritic spines. *Neuron* 53:249-260.
 67. Kennedy, M. B., H. C. Beale, H. J. Carlisle, and L. R. Washburn. 2005. Integration of biochemical signalling in spines. *Nature reviews. Neuroscience* 6:423-434.
 68. Yoshimura, Y., T. Shinkawa, M. Taoka, K. Kobayashi, T. Isobe, and T. Yamauchi. 2002. Identification of protein substrates of Ca(2+)/calmodulin-dependent protein kinase II in the postsynaptic density by protein

- sequencing and mass spectrometry. *Biochem Biophys Res Commun* 290:948-954.
69. Okamoto, K., R. Narayanan, S. H. Lee, K. Murata, and Y. Hayashi. 2007. The role of CaMKII as an F-actin-bundling protein crucial for maintenance of dendritic spine structure. *Proceedings of the National Academy of Sciences of the United States of America* 104:6418-6423.
 70. Lee, S. J., Y. Escobedo-Lozoya, E. M. Szatmari, and R. Yasuda. 2009. Activation of CaMKII in single dendritic spines during long-term potentiation. *Nature* 458:299-304.
 71. Ramakers, G. J. A. 2002. Rho proteins, mental retardation and the cellular basis of cognition. *Trends in neurosciences* 25:191-199.
 72. Saneyoshi, T., D. A. Fortin, and T. R. Soderling. 2010. Regulation of spine and synapse formation by activity-dependent intracellular signaling pathways. *Current opinion in neurobiology* 20:108-115.
 73. Zhu, J. J., Y. Qin, M. Zhao, L. Van Aelst, and R. Malinow. 2002. Ras and Rap control AMPA receptor trafficking during synaptic plasticity. *Cell* 110:443-455.
 74. Patterson, M. A., E. M. Szatmari, and R. Yasuda. 2010. AMPA receptors are exocytosed in stimulated spines and adjacent dendrites in a Ras-ERK-dependent manner during long-term potentiation. *Proceedings of the National Academy of Sciences of the United States of America* 107:15951-15956.
 75. Harvey, C. D., R. Yasuda, H. Zhong, and K. Svoboda. 2008. The spread of Ras activity triggered by activation of a single dendritic spine. *Science* 321:136-140.
 76. Murakoshi, H., H. Wang, and R. Yasuda. 2011. Local, persistent activation of Rho GTPases during plasticity of single dendritic spines. *Nature* 472:100-104.
 77. Byrne, M. J., M. N. Waxham, and Y. Kubota. 2011. The impacts of geometry and binding on CaMKII diffusion and retention in dendritic spines. *Journal of computational neuroscience* 31:1-12.
 78. Lisman, J. E., and A. M. Zhabotinsky. 2001. A model of synaptic memory: a CaMKII/PP1 switch that potentiates transmission by organizing an AMPA receptor anchoring assembly. *Neuron* 31:191-201.
 79. Fukunaga, K., D. Muller, and E. Miyamoto. 1995. Increased phosphorylation of Ca²⁺/calmodulin-dependent protein kinase II and its endogenous substrates in the induction of long-term potentiation. *J Biol Chem* 270:6119-6124.
 80. Barria, A., D. Muller, V. Derkach, L. C. Griffith, and T. R. Soderling. 1997. Regulatory phosphorylation of AMPA-type glutamate receptors by CaM-KII during long-term potentiation. *Science* 276:2042-2045.
 81. Harvey, C. D., and K. Svoboda. 2007. Locally dynamic synaptic learning rules in pyramidal neuron dendrites. *Nature* 450:1195-1200.
 82. Malinow, R., and R. C. Malenka. 2002. AMPA receptor trafficking and synaptic plasticity. *Annual review of neuroscience* 25:103-126.
 83. Brecht, D. S., and R. A. Nicoll. 2003. AMPA receptor trafficking at excitatory synapses. *Neuron* 40:361-379.
 84. Collingridge, G. L., J. T. Isaac, and Y. T. Wang. 2004. Receptor trafficking and synaptic plasticity. *Nature reviews. Neuroscience* 5:952-962.
 85. Sheng, M., and M. J. Kim. 2002. Postsynaptic signaling and plasticity mechanisms. *Science* 298:776-780.
 86. Nusser, Z. 2000. AMPA and NMDA receptors: similarities and differences in their synaptic distribution. *Current opinion in neurobiology* 10:337-341.
 87. Richards, D. A., V. De Paola, P. Caroni, B. H. Gahwiler, and R. A. McKinney. 2004. AMPA-receptor activation regulates the diffusion of a membrane marker in parallel with dendritic spine motility in the mouse hippocampus. *The Journal of physiology* 558:503-512.
 88. Triller, A., and D. Choquet. 2005. Surface trafficking of receptors between synaptic and extrasynaptic membranes: and yet they do move! *Trends in neurosciences* 28:133-139.
 89. Adesnik, H., R. A. Nicoll, and P. M. England. 2005. Photoinactivation of native AMPA receptors reveals their real-time trafficking. *Neuron* 48:977-985.
 90. Ashby, M. C., S. R. Maier, A. Nishimune, and J. M. Henley. 2006. Lateral diffusion drives constitutive exchange of AMPA receptors at dendritic spines and is regulated by spine morphology. *The Journal of neuroscience*

- 26:7046-7055.
91. Borgdorff, A. J., and D. Choquet. 2002. Regulation of AMPA receptor lateral movements. *Nature* 417:649-653.
 92. Ehlers, M. D., M. Heine, L. Groc, M. C. Lee, and D. Choquet. 2007. Diffusional trapping of GluR1 AMPA receptors by input-specific synaptic activity. *Neuron* 54:447-460.
 93. Passafaro, M., V. Piech, and M. Sheng. 2001. Subunit-specific temporal and spatial patterns of AMPA receptor exocytosis in hippocampal neurons. *Nature neuroscience* 4:917-926.
 94. Park, M., J. M. Salgado, L. Ostroff, T. D. Helton, C. G. Robinson, K. M. Harris, and M. D. Ehlers. 2006. Plasticity-induced growth of dendritic spines by exocytic trafficking from recycling endosomes. *Neuron* 52:817-830.
 95. Czondor, K., and O. Thoumine. 2013. Biophysical mechanisms regulating AMPA receptor accumulation at synapses. *Brain research bulletin* 93:57-68.
 96. Newpher, T. M., and M. D. Ehlers. 2008. Glutamate receptor dynamics in dendritic microdomains. *Neuron* 58:472-497.
 97. Opazo, P., and D. Choquet. 2011. A three-step model for the synaptic recruitment of AMPA receptors. *Molecular and cellular neurosciences* 46:1-8.
 98. Kennedy, M. J., I. G. Davison, C. G. Robinson, and M. D. Ehlers. 2010. Syntaxin-4 defines a domain for activity-dependent exocytosis in dendritic spines. *Cell* 141:524-535.
 99. Yang, Y., X. B. Wang, M. Frerking, and Q. Zhou. 2008. Delivery of AMPA receptors to perisynaptic sites precedes the full expression of long-term potentiation. *Proceedings of the National Academy of Sciences of the United States of America* 105:11388-11393.
 100. Heine, M., L. Groc, R. Frischknecht, J. C. Beique, B. Lounis, G. Rumbaugh, R. L. Huganir, L. Cognet, and D. Choquet. 2008. Surface mobility of postsynaptic AMPARs tunes synaptic transmission. *Science* 320:201-205.
 101. Czondor, K., M. Mondin, M. Garcia, M. Heine, R. Frischknecht, D. Choquet, J. B. Sibarita, and O. R. Thoumine. 2012. Unified quantitative model of AMPA receptor trafficking at synapses. *Proceedings of the National Academy of Sciences of the United States of America* 109:3522-3527.
 102. Ashby, M. C., S. A. De La Rue, G. S. Ralph, J. Uney, G. L. Collingridge, and J. M. Henley. 2004. Removal of AMPA receptors (AMPARs) from synapses is preceded by transient endocytosis of extrasynaptic AMPARs. *The Journal of neuroscience : the official journal of the Society for Neuroscience* 24:5172-5176.
 103. Miesenböck, G., D. A. De Angelis, and J. E. Rothman. 1998. Visualizing secretion and synaptic transmission with pH-sensitive green fluorescent proteins. *Nature* 394:192-195.
 104. Makino, H., and R. Malinow. 2009. AMPA receptor incorporation into synapses during LTP: the role of lateral movement and exocytosis. *Neuron* 64:381-390.
 105. Tardin, C., L. Cognet, C. Bats, B. Lounis, and D. Choquet. 2003. Direct imaging of lateral movements of AMPA receptors inside synapses. *The EMBO journal* 22:4656-4665.
 106. Dahan, M., S. Levi, C. Luccardini, P. Rostaing, B. Riveau, and A. Triller. 2003. Diffusion dynamics of glycine receptors revealed by single-quantum dot tracking. *Science* 302:442-445.
 107. Nair, D., E. Hossy, J. D. Petersen, A. Constals, G. Giannone, D. Choquet, and J. B. Sibarita. 2013. Super-resolution imaging reveals that AMPA receptors inside synapses are dynamically organized in nanodomains regulated by PSD95. *The Journal of neuroscience : the official journal of the Society for Neuroscience* 33:13204-13224.
 108. MacGillavry, H. D., Y. Song, S. Raghavachari, and T. A. Blanpied. 2013. Nanoscale scaffolding domains within the postsynaptic density concentrate synaptic AMPA receptors. *Neuron* 78:615-622.
 109. Granger, A. J., Y. Shi, W. Lu, M. Cerpas, and R. A. Nicoll. 2013. LTP requires a reserve pool of glutamate receptors independent of subunit type. *Nature* 493:495-500.
 110. Sheng, M., R. Malinow, and R. Huganir. 2013. Neuroscience: Strength in numbers. *Nature* 493:482-483.
 111. Renner, M., D. Choquet, and A. Triller. 2009. Control of the postsynaptic membrane viscosity. *The Journal of neuroscience : the official journal of the Society for Neuroscience* 29:2926-2937.

112. Colgan, L. A., and R. Yasuda. 2014. Plasticity of dendritic spines: subcompartmentalization of signaling. *Annual review of physiology* 76:365-385.
113. Yuste, R. 2013. Electrical compartmentalization in dendritic spines. *Annual review of neuroscience* 36:429-449.
114. Segev, I., and W. Rall. 1998. Excitable dendrites and spines: earlier theoretical insights elucidate recent direct observations. *Trends in neurosciences* 21:453-460.
115. Holthoff, K., D. Zecevic, and A. Konnerth. 2010. Rapid time course of action potentials in spines and remote dendrites of mouse visual cortex neurons. *The Journal of physiology* 588:1085-1096.
116. Carter, B. C., A. J. Giessel, B. L. Sabatini, and B. P. Bean. 2012. Transient sodium current at subthreshold voltages: activation by EPSP waveforms. *Neuron* 75:1081-1093.
117. Popovic, M. A., X. Gao, N. T. Carnevale, and D. Zecevic. 2014. Cortical dendritic spine heads are not electrically isolated by the spine neck from membrane potential signals in parent dendrites. *Cerebral cortex* 24:385-395.
118. Araya, R., J. Jiang, K. B. Eisenthal, and R. Yuste. 2006. The spine neck filters membrane potentials. *Proceedings of the National Academy of Sciences of the United States of America* 103:17961-17966.
119. Harnett, M. T., J. K. Makara, N. Spruston, W. L. Kath, and J. C. Magee. 2012. Synaptic amplification by dendritic spines enhances input cooperativity. *Nature* 491:599-602.
120. Shepherd, G. M. 1996. The dendritic spine: a multifunctional integrative unit. *Journal of neurophysiology* 75:2197-2210.
121. Tsay, D., and R. Yuste. 2004. On the electrical function of dendritic spines. *Trends in neurosciences* 27:77-83.
122. Harris, K. M., and J. K. Stevens. 1988. Dendritic spines of rat cerebellar Purkinje cells: serial electron microscopy with reference to their biophysical characteristics. *The Journal of neuroscience : the official journal of the Society for Neuroscience* 8:4455-4469.
123. Koch, C., and A. Zador. 1993. The function of dendritic spines: devices subserving biochemical rather than electrical compartmentalization. *The Journal of neuroscience : the official journal of the Society for Neuroscience* 13:413-422.
124. Tanaka, J., Y. Horiike, M. Matsuzaki, T. Miyazaki, G. C. Ellis-Davies, and H. Kasai. 2008. Protein synthesis and neurotrophin-dependent structural plasticity of single dendritic spines. *Science* 319:1683-1687.
125. Grunditz, A., N. Holbro, L. Tian, Y. Zuo, and T. G. Oertner. 2008. Spine neck plasticity controls postsynaptic calcium signals through electrical compartmentalization. *The Journal of neuroscience : the official journal of the Society for Neuroscience* 28:13457-13466.
126. Hao, J., and T. G. Oertner. 2012. Depolarization gates spine calcium transients and spike-timing-dependent potentiation. *Current opinion in neurobiology* 22:509-515.
127. Holbro, N., A. Grunditz, J. S. Wiegert, and T. G. Oertner. 2010. AMPA receptors gate spine Ca(2+) transients and spike-timing-dependent potentiation. *Proceedings of the National Academy of Sciences of the United States of America* 107:15975-15980.
128. Araya, R., V. Nikolenko, K. B. Eisenthal, and R. Yuste. 2007. Sodium channels amplify spine potentials. *Proceedings of the National Academy of Sciences of the United States of America* 104:12347-12352.
129. Giessel, A. J., and B. L. Sabatini. 2010. M1 muscarinic receptors boost synaptic potentials and calcium influx in dendritic spines by inhibiting postsynaptic SK channels. *Neuron* 68:936-947.
130. Ngo-Anh, T. J., B. L. Bloodgood, M. Lin, B. L. Sabatini, J. Maylie, and J. P. Adelman. 2005. SK channels and NMDA receptors form a Ca2+-mediated feedback loop in dendritic spines. *Nature neuroscience* 8:642-649.
131. Santamaria, F., J. Gonzalez, G. J. Augustine, and S. Raghavachari. 2010. Quantifying the effects of elastic collisions and non-covalent binding on glutamate receptor trafficking in the post-synaptic density. *PLoS Comput Biol* 6:e1000780.
132. O'Brien, R. J., D. Xu, R. S. Petralia, O. Steward, R. L. Huganir, and P. Worley. 1999. Synaptic clustering of AMPA receptors by the extracellular immediate-early gene product Narp. *Neuron* 23:309-323.

133. Saglietti, L., C. Dequidt, K. Kamieniarz, M. C. Rousset, P. Valnegri, O. Thoumine, F. Beretta, L. Fagni, D. Choquet, C. Sala, M. Sheng, and M. Passafaro. 2007. Extracellular interactions between GluR2 and N-cadherin in spine regulation. *Neuron* 54:461-477.
134. Gudheti, M. V., N. M. Curthoys, T. J. Gould, D. Kim, M. S. Gunewardene, K. A. Gabor, J. A. Gosse, C. H. Kim, J. Zimmerberg, and S. T. Hess. 2013. Actin mediates the nanoscale membrane organization of the clustered membrane protein influenza hemagglutinin. *Biophysical journal* 104:2182-2192.
135. Allison, D. W., A. S. Chervin, V. I. Gelfand, and A. M. Craig. 2000. Postsynaptic scaffolds of excitatory and inhibitory synapses in hippocampal neurons: maintenance of core components independent of actin filaments and microtubules. *The Journal of neuroscience : the official journal of the Society for Neuroscience* 20:4545-4554.
136. Kusters, R., and C. Storm. 2014. Impact of morphology on diffusive dynamics on curved surfaces. *Phys Rev E Stat Nonlin Soft Matter Phys* 89:032723.
137. Saffman, P. G., and M. Delbruck. 1975. Brownian motion in biological membranes. *Proceedings of the National Academy of Sciences of the United States of America* 72:3111-3113.
138. Domanov, Y. A., S. Aimon, G. E. Toombes, M. Renner, F. Quemeneur, A. Triller, M. S. Turner, and P. Bassereau. 2011. Mobility in geometrically confined membranes. *Proceedings of the National Academy of Sciences of the United States of America* 108:12605-12610.
139. Daniels, D. R., and M. S. Turner. 2007. Diffusion on membrane tubes: a highly discriminatory test of the Saffman-Delbruck theory. *Langmuir* 23:6667-6670.
140. Takamori, S., M. Holt, K. Stenius, E. A. Lemke, M. Gronborg, D. Riedel, H. Urlaub, S. Schenck, B. Brugger, P. Ringler, S. A. Muller, B. Rammner, F. Gräter, J. S. Hub, B. L. De Groot, G. Mieskes, Y. Moriyama, J. Klingauf, H. Grubmüller, J. Heuser, F. Wieland, and R. Jahn. 2006. Molecular anatomy of a trafficking organelle. *Cell* 127:831-846.
141. Kusters, R., S. Paquay, and C. Storm. 2014. Confinement without boundaries: Anisotropic diffusion on the surface of a cylinder. In *ArXiv e-prints*. 3564.
142. Wang, Z., J. G. Edwards, N. Riley, D. W. Provan, Jr., R. Karcher, X. D. Li, I. G. Davison, M. Ikebe, J. A. Mercer, J. A. Kauer, and M. D. Ehlers. 2008. Myosin Vb mobilizes recycling endosomes and AMPA receptors for postsynaptic plasticity. *Cell* 135:535-548.
143. Kusters, R., T. van der Heijden, B. Kaoui, J. Harting, and C. Storm. 2014. Forced transport of deformable containers through narrow constrictions. *Physical Review E* 90:033006.



Probing the Interplay between Dendritic Spine Morphology and Membrane-Bound Diffusion

Max Adrian¹, Remy Kusters², Cornelis Storm^{2,3}, Casper C. Hoogenraad¹ and Lukas C. Kapitein¹

¹ *Division of Cell Biology, Faculty of Science, Utrecht University, Utrecht, The Netherlands,*

² *Department of Applied Physics, Eindhoven University of Technology, Eindhoven, The Netherlands,*

³ *Institute for Complex Molecular Systems, Eindhoven University of Technology, Eindhoven, The Netherlands.*

ABSTRACT

Dendritic spines are protrusions along neuronal dendrites that harbor the majority of excitatory postsynapses. Their distinct morphology, often featuring a bulbous head and small neck that connects to the dendritic shaft, has been shown to facilitate compartmentalization of electrical and cytoplasmic signaling stimuli elicited at the synapse. The extent to which spine morphology also forms a barrier for membrane-bound diffusion has remained unclear. Recent simulations suggested that especially the diameter of the spine neck plays a limiting role in this process. Here, we examine the connection between spine morphology and membrane-bound diffusion through a combination of photoconversion, live-cell super-resolution experiments and numerical simulations. Local photoconversion was used to obtain the time scale of diffusive equilibration in spines and followed by global sparse photoconversion to determine spine morphologies with nanoscopic resolution. These morphologies were subsequently used to assess the role of morphology on the diffusive equilibration. From the simulations, we could determine a robust relation between the equilibration time scale and a generalized shape factor calculated using both spine neck width and neck length, as well as spine head size. Experimentally, we found that diffusive equilibration was often slower, but rarely faster than predicted from the simulations, indicating that other biological confounders further reduce membrane-bound diffusion in these spines. This shape-dependent membrane-bound diffusion in mature spines may contribute to spine-specific compartmentalization of neurotransmitter receptors and signaling molecules and thereby support long-term plasticity of synaptic contacts.

INTRODUCTION

Dendritic spines are subcellular compartments that protrude from the dendritic shaft and typically consist of a micron-sized head connected to the dendrite by a thin neck (1). Interestingly, spine morphology is neither homogenous nor static. Spine morphologies have been classified as “filopodia-like”, “stubby” and “mushroom-shaped”. Changes in spine morphology over time have been linked to neuronal activity and learning paradigms both *in vitro* and *in vivo* (2–4). The maturation of spines, from filopodia to mature mushroom spines with a large post-synaptic density (PSD) in the head, has been described previously (5, 6), explaining the large variety of spine shapes along a dendrite. Importantly, spine size has also been correlated to synaptic strength – a measure often based on the amount of glutamate receptors located in the spine and integrated into the PSD (7). These receptors can reach the synapse either through lateral diffusion in the plasma membrane or by local exocytosis from intracellular storage pools (8). Many studies have characterized the motility and retention of glutamate receptors in spines (9–12). More recently, theoretical and numerical simulations have suggested that the morphology of spines may alter the capturing and compartmentalization of glutamate receptors (13–15).

Compartmentalization in spines has already been observed both for electrical stimuli (16, 17) and cytoplasmic diffusion (18–20). For both, mushroom-like spines have shown less coupling to the dendritic shaft. Less clear is the role of spine morphology in membrane-bound diffusion. Early studies showed that mushroom-like spines recover more slowly from bleaching fluorescent markers in the membrane than stubby spines (21). It was also shown that spines can retain membrane-associated signaling molecules like the small GTPase Ras,

preventing them from spreading along the dendrite (22). Based on this, we hypothesized that the spine morphology and particularly the neck diameter may play a role in regulating diffusion speed (13, 23). However, dendritic spines are too small to measure accurately with conventional fluorescent microscopy, necessitating the use of super-resolution microscopy to directly correlate diffusion time constants with morphology parameters (24).

Here we use single molecule localization microscopy and photoconversion of a small exogenous membrane-bound probe to accurately quantify spine morphology and diffusion rates. We then compare the diffusion measurements with particle simulations carried out on the same morphologies, to explore the contribution of spine morphology to the time scale of membrane-bound diffusion out of spines. We find that the overall shape of the spine does influence diffusion as expected from simulations. However, many spines, particularly filopodia-like spines, showed slower diffusion than expected purely based on spine shape, indicating that other biological confounders influence membrane-bound diffusion in these spines.

MATERIAL & METHODS

Ethics Statement

All animal experiments were performed in compliance with the guidelines for the welfare of experimental animals issued by the Government of The Netherlands and approved by the Animal Ethical Review Committee (DEC) of Utrecht University.

Neuron Culture & Transfection

Primary hippocampal cultures were prepared from embryonic day 18 (E18) rat brains. Cells were plated on coverslips coated with poly-L-lysine (30 $\mu\text{g}/\text{ml}$) and laminin (2 $\mu\text{g}/\text{ml}$) at a density of 100,000/well. Hippocampal cultures were grown in Neurobasal medium (NB) supplemented with B27, 0.5 mM glutamine, 12.5 μM glutamate and penicillin/streptomycin. Hippocampal neurons at 19-24DIV were transfected using Lipofectamine 2000 (Invitrogen). Briefly, DNA (3.6 $\mu\text{g}/\text{well}$) was mixed with 3 μl Lipofectamine 2000 in 200 μl NB, incubated for 30 minutes and then added to the neurons in NB with 0.5mM glutamine at 37°C in 5% CO_2 for 60 to 90 min. Next, neurons were washed with NB and transferred in the original medium at 37°C in 5% CO_2 . 2-3 days after transfection, neurons were transferred to imaging buffer (NaCl 120, KCl 3, HEPES 10, CaCl_2 2, MgCl_2 2, D-Glucose 10mM, adjusted to pH 7.35 and 240mOsm) and imaged for up to 1h at 37°C and 5% CO_2 .

To label the plasma membrane, we generated mem-mEos, a fusion of the green-to-red photoconvertible fluorescent protein mEos3.2 (25) to the carboxy-terminal CAAX motif of hKras (26) by amplifying mEos3.2 using extension PCR (FW: 5'-atggggcgcgcccttaagataaaacacattacaagacatacatcgctctggcattgtcaggcaatccagaatgag, RV: caagctagcgccaccatgagtgcgattaagccagacatgaa), followed by insertion into the β -actin vector with NheI and AscI. Farnesyltransferases will modify the CAAX motif with a hydrophobic farnesyl group (prenylation) that will target the protein to cellular membranes.

Live Cell Imaging

Dendrites were imaged on a Nikon TE2000E based TIRF microscope equipped with a LightHub4 compact laser combiner (Omicron) with LuxX 405nm 60mW, LuxX 488nm 100mW and Cobolt Jive 561nm 100mW lasers. The excitation light illuminates the sample in an oblique, near-critical angle through a CFI Apo TIRF 100x 1.49 N.A. oil objective (Nikon). Images with an effective pixel size of 64nm were acquired on an Evolve 512 EMCCD camera (Photometrics). The setup also contains a motorized stage (Prior), a Perfect Focus System (Nikon), a quad-band dichroic mirror (Chroma C166680), an incubation chamber (Tokai Hit; INUBG2E-ZILCS) and an ILas0 FRAP system (Roper Scientific France/Institut Curie). MetaMorph 7.7.6 software (Molecular Devices) was used to control the camera and all motorized parts.

For diffusion measurements, the center quadrant of the camera was used to record fluorescence images in the 561nm channel at 50ms interval in stream mode. Following a baseline measurement of 15 frames, a 405nm laser pulse was targeted to a diffraction-limited spot in the spine head to induce photoconversion of mEOS from green to red and the red fluorescence was subsequently followed for 400 frames. The same region of the dendrite was subsequently used for PALM acquisition at 30ms intervals for 6000 frames (Figure 1). 561nm and 405nm laser intensities were manually increased to achieve optimal photoconversion/bleaching dynamics to detect single molecules.

Image Analysis

Images were analysed and measured in ImageJ (NIH) and subsequent data analysis, statistical testing and plotting was carried out in R (version 3.0.0). Unless otherwise indicated, linear regression coefficients were tested for significance with a two-tailed t-test and the obtained variance is indicated as multiple R-squared. Significance code used is 0<***<0.001<**<0.01<*<0.05<ns<1.

Diffusion measurement analysis:

Fluorescence intensities in a ROI encompassing the entire targeted dendritic spine were background-subtracted with the average of the 15 frames before photoactivation and normalized to the maximum intensity recorded. The resulting intensity curves were fitted with a single exponential function of the form

$$(1) \quad y = ae^{-t/\tau} + b ,$$

Where t denotes time and τ is the characteristic time scale, and a and b denote amplitude and offset. To be considered a successful measurement, we applied a cutoff on the acceptable plateau b of 0.2 and only considered fits with a $R^2 > 0.7$.

Super-resolved morphology analysis:

To reconstruct super-resolved images of the single molecule localisations, we used a custom-written analysis software DoM (27) (https://github.com/ekatruxha/DoM_Utrecht/). We

reconstructed images at 10nm pixel size after using a correlation-based drift correction in steps of 1000 frames and applying an automated cut-off (approx. 0.3px) for localization precision. The resulting reconstructions were cropped and binarized by thresholding after removal background noise and Gaussian blurring. The base, tip and head/neck transition point of spines were annotated manually to draw a spline through the major axis of the spine. Subsequently line scans perpendicular to this axis were taken at every pixel, averaging over 10px each (Figure 1D). The full width at half maximum (FWHM) of each linescan was defined as the spine's width at this location. The average of all width measurements along the spine neck and the average of the 10 largest width measurements in the spine head were defined as neck width and head width, respectively. The spine and neck length were given by the length of the splines used for the initial line scans. Spines with a mean head width smaller than 1.5x the mean neck width were classified as filopodia-like spines.

Simulations

To simulate the role of spine shape on the diffusion of membrane-bound markers we performed Langevin dynamics simulations using the standard molecular dynamics package LAMMPS (<http://lammps.sandia.gov/>), supplemented with a Rattle contain algorithm to implement a prescribed shape for the dendritic spine (28). We used a Langevin damping time of $\tau = 0.1$ Simulation Units (SU), and assumed that particles have no mutual interactions. To fit the experimental super-resolution data, we parametrized the spine shape using the following function,

$$(2) \quad r^2(x) = \left(k - \frac{x^2}{m^2}\right) \left(1 + (A \sin lx^2)^n\right),$$

where k is the radius of the neck, $k * m$ equals the height of the spine and l and A are shape parameters that are optimized to fit the overall shape of the spine. We have used integer values for n , ranging from 1-8 to optimally fit the shape of the spine (Figure 3D). Note here that increasing n increases the curvature at the zone connecting head and neck. Larger values ($n = 6-8$) typically fit long thin necks with large heads, while lower values ($n = 1-2$) suit stubby or thin spines. Spines that had a distinct non-monotonic increase in radius as function of height could not be fitted with Eq. 2 and were excluded from the analysis.

Once the shape of the spine is created, we prepared the system as follows: the surface of the dendritic spine was uniformly covered with 1000 non-interacting particles, representing the receptor proteins. These particles diffuse across the surface of the spine, and were removed from the system once they exit the base of the spine. We measured the concentration of particles $C(t)$ as function of time t which, similarly to the experiments decayed exponentially,

$$(3) \quad \frac{C(t)}{C(0)} = e^{-t/\tau},$$

where τ is the characteristic timescale of decay, i.e., a measure for the amount of confinement.

To compare the diffusive timescales obtained from the Langevin dynamics simulations with those obtained from the experiments, we needed to relate the simulation units of time and distance from the simulations with those in the experiments. Therefore, we first calculated the Mean Squared Displacement (MSD) for particles on a planar surface with parameters

otherwise identical parameters to those in the curved, spine case, and compared this with the experimentally obtained 2D diffusion coefficient of $0.022 \mu\text{m}^2/\text{s}$. The latter was measured by linking single-molecule localizations from 3 dendrites into 1044 trajectories, followed by calculating the Mean Squared Displacement (MSD) versus time delay t . Linear fitting of $\text{MSD} = 4Dt$ to the first three points of the curve (excluding zero) then yielded the estimate for D . In our simulation we have fixed the spatial dimension such that $1 \mu\text{m}$ corresponds to 10SU_x (spatial Simulation Unit: SU). To reach a mean square displacement of $(10 \text{SU}_x)^2$ a particle needed on average 25 000 simulation time steps δt_{sim} , indicating a simulated diffusion coefficient of $10^{-3} \text{SU}_x^2/\delta t_{\text{sim}}$ or $10^{-5} \mu\text{m}^2/\delta t_{\text{sim}}$. Hence, δt_{sim} corresponds to $10^{-5}/0.022$ seconds.

RESULTS

To study how membrane-bound diffusion is influenced by the morphology of dendritic spines, we set up an assay that enabled us to measure membrane-based diffusion in combination with sub-diffractive imaging of the shape of individual spines in living hippocampal neurons. Both measurements are based on a single exogenous probe, mem-mEos, to minimally interfere with the system and to prevent interactions of the probe with other proteins in the spine head (Figure 1).

Conventional light microscopy cannot accurately resolve the detailed morphology of dendritic spines (Figure 1B). The neck of dendritic spines is particularly challenging: Typically it has a diameter of 50-200nm, as measured by electron microscopy (1), which falls below the diffraction limit of fluorescence microscopy. Therefore we used live photoactivated localization microscopy (PALM) (Figure 1A, C), allowing to localize single fluorescent proteins with sub-diffraction accuracy, and to reconstruct the images at 10nm pixel size. These images were further processed to measure the FWHM along the major axis of the spine from which the shape parameters spine length, neck length, head width and neck width can be extracted (Figure 1D).

To correlate spine morphology with the associated equilibration time scale τ , we also measured bulk diffusion in the same spines by photoconversion. Converting the same fluorescent probe mem-mEos from green to red emission by locally exposing spine heads to a diffraction-limited spot of 405nm light, we followed the subsequent decay of red fluorescence intensity in the spine over time and fitted the measurements with a single exponential decay function (Figure 1E). From this function we derived the time constant τ as readout for the diffusive time scale of spine equilibration, in which high values for τ indicate slow diffusion rates (Figure 1F).

The resulting shape measurements of $n=128$ spines in $N=5$ experiments (Figure 2) are consistent with earlier EM-based spine dimensions (1) and with measurements done with STED super-resolution microscopy in organotypic and acute slice of mice brains (29) (Figure 2I). A small overall increase in the spine dimensions compared to the latter study may be explained by the localization of our probe to the plasma membrane rather than the cytoplasm, resulting in overall widening of the FWHM. No strong interdependence of spine length and neck width or head width was observed (Figure 2E, F). Remarkably and contrary to earlier studies (29), we did find a significant correlation between neck width and head width (Figure 2G). Less surprisingly, neck length and spine length correlated strongly. In order to compare

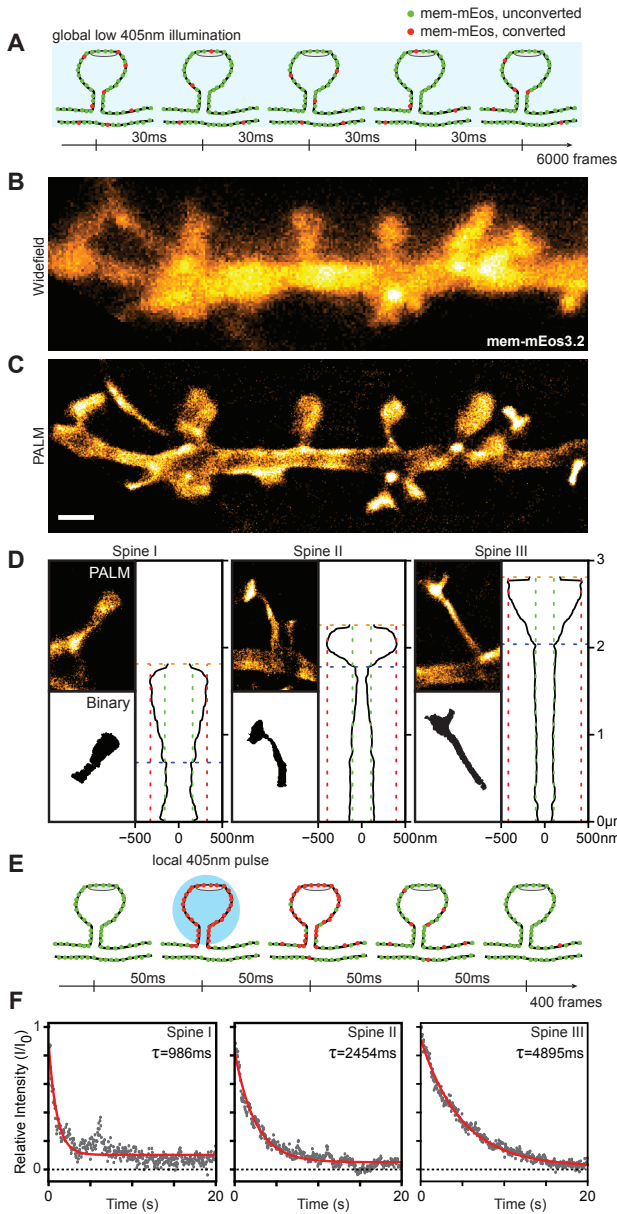


FIGURE 1 | Imaging diffusion morphology and membrane-bound diffusion of living dendritic spines.

(A) Assay for live PALM imaging of dendritic spines: Global low intensity 405nm illumination results in stochastic photoconversion of mEos3.2-CAAX (mem-mEos) allowing detection of individual molecules for PALM detection over 6000 frames. **(B, C)** Widefield (B) and super-resolved (C) image of the same dendrite expressing mem-mEos. **(D)** Morphology analysis of three dendritic spines. PALM reconstructions (top) were binarized (bottom) and a spline was fitted through the major axis of each spine. Plotting the FWHM along this axis (right) allows reconstructing spine morphology and measuring neck width (green), head width (red) and spine (orange) and neck length (blue). **(E)** Assay for diffusion measurements: Spines were imaged at 561nm in 50ms intervals for 400 frames and locally photoconverted after 15 frames with a local laser pulse of 405nm wavelength. **(F)** Intensity traces of photoconverted mem-mEos signal over time for the three spines shown in (D) Red line indicates fit of exponential decay from which the indicated τ was derived.

our results with previous simulation studies (13), we therefore focused on spine length rather than neck length. In conclusion, PALM nanoscopy allowed us to precisely parameterize dendritic spine morphologies of living neurons.

In earlier simulations, we have explored the effect of neck width on τ , while keeping other parameters constant (13, 14). We found that τ increased by decreasing the width of the spine neck. Increasing the size of the head for a given neck width should also increase τ .

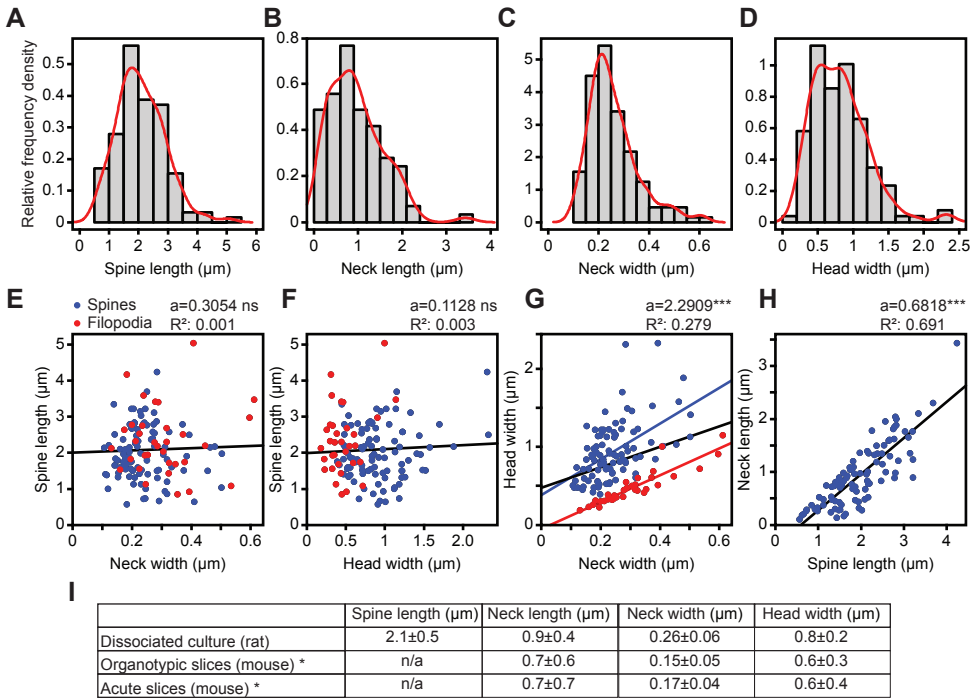


FIGURE 2 | Distribution dendritic spine morphology measurements.

(A-D) Histograms showing the distribution of measured spine lengths (A), neck lengths (B), neck widths (C) and head widths (D) ($n=128$ spines), red line indicates relative frequency density. (E-H) Correlations of spine morphology parameters against each other. Red dots indicate filopodia-like spines (mean head width $< 1.5 \times$ the mean neck width, $n=33$), blue dots indicate mushroom-like spines (all others, $n=95$). Black lines show fitted regression with slope a and goodness of fit as indicated at the top; in (G) blue and red lines show separate regressions for mushroom and filopodia-like spines, respectively. (I) Comparison of spine morphology measured in this study in dissociated rat hippocampal neurons with live PALM microscopy and spines measured in organotypic and acute slices of mouse hippocampi using STED microscopy. Asterisk indicates datasets published previously (29). Data are shown as mean \pm IQR (Q3-Q1) in μm .

Indeed, using a similar approach as in earlier simulations (13, 14), we found that, with constant neck width and length, τ scaled nearly linearly with the surface area of the spine head (Figure 3A, B). Nevertheless, τ should also depend on the exact shape of the head. Indeed, for a spine with a given surface area and neck radius, τ could be altered by changing the aspect ratio of the head (i.e. by altering head width and spine length) (Figure 3C). Therefore, to directly compare experimental values with the predictions based on simulations, we decided to perform simulations using measured spine morphologies to directly predict τ for specific spines, assuming it is solely governed by its shape, while the membrane-bound diffusion constant D is similar in all spines.

Firstly, the width measurements were fitted with the function in Eq.2 (Figure 3D). This

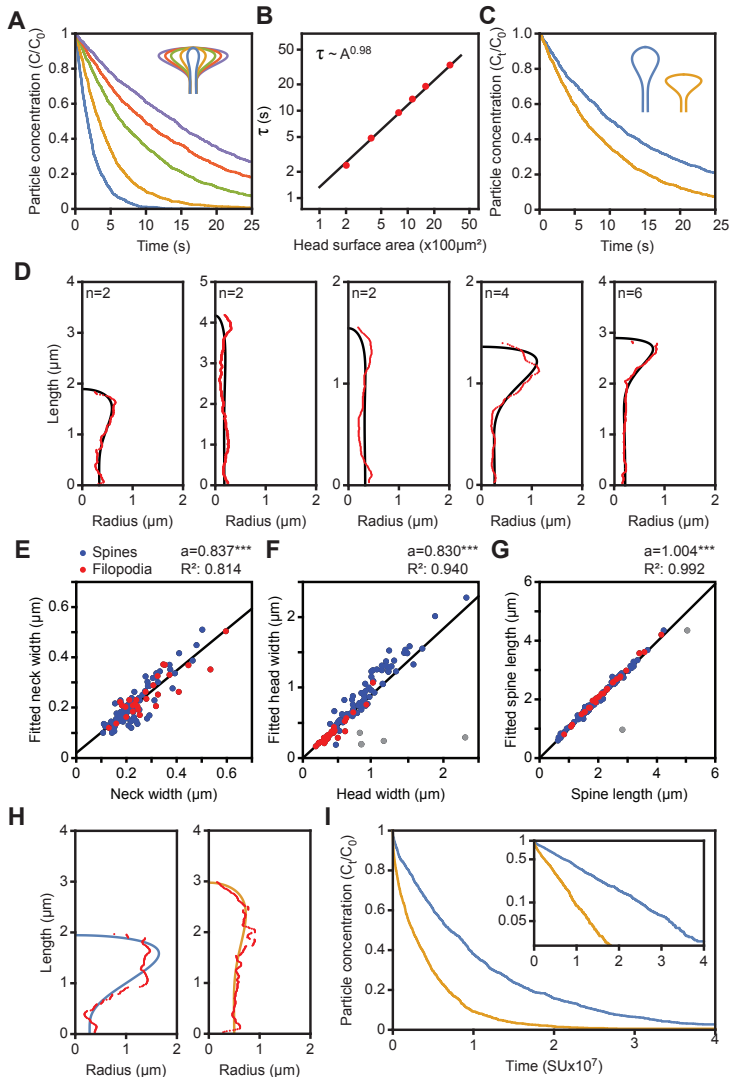


FIGURE 3 | Simulation of particle diffusion on spine shapes fitted on measured spine morphologies.

(A) Decay of particle concentration simulated in spines with varying head sizes and surface area. (B) Log-Log plot of the time constant τ as function of the surface area of the spine head. (C) Decay of particle concentration in spines with equal surface area and neck diameter but different overall shape (shown in inset). (D) Five examples of measured spine morphology data (red) fitted with a function shown in Equation (2) (black). For each example the exponent n of the function is given. (E-G) Fitted versus measured spine morphology parameters ($n=100$). Blue and red dots indicate mushroom-like ($n=74$) and filopodia-like spines ($n=26$), respectively. Black lines show fitted regression with slope a and goodness of fit as indicated at the top. Grey dots indicate six outliers that have been excluded from further analysis. (H) Examples of measured (red) and fitted (blue/yellow) morphology profiles for two spines. (I) Decay of particle concentration simulated for the two spine morphologies shown in (H). Inset shows the same dataset in a semilog plot.

function could subsequently be used to generate surfaces of revolution that closely resemble the shape of spines measured initially (see Materials & Methods for details). The fitted spine morphology values closely matched the values from the initial measurements in all but six spines, which were excluded from further analysis (Figure 3E-G). Secondly, we used the spine morphology parameters obtained from fitting to perform particle diffusion simulations, starting with a homogenous distribution of particles on the spine surface diffusing until they escape the system at the boundary of the spine neck, as described previously (13). From the decay of particle concentration the simulated diffusion time constant τ could be derived in the same manner as this was done in the photoconversion experiment (Figure 3H, I). Thus, by fitting parameterized surfaces of revolution to spine morphology data, we could execute particle simulations on realistic spine shapes to determine their expected diffusion time constant τ .

We performed these simulation for all $n=100$ spines that we could fit using Eq. 2 (Figure 3E-G). This resulted in a distribution of diffusion time constants with a mean of 1.9 ± 1.5 s (mean \pm SD) ranging from 0.1 to 7.6 s (Figure 4A). For the experimentally obtained time constants, the overall distribution was shifted towards higher τ values and the mean was 2.3 ± 1.0 s in a range from 0.6 to 5.7 s (Figure 4B). Plotting the numerically obtained time constant against the experimental values for each spine revealed a good correlation between the two (Figure 5C), although the simulated value were often lower than the experimental values; especially for filopodia-like spines. Indeed, the ratio of experimental and simulated τ showed a frequency density distribution peaking at 1.07, but with a shoulder towards higher values compared to a normal distribution. This indicates that the simulations underestimate the time constants for a subpopulation of spines (i.e. the simulations predict faster diffusion than measured by photoconversion).

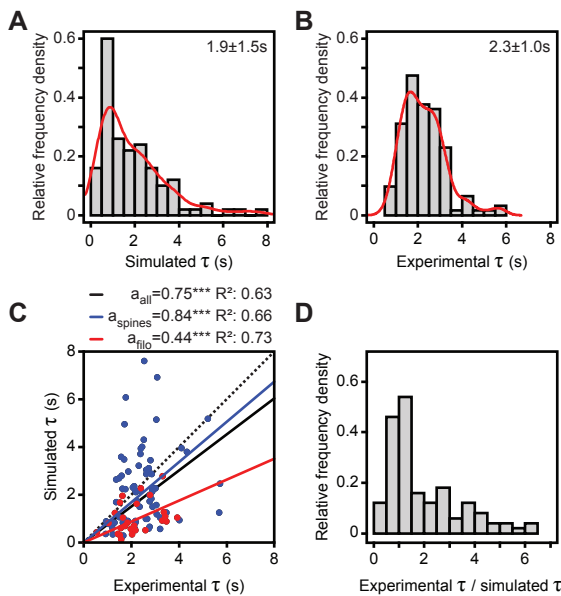


FIGURE 4 | Comparison of experimental and simulated diffusion kinetics in dendritic spines

(A, B) Histograms of simulated (A) and experimentally measured (B) diffusion time constants τ for $n=100$ and $n=128$ spines, respectively. Mean \pm SD is indicated. Red line indicates relative frequency density. (C) Simulated versus measured diffusion time constants τ ($n=100$). Blue and red dots indicate mushroom-like ($n=74$) and filopodia-like spines ($n=26$), respectively. Black, blue and red lines show fitted regressions with their slopes a and goodness of fit indicated at the top for all, mushroom-like spines and filopodia-like spines, respectively. (D) Histogram of the ratio between experimental τ and simulated τ for $n=100$ spines.

Next we examined how the simulated diffusion time constants depended on the morphology parameters used for the simulations. While τ correlated linearly with spine length and, to a lesser extent, with head width, there was no apparent dependence of the neck width (Figure 5A-C). For the experimentally measured diffusion time constants, we did not observe clear correlations (Figure 5D-F). This counterintuitive observation results from the multidimensionality of spine morphologies. While in previous simulations all but one of the shape parameters were kept constant (13), in our dataset the correlations for each morphology parameter are confounded by changes in the remaining parameters (e.g. a spine with a thin neck may be shorter than a spine with a wider neck).

To reduce the dimensionality of the problem, we searched to establish a shape factor S that combined the dependence of spine length l_{spine} , head width w_{head} and neck width w_{neck} in one metric, such that τ is governed by S and D in the following way

$$(4) \quad \tau[s] = \frac{S[\mu m^2]}{D[\mu m^2/s]}.$$

Considering that the dimension of S should be mm^2 and that increasing l_{spine} and w_{head} should increase τ , whereas increasing w_{neck} should decrease τ , we established the following hypothetical dependence:

$$(5) \quad S_a = \frac{l_{spine}^\alpha * w_{head}^\alpha}{w_{neck}^{2\alpha-2}},$$

where α denotes the power of the dependence on l_{spine} and w_{head} . To find the proper value of α , we plotted the simulated τ values, t_{sim} , against the shape factor S_α for $\alpha = 2, 1.6$ and 1.3 and found that this dependence was linear for $\alpha = 1.3$, with most points following this dependence ($R^2=0.71$, Figure 5G-J). Thus, by reducing multiple spine morphology parameters into a single shape factor $S_{1.3}$, we find a clear relation between this shape factor and the simulated diffusion time constant, as we would expect from earlier simulations (13).

Finally, to examine whether the experimentally observed timescale t_{exp} of membrane-bound diffusion followed a similar dependence on the shape factor, we plotted t_{exp} against the shape factor $S_{1.3}$ calculated using experimental value for the shape parameters (Figure 5K, L). We found that for most spines the values are scattered in an area whose lower boundary was set by the simulated data points, although for some spines with large heads ($w_{head} > 1.5$ mm) the experimental values were lower than predicted. These results suggest that spine morphology establishes the lower bound for the time constant of membrane-bound diffusion, but that other mechanisms often limit the diffusive time scale to an even greater extent.

DISCUSSION

Here we use super-resolution microscopy of spine morphology and bulk photo-conversion of a membrane-bound fluorescent protein, mem-mEos, to examine how spine morphology affects the time scale of diffusive equilibration. By comparing the measured time constants with particle simulations carried out on the same spine morphologies, we show that spine morphology determines the lower-bound for diffusive equilibration, but that additional mechanism slow down equilibration beyond the time scale set by spine shape.

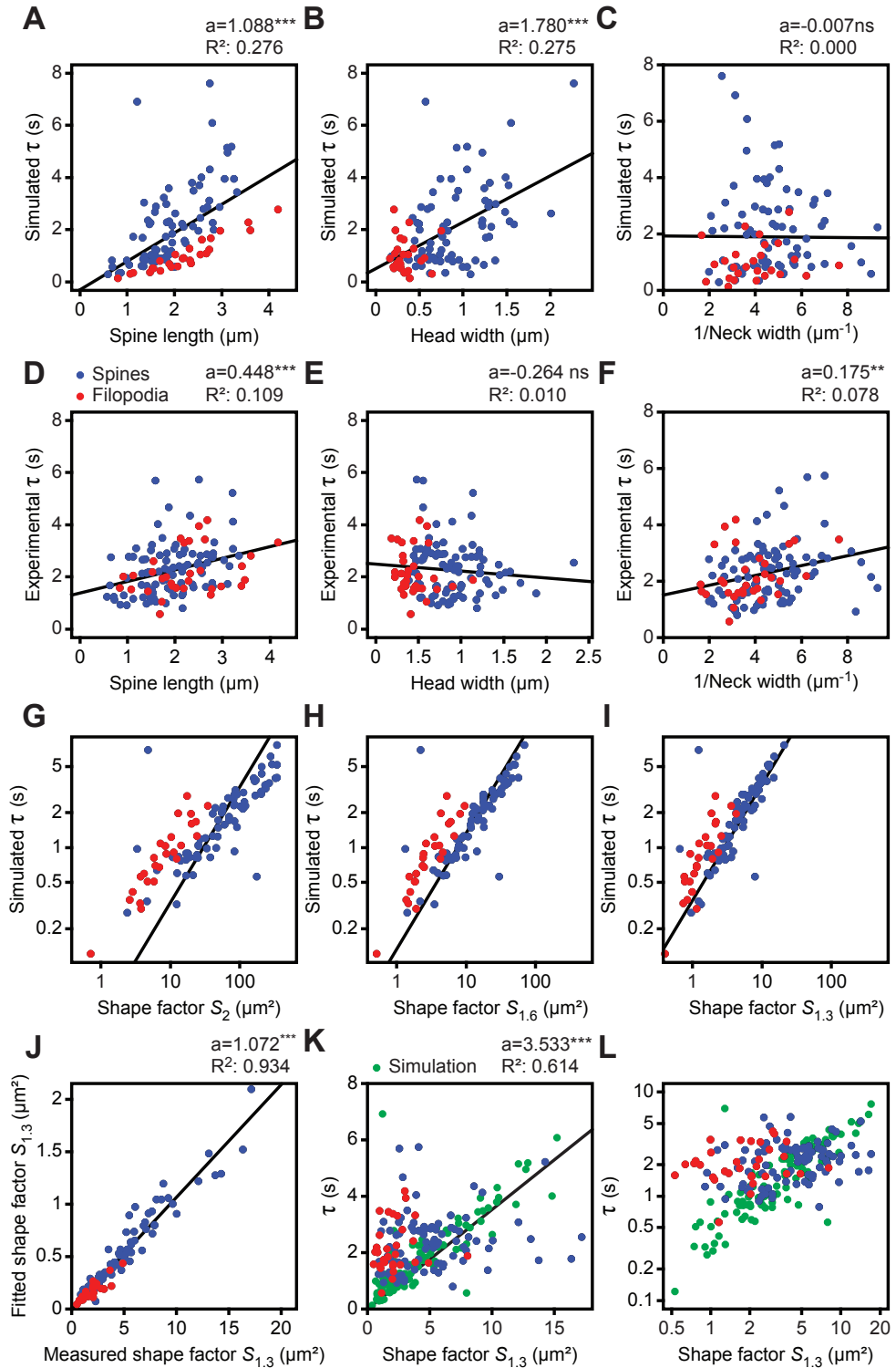


FIGURE 5 | Spine morphology sets the lower bound for the diffusion time constant

(A-F) Correlations of simulated (A-C) and measured (D-F) diffusion time constants τ and spine morphology parameters ($n=100$, 122 spines). Blue and red dots indicate mushroom-like and filopodia-like spines, respectively. Black lines show fitted regression with slope a and goodness of fit as indicated at the top. **(G-I)** Simulated diffusion time constants τ plotted against three different shape factors defined by Eq. 5 using $\alpha = 2$, 1.6 and 1.3, respectively. Blue and red dots indicate mushroom-like ($n=74$) and filopodia-like spines ($n=26$), respectively. Black lines with slope of 1 are plotted to illustrate linear dependence. **(J)** Shape factors $S_{1.3}$ derived from measured morphology parameters versus shape factors from morphology parameters obtained from fitting ($n=100$). Blue and red dots indicate mushroom-like ($n=74$) and filopodia-like spines ($n=26$), respectively. Black line shows fitted regression with slope a and goodness of fit as indicated at the top. **(K-L)** Measured diffusion time constants τ ($n=122$) plotted against the shape factor $S_{1.3}$ on linear (K) or logarithmic (L) axes. Blue and red dots indicate mushroom-like ($n=74$) and filopodia-like spines ($n=26$), respectively. Black lines show fitted regression with slope a and goodness of fit indicated at the top. Green dots illustrate τ obtained from simulation versus shape factor $S_{1.3}$ obtained using morphology parameters obtained from fitting.

We picked mem-mEos as membrane-bound probe, both to visualize spine morphology and to measure membrane-bound diffusion. This probe is ideally suited for this assay as it is unlikely to interact with scaffolding proteins in or around the post-synaptic density, as most receptors would. Our imaging approach currently precludes us from obtaining three-dimensional morphology data. Therefore spine geometry was assumed to be symmetrical. Nevertheless, our morphology data closely correspond with electron-microscopy and other super-resolution fluorescence microscopy studies (1, 24, 29). Also fluorescence microscopy enabled us to image a larger variety of shapes compared to more labor-intensive electron microscopy approaches (15) and, importantly, allowed for imaging live dendrites directly after the photoconversion experiment without any need for fixation or correlative techniques. We chose to measure bulk diffusion using photoconversion, as it closely resembles the simulation approach of particles released homogeneously on the spine escaping through the spine neck and circumvents the challenges associated with measuring single-particle motility on a curved surface (30).

Remarkably, we did not observe a direct correlation between τ and spine neck width, which had been predicted by previous simulation studies (13, 15). However, whereas in simulations all spine morphology parameters can be precisely controlled and the neck widths can be changed while keeping other parameters constant, we are bound by experimental values. Interestingly, we found a clear experimental correlation between spine width and neck width, demonstrating that wider heads often come with wider necks (Figure 2G). In this way, the increased equilibration due to the wider neck is opposed by a greater head size, which explains why we did not find a correlation between τ and neck width alone. To circumvent the problem of confounding shape parameters, we defined a shape factor S that combined the expected morphology effects on membrane-bound diffusion. From this, we found that $\tau \sim w_{neck}^{-0.6}$ and $\tau \sim l_{spine}^{1.3}$, which is similar to the predictions of earlier simulations (13).

Because for most spines $t_{exp} > t_{sim}$, we conclude that spine morphology establishes the lower bound for the time constant of membrane-bound diffusion, but that other mechanisms

often limit the diffusive time scale to a greater extent. The cytoskeleton, especially sub-membranous actin, influences diffusion through corralling or by anchoring proteins in the plasma membrane (31, 32). It has also been shown that the septin family of proteins, and particularly Sept7, hamper the diffusion of trans-membrane proteins or proteins anchored to the inner leaflet (33, 34). Furthermore, also membrane curvature (14, 35) or lipid composition (36–38) influence the effective local diffusion coefficient (33, 39), whereas we have used a uniform diffusion coefficient based on single molecule tracking along dendrites and spines (see Materials & Methods). Remarkably, for some spines with large heads ($w_{head} > 1.5 \mu\text{m}$) the experimental values for τ were lower than predicted, which may be due to insufficient photoconversion as a result of using a near diffraction-limited spot in a large spine. In such a case only a part of the spine surface would be photoconverted which would hamper comparison with simulations based on homogenous particle distribution. Alternatively, large mature spines might harbor an extensive PSD that excludes diffusion of our probe, effectively lowering the available surface for diffusion.

In summary, this study demonstrates that exact spine morphology contributes to retaining membrane-bound probes. Our results also show that morphology alone does not explain all diffusive behavior of our probe, but likely works in concert with other retention mechanisms mediated by cytoskeletal structures or the lipid composition of the membrane. Together these mechanisms may be important in compartmentalizing glutamate receptors, ion channels or membrane-bound signaling proteins in spines according to their synaptic strength and activity levels (23).

ACKNOWLEDGEMENTS

We thank the neuron culture team for preparing the dissociated neuron cultures and E. Katrukha for help with the data analysis. This work is supported by the Foundation for Fundamental Research on Matter FOM, which is part of the Netherlands Organization for Scientific Research (NOW), and supported by the European Research Council (ERC Starting Grant to L.C.K., ERC Consolidator Grant to C.C.H.).

AUTHOR CONTRIBUTIONS

M.A. and L.C.K. designed the study. M.A. performed and analyzed experiments. R.K. performed and analyzed simulations under supervision of C.S.. C.C.H. contributed neuron cultures and advice. M.A. and L.C.K. wrote the manuscript. L.C.K. supervised the project.

REFERENCES

1. Bourne, J.N., and K.M. Harris. 2008. Balancing structure and function at hippocampal dendritic spines. *Annu. Rev. Neurosci.* 31: 47–67.
2. Schikorski, T., and C.F. Stevens. 1999. Quantitative fine-structural analysis of olfactory cortical synapses. *Neurobiology.* 96: 4107–4112.
3. Arellano, J.I. 2007. Ultrastructure of dendritic spines: correlation between synaptic and spine morphologies. *Front. Neurosci.* 1: 131–143.
4. Holtmaat, A., and K. Svoboda. 2009. Experience-dependent structural synaptic plasticity in the mammalian brain. *Nat. Rev. Neurosci.* 10: 647–658.
5. Mattison, H. a, D. Popovkina, J.P.Y. Kao, and S.M. Thompson. 2014. The role of glutamate in the morphological

- and physiological development of dendritic spines. *Eur. J. Neurosci.* 39: 1761–1770.
6. Hu, H.-T., and Y.-P. Hsueh. 2014. Calcium influx and postsynaptic proteins coordinate the dendritic filopodium-spine transition. *Dev. Neurobiol.* 74: 1011–1029.
 7. Yuste, R., and T. Bonhoeffer. 2001. Morphological changes in dendritic spines associated with long-term synaptic plasticity. *Annu. Rev. Neurosci.* 24: 1071–89.
 8. Opazo, P., and D. Choquet. 2011. A three-step model for the synaptic recruitment of AMPA receptors. *Mol. Cell. Neurosci.* 46: 1–8.
 9. Ehlers, M.D., M. Heine, L. Groc, M. Lee, and D. Choquet. 2007. Diffusional trapping of GluR1 AMPA receptors by input-specific synaptic activity. *Neuron.* 54: 447–60.
 10. Opazo, P., S. Labrecque, C.M. Tigaret, A. Frouin, P.W. Wiseman, P. De Koninck, and D. Choquet. 2010. CaMKII triggers the diffusional trapping of surface AMPARs through phosphorylation of stargazin. *Neuron.* 67: 239–52.
 11. Triller, A., and D. Choquet. 2005. Surface trafficking of receptors between synaptic and extrasynaptic membranes: and yet they do move! *Trends Neurosci.* 28: 133–9.
 12. Nair, D., E. Hossy, J.D. Petersen, a. Constals, G. Giannone, D. Choquet, and J.-B. Sibarita. 2013. Super-Resolution Imaging Reveals That AMPA Receptors Inside Synapses Are Dynamically Organized in Nanodomains Regulated by PSD95. *J. Neurosci.* 33: 13204–13224.
 13. Kusters, R., L.C. Kapitein, C.C. Hoogenraad, and C. Storm. 2013. Shape-Induced Asymmetric Diffusion in Dendritic Spines Allows Efficient Synaptic AMPA Receptor Trapping. *Biophys. J.* 105: 2743–2750.
 14. Kusters, R., and C. Storm. 2014. Impact of morphology on diffusive dynamics on curved surfaces. *Phys. Rev. E.* 89: 32723.
 15. Simon, C.M., I. Hepburn, W. Chen, and E. De Schutter. 2013. The role of dendritic spine morphology in the compartmentalization and delivery of surface receptors. *J. Comput. Neurosci.* : 483–497.
 16. Yuste, R. 2013. Electrical Compartmentalization in Dendritic Spines. *Annu. Rev. Neurosci.* 36: 429–449.
 17. Araya, R., T.P. Vogels, and R. Yuste. 2014. Activity-dependent dendritic spine neck changes are correlated with synaptic strength. *Proc. Natl. Acad. Sci.* 111: E2895–E2904.
 18. Noguchi, J., M. Matsuzaki, G.C.R. Ellis-Davies, and H. Kasai. 2005. Spine-Neck Geometry Determines NMDA Receptor-Dependent Ca²⁺ Signaling in Dendrites. *Neuron.* 46: 609–622.
 19. Bloodgood, B.L., and B.L. Sabatini. 2005. Neuronal activity regulates diffusion across the neck of dendritic spines. *Science.* 310: 866–9.
 20. Svoboda, K., D.W. Tank, and W. Denk. 1996. Direct measurement of coupling between dendritic spines and shafts. *Science.* 272: 716–719.
 21. Ashby, M.C., S.R. Maier, A. Nishimune, and J.M. Henley. 2006. Lateral diffusion drives constitutive exchange of AMPA receptors at dendritic spines and is regulated by spine morphology. *J. Neurosci.* 26: 7046–55.
 22. Harvey, C.D., R. Yasuda, H. Zhong, and K. Svoboda. 2008. The spread of Ras activity triggered by activation of a single dendritic spine. *Science.* 321: 136–40.
 23. Adrian, M., R. Kusters, C.J. Wierenga, C. Storm, C.C. Hoogenraad, and L.C. Kapitein. 2014. Barriers in the brain: resolving dendritic spine morphology and compartmentalization. *Front. Neuroanat.* 8: 142.
 24. Bethge, P., R. Chéreau, E. Avignone, G. Marsicano, and U.V. Nägerl. 2013. Two-Photon Excitation STED Microscopy in Two Colors in Acute Brain Slices. *Biophys. J.* 104: 778–85.
 25. Zhang, M., H. Chang, Y. Zhang, J. Yu, L. Wu, W. Ji, J. Chen, B. Liu, J. Lu, Y. Liu, J. Zhang, P. Xu, and T. Xu. 2012. Rational design of true monomeric and bright photoactivatable fluorescent proteins. *Nat. Methods.* 9: 727–9.
 26. Hancock, J.F., H. Paterson, and C.J. Marshall. 1990. A polybasic domain or palmitoylation is required in addition to the CAAX motif to localize p21ras to the plasma membrane. *Cell.* 63: 133–139.
 27. Chazeau, A., E.A. Katrukha, C.C. Hoogenraad, and L.C. Kapitein. 2016. Studying neuronal microtubule organization and microtubule-associated proteins using single molecule localization microscopy. *Methods*

- Cell Biol. 131: 127–149.
28. Paquay, S., and R. Kusters. 2016. A Method for Molecular Dynamics on Curved Surfaces. *Biophys. J.* 110: 1226–1233.
 29. Tønnesen, J., G. Katona, B. Rózsa, and U.V. Nägerl. 2014. Spine neck plasticity regulates compartmentalization of synapses. *Nat. Neurosci.* 17: 678–685.
 30. Oswald, F., E. L. M. Bank, Y.J.M. Bollen, and E.J.G. Peterman. 2014. Imaging and quantification of transmembrane protein diffusion in living bacteria. *Phys. Chem. Chem. Phys.* 16: 12625–34.
 31. Honkura, N., M. Matsuzaki, J. Noguchi, G.C.R. Ellis-Davies, and H. Kasai. 2008. The subspine organization of actin fibers regulates the structure and plasticity of dendritic spines. *Neuron.* 57: 719–29.
 32. Korobova, F., and T. Svitkina. 2010. Molecular architecture of synaptic actin cytoskeleton in hippocampal neurons reveals a mechanism of dendritic spine morphogenesis. *Mol. Biol. Cell.* 21: 165–76.
 33. Ewers, H., T. Tada, J.D. Petersen, B. Racz, M. Sheng, and D. Choquet. 2014. A Septin-Dependent Diffusion Barrier at Dendritic Spine Necks. *PLoS One.* 9: e113916.
 34. Tada, T., A. Simonetta, M. Batteredon, M. Kinoshita, D. Edbauer, and M. Sheng. 2007. Role of Septin cytoskeleton in spine morphogenesis and dendrite development in neurons. *Curr. Biol.* 17: 1752–8.
 35. Domanov, Y. a, S. Aimon, G.E.S. Toombes, M. Renner, F. Quemeneur, A. Triller, M.S. Turner, and P. Bassereau. 2011. Mobility in geometrically confined membranes. *Proc. Natl. Acad. Sci. U. S. A.* 108: 12605–10.
 36. Ueda, Y., and Y. Hayashi. 2013. PIP3 Regulates Spinule Formation in Dendritic Spines during Structural Long-Term Potentiation. *J. Neurosci.* 33: 11040–11047.
 37. Fukata, Y., A. Dimitrov, G. Boncompain, O. Vielemeyer, F. Perez, and M. Fukata. 2013. Local palmitoylation cycles define activity-regulated postsynaptic subdomains. *J. Cell Biol.* 202: 145–61.
 38. Hering, H., C.-C. Lin, and M. Sheng. 2003. Lipid rafts in the maintenance of synapses, dendritic spines, and surface AMPA receptor stability. *J. Neurosci.* 23: 3262–71.
 39. Shim, S.-H., C. Xia, G. Zhong, H.P. Babcock, J.C. Vaughan, B. Huang, X. Wang, C. Xu, G.-Q. Bi, and X. Zhuang. 2012. Super-resolution fluorescence imaging of organelles in live cells with photoswitchable membrane probes. *Proc. Natl. Acad. Sci.* 109: 13978–13983.



Positioning of AMPA Receptor-containing Endosomes Regulates Synapse Architecture

Marta Esteves da Silva¹, **Max Adrian**¹, Philipp Schätzle¹, Joanna Lipka^{1,3}, Takuya Watanabe⁴, Sukhee Cho⁴, Kensuke Futai⁴, Corette J. Wierenga¹, Lukas C. Kapitein^{1,2} and Casper C. Hoogenraad^{1,2}

¹ Cell Biology, Faculty of Science, Utrecht University, 3584 CH Utrecht, The Netherlands,

² Department of Neuroscience, Erasmus Medical Center, 3015GE Rotterdam, The Netherlands,

³ International Institute of Molecular and Cell Biology, 02-109 Warsaw, Poland,

⁴ Department of Psychiatry, Brudnick Neuropsychiatric Research Institute, University of Massachusetts Medical School, Worcester MA 01605, USA.

ABSTRACT

Lateral diffusion in the membrane and endosomal trafficking both contribute to the addition and removal of AMPA receptors (AMPARs) at postsynaptic sites. However the spatial coordination between these mechanisms has remained unclear, because little is known about the dynamics of AMPAR containing endosomes. In addition, how the positioning of AMPAR-containing endosomes affects synapse organization and functioning has never been directly explored. Here, we used live-cell imaging in hippocampal neuron cultures to show that intracellular AMPARs are transported in Rab11-positive recycling endosomes, which frequently enter dendritic spines and depend on the microtubule and actin cytoskeleton. By using chemically-induced dimerization systems to recruit kinesin (KIF1C) or myosin (MyosinV/VI) motors to Rab11-positive recycling endosomes, we control their trafficking and found that induced removal of recycling endosomes from spines decreases surface AMPAR expression and PSD-95 clusters at synapses. Our data suggest a mechanistic link between endosome positioning and the postsynaptic structure and composition.

INTRODUCTION

Most fast excitatory signaling in the brain is mediated by AMPA-type glutamate receptors and changes in the number of these receptors at synapses are thought to underlie information storage in the brain (1). AMPA receptors (AMPARs) exchange between synaptic and extrasynaptic sites by lateral diffusion in the plasma membrane, whereas endosomal recycling and trafficking followed by exocytosis is believed to maintain a supply of extrasynaptic AMPARs on the membrane (2, 3). However, the spatial coordination between these two major AMPAR transport mechanisms has remained unclear, because, in contrast to lateral receptor diffusion, little is known about the dynamics of AMPAR containing endosomes.

Excitatory synapses are mostly located at small dendritic protrusions, called spines, which are often connected to dendritic shaft through a narrow membrane tube of 100-200 nm diameter, called the spine neck. This architecture is believed to biochemically isolate the spine from the rest of dendrite, because it slows down both cytoplasmic and membrane-based diffusion. Simulations suggested that secretion inside spines dramatically increases the fraction of receptors captured at synapses, compared to secretion near the base of the spine neck (4). In addition, endosomes are known to often function as signaling hub, and their precise position either inside or outside spines would also strongly affect signaling persistence, given the biochemical isolation of spines (5). However, how the positioning of AMPAR-containing endosomes affects synapse architecture has never been directly explored.

Here we use high-resolution live-cell imaging to examine the intracellular dynamics of AMPAR-containing endosomes. We found that AMPARs move in highly dynamic Rab11 endosomes that frequently enter and exit dendritic spines. Whereas long-range transport is largely microtubule (MT)-based, spine entries mostly depend on actin-based myosin motors. By repositioning endosomes, we found that removal of recycling endosomes from dendritic spines decreased the level of AMPAR at the spine membrane, as well as PSD-95 clusters at synapses. Our data demonstrate that recycling endosome trafficking directly affects synaptic function and suggest a mechanistic link between endocytic recycling and the structure and composition of the synapse.

RESULTS

Intracellular AMPA receptors are transported in recycling endosomes

To directly probe AMPAR vesicle trafficking in hippocampal neurons, we co-express HA-GluA1 and GFP-GluA2 and precisely control the timing and level of GFP-GluA2 receptor expression using a doxycycline regulated gene expression system. The majority of the GluA2 receptors is localized to the plasma membrane or retained in the endoplasmic reticulum, which appear as diffusive signals throughout the dendrites (Fig.1A). To selectively visualize intracellular vesicular GFP-GluA2, most of the fluorescence from the dendritic part in the field of view was bleached before image acquisition. Neurons expressing low levels of GFP-GluA2 revealed vesicle-like structures in the dendritic shaft and dendritic spines that were rapidly moving (Fig.1A,B). In the dendritic shaft, GFP-GluA2 motility was directed both away from and towards the cell body and reversals were also frequently observed (Fig.1C). Intracellular AMPARs most likely follow the endosomal transport routes (6-10). To examine the identity of GFP-GluA2 containing vesicles, neurons were co-transfected with HA-GluA1 and GFP-GluA2 and stained for Rab11, a marker for recycling endosomes. Due to the high abundance of GluA1/2 in other cellular compartments only a minor fraction is colocalized with endogenous Rab11 in fixed neurons (Fig.S1A,B). Live-cell imaging in conditioned medium with constant osmolality, showed that ~80% of Rab11-positive recycling endosomes in the dendrites are motile (Fig.S2A-E). Live imaging directly after bleaching revealed that 96.0 ± 1.5 % of the motile GFP-GluA2 containing vesicles contained mRFP-Rab11, whereas 77.6 ± 1.2 % of all motile Rab11 positive vesicles also contained GluA2 (Fig.1D, Table S1). The average density of moving GFP-GluA2 vesicles per mm/min was 0.37 ± 0.09 (Fig.1E) with a mean vesicle velocity of 1.05 ± 0.09 mm/s in control conditions (Fig.1F). Co-expression of Rab11 increased the GluA2 vesicle speed to values similar to those for endosomal vesicles with Transferrin Receptor (TfR) (Fig.1F). Interestingly, highly dynamic clusters of GluA2 could be observed within the motile Rab11-positive recycling endosomes (Fig.S1C-I). These intra-endosomal subdomains may localize signal responses or concentrate components for further endosomal sorting. We next determined whether Rab11 vesicle trafficking in dendrites depends on the actin or MT cytoskeleton. While blocking F-actin assembly by latrunculin B (10 μ M) treatments did not affect Rab11 vesicles dynamics along the dendrites, addition of low concentrations of nocodazole (300 nM) to inhibit MT dynamics decreased their motility to ~40% (Fig.1G and S2F-G). After nocodazole treatment, the majority of the Rab11-positive recycling endosomes accumulate in enlarged and immobile clusters in the dendritic shaft. Addition of nocodazole and latrunculin B to the neurons has a similar effect as nocodazole alone (Fig.1G and Fig.S2F-G). Consistently, expression of dominant-negative constructs to abrogate Myosin V or Myosin VI function did not affect the GFP-GluA2 vesicle speed (Fig.1F). These results suggest that intracellular AMPARs are transported in Rab11-positive recycling endosomes along dynamic MT tracks within the dendritic shaft.

Endosomal entry in spines correlates with an increase in surface AMPA receptors

SEP-labeled GluA subunits have been used to visualize postsynaptic exocytosis in dendrites and AMPAR dynamics on the plasma membrane. Here, we determine the correlation between recycling endosome dynamics and AMPAR exocytosis by simultaneously imaging tagRFP-Rab11 and SEP-GluA1. As reported previously (11), AMPARs undergo exocytosis not only

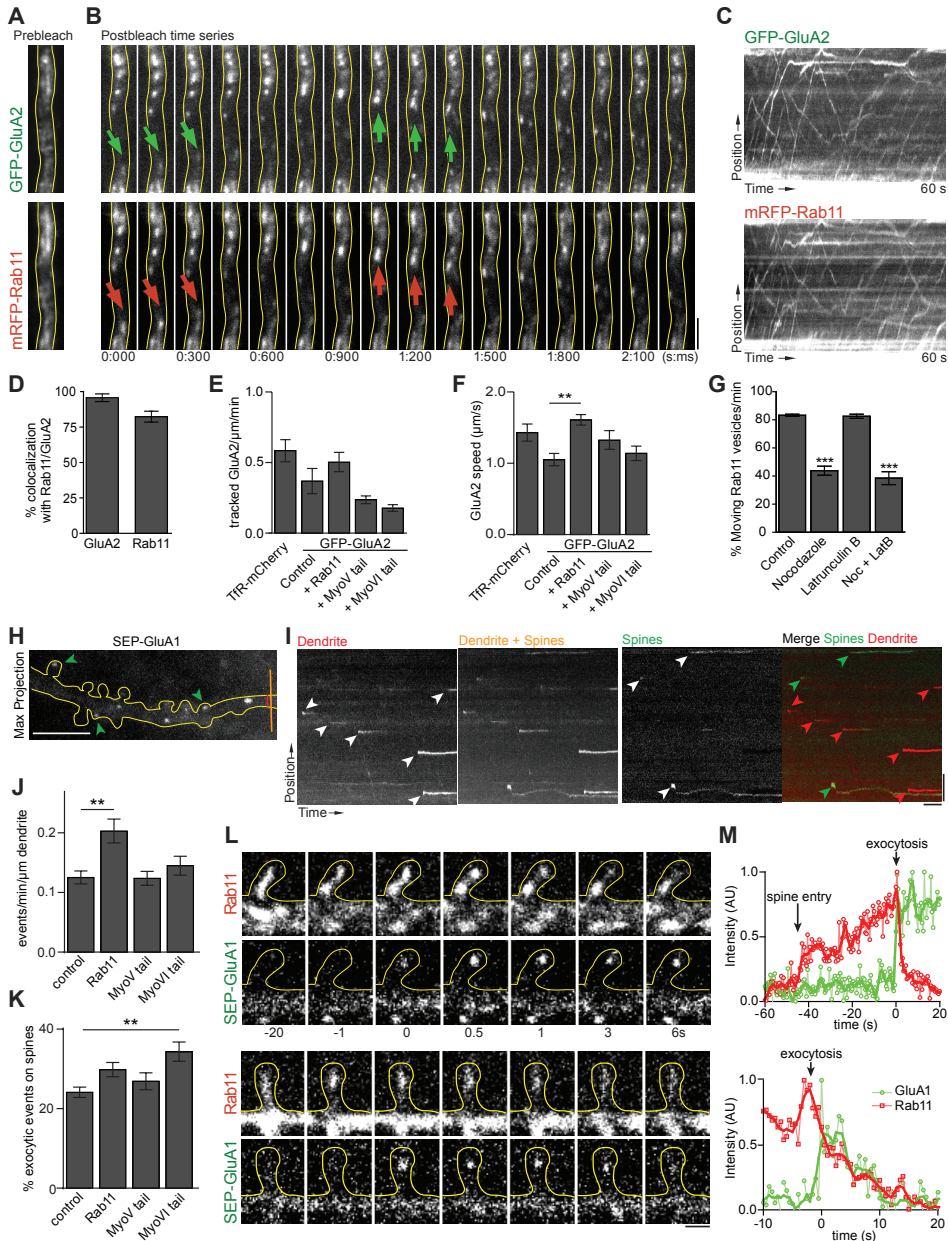


Figure 1 | Rab11-positive recycling endosomes transport GluA1/A2 in dendrites and spines

A-B. Stills from a dual-color time-lapse recording of a rat hippocampal neuron expressing GluA1, GFP-GluA2 (top) and mRFP-Rab11 (bottom). **A.** Prebleach overview of GFP-GluA2 and mRFP-Rab11; **B.** post-bleach time series. Arrows mark motile vesicles positive for both GFP-GluA2 and mRFP-Rab11. **C.** Kymograph of the recording in **B** showing prevalent co-motility of GFP-GluA2 and mRFP-Rab11. **D.** Average colocalization between intracellular GFP-GluA2 and mRFP-Rab11 in dendrites. **E-F.** Quantification of the number of tracked vesicles/μm/min (**E**) and the vesicle speeds (**F**) of neurons expressing TfR-mCherry or GFP-GluA2 under indicated conditions. **G.** Quantification

of the percentage of motile Rab11-positive recycling endosomes in 1 min timelapse acquisition under the indicated conditions. **H-I.** Quantification of SEP-GluA1 exocytic events in dendrites. (H) Maximum projection of SEP-GluA1 signal of 500 frames recorded at 5fps after bleaching the dendrite. Yellow and red bar show projection width of kymographs shown in I. Green arrows show exocytic events in spines detected by the kymograph in I. (I) Kymographs of dendrite shown in (H) with different widths to visualize exocytosis in the dendritic shaft and spines. Scale bars are 10s and 5 μ m. **J-K.** Quantification of the number of exocytic events per dendrite (J) and the fraction of events in dendritic spines (K) under indicated conditions. **L.** Stills from two time-lapse recordings of neurons expressing tagRFP-Rab11 (top panels) and SEP-GluA1 (bottom panels). Time is indicated relative to exocytic event in SEP channel. Solid line indicates outline of a single dendritic spine. **M.** Quantification of fluorescence intensity of tagRFP-Rab11 (red) and SEP-GluA1 (green) in dendritic spines shown in L. Dots indicate measurements connected with dim lines, thick lines are smoothed values over 4 adjacent values. Upper graph reveals prolonged retention of SEP-GluA1 fluorescence in the spine head, while lower graph shows rapid loss of SEP-GluA1 signal. Graphs represent mean \pm SEM. Statistical significance was determined by using Kruskal-Wallis test or one-way ANOVA and Dunnett's multiple comparison post hoc test, respectively; ** $p < 0.01$, *** $p < 0.001$. Scale bar is 5 μ m (B,C,I). See also Figure S1, S2 and Table S1.

in dendritic shafts but also in dendritic spines (Fig.1I). Under basal conditions, generally few exocytic events releasing GluA1 could be observed (0.13 ± 0.01 events/min/ μ m dendrite) (Fig.1J), but the number of events in spines contributes to $24.1 \pm 1.3\%$ of the total amount of events recorded on dendrites (Fig.1K). Co-expression of Rab11 leads to a slight increase in the total number exocytic GluA1 events (Fig.1J). Some of the events in spines followed the entry of dynamic Rab11 vesicles and the appearance of SEP-GluA1 was accompanied by the disappearance of the Rab11 signal (Fig.1L,M, Video S1), suggesting a correlation between Rab11-positive recycling endosomes trafficking and AMPAR exocytosis in spines. Expression of dominant-negative constructs to abrogate MyosinV or MyosinVI function did not affect GluA1 exocytosis in dendrites (Fig.1J). However, inhibiting MyosinVI increased the number of exocytic events in spines (Fig.1K). After exocytosis the SEP-GluA1 fluorescence showed two distinct behaviors in individual spines; it either remained in the spine head for prolonged times in the order of tens of seconds (Fig.1L, top) or fade within few seconds (Fig.1L, bottom), most likely reflecting the differential GluA1 retention in spine heads (11). Consistently, these data suggest that recycling endosomes in spines contribute to an increase in surface AMPARs.

Recycling endosomes move along both actin and microtubules in dendritic spines

We frequently observed Rab11 vesicles containing GFP-GluA2 in dendritic spines (Fig.2A and Video S2). Under basal conditions, GFP-GluA2 positive Rab11 vesicles move in and out of spines (Fig.2B and Fig.S2A). The recycling endosomes that enter spines did not necessarily emerge from immobile storage sites near the spine base, but frequently moved from distant dendritic regions. Similarly, GluA1/2 positive endosomal vesicles that left the spines were often not retained near the base of spine, but quickly move away in the anterograde or retrograde direction within the adjacent dendrite. On average $22.6 \pm 2.3\%$ of all immobile Rab11 vesicles were at the base of spine (Fig.S2D). To determine the role of MT and actin dynamics on Rab11-positive recycling endosomes trafficking in dendritic spines, neurons were treated with low concentrations of nocodazole (300 nM) and/or latrunculin B (10 μ M).

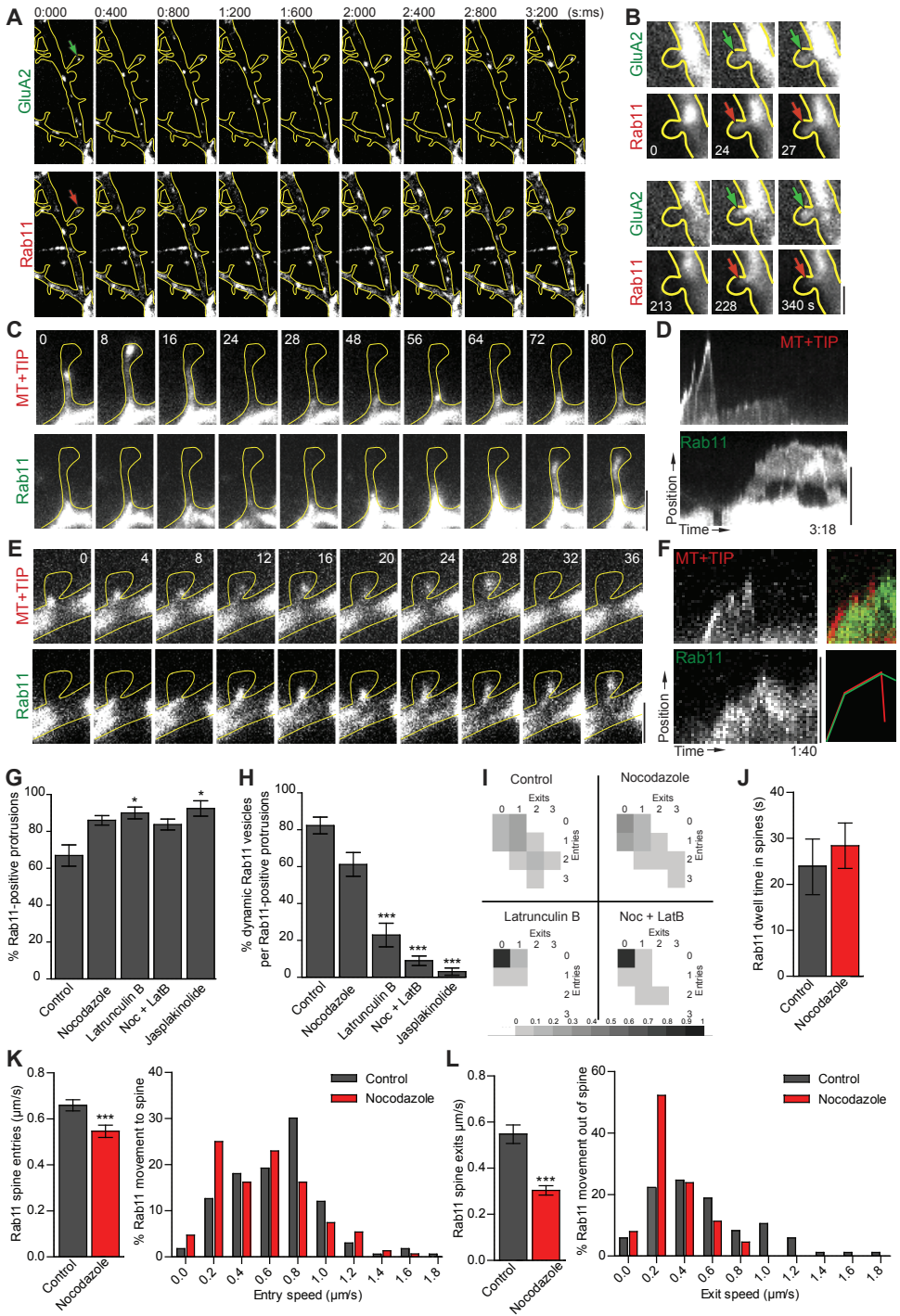


Figure 2 | Recycling endosomes transport into dendritic spines depends on microtubule dynamics

A-B. Stills from a dual-color time-lapse recording of a rat hippocampal neuron expressing GluA1, GFP-GluA2 (top) and mRFP-Rab11 (bottom). Arrows mark motile vesicles positive for both markers. **C-F.** Stills (C,E) and kymograph (D,F) from a dual-color time-lapse recording of a neuron expressing GFP-Rab11 (bottom) and mCherry-MT+TIP (top). (F) Overlay of green and red channels shows complete overlap. **G.** Quantification of the percentage of dendritic protrusions targeted by Rab11-positive recycling endosomes along 20 μm of dendrite during 5 minutes timelapse in the different conditions. **H.** Quantification of the percentage of dynamic Rab11-positive recycling endosomes, i.e. either one exit or one entry from a dendritic protrusion, per number of targeted protrusions, in the different conditions. **I.** Schematic heatmap showing the dynamic distribution of Rab11-positive recycling endosomes in dendritic spines during 5 minutes timelapse, under different conditions. **J.** Quantification of Rab11-vesicles dwell time in spines before and after nocodazole treatment. **K-L.** Quantification of Rab11-positive recycling endosomes entry (K) and exit (L) speeds in spines in control and nocodazole conditions. Graphs represent mean \pm SEM. Statistical significance was determined using Kruskal-Wallis test and Dunn's multiple comparison post hoc test, * $p < 0.05$, *** $p < 0.001$ (Fig.2G-H). and unpaired t-test with Mann Whitney correction, *** $p < 0.001$ (Fig.2J-L). Scale bar is 5 μm (A), 1 μm (B), 2 μm (C-F). See also Figure S3 and Table S1.

In untreated live neurons at DIV14, ~65% of dendritic spines are targeted by Rab11-positive recycling endosomes, and ~80% of the endosomes in spines are dynamic (Fig.2G-I, Fig.S3A). Both nocodazole and/or latrunculin B treatments increased the number of targeted spines (Fig.2G) and decreased the endosome dynamics in spines (Fig.2H). The effect on recycling endosomal dynamics is mild in the case of nocodazole but much more severe with latrunculin B and the combination of both drugs (Fig.2G-I, Fig.S3A). Consistent with previous data (9, 12, 13), we found that MyosinV is involved in proper endosome trafficking in spines (Fig. S3B-E). The data also suggest that MyosinVI has a role in Rab11 vesicle transport in spines (Fig.S3D). Previous studies have shown that MyosinVI is enriched in the postsynaptic density and disruption of its function leads to synaptic loss (14, 15).

Since recent work demonstrated that spines contain dynamic MTs (16-18), we next investigated in more detail the role of MT on Rab11 vesicle dynamics in spines. To visualize MT dynamics in spines, we expressed mCherry-MT+TIP to specifically label growing MT plus-ends (19). MT spine entry events were readily detected from comet displacements, whereas depolymerizing MTs (lacking a clear comet at the tip) could also be observed within spines (Fig.2C-F). Co-expression of mCherry-MT+TIP and GFP-Rab11 revealed that recycling endosomes move in and out of spines in both the presence and absence of MTs (Fig. 2C-F). In untreated neurons, fast imaging of Rab11 vesicle dynamics within spines revealed that the mean entry speed is $0.66 \pm 0.024 \mu\text{m}/\text{sec}$, the mean exit speed is $0.55 \pm 0.04 \mu\text{m}/\text{sec}$ and the average dwell time of dynamic Rab11 vesicles is 24 seconds (Fig.2J-L). Treating neurons with low concentrations of nocodazole (300 nM) decreased both the average entry and exit speeds of endosomes in spines (Fig.2K-L). Interestingly, inhibiting microtubule dynamics resulted in a marked shift of the velocity distribution profiles toward lower speeds (Fig.2K-L), suggesting that the velocity of Rab11 vesicles in spines is higher with MTs, compared to spines without MTs. This is consistent with microtubule-based motility being generally faster than actin-based motility (20). At one point, the endosomal spine entry precisely coincided with the entry of a MT, suggesting that here Rab11 trafficking was limited by the MT growth speed (Fig.2E-F, entry speeds ~0.05 mm/s). Although we cannot exclude that drug treatments have an indirect effect

on the Rab11 vesicle dynamics in spines, it seems likely that recycling endosomes can exploit both dynamic actin and MT-based strategies to enter dendritic spines.

Controlled transport of Rab11 positive recycling endosomes in dendritic spines

Translocation of Rab11-positive recycling endosomes to spines has been shown to be important for spine growth (8, 10). To determine the role of recycling endosomes for overall spine morphology and postsynaptic organization, we co-transfected neurons with GFP to highlight neuronal morphology and a Rab11 dominant negative construct (Rab11-S25N) or Rab11a shRNA. While expression of wildtype GFP-Rab11 does not affect spine morphology, blocking or depleting Rab11 highly affected the morphology of spines, showing a marked decrease in the total number of protrusions and dendritic spines (Fig.3A). To determine if the morphological effect upon disruption of Rab11 correlates with changes in postsynaptic organization, alterations in the number and area of clusters of the postsynaptic marker Homer-1 were analyzed. The number of Homer-1 clusters in protrusions decreased in both Rab11 knockdown or dominant negative conditions (Fig.3B), without significantly affecting the area of the clusters (Fig.3C). Together, these data indicate that Rab11-positive recycling endosomes play an important role in dendritic spine morphology and postsynaptic organization.

To determine the short-term effects of Rab11-positive recycling endosomes trafficking on spine morphology and synaptic function, we developed an inducible trafficking assay to directly control endosomal transport in dendritic spines. In this assay, FRB-FKBP heterodimerization is used to induce the binding of kinesin motors, myosin motors or adaptors to Rab11 vesicles during live-cell recordings (21). For these experiments, Rab11 vesicles were labeled by expressing FKBP-Rab11, a fusion construct of Rab11 with FKBP12, a domain that binds to an FRB domain in the presence of rapalog AP21967 (Fig.3D). FKBP-Rab11 targets specifically recycling endosomes (Fig.S1J). FRB is fused to truncated Kinesin-3 motor KIF1C, and MyosinVI motors, which contains the motor domain and coiled-coil dimerization region (KIF1C-FRB and MyosinVI-FRB). Alternatively, MyosinV was recruited through the MyosinV binding domain (MBD) of melanophilin (MBD-FRB). Inducing the FKBP-Rab11 interaction with various motor proteins did not affect SEP-TfR exocytosis (Fig.3D), indicating that attachment of FKBP-Rab11 to motors does not interfere with global recycling endosome function.

First we focused on KIF1C-induced Rab11 trafficking. Addition of rapalog to neurons co-expressing KIF1C-FRB and FKBP-GFP-Rab11 induced targeting of Rab11-positive recycling endosomes from the shaft into dendritic spines (Fig.S4A-C). Quantification in fixed neurons revealed a marked increase in the number of Rab11 targeted spines after 30 minutes of rapalog treatment (Fig.3E). Live-cell imaging of KIF1C-induced Rab11 vesicle dynamics within the spines showed no effect on the entry and exit speeds (Fig.S4D). Interestingly, we also found an increase of non-typical spine cargoes, such as peroxisomes (21) into dendritic spines after KIF1C recruitment (Fig.S4I-K). In contrast, recruitment of non-processive mutant KIF1C-T306M (Fig.S4F-K) did not affect spine targeting. These results demonstrate that the recruitment of an active microtubule-based motor can result in spine entries.

We next focused on MyosinV- and VI-induced Rab11 trafficking. Addition of rapalog to

neurons co-expressing MBD-FRB and FKBP-GFP-Rab11 induced a rapid burst of recycling endosomes from the shaft into many dendritic spines but are also able to move back out (Fig.3E-G; Video S3). Quantification showed that MyosinV-induced Rab11 trafficking does not increase the average entry speed (Fig.3I), but changes the number of targeted spines (Fig.3E,F). Interestingly, the mean exit speed is decreased by MBD recruitment, suggesting that MyosinV can oppose active spine exit events (Fig.3J). In contrast, addition of rapalog to neurons expressing MyosinVI-FRB caused Rab11-positive recycling endosomes to move away from the spines into the dendrites (Fig.3E,H; Video S4). Quantification showed that MyosinVI-induced Rab11 trafficking does not influence the average entry and exit speeds (Fig.3K-L). These data indicate that MyosinV- and MyosinVI-induced Rab11 trafficking primarily influence the number of targeted spines.

We next tested whether induced targeting or removal of recycling endosomes affects spine morphology. Under both conditions, we observed no differences in the total number of protrusions, spines or filopodia 30 minutes after rapalog addition (Fig.4A). Cumulative frequency plots revealed that also the width and length of spines on dendrites was not changed significantly (Fig.4B). We next determined whether these manipulations influence spine growth following chemical LTP (cLTP). Consistent with previous studies (7, 9), cLTP stimulation using glycine treatment increased spine size in control neurons (Fig.4C). In the rapalog experiments where MBD or MyosinVI is recruited to Rab11 vesicles, the increase in spine size after cLTP was still apparent (Fig.4C). These data suggest that under normal and cLTP conditions induced targeting or removal of recycling endosomes does not immediately affect the morphology of dendritic protrusions.

Removal of Rab11 from spines decreases surface GluA1 and PSD-95 clusters

Given that intracellular AMPARs are transported in recycling endosomes, we explored the functional effects on synapses of induced Rab11-positive recycling endosomes trafficking by measuring AMPAR-mediated miniature excitatory postsynaptic currents (mEPSCs). The influence of MyosinV-induced targeting and MyosinVI-induced removal of recycling endosomes was tested in DIV14-16 neurons transfected for 3 days. During the 20 minutes recordings after rapalog addition, we observed no changes in the frequency or amplitude of mEPSCs between all tested conditions (Fig.4D-F). We next analyzed surface AMPAR levels in individual spines of DIV20-22 neurons by measuring SEP-GluA1 intensity before and after rapalog treatment. MyosinVI-induced removal of Rab11-positive recycling endosomes from spines was associated with a marked decrease in SEP-GluA1 (Fig.4G-H). To determine if the short-term effects of altered Rab11-positive recycling endosomes trafficking affect the structural organization of the synapse, we visualized the postsynaptic marker PSD-95 and Homer-1 clusters (Fig.4I-M). There is a marked decrease in the intensity of PSD-95 clusters upon removal of recycling endosomes (Fig.4J,K), while no effect on Homer-1 was observed (Fig.4L,M). We conclude that removal of recycling endosomes from spines on the short-term decreases surface AMPARs and PSD-95 clusters without affecting spine morphology and overall PSD architecture.

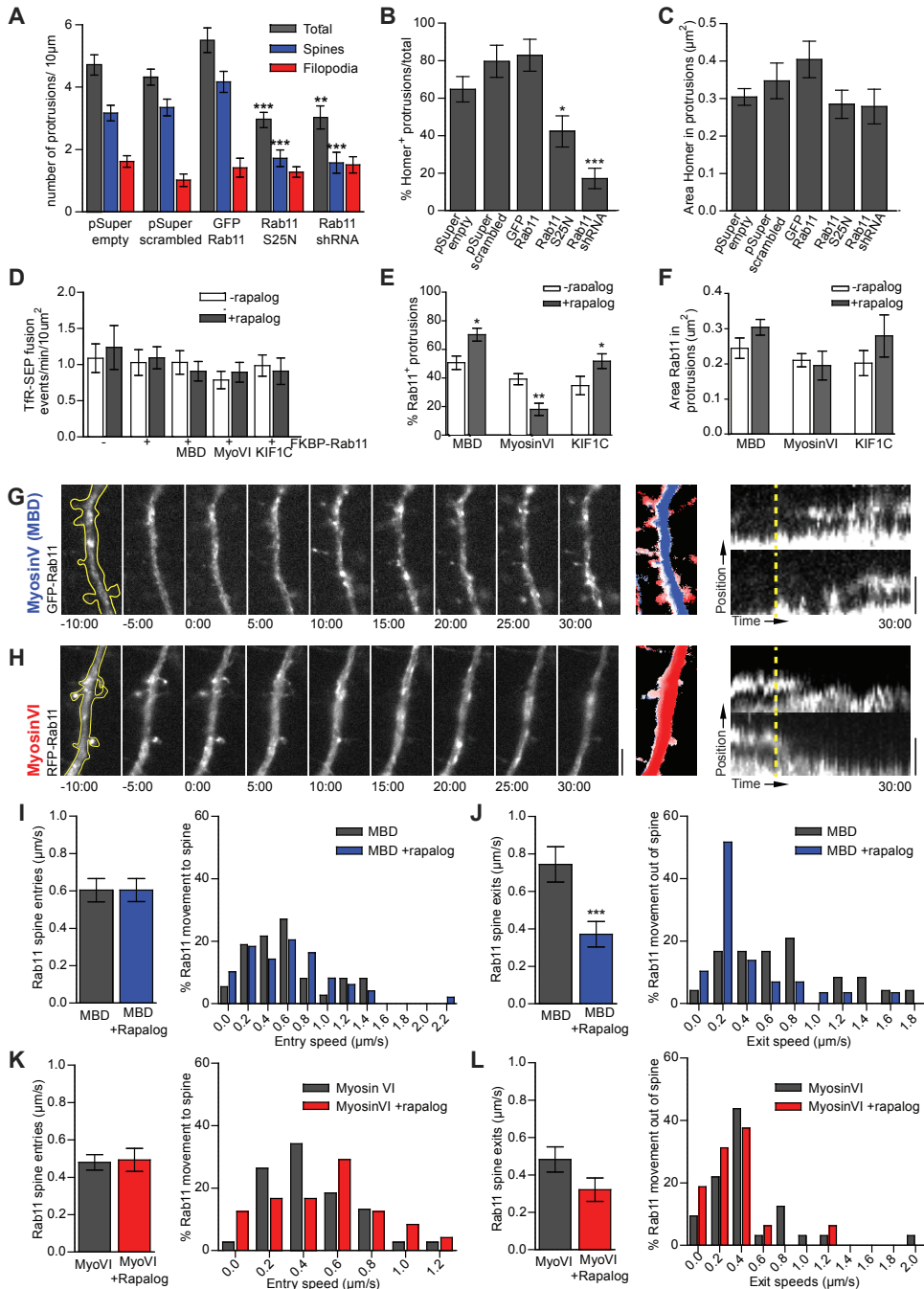


Figure 3 | Time-dependent effect of recycling endosome removal from spines

A. Quantification of protrusions per 10 μm dendrite. Classification was based on head width/length ratio (<0.5 = filopodia; ≥0.5 = spine). **B-C.** Quantification of Homer-positive protrusions per 10 μm regions of dendrite (B) and area of Homer clusters (C). **D.** Induced dimerization of Rab11-vesicles with different motors does not affect fusion of TfR to the surface of COS7 cells. **E-F.** Induced

dimerization of MyosinV (MBD) and KIF1C to Rab11-positive recycling endosomes increases their number in dendritic protrusions, whereas coupling of MyosinV to Rab11-positive recycling endosomes removes them from spines. There is no significant effect in the area of Rab11 vesicles in protrusions upon dimerization. **G-H.** Left panels: Stills from time lapse recordings of Rab11-positive recycling endosomes during which rapalog was added at time 0:00 to recruit MyosinV through MBD (G) or MyosinVI (H). Scale bar is 5 μ m. Middle panels: Overlay of sequential binarized frames, color coded for time from blue to white (-10:00 to 0:00) and white to red (0:00-30:00), first frames are on top. Right panels: corresponding kymographs along the length of spines, showing altered dynamics and localization of Rab11 vesicles upon addition of rapalog (marked with dotted lines). Time scale is min:sec. **I-L.** Quantification of Rab11-positive recycling endosomes entry (I,K) and exit (J,L) speeds in spines before and after induced recruitment of MBD (I,J) or MyosinVI (K,L). Graphs show mean \pm SEM. Statistical significance was determined using Kruskal-Wallis test and Dunn's multiple comparison post hoc test, * $p < 0.05$, *** $p < 0.001$ (A-C), unpaired t-test with Mann Whitney correction, * $p < 0.05$, ** $p < 0.01$, *** $p < 0.001$ (D-L). Scale bar is 2 μ m (H). See also Figure S3 and Table S1.

DISCUSSION

Here we demonstrate that AMPARs are transported in Rab11-positive recycling endosomes along MT tracks within the dendritic shaft and use both the MT and actin cytoskeleton to enter dendritic spines. Inhibiting actin or microtubule dynamics both decrease endosome trafficking in spines. We also demonstrate that Rab11 can enter dendritic spines in a myosin (MyosinV) and kinesin (KIF1C) dependent manner. However, under basal conditions the frequency of MT-spine invasions is relatively low, making actin-based transport a more generic way of driving cargo trafficking in spines. By using chemically induced dimerization to recruit MyosinV motors to Rab11-positive cargoes, we are able to control the position and trafficking of Rab11-positive recycling endosomes in spines. We demonstrate that targeting Rab11-positive recycling endosomes to spines does not significantly affect surface AMPAR levels, indicating that the supply of Rab11-positive recycling endosomes to spines is not the rate-limiting step in determining surface levels of AMPARs. On the other hand, we found that removal of Rab11-positive recycling endosomes from spines by MyosinVI was associated with a marked decrease in surface AMPAR levels and PSD-95 cluster size. We believe that this phenotype is the result of removal of the endosome from spines, however we cannot exclude that reduced AMPAR levels is an effect of globally disrupting endosome trafficking throughout the neuron. We envision two scenarios for this effect that are not mutually exclusive. First, Rab11-positive recycling endosomes could directly control the surface expression of AMPARs by reducing the AMPAR reserve pool and decreasing endocytic recycling within spines. Second, it is possible that Rab11-positive recycling endosomes controls synaptic AMPAR levels by directly or indirectly maintaining PSD-95 levels at synapses. This model fits with current observations that AMPAR density depends on structural alterations within the postsynaptic density (22, 23). Our results also showed that induced addition and removal of Rab11 recycling endosomes from spines for short time periods does not have an impact on spine growth following chemical LTP stimulation. This is an interesting finding because it shows that local translocation of Rab11 vesicles for a short time interval (~30 minutes rapalog treatment), is not sufficient to cause the plasticity changes that were previously observed after longer-term blockage of endosomal recycling (7, 9). Future work will be needed to resolve the precise chronology of the various trafficking events during LTP and to determine

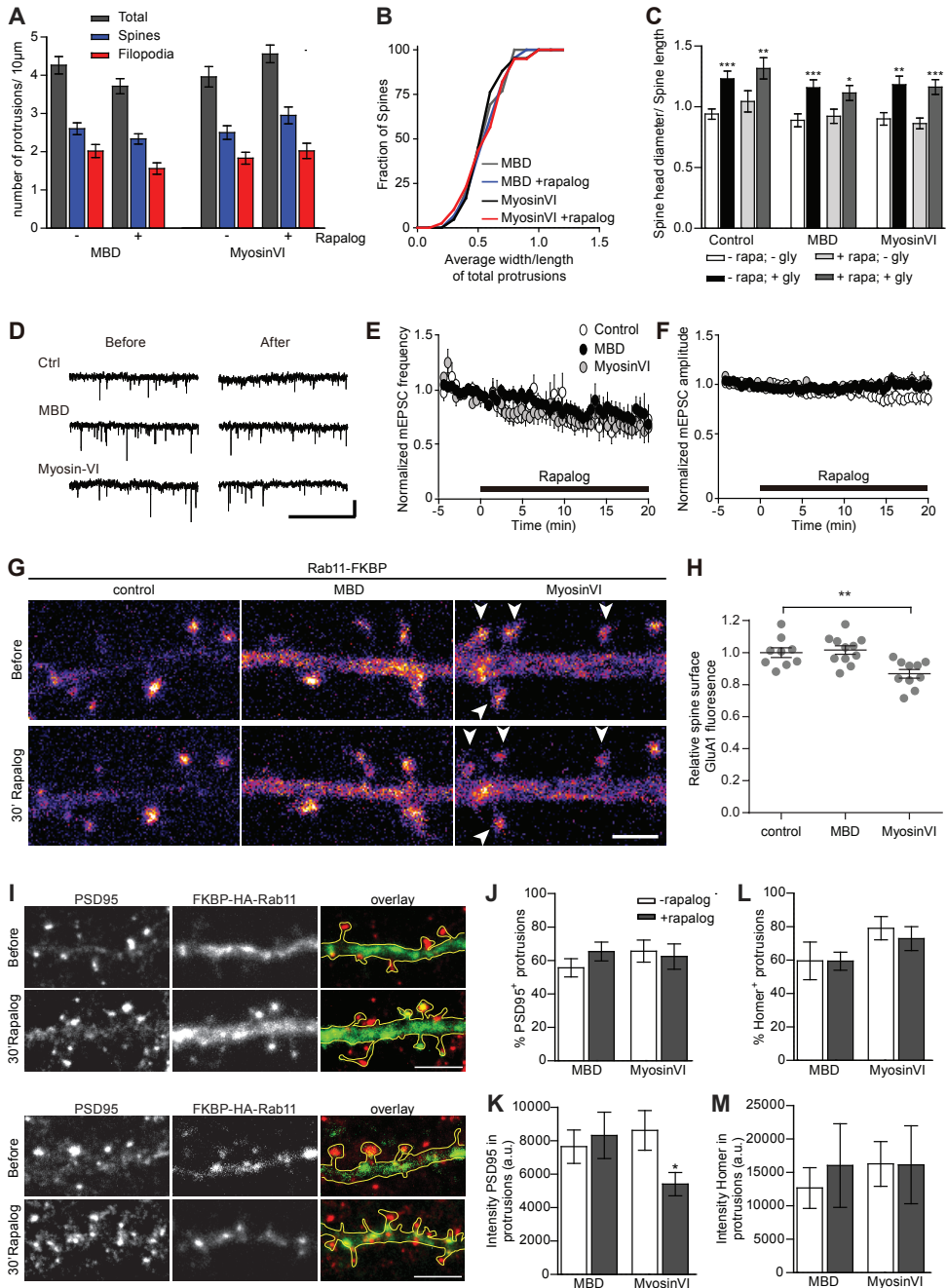


Figure 4 | Removal of recycling endosomes decreases synaptic GluA1 levels and PSD-95 cluster size.

A. Quantification of protrusions before and after induced dimerization of recycling endosomes to MyosinV(MBD)/VI motors. **B.** Cumulative frequency of average width/length of total protrusion before and after induced dimerization of Rab11 endosomes to MBD or MyosinVI. **C.** Rapalog

(rapa)-induced recruitment of MBD or MyosinVI to recycling endosomes following a glycine (gly)-based chemical LTP protocol. **D-F.** Sample traces of mEPSCs recorded before and 20 minutes after application of rapalog (scale bar: 20 pA/2 s). Summary graph of the averaged time course of frequency (E) and amplitude (F) of mEPSCs. Averaged mEPSP amplitudes and frequencies were measured every 30 sec, and the values were normalized to the values measured during the baseline period (-5 to 0 min). Rapalog (100 nM) was applied at 0 min. **G.** Typical examples of SEP-GluA1 levels in dendrites expressing Rab11-FKBP and mCherry (control), mRFP-MBD-FRB or MyosinVI-mRFP-FRB before and after 30 minutes of rapalog addition. Images are pseudocoloured for intensity (purple: low to yellow/white: high). **H.** Quantification of relative average SEP-GluA1 fluorescence intensity after 30 minutes rapalog treatment in dendritic spines of neurons expressing mCherry (control), mRFP-MBD-FRB or MyosinVI-mRFP-FRB. **I.** Immunostaining of dendritic protrusions with PSD-95 (red) before and after induced dimerization of Rab11 recycling endosomes (green) to MBD or MyosinVI. **J-K.** Quantification of number of PSD-95-positive protrusions (J) and PSD-95 intensity (K) per 10 μ m regions of dendrite before/after induced dimerization of Rab11 endosomes to MBD or MyosinVI. **L-M.** Quantification of number of Homer-positive protrusions (L) and Homer intensity (M) per 10 μ m dendritic region before/after induced dimerization of Rab11 to MBD or Myosin VI. Graphs show mean \pm SEM. Statistical significance was determined using an unpaired t-test with Mann Whitney correction, * $p < 0.05$, ** $p < 0.01$, *** $p < 0.001$ (C, J-M), one-way-ANOVA and Bonferroni's multiple comparison post hoc test, ** $p < 0.01$ (H). Scale bar is 2 μ m (G), 5 μ m (I). See also Table S1.

which specific organelles and spine substructures are remodel over different time periods. Based on the involvement of endosomes in mediating signal transduction responses in other systems (24), our findings imply that the specific positioning of recycling endosomes is an important factor in controlling different aspect of synapse architecture.

EXPERIMENTAL PROCEDURES

Expression constructs

Fluorescently or HA-tagged MyosinVI(1-1041)-FRB, MBD(147-240)-FRB and PEX-FKBP heterodimerisation constructs have been described (21). All other constructs were created using PCR based strategies. Fluorescently or HA-tagged FKBP-Rab11, KIF1C(1-496)-FRB, KIF1C(1-496)-T306M-FRB (rigor mutant) were generated in GW1 and/or p β actin expression vectors. For details see supplemental experimental procedures.

Hippocampal neuron cultures, transfections and electrophysiology

Primary hippocampal cultures were prepared from embryonic day 18 (E18) rat brains (16). For electrophysiology experiments, hippocampal primary cultures were prepared from postnatal 1-3 days old C57BL6 mice of either sex as described previously (10). For details see supplemental experimental procedures.

Live cell imaging microscopy

Live cell imaging was performed using two-color Total Internal Reflection Fluorescence (TIRF) or laser confocal spinning disk microscopy. All imaging was performed in full

conditioned Neurobasal medium at 37°C and 5% CO₂ unless otherwise indicated. For details see supplemental experimental procedures.

Live cell imaging of Rab11 and GFP-GluA2 dynamics

To probe intracellular AMPA receptor vesicle transport in neurons, we coexpressed pTRE-GFP-GluA2 with HA-GluA1 and precisely control the timing and level of GluA2 expression using a doxycycline (DOX) regulated gene expression system. To image Rab11-positive recycling endosomes dynamics in dendritic spines, time-lapses of 5 minutes were acquired, with 5 seconds interval between acquisitions. For details see supplemental experimental procedures.

Live cell imaging and analysis of Rab11 and SEP-GluA1 dynamics

To visualize exocytic events of Rab11-positive recycling endosomes containing AMPA receptors, we performed simultaneous dual-color imaging of tagRFP-Rab11 and SEP-GluA1 at 2 frames per second for up to 3 minutes. Events showing sudden local increase of SEP fluorescence were manually counted in ImageJ and classified as spine or dendritic events. To quantify membrane bound amount of GluA1 in rapalog experiments, background-subtracted maximum projections of SEP-GluA1 fluorescence intensity before and after 30 min of rapalog treatment in ~15 randomly selected spines per imaged dendrite was measured in ImageJ and expressed as a ratio. These ratios were then averaged per dendrite. For details see supplemental experimental procedures.

Statistical Methods

Unless otherwise noted, the graphs represent mean \pm SEM. Statistical significance was determined using the Kruskal-Wallis test or one-way ANOVA and Dunn's multiple comparison post hoc test, Wilcoxon test for paired data, an unpaired t-test with Mann Whitney correction. * $p < 0.05$, ** $p < 0.01$, *** $p < 0.001$. The statistical test(s) used for each experiments is indicated in each figure legend. The exact value of n (number of neurons analyzed) and N (number of independent experiments) and the mean \pm SEM for each graph presented in the paper is summarized in Supplementary Table 1.

AUTHOR CONTRIBUTIONS

M.A., M.E.d.S., P.S., J.L. and L.C.K. performed experiments. M.A., M.E.d.S., and L.K. analyzed the data. T.W., S.C. and K.F. performed electrophysiology experiments and analyzed the data. M.E.d.S., L.C.K. and C.C.H. designed the research and wrote the paper. C.J.W., L.C.K. and C.C.H. supervised the project.

ACKNOWLEDGEMENTS

We are grateful to Dr. Terunaga Nakagawa for pTRE-GFP-GluA1-FLAG, Dr. Daniel Choquet for SEP-GluA1, Dr. Folma Buss for Myosin VI tail construct. This work was supported by the Erasmus Medical Center (EMC fellowship, LCK), the Netherlands Organization for Scientific Research (NWO-ALW-VENI, LCK; NWO-ALW-VICI, CCH), the Netherlands Organization

for Health Research and Development (ZonMW-TOP, CCH; ZonMW-VIDI, CW), and EMBO Young Investigators Program (YIP, CCH). This work is part of the research programme of the Foundation for Fundamental Research on Matter (FOM), which is part of NWO. MEdS is supported by Fundação para a Ciência e Tecnologia (FCT-Portugal). PS is supported by the Swiss National Science Foundation (SNSF). JL is supported by International PhD Project Programme of Foundation for Polish Science (studies of nucleic acids and proteins—from basic to applied research) cofinanced by the European Union-Regional Development Fund and cosupervised by prof. Jacek Jaworski. KF was supported by the Whitehall Foundation (2012-08-44) and Japan Foundation for Pediatric Research (JFPR).

REFERENCES

1. Huganir, R. L., and R. A. Nicoll. 2013. AMPARs and synaptic plasticity: the last 25 years. *Neuron* 80:704-717.
2. Newpher, T. M., and M. D. Ehlers. 2008. Glutamate receptor dynamics in dendritic microdomains. *Neuron* 58:472-497.
3. Czondor, K., M. Mondin, M. Garcia, M. Heine, R. Frischknecht, D. Choquet, J. B. Sibarita, and O. R. Thoumine. 2012. Unified quantitative model of AMPA receptor trafficking at synapses. *Proceedings of the National Academy of Sciences of the United States of America* 109:3522-3527.
4. Adrian, M., R. Kusters, C. J. Wierenga, C. Storm, C. C. Hoogenraad, and L. C. Kapitein. 2014. Barriers in the brain: resolving dendritic spine morphology and compartmentalization. *Frontiers in neuroanatomy* 8:142.
5. Colgan, L. A., and R. Yasuda. 2014. Plasticity of dendritic spines: subcompartmentalization of signaling. *Annual review of physiology* 76:365-385.
6. Brown, T. C., S. S. Correia, C. N. Petrok, and J. A. Esteban. 2007. Functional compartmentalization of endosomal trafficking for the synaptic delivery of AMPA receptors during long-term potentiation. *The Journal of neuroscience : the official journal of the Society for Neuroscience* 27:13311-13315.
7. Park, M., E. C. Penick, J. G. Edwards, J. A. Kauer, and M. D. Ehlers. 2004. Recycling endosomes supply AMPA receptors for LTP. *Science* 305:1972-1975.
8. Park, M., J. M. Salgado, L. Ostroff, T. D. Helton, C. G. Robinson, K. M. Harris, and M. D. Ehlers. 2006. Plasticity-induced growth of dendritic spines by exocytic trafficking from recycling endosomes. *Neuron* 52:817-830.
9. Wang, Z., J. G. Edwards, N. Riley, D. W. Provance, Jr., R. Karcher, X. D. Li, I. G. Davison, M. Ikebe, J. A. Mercer, J. A. Kauer, and M. D. Ehlers. 2008. Myosin Vb mobilizes recycling endosomes and AMPA receptors for postsynaptic plasticity. *Cell* 135:535-548.
10. Hoogenraad, C. C., I. Popa, K. Futai, E. Martinez-Sanchez, P. S. Wulf, T. van Vlijmen, B. R. Dortland, V. Oorschot, R. Govers, M. Monti, A. J. Heck, M. Sheng, J. Klumperman, H. Rehmann, D. Jaarsma, L. C. Kapitein, and P. van der Sluijs. 2010. Neuron specific Rab4 effector GRASP-1 coordinates membrane specialization and maturation of recycling endosomes. *PLoS Biol* 8:e1000283.
11. Petrini, E. M., J. Lu, L. Cognet, B. Lounis, M. D. Ehlers, and D. Choquet. 2009. Endocytic trafficking and recycling maintain a pool of mobile surface AMPA receptors required for synaptic potentiation. *Neuron* 63:92-105.
12. Correia, S. S., S. Bassani, T. C. Brown, M. F. Lise, D. S. Backos, A. El-Husseini, M. Passafaro, and J. A. Esteban. 2008. Motor protein-dependent transport of AMPA receptors into spines during long-term potentiation. *Nature neuroscience* 11:457-466.
13. Wagner, W., S. D. Brenowitz, and J. A. Hammer, 3rd. 2011. Myosin-Va transports the endoplasmic reticulum into the dendritic spines of Purkinje neurons. *Nat Cell Biol* 13:40-48.
14. Nash, J. E., V. J. Appleby, S. A. Correa, H. Wu, S. M. Fitzjohn, C. C. Garner, G. L. Collingridge, and E. Molnar. 2010. Disruption of the interaction between myosin VI and SAP97 is associated with a reduction in the number of AMPARs at hippocampal synapses. *J Neurochem* 112:677-690.
15. Osterweil, E., D. G. Wells, and M. S. Mooseker. 2005. A role for myosin VI in postsynaptic structure and

- glutamate receptor endocytosis. *J Cell Biol* 168:329-338.
16. Jaworski, J., L. C. Kapitein, S. M. Gouveia, B. R. Dortland, P. S. Wulf, I. Grigoriev, P. Camera, S. A. Spangler, P. Di Stefano, J. Demmers, H. Krugers, P. Defilippi, A. Akhmanova, and C. C. Hoogenraad. 2009. Dynamic microtubules regulate dendritic spine morphology and synaptic plasticity. *Neuron* 61:85-100.
 17. Gu, J., B. L. Firestein, and J. Q. Zheng. 2008. Microtubules in dendritic spine development. *The Journal of neuroscience : the official journal of the Society for Neuroscience* 28:12120-12124.
 18. Hu, X., C. Viesselmann, S. Nam, E. Merriam, and E. W. Dent. 2008. Activity-dependent dynamic microtubule invasion of dendritic spines. *The Journal of neuroscience : the official journal of the Society for Neuroscience* 28:13094-13105.
 19. Yau, K. W., S. F. van Beuningen, I. Cunha-Ferreira, B. M. Cloin, E. Y. van Battum, L. Will, P. Schatzle, R. P. Tas, J. van Krugten, E. A. Katrukha, K. Jiang, P. S. Wulf, M. Mikhaylova, M. Harterink, R. J. Pasterkamp, A. Akhmanova, L. C. Kapitein, and C. C. Hoogenraad. 2014. Microtubule Minus-End Binding Protein CAMSAP2 Controls Axon Specification and Dendrite Development. *Neuron* 82:1058-1073.
 20. Kapitein, L. C., P. van Bergeijk, J. Lipka, N. Keijzer, P. S. Wulf, E. A. Katrukha, A. Akhmanova, and C. C. Hoogenraad. 2013. Myosin-V opposes microtubule-based cargo transport and drives directional motility on cortical actin. *Curr Biol* 23:828-834.
 21. Kapitein, L. C., M. A. Schlager, W. A. van der Zwan, P. S. Wulf, N. Keijzer, and C. C. Hoogenraad. 2010. Probing intracellular motor protein activity using an inducible cargo trafficking assay. *Biophysical journal* 99:2143-2152.
 22. Bosch, M., J. Castro, T. Saneyoshi, H. Matsuno, M. Sur, and Y. Hayashi. 2014. Structural and Molecular Remodeling of Dendritic Spine Substructures during Long-Term Potentiation. *Neuron* 82:444-459.
 23. Meyer, D., T. Bonhoeffer, and V. Scheuss. 2014. Balance and stability of synaptic structures during synaptic plasticity. *Neuron* 82:430-443.
 24. Miaczynska, M., L. Pelkmans, and M. Zerial. 2004. Not just a sink: endosomes in control of signal transduction. *Curr Opin Cell Biol* 16:400-406.

SUPPLEMENTAL EXPERIMENTAL PROCEDURES

Ethics Statement

All animal experiments were performed in compliance with the guidelines for the welfare of experimental animals issued by the Government of The Netherlands. All animal experiments were approved by the Animal Ethical Review Committee (DEC) of the Erasmus Medical Center and Utrecht University and the Institutional Animal Care and Use Committee (IACUC) at University of Massachusetts Medical School.

Expression constructs

The following mammalian expression plasmids have been described previously: pGW1-mRFP, pGW1-GFP, p β actin-HA- β -Galactosidase (1), pSuper vector (2), SEP-GluA1 (3), HA-GluA1 and HA-GluA2 (4), pTRE-GFP-GluA1, pTRE-GFP-GluA2-FLAG and pTet-on-Ad (5), mCherry-MT+TIP (6), mRFP-Rab11a, GFP-Rab11a, HA-Rab11a, GFP-Rab11-S25N (7), mRFP-Rab6 (8), rat Rab11a shRNA (9), MyosinVa and MyosinVb tails (10), MyosinVI tail (11), MyosinVI-(aa1-1041)-FRB, GFP-, mRFP- and HA-MBD-(aa147-240)-FRB, Pex-mRFP-FKBP (12), TfR-SEP (Park et al 2004), MARCKS-eGFP (13). All other constructs were created using PCR based strategies. KIF1C-(aa1-496)-HA-FRB, KIF1C(aa1-496)-T306M-GFP-FRB (rigor mutant, adapted from a KIF1A mutation (14)), and FKBP-TdTomato-Rab11 were

generated in pβactin expression vector. TagRFP-Rab11a, FKBP-GFP-Rab11a and FKBP-HA-Rab11a fusions were generated in GW1 expression vectors. The dominant-negative MyosinVa (aa1242-1830) and MyosinVb (aa1233-1848) constructs (MyoV-tail) and MyosinVI construct (aa846-1277, MyoVI-tail) were cloned into GW1 expression vectors.

Hippocampal neuron cultures, transfections and drug treatments

Primary hippocampal cultures were prepared from embryonic day 18 (E18) rat brains (15, 16). Cells were plated on coverslips coated with poly-L-lysine (30 µg/ml) and laminin (2 µg/ml) at a density of 100,000/well. Hippocampal cultures were grown in Neurobasal medium (NB) supplemented with B27, 0.5 mM glutamine, 12.5 µM glutamate and penicillin/streptomycin. Hippocampal neurons at 14-21DIV were transfected using Lipofectamine 2000 (Invitrogen). Briefly, DNA (3.6 µg/well) was mixed with 3 ml Lipofectamine 2000 in 200 ml NB, incubated for 30 minutes and then added to the neurons in NB with 0.5mM glutamine at 37°C in 5% CO₂ for 45 min to 1 hour. Next, neurons were washed with NB and transferred in the original medium at 37°C in 5% CO₂ for 2-4 days. To induce expression of GFP-GluA2 + HA-GluA1 in hippocampal neurons, doxycycline (Sigma) was added to a final concentration of 1mg/ml 24-30 hours prior to microscopy. 300 nM nocodazole, 10 µM latrunculin B (Sigma) or 10 µM jasplakinolide (Tocris) were added to neuron cultures and imaged after 1 min and up to 1hr after addition. Rapalog (AP21967) was dissolved to 0.1 mM in ethanol. 5 minutes prior to imaging, 0.2 ml of culture medium with rapalog (400 nM) was added to establish a final rapalog concentration of 100 nM.

The cLTP protocol was used combined with rapalog treatment transfected neurons were either left untreated (- rapalog) or treated with 100nM rapalog (+ rapalog) for 15 minutes at 37°C in 5% CO₂. After that, neurons were washed with warm extracellular solution (ECS) of the following composition (mM): NaCl, 120; CaCl₂, 1.3; MgCl₂, 2; KCl, 3.0; HEPES, 10; glucose, 10; Bicuculline, 0.02 (pH 7.4 and osmolarity between 240 and 250mOsmol). Neurons were either left untreated (- rapalog; - glycine) or treated with 200µM glycine (- rapalog; + glycine) or 100nM rapalog (+ rapalog; - glycine) or 200µM glycine plus 100nM rapalog (+ rapalog; + glycine; all conditions in ECS). After 20 minutes at 37°C in 5% CO₂, neurons were fixed for 10 min with 4% paraformaldehyde (PFA)/4% sucrose in PBS at room temperature.

Immunohistochemistry and dendritic spine analysis

For immunohistochemistry, neurons were fixed for 10 min with 4% paraformaldehyde (PFA)/4% sucrose in PBS at room temperature. In rapalog experiments, neurons were fixed after 30 minutes of 100nM rapalog treatment. After fixation cells were washed 3 times for 5 minutes in PBS at room temperature and incubated with the primary-antibody mix in GDB buffer (0.2% BSA, 0.8M NaCl, 0.5% Triton X-100, 30mM phosphate buffer, pH 7.4) overnight at 4°C. Next the neurons were washed 3 times for 5 minutes in PBS at room temperature and incubated with the secondary-antibody mix in GDB buffer for at most 1 hour at room temperature. Neurons were then washed 3 times for 5 min in PBS at room temperature and subsequently mounted on slides in Vectashield mounting medium (Vector Laboratories). Confocal images were acquired using LSM700 (Zeiss) with a 63x/1.40 Oil DIC objective and additional 1.3 zoom using 488nm, 555nm and 633 nm laser lines. A total thickness of

5 μm was scanned for each position and maximum intensity projections were generated for analysis. Imaging settings were kept the same when pictures were compared for fluorescence intensity. The following primary and secondary antibodies were used in this study: mouse anti-PSD-95 antibody (Neuromab, catalog number 75-028), rabbit anti-Homer1 antibody (Synaptic Systems, catalog number 160 002), and rabbit anti Rab11 antibody (Invitrogen, catalog number 71-5300) and Alexa 488-, Alexa 568- and Alexa 633- conjugated secondary antibodies (Invitrogen). Morphology of dendritic protrusions was measured manually in ImageJ, by tracing the width of heads and the length of the protrusion along 10 μm dendritic regions. Protrusions were classified as spines or filopodia according to head width to length ratio (filopodia corresponds to protrusions with ratio below 0.5 and spines have ratio equal to or bigger than 0.5). On the same selected regions, the number and size of PSD-95 and Homer1 clusters were measured manually. The colocalization of overexpressed GluA subunits and endogenous Rab11 was performed using ComDet ImageJ plugin version 0.3.4 (<https://github.com/ekatruxha/ComDet>).

Live cell imaging microscopy

All imaging was performed in full conditioned medium at 37°C and 5% CO₂ unless otherwise indicated. Most live cell imaging was performed using two-color Total Internal Reflection Fluorescence (TIRF) or laser confocal spinning disk microscopy. For TIRF microscopy, a Nikon Eclipse TE2000E (Nikon) with a CFI Apo TIRF 100x 1.49 N.A. oil objective (Nikon) was used, as described previously (1, 16). Briefly, simultaneous dual-color TIRFM was achieved using a DualView (DV2, Photometrics) with beam splitter (Chroma, 565DCXR) and additional emitter (Chroma, ET525/25) in the GFP light path, generating two images on the same chip of a sensitive EMCCD camera (QuantEM or Evolve, both Photometrics). An additional 2.5x magnification lens (Nikon, VM Lens C-2.5x) was employed to compensate the larger pixel size and prevent undersampling of the point-spread function. To visualize intracellular vesicular GFP-GluA2, most of the fluorescence from the dendritic part in the field of view was bleached before image acquisition using the FRAP scanning head 3 FRAP L5 D – CURIE (Curie Institute) in combination with both the 488 nm and 561 nm laser line. Kymographs were created in Metamorph (Universal Imaging) or ImageJ. Experiments in which Rab11 was redistributed using rapalog were performed on the same setup, but using a 40x 1.4 N.A. oil objective, a mercury lamp for excitation and a Coolsnap camera for detection (Photometrics) (17).

For spinning disk microscopy, a Nikon Eclipse-Ti (Nikon) microscope with CFI Apo TIRF 100x, 1.49 NA, Plan Apo VC 100x N.A. 1.40 or Plan Apo 60x N.A. 1.30 oil objectives (Nikon) was used. The microscope is equipped with a motorized stage (ASI; MS-2000), a Perfect Focus System (Nikon), an incubation chamber (Tokai Hit; INUBG2E-ZILCS) and uses MetaMorph 7.7.6 software (Molecular Devices) to control the camera and all motorized parts. Confocal excitation and detection is achieved using 100 mW Cobolt Calypso 491nm and 100mW Cobolt Jive 561nm lasers and a Yokogawa spinning disk confocal scanning unit (CSU-X1-A1; Yokogawa) equipped with a triple-band dichroic mirror (z405/488/568transpc; Chroma) and a filter wheel (CSU-X1-FW-06P-01; Yokogawa) containing GFP (ET-GFP (49002)), mCherry (ET-mCherry (49008)) and mCherry/GFP (ET-mCherry/GFP (59022)) emission filters (all Chroma). Confocal images were acquired with a Evolve 512 EMCCD camera (Photometrics) at a final magnification of 66 nm/pixel, including the additional 2.0×

magnification introduced by an additional lens mounted between scanning unit and camera (Edmund Optics). Simultaneous dual-color imaging was performed using a DualView beam splitter (DV2, Roper).

Live cell imaging and analysis of GFP-GluA2 and Rab11 dynamics

To probe intracellular AMPA receptor vesicle transport in neurons, we precisely control the timing and level of receptor expression using a doxycycline (DOX) regulated gene expression system. pTRE-GFP-GluA2 expression was silenced by binding of the reverse tetracycline-controlled transcriptional activator (pTet-on-Ad) in the absence of doxycycline (DOX) to the cultures (5). To facilitate the formation of heterotetrameric complexes we coexpressed pTRE-GFP-GluA2 with HA-GluA1. After incubation with DOX for 25-30 hours, high-resolution total-internal reflection (TIRF) microscopy was performed. In GFP-GluA2 expressing neurons there is a major contribution from surface receptors, which appear as diffusive signals on the plasma membrane. However, we visualized the intracellular pool of GluA2 receptors directly after bleaching a large dendritic area by fast image acquisition over relatively short time intervals. During this imaging period, ~95% of the GFP-GluA2 signal is observed in fast moving Rab11-positive vesicles, suggesting that these GluA2 receptors are located inside the cell rather than on its cell membrane. After ~100 seconds, we observe recovery of fluorescence by a diffusive distribution throughout the bleached area, most likely due to the lateral diffusion of GFP-GluA2 receptors at the plasma membrane. As a result of the increase in the diffusive fluorescent signal it is challenging to detect and follow intracellular GluA2 receptor trafficking for longer time periods after bleaching. Thus our approach is limited to pools of GFP-GluA2 receptor that are mobile and move quickly into the bleached area. Cui-Wang and colleagues (18) showed that the internal diffusion of ER retained GluA2 receptors is around the same time scale as that of mobile receptors at the plasma membrane, suggesting that GluA2 receptor diffusion at the ER could also contribute to the increase in overall fluorescent signal in the dendrites. The ER retained GluA2 receptors are also bleached in our experiments and we probably do not detect the slow release of receptors from ER exit sites due to the increase in diffusive fluorescent signal throughout the bleached area (from both the plasma membrane and ER pools).

To visualize Rab11-positive recycling endosomes transport in cultured hippocampal neurons, we performed imaging of GFP-Rab11 in dendritic shafts for 1 minute at an acquisition rate of 4 frames per second. To image Rab11-positive recycling endosomes dynamics in dendritic spines, time-lapses of 5 minutes were acquired, with 5 seconds interval between acquisition and a z-stack stream at every timepoint, to guarantee the entire dendritic complexity is imaged. mRFP was also imaged to assess neuronal morphology. To quantify speeds of Rab11-positive recycling endosomes entry or exits in spines, 5 minutes stream acquisition was performed, at an acquisition rate of 5 frames per second. To visualize the distribution of spine entry and exit speeds, data was plotted in cumulative frequency plots with bins of 0.2 μ m (the first bin in each plot is only 0.1 μ m.) In rapalog experiments, 3 minutes of stream acquisition was performed, at an acquisition rate of 5 frames per second. The same neurons were imaged before and after rapalog from 0 to 10 minutes (3 neurons per coverslip). All imaging experiments are performed in conditioned Neurobasal medium. Other solutions used to test different imaging conditions, include Ringers solution (10mM Hepes, 155mM NaCl, 2 mM CaCl₂, 1mM MgCl₂, 2mM NaH₂PO₄, 10mM glucose, pH 7.2), and Artificial CerebroSpinal Fluid (ACSF, 126mM

NaCl, 3mM KCl, 2.5mM CaCl₂, 1.3mM MgCl₂, 1.25mM NaH₂PO₄, 26mM NaHCO₃, 20mM glucose). The osmolality was measured using a semi-micro osmometer K-7400 (Knauer). To quantify Rab11-positive recycling endosomes movements along the dendritic shafts, kymographs of 5 μm dendritic fractions were made in ImageJ and manually counted. Rab11-positive recycling endosomes dynamic entries or exits from dendritic spines were also manually counted, along 20 μm of dendrite. Manual tracking of the timelapse movies was obtained by tracking individual clustered vesicle displacements on each frame.

Live cell imaging and analysis of Rab11 and SEP-GluA1 dynamics

To visualize exocytic events of Rab11-positive recycling endosomes containing AMPA receptors, we performed simultaneous dual-color imaging of tagRFP-Rab11 and SEP-GluA1 at 2 frames per second for up to 3 minutes. Events showing sudden local increase of SEP fluorescence were manually counted in ImageJ and classified as spine or dendritic events. To quantify membrane bound amount of GluA1 in rapalog experiments, background-subtracted maximum projections of SEP-GluA1 fluorescence intensity before and after 30min of rapalog treatment in ~15 randomly selected spines per imaged dendrite was measured in ImageJ and expressed as a ratio. These ratios were then averaged per dendrite. Representative examples of these spines are shown in ImageJ's "Fire" LUT. Only cells in which the SEP signal was sensitive to an acid wash at pH 6.0 were analyzed in these experiments.

Electrophysiology

Hippocampal primary cultures were prepared from postnatal 1-3 days old C57BL6 mice of either sex as described previously (19). Neurons were transfected at days 11–13 in vitro (DIV) using Lipofectamine 2000 (Invitrogen), and were assayed 3 days after transfection. Expression vectors for FKBP-HA-Rab11 and HA-MBD-FRB or MyoVI-MD-GFP-FRB were transfected together with pCAG-EGFP at a ratio of 1:1:0.5 by weight. The extracellular solution was (in mM): 119 NaCl, 2.5 KCl, 4 CaCl₂, 4 MgCl₂, 26 NaHCO₃, 1 NaH₂PO₄ and 11 glucose, gassed with 5% CO₂/95% O₂, pH 7.4. Whole-cell voltage clamp recordings were made from gene transfected hippocampal pyramidal neurons (visualized by co-transfecting GFP). The patch recording pipettes (2–4 MΩ) were filled with internal solution containing (in mM): 115 cesium methanesulfonate, 20 CsCl, 10 HEPES, 2.5 MgCl₂, 4 adenosine triphosphate disodium salt, 0.4 guanosine triphosphate trisodium salt, 10 sodium phosphocreatine, and 0.6 EGTA, at pH 7.25 with CsOH. To measure AMPA receptor-mediated miniature EPSC, picrotoxin (0.1 mM, Sigma) and tetrodotoxin (0.001 mM, Ascent Scientific) was added to ACSF and neurons were voltage clamped at $V_{\text{hold}} = -70$ mV. Events smaller than 5 pA were excluded from the analysis. Experiments and analysis were done blind to the DNA constructs used.

COS7 cell culture, transfection and imaging

COS7 cells were cultured in Dulbecco's modified Eagle's medium/Ham's F10 medium (50/50%) containing 10% fetal calf serum and 1% penicillin/streptomycin, and 2 days before transfection the cells were plated on 24 mm diameter coverslips. Cells were transfected with Eugene6 transfection reagent (Roche) according to the manufacturer's protocol and grown for 24 hours prior to imaging or fixation. 1 minute of stream acquisition was performed, at an acquisition rate of 4 frames per second. On rapalog experiments, cells were imaged after 1 to

30 minutes of 100nM rapalog.

Figure	Condition	n	N	
Fig.1D	GluA2	90 (Rab11 endosomes)	5 (neurons)	
	Rab11	79 (GluA2 clusters)	5 (neurons)	
Fig.1E-F	TfR-mCherry	6 (dendrites)	3	0.59 ± 0.08 C
	GFP-GluA2 + Control	14 (dendrites)	3	0.37 ± 0.09 C
	GFP-GluA2 + Rab11	30 (dendrites)	3	0.50 ± 0.07 C
	GFP-GluA2 + MyoV tail	12 (dendrites)	3	0.24 ± 0.03 C
	GFP-GluA2 + MyoVI tail	8 (dendrites)	3	0.18 ± 0.02 C
Fig.1G	Control	30	6	
	Nocodazole	12	2	
	Latrunculin	11	2	
	Noc + LatB	8	2	
Fig.1J-K	Control	23 (dendrites)	3	0.13 ± 0.01
	Rab11	24 (dendrites)	3	0.20 ± 0.02
	MyoV tail	25 (dendrites)	3	0.13 ± 0.01
	MyoVI tail	23 (dendrites)	3	0.14 ± 0.01
Fig.2G-H	Control	23	4	66.1
	Nocodazole	24	4	83.
	Latrunculin	18	3	90.
	Noc + LatB	17	2	83
	Jasplakinolide	10	2	92
Fig.2J-L	Control	16	2	23.9 ± 5.9 s; 0
	Nocodazole	11	2	28.4 ± 4.9 s; 0
Fig.3A-C	pSuper empty	29	3	4.70 ± C
	pSuper scrambled	12	3	4.32 ± C
	GFP-Rab11	12	3	5.50 ± C
	Rab11 S25N	32	3	2.94 ± C
	Rab11 shRNA	18	3	3.03 ± 0
Fig.3B-C	pSuper empty	19	3	64.8
	pSuper scrambled	12	3	79.7
	GFP-Rab11	12	3	82.9
	Rab11 S25N	19;15	3	42.28
	Rab11 shRNA	12;6	3	17.13
Fig.3D	Control	20 (COS7 cells)	2	1.085 ± 0.20
	FKBP-Rab11	16 (COS7 cells)	2	1.02 ± 0.18
	FKBP-Rab11 + MBD-FRB	16 (COS7 cells)	2	1.026 ± 0.10
	FKBP-Rab11 + MyoVI-FRB	15 (COS7 cells)	2	0.78 ± 0.12
	FKBP-Rab11 + Kif1C-FRB	16 (COS7 cells)	2	0.98 ± 0.15
Fig.3E	MBD	20	2	49.8
	MBD + rapalog	28	2	69.1
	MyosinVI	21	2	38.4
	MyosinVI + rapalog	15	2	17.5
	Kif1C	10	2	33.9
	Kif1C + rapalog	10	2	50.8
	Fig.3I-J	MBD	8	3
Fig.3K-L	MBD + rapalog	8	3	0.60 ± C
	MyosinVI	8	3	0.50 ± C
Fig.3K-L	MyosinVI + rapalog	8	3	0.49 ± C
	Fig.4A-B	MBD	38	2
Fig.4C	MBD + rapalog	44	2	3.71 ± 0
	MyosinVI	44	2	3.96 ± C
	MyosinVI + rapalog	38	2	4.56 ± 0
	Control	16; 14; 14; 16	2	0.94 ± 0.04; 1.2

Table S1 | Overview of all data analyzed and quantified in this study

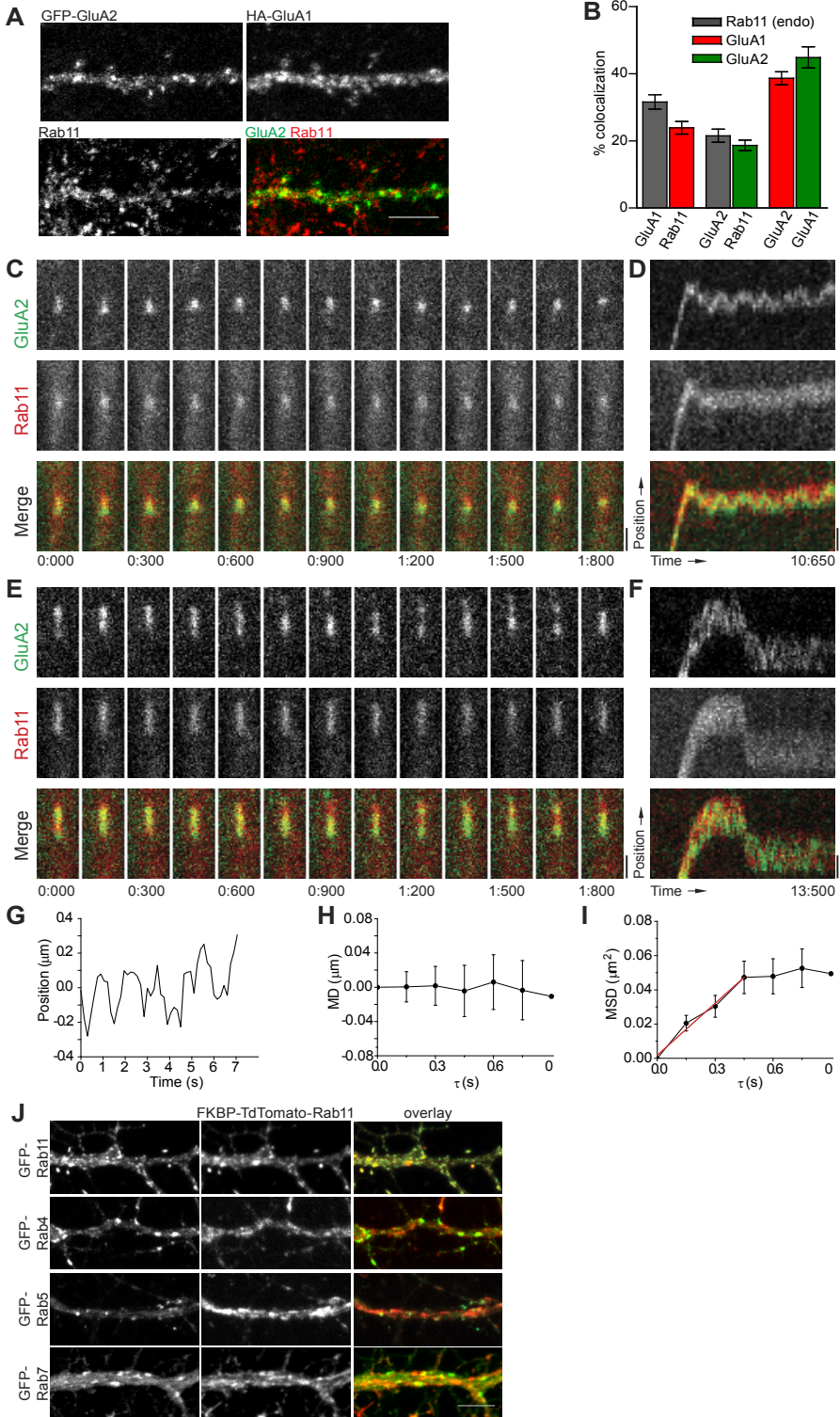


Figure S1 | AMPA-receptors undergo confined diffusion inside Rab11-positive recycling endosomes

A. Immunostaining of endogenous Rab11 with coexpressed GluA1 and GluA2 shows partial colocalization. Scale bar is 5mm. Zoomed area: scale bar is 2 mm. **B.** Quantification of colocalization between coexpressed GluA1, GluA2 and intracellular Rab11 (n=11; N=2). **C,E.** Stills from a dual-color time-lapse recording of a rat hippocampal neuron expressing GluA1, GFP-GluA2 (top) and mRFP-Rab11 (bottom). Time is indicated as seconds:milliseconds. Scale bar is 1 μ m. **D,F.** Kymographs of the recording shown in C and E, respectively, showing motility of single (D) or multiple (F) GFP-GluA2 clusters inside the Rab11-positive recycling endosome. Scale bar is 1 μ m. **G.** Example trajectory of a GFP-GluA2 cluster during a nonmotile episode of the Rab11-positive recycling endosome. **H.** Average mean displacement of 7 GFP-GluA2 clusters for different time intervals τ during during nonmotile episodes of Rab11-positive recycling endosomes, revealing that clusters undergo no net displacements when the endosomes are immobile. **I.** Average mean squared displacement for different time intervals τ for 7 clusters during nonmotile endosome episodes, revealing that the clusters undergo confined diffusion limited by the endosome boundaries, with an initial diffusion constant of 0.05 mm²/s. **J.** Dendritic colocalization of FKBP-tdTomato-Rab11 with other Rab11 construct and other overexpressed endosomal markers. There is a high degree of colocalization between the two Rab11 constructs, and only minor colocalization with the other endosomal markers. Scale bar is 5 mm.

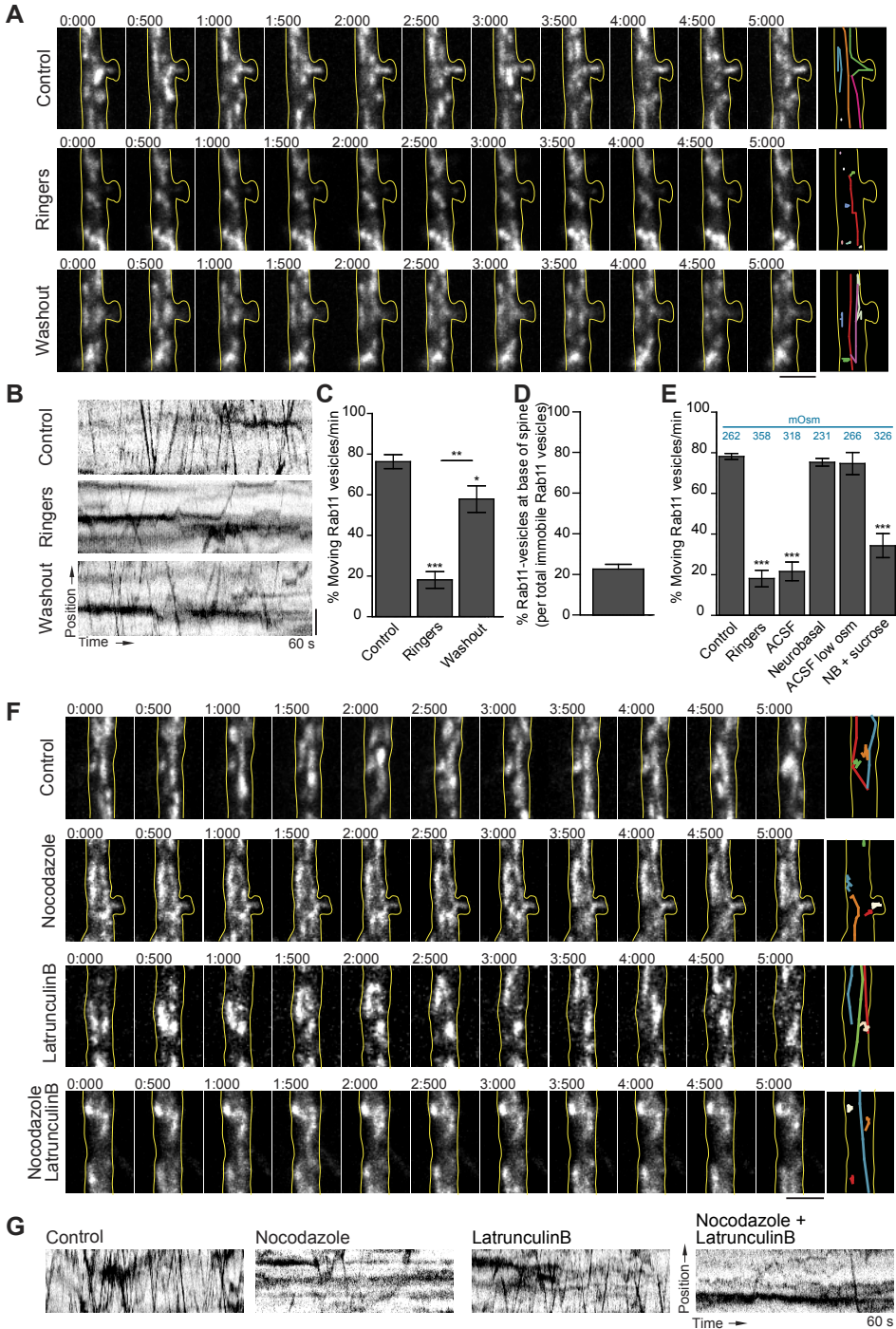


Figure S2 | Microtubule-targeting drug affect endosome motility in the dendritic shaft

A. Stills from a 60 seconds time-lapse recording of rat hippocampal neurons at DIV14-17 expressing GFP-Rab11, when imaged in different solutions. Vesicle manual tracking shows motile and non-

motile Rab11-positive recycling endosomes. Time is indicated as seconds:milliseconds. All cells were first imaged in conditioned medium (CM) which was replaced by Ringers buffer for 5 minutes and then washed out with CM for 15-20 minutes. Rab11-positive recycling endosomes are mobile in CM, but quickly become immobile in Ringers buffer. Motility is partially recovered after washout. Scale bar is 2 μm . **B.** Kymographs of the recordings in A, showing the motility of the recycling endosomes in the described conditions. Scale bar is 2 μm . **C.** Quantification of the percentage of motile Rab11-positive recycling endosomes in 1min timelapse acquisition under the indicated conditions (n=6, N=2). Replacing the CM before imaging with Ringer's or artificial cerebrospinal fluid (ACSF) solutions markedly reduced Rab11 vesicles motility in the dendrites, which was due to the difference in osmolarity of these solutions compared to CM. By returning the neurons to CM and washing out the Ringer's solution, most of the Rab11 vesicles motility is recovered. **D.** Quantification of the fraction of immobile Rab11-vesicles at the base of the spine (n=17, N=2). **E.** Quantification of the percentage of motile Rab11- positive vesicles in 1min timelapse acquisition under the indicated conditions (Control: n=10; Ringers: n=6; ACSF: n=6; Neurobasal: n=6; ACSF low osm: n=4; NB + Sucrose: n=4; N=2). Osmolality of each solution is indicated in blue. **F.** Stills from a 60 seconds time-lapse recording of rat hippocampal neurons expressing GFP-Rab11. Manual vesicle tracking shows motile and non-motile Rab11-positive recycling endosomes. Time is indicated as seconds:milliseconds. Neurons were imaged either in control conditions or after 3 minutes in 300nM nocodazole, 10 μM latrunculin B or a combination of both. Scale bar is 2 μm . **G.** Kymographs of the recordings in F, showing the motility of the vesicles in the different conditions. Scale bar is 2 μm . Graphs represent mean \pm SEM. Statistical significance was determined by using the Wilcoxon test for paired data, * $p < 0.05$, ** $p < 0.01$, *** $p < 0.001$ (C), Kruskal-Wallis test and Dunn's multiple comparison post hoc test, *** $p < 0.001$ (E).

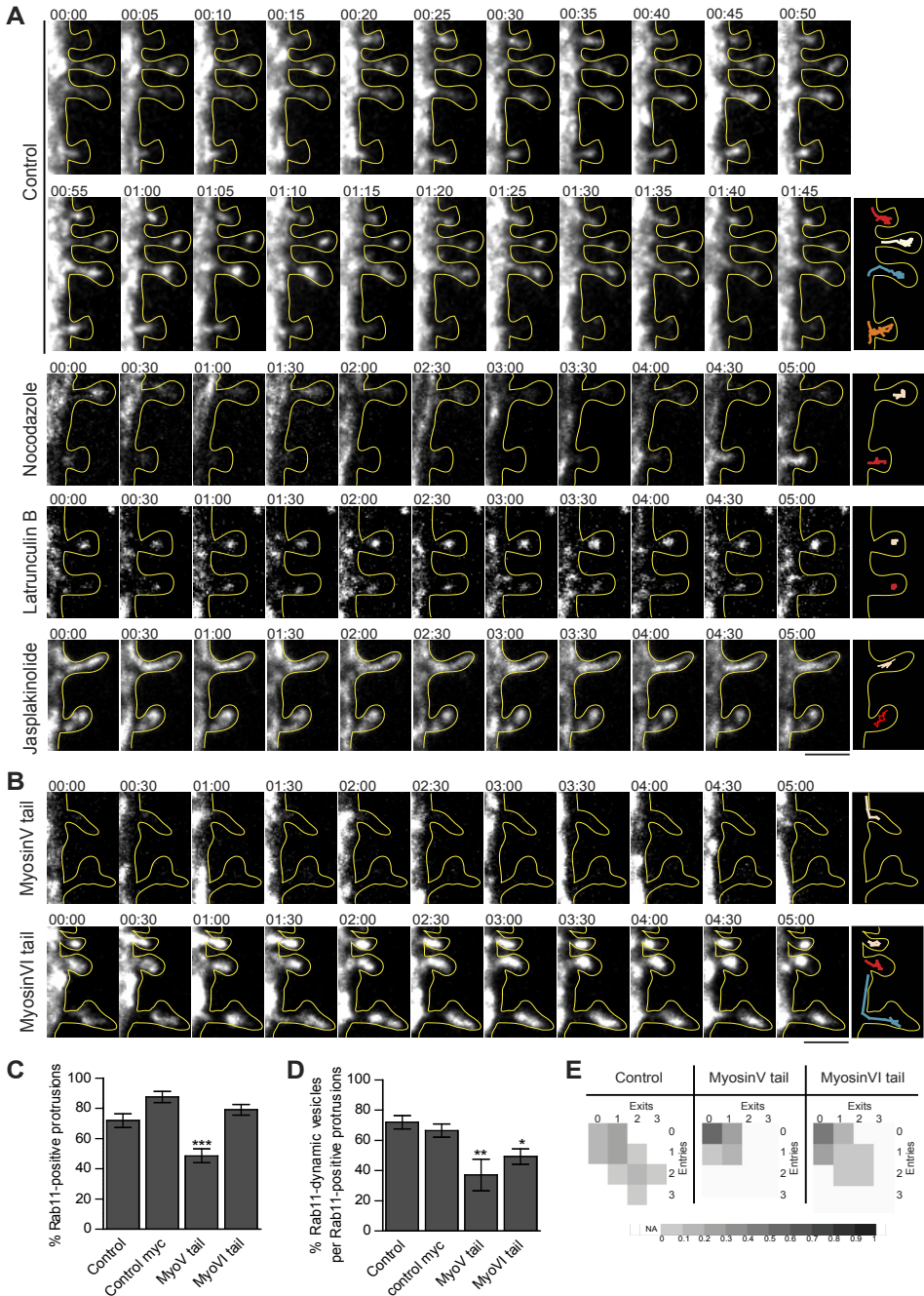


Figure S3 | Blockade of MyosinV and MyosinVI differentially affects recycling endosome entry in spines.

A. Stills from a 5 minutes time-lapse recording of rat hippocampal neurons expressing GFP-Rab11. Vesicle manual tracking shows motile and non-motile Rab11-positive recycling endosomes. Time is indicated as minutes:seconds. Neurons were imaged either in control conditions or after 5 minutes

in 300nM nocodazole, 10 μ M latrunculin B or a combination of both, and 10 μ M jasplakinolide. Scale bar is 2 μ m. **B.** Stills from a 5 minutes time-lapse recording of rat hippocampal neurons expressing GFP-Rab11 and myc-MyosinV tail or myc-MyosinVI tail. Vesicle manual tracking shows motile and non-motile Rab11 endosomes. Time is indicated as minutes:seconds. Scale bar is 2 μ m. **C.** Rab11-positive recycling endosomes are less targeted to dendritic protrusion when myosinV function is blocked but not MyosinVI. **D.** Rab11-positive recycling endosomes dynamics is affected when either MyosinV or MyosinVI function is inhibited (control: n=16; control myc: n=20; MyosinV tail: n=12; MyosinVI tail: n=21, N=2). **E.** Schematic heatmap showing the dynamic distribution of Rab11-positive recycling endosomes. Inhibition of MyosinV tail affects mostly entries in protrusions, whereas inhibition of MyosinVI tail halts Rab11 vesicles exits from protrusions. Graphs represent mean \pm SEM. Statistical significance was determined using Kruskal-Wallis test and Dunn's multiple comparison post hoc test, * p<0.05.

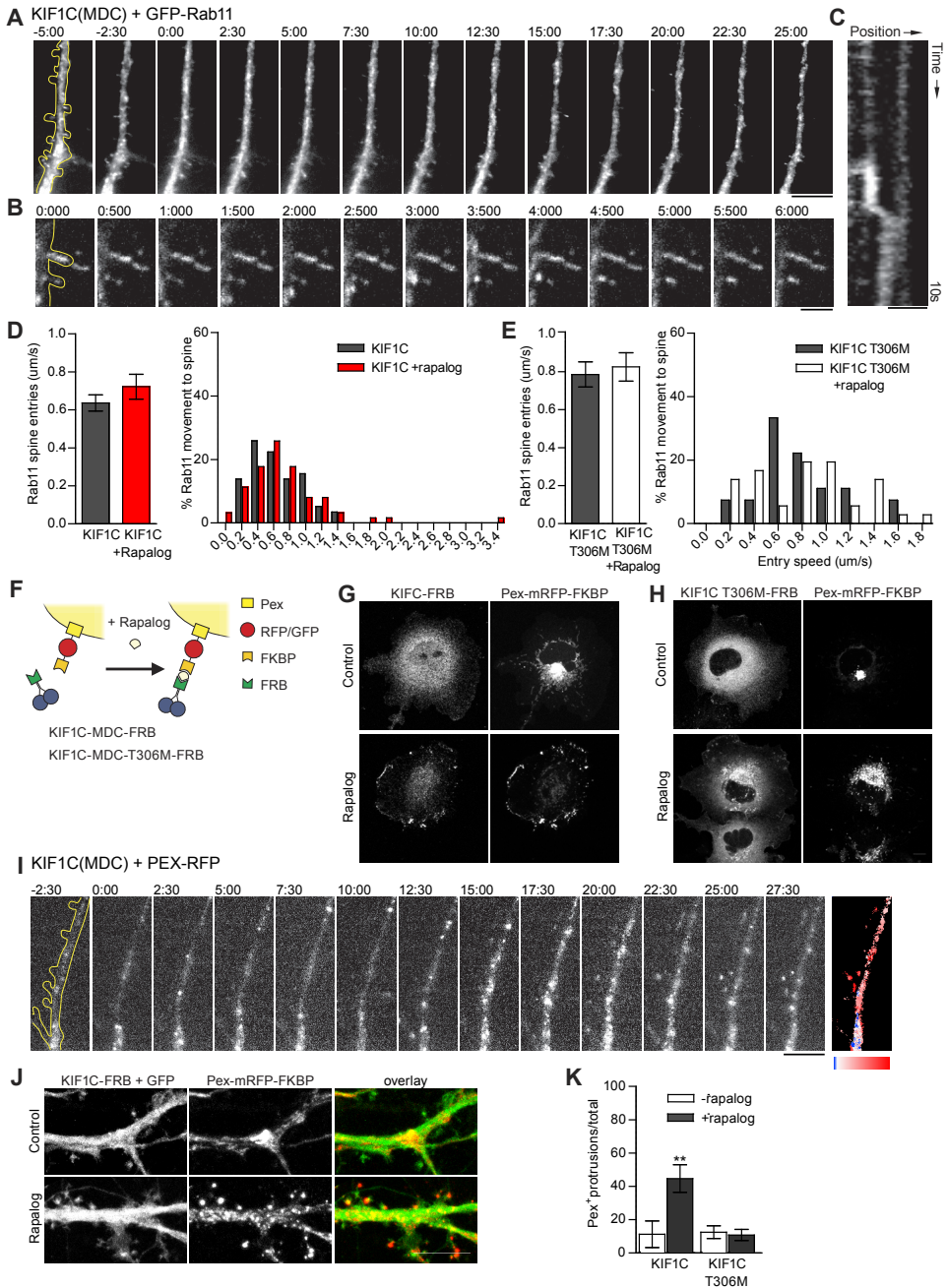


Figure S4 | Chemically-induced recruitment of KIF1C to recycling endosomes promotes their targeting to dendritic spines

A. Stills from a 45 minute time lapse recording. Dimerization of KIF1C to Rab11 endosomes increases their number along the dendritic shaft. Scale bar is 10 μ m. **B.** Occasionally, induced dimerization also promotes the entry of new Rab11 endosomes in dendritic spines. Scale bar is 2 μ m. **C.** Kymograph of the timelapse depicted in B, showing the translocation of the endosome to the dendritic

spines. Scale bar is 1 μm . **D.** Quantification of Rab11-vesicles entry speeds in spines before and after induced recruitment of KIF1C. $n=9$; $N=3$. **E.** Quantification of Rab11-vesicles entry speeds in spines before and after induced recruitment of KIF1C T306M. $n=9$; $N=3$. **F.** Schematic diagram of the inducible recruitment of KIF1 motors to peroxisomes using rapalog-induced heterodimerization of FRB and FKBP. KIF1 motors are coupled to FRB. **G-H.** Recruitment of peroxisomes to KIF1 motors in COS7, shown translocation to the periphery of the cells upon dimerization with KIF1C (G) but not the mutant KIF1C T306M (H). Scale bar is 10 μm . **I.** Dimerization of KIF1C to peroxisomes causes their translocation from the dendritic shaft to spines. Scale bar is 10 μm . **J.** Representative fixed neuron showing recruitment of peroxisomes to spines upon KIF1C recruitment. Scale bar is 10 μm . **K.** Quantification of translocation of peroxisomes to spines upon recruitment to KIF1. Recruitment of KIF1C causes a significant increase in the number of peroxisomes in spines, but the mutant KIF1C T306M. (KIF1C: $n=9$; KIF1C T306M: $n=12$; $N=2$). Graphs show mean \pm SEM. Statistical significance was determined using an unpaired t-test with Mann Whitney correction, ** $p<0.01$ (D-E,K).

SUPPLEMENTAL MOVIES

Supplemental video 1

This video corresponds to Fig.1L. Exocytosis of SEP-tagged GluA1 from a tagRFPT-labelled Rab11-positive recycling endosome in a dendritic spine. White line indicates spine outline. Total time: 80 seconds. Acquisition was performed at 1 second per frame. 20x sped up. (AVI, 1.5MB).

Supplemental video 2

This video corresponds to Fig.2A. GFP-tagged AMPA receptor subunit GluA2 is transported in mRFP-tagged Rab11-positive recycling endosomes. Total time: 60 seconds. Acquisition was performed at 200 milliseconds per frame. 20x sped up. (AVI, 10,5MB).

Supplemental video 3

This video corresponds to Fig.3G. MBD recruitment to GFP-tagged Rab11-positive recycling endosomes upon rapalog application causes relocation of recycling endosomes from dendritic shafts to spines. Total time: 40 minutes. Acquisition was performed at 30 seconds per frame. 20x sped up. (AVI, 0.5 MB).

Supplemental video 4

This video corresponds to Fig.3H. MyosinVI recruitment to GFP-tagged Rab11-positive recycling endosomes upon rapalog application causes translocation of recycling endosomes from spines to the dendritic shafts. Total time: 40 minutes. Acquisition was performed at 30 seconds per frame. 20x sped up. (AVI, 0.4 MB).

SUPPLEMENTAL REFERENCES

1. Jaworski, J., L. C. Kapitein, S. M. Gouveia, B. R. Dortland, P. S. Wulf, I. Grigoriev, P. Camera, S. A. Spangler, P. Di Stefano, J. Demmers, H. Krugers, P. Defilippi, A. Akhmanova, and C. C. Hoogenraad. 2009. Dynamic microtubules regulate dendritic spine morphology and synaptic plasticity. *Neuron* 61:85-100.
2. Brummelkamp, T. R., R. Bernards, and R. Agami. 2002. A system for stable expression of short interfering RNAs in mammalian cells. *Science* 296:550-553.
3. Petrini, E. M., J. Lu, L. Cognet, B. Lounis, M. D. Ehlers, and D. Choquet. 2009. Endocytic trafficking and recycling maintain a pool of mobile surface AMPA receptors required for synaptic potentiation. *Neuron* 63:92-105.
4. Hoogenraad, C. C., A. D. Milstein, I. M. Ethell, M. Henkemeyer, and M. Sheng. 2005. GRIP1 controls dendrite morphogenesis by regulating EphB receptor trafficking. *Nature neuroscience* 8:906-915.

5. Shanks, N. F., T. Maruo, A. N. Farina, M. H. Ellisman, and T. Nakagawa. 2010. Contribution of the global subunit structure and stargazin on the maturation of AMPA receptors. *The Journal of neuroscience : the official journal of the Society for Neuroscience* 30:2728-2740.
6. Yau, K. W., S. F. van Beuningen, I. Cunha-Ferreira, B. M. Cloin, E. Y. van Battum, L. Will, P. Schatzle, R. P. Tas, J. van Krugten, E. A. Katrukha, K. Jiang, P. S. Wulf, M. Mikhaylova, M. Harterink, R. J. Pasterkamp, A. Akhmanova, L. C. Kapitein, and C. C. Hoogenraad. 2014. Microtubule Minus-End Binding Protein CAMSAP2 Controls Axon Specification and Dendrite Development. *Neuron* 82:1058-1073.
7. Hoogenraad, C. C., I. Popa, K. Futai, E. Martinez-Sanchez, P. S. Wulf, T. van Vlijmen, B. R. Dortland, V. Oorschot, R. Govers, M. Monti, A. J. Heck, M. Sheng, J. Klumperman, H. Rehmann, D. Jaarsma, L. C. Kapitein, and P. van der Sluijs. 2010. Neuron specific Rab4 effector GRASP-1 coordinates membrane specialization and maturation of recycling endosomes. *PLoS Biol* 8:e1000283.
8. Schlager, M. A., L. C. Kapitein, I. Grigoriev, G. M. Burzynski, P. S. Wulf, N. Keijzer, E. de Graaff, M. Fukuda, I. T. Shepherd, A. Akhmanova, and C. C. Hoogenraad. 2010. Pericentrosomal targeting of Rab6 secretory vesicles by Bicaudal-D-related protein 1 (BICDR-1) regulates neuritogenesis. *EMBO J* 29:1637-1651.
9. Bravo-Cordero, J. J., R. Marrero-Diaz, D. Megias, L. Genis, A. Garcia-Grande, M. A. Garcia, A. G. Arroyo, and M. C. Montoya. 2007. MT1-MMP proinvasive activity is regulated by a novel Rab8-dependent exocytic pathway. *EMBO J* 26:1499-1510.
10. Nedvetsky, P. I., E. Stefan, S. Frische, K. Santamaria, B. Wiesner, G. Valenti, J. A. Hammer, 3rd, S. Nielsen, J. R. Goldenring, W. Rosenthal, and E. Klussmann. 2007. A Role of myosin Vb and Rab11-FIP2 in the aquaporin-2 shuttle. *Traffic* 8:110-123.
11. Buss, F., S. D. Arden, M. Lindsay, J. P. Luzio, and J. Kendrick-Jones. 2001. Myosin VI isoform localized to clathrin-coated vesicles with a role in clathrin-mediated endocytosis. *EMBO J* 20:3676-3684.
12. Kapitein, L. C., M. A. Schlager, W. A. van der Zwan, P. S. Wulf, N. Keijzer, and C. C. Hoogenraad. 2010. Probing intracellular motor protein activity using an inducible cargo trafficking assay. *Biophysical journal* 99:2143-2152.
13. Schatzle, P., J. Ster, D. Verbich, R. A. McKinney, U. Gerber, P. Sonderegger, and J. M. Mateos. 2011. Rapid and reversible formation of spine head filopodia in response to muscarinic receptor activation in CA1 pyramidal cells. *J Physiol* 589:4353-4364.
14. Lee, J. R., H. Shin, J. Ko, J. Choi, H. Lee, and E. Kim. 2003. Characterization of the movement of the kinesin motor KIF1A in living cultured neurons. *The Journal of biological chemistry* 278:2624-2629.
15. Goslin, K., and G. Banker. 1989. Experimental observations on the development of polarity by hippocampal neurons in culture. *J Cell Biol* 108:1507-1516.
16. Kapitein, L. C., M. A. Schlager, M. Kuijpers, P. S. Wulf, M. van Spronsen, F. C. MacKintosh, and C. C. Hoogenraad. 2010. Mixed microtubules steer dynein-driven cargo transport into dendrites. *Curr Biol* 20:290-299.
17. Kapitein, L. C., P. van Bergeijk, J. Lipka, N. Keijzer, P. S. Wulf, E. A. Katrukha, A. Akhmanova, and C. C. Hoogenraad. 2013. Myosin-V opposes microtubule-based cargo transport and drives directional motility on cortical actin. *Curr Biol* 23:828-834.
18. Cui-Wang, T., C. Hanus, T. Cui, T. Helton, J. Bourne, D. Watson, K. M. Harris, and M. D. Ehlers. 2012. Local zones of endoplasmic reticulum complexity confine cargo in neuronal dendrites. *Cell* 148:309-321.
19. Futai, K., C. D. Doty, B. Baek, J. Ryu, and M. Sheng. 2013. Specific trans-synaptic interaction with inhibitory interneuronal neuroligin underlies differential ability of neuroligins to induce functional inhibitory synapses. *The Journal of neuroscience : the official journal of the Society for Neuroscience* 33:3612-3623.



Optogenetic Control of Organelle Transport and Positioning

Petra van Bergeijk*, **Max Adrian***, Casper C. Hoogenraad and
Lukas C. Kapitein

Cell Biology, Faculty of Science, Utrecht University, 3584 CH Utrecht, The Netherlands.

Nature (2015) 518: 111–114

ABSTRACT

Proper positioning of organelles by cytoskeleton-based motor proteins underlies cellular events such as signaling, polarization, and growth (1–8). For many organelles, however, the precise connection between position and function has remained unclear, because strategies to control intracellular organelle positioning with spatiotemporal precision are lacking. Here, we establish optical control of intracellular transport by using light-sensitive heterodimerization to recruit specific cytoskeletal motor proteins (kinesin, dynein or myosin) to selected cargoes. We demonstrate that the motility of peroxisomes, recycling endosomes and mitochondria can be locally and repeatedly induced or stopped, allowing rapid organelle repositioning. We applied this approach in primary rat hippocampal neurons to test how local positioning of recycling endosomes contributes to axon outgrowth and found that dynein-driven removal of endosomes from axonal growth cones reversibly suppressed axon growth, whereas kinesin-driven endosome enrichment enhanced growth. Our strategy for optogenetic control of organelle positioning will be widely applicable to explore site-specific organelle functions in different model systems.

RESULTS & DISCUSSION

Eukaryotic cells use cytoskeletal motor proteins to control the transport and positioning of proteins, RNAs and organelles (1). In neurons, mitochondria positioning contributes to synapse functioning and axon branching (2,7,8), whereas positioning of Golgi outposts is thought to control dendrite development. Likewise, specific positioning of endosomes has been proposed to contribute to polarization and local outgrowth, either through selective delivery of building blocks or through localized signaling (5,9–12). In many cases, however, directly resolving the role of specific organelle positioning has remained challenging. Disruption of cytoskeletal elements and inhibition of motor proteins or adaptor molecules have been frequently used to alter organelle positioning, but these approaches often lack target selectivity as well as spatial specificity. Therefore, a tool to modulate locally the distribution of specific organelles with spatiotemporal accuracy is required.

Using light-induced heterodimerization to recruit specific motors to selected cargoes might enable spatiotemporal control of intracellular transport, but whether such light-induced interactions can withstand motor-induced forces has remained unclear (13,14). To test this, we first used light-induced binding to couple microtubule-based motors to peroxisomes in monkey COS-7 cells, because these vesicular organelles are largely immobile in the perinuclear region and any movement induced by light-targeted motor proteins could easily be observed (15). Peroxisomes were labelled using PEX-LOV, a fusion between the peroxisomal targeting signal of PEX3 and a photosensitive LOV domain from *Avena sativa* phototropin 1, which cages a small peptide that binds the engineered PDZ domain ePDZb1 after exposure to blue light (14) (Figures 1A and 1B). In addition, ePDZb1 was fused to the plusend-directed kinesin-3 KIF1A to create KIF-PDZ. After co-expression of these two constructs and illumination with blue light, we observed the rapid redistribution of peroxisomes from the centre to the periphery of the cell where most microtubule plusends are located (Figures 1C and 1D). Similarly, light-induced recruitment of minusend-directed dynein using the amino terminus of BICD2 (BICDN) fused to ePDZb1 (BICDN-PDZ) triggered the accumulation of peroxisomes at the centre of the cells (Figures S1A–S1C). Importantly, peroxisome

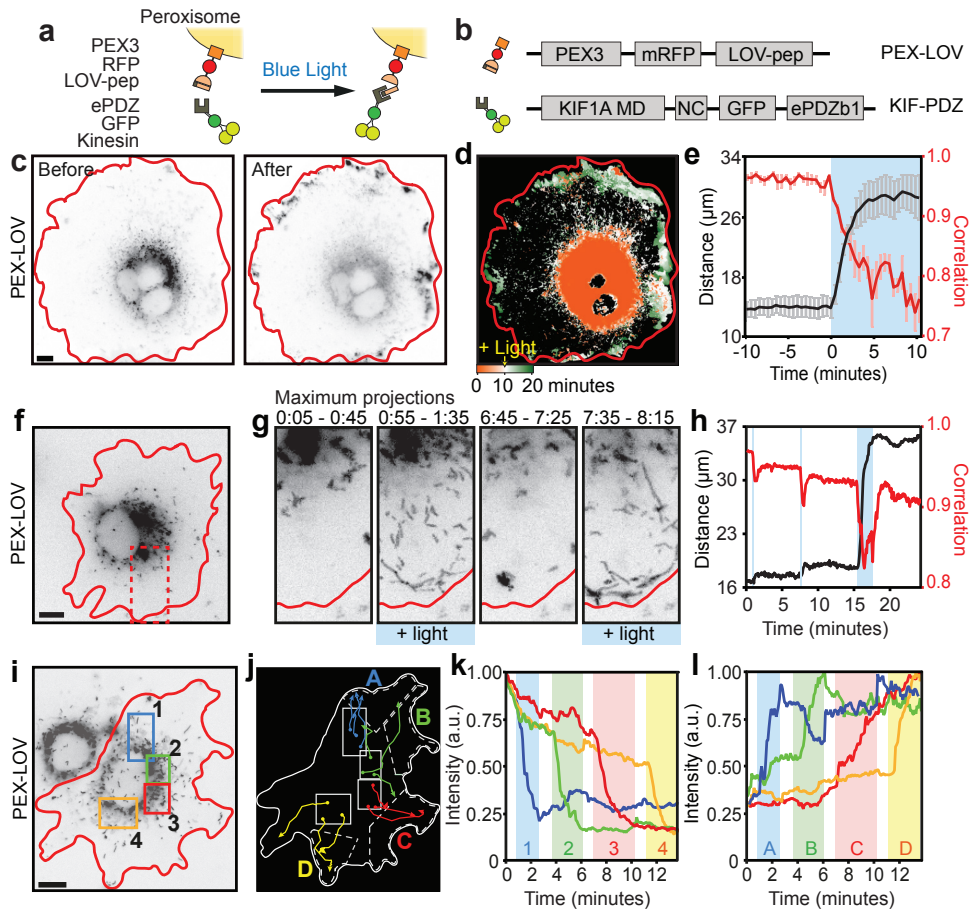


Figure 1 | Local and reversible activation of microtubule-based transport with light.

(A, B) Assay and constructs. MD, motor domain; NC, neck coil. (C) Peroxisome distribution before and after light-induced recruitment of KIF-PDZ. (D) Color-coded overlay of time series. (E) Displacement (black, expressed in $R_{90\%}$) and correlation (frame-to-frame similarity from 0 to 1, red) versus time ($n = 6$ cells, mean \pm SEM). Blue marks illumination. (F, G) Reversible activation using pulsed light. Maximum intensity projections during periods of 40 seconds. (H) Displacement (black, $R_{90\%}$) and correlation (red) versus time. (I-L), Local activation using sequential illumination of four regions I, resulting in outward targeting to adjacent regions (J, showing example trajectories), quantified using normalized fluorescence intensity (K, L, colored boxes mark blue-light illumination). Scale bars, 10 μ m.

redistribution did not alter the spatial organization of mitochondria, the endoplasmic reticulum, or the actin and microtubule cytoskeleton (Figures 2A and 2B).

To quantify peroxisome motility, we first used image correlation analysis to measure the overall frame-to-frame similarity before and after exposure to blue light (16). In the absence of transport, two subsequent images are largely identical and the correlation index will

be close to 1, whereas a value of 0 indicates that all organelles have moved to previously unoccupied positions. After light-induced recruitment of KIF1A, the correlation index rapidly decreased from 0.97 ± 0.01 (mean \pm SEM) to 0.76 ± 0.04 , reflecting the induction of continuous peroxisome motility (Figure 1E). By contrast, dynein recruitment eventually increased the correlation index, because most peroxisomes accumulated at the same position in the centre of the cell (Figures S1C and S1D). To quantify this overall peroxisome repositioning, we calculated for each time point the radius of the circle required to enclose 90% of the fluorescence intensity of the peroxisomes, $R_{90\%}$, and found a large increase from $14 \pm 2 \mu\text{m}$ to $29 \pm 3 \mu\text{m}$ on recruitment of KIF1A (Figure 1E). By contrast, $R_{90\%}$ decreased from $15.4 \pm 0.3 \mu\text{m}$ to $12.8 \pm 0.6 \mu\text{m}$ on recruitment of dynein (Figure S1D). Thus, rapid organelle redistribution can be induced by using light to recruit microtubule motors.

To achieve spatiotemporal control, recruitment of motors should be both reversible and locally restricted. To test the reversibility of motility induction, we exposed cells expressing KIF-PDZ and PEX-LOV to three consecutive periods of blue light, interspersed with ~ 7 minutes without blue-light exposure. Whereas peroxisomes moved outwards during blue-light illumination, movement was arrested within seconds without blue light (Figures 1F and 1G). By contrast, remained stable without stimulation (Figure 1H), indicating that peroxisomes do not spontaneously return to their original position after motor dissociation (Figure S3A). To test whether transport could be induced locally, we sequentially illuminated four different regions within a cell (Figures 1I and 1J). Peroxisomes in the activated region rapidly redistributed to non-exposed areas, whereas non-exposed peroxisomes remained stationary (Figure 1J). The fluorescence intensity in the illuminated boxes 1–4 decreased by 60–75%, coinciding with a 180–280% increase in the adjacent peripheral boxes A–D (Figures 1J–L). These results demonstrate that transport of intracellular cargo can be induced with spatiotemporal precision.

We have previously shown that Myosin-V can oppose kinesin-driven transport in actin-dense regions (16), suggesting that light-induced recruitment of Myosin-V can be used to anchor organelles at specific sites. To test this, Myosin-Vb was recruited to peroxisomes preloaded with the kinesin-2 KIF17 (refs 15, 16) (Figures 2A and 2B). Whereas the attached kinesin motor ensured continuous motility of many peroxisomes near the cell periphery (Figure 2C), this motility was arrested after recruitment of Myosin-Vb, resulting in a 30% increase of the correlation index (Figure 2D). Local illumination increased the correlation index to similar levels, but only in the exposed region (Figures 2C and 2D). Moreover, individual peroxisome trajectories showed on average four times smaller frame-to-frame displacements during illumination compared to before and after stimulation (Figures 2E and 2F). These data demonstrate that organelle motility can be stalled with spatiotemporal precision through light-induced recruitment of Myosin-Vb.

We next used RAB11-positive recycling endosomes to test our method on organelles whose proper physiological functioning depends on selective transport and positioning. Because C-terminal tagging of both LOVpep and RAB11 is incompatible with their function, we developed two alternative strategies to enable light-induced coupling of motor proteins to recycling endosomes. First, Rab11 was cloned behind the photolyase homology region of Cryptochrome-2 (13) (CRY-RAB11). Upon photoexcitation, Cryptochrome-2 binds CIBN, resulting in recruitment of CIBN-tagged motor proteins to RAB11 recycling endosomes

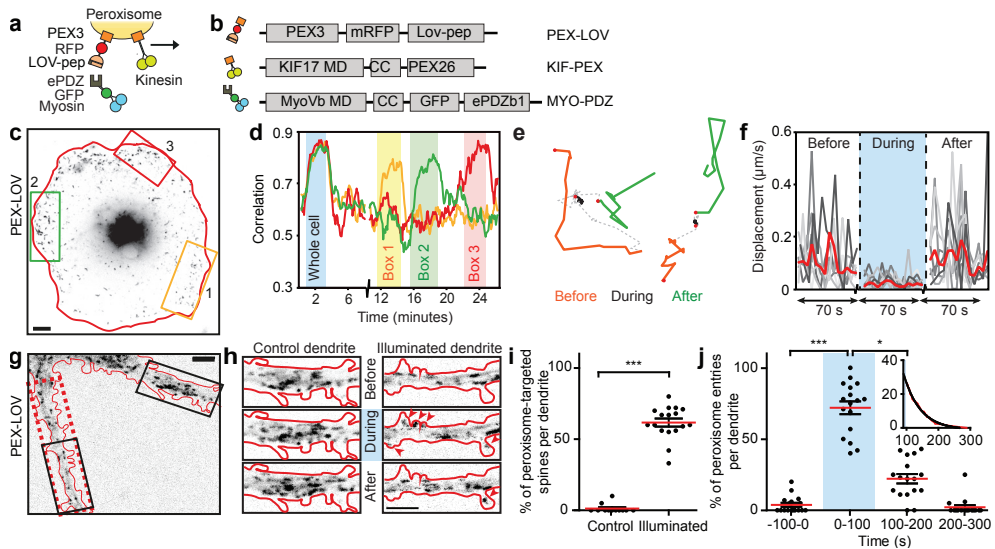


Figure 2 | Light-induced Myosin-Vb recruitment anchors organelles or targets them into dendritic spines.

(A, B) Assay and constructs. CC, coiled-coil. **(C)** Peroxisome distribution in cell expressing PEX-LOV, KIF-PEX and MYO-PDZ. **(D)** Correlation time trace for areas shown in C. **(E)** Peroxisome trajectories with 70-second episodes before, during and after MyosinVb recruitment. **(F)** Frame-to-frame displacements of peroxisomes (5 s interval). Red denotes the average of nine individual peroxisome trajectories. **(G)** Peroxisome distribution in primary hippocampal neuron expressing PEX-LOV and MYO-PDZ. Dashed red rectangle was illuminated. **(H)** Thirty-second maximum projections of regions from G. Arrowheads mark peroxisomes in spines. **(I)** Spine targeting in control ($n = 12$) and illuminated ($n = 17$) dendrites, in three independent experiments. Mean \pm SEM, *** $p < 0.0001$. Mann-Whitney test, **(J)** Spine entries over time. Mean \pm SEM, * $p < 0.05$, *** $p < 0.0001$. Kruskal-Wallis analysis of variance (ANOVA), Dunn's post-hoc test, $n = 17$ dendrites. Inset: entry probability after illumination (red) fitted with exponential decay $\exp(-t/\lambda)$ (black, $\lambda = 36.36$ s). Scale bars, 5 μ m, except C, 10 μ m.

(Figures S4A and S4B). Using these constructs, light-induced binding of KIF1A or BICDN induced an increased flow of recycling endosomes to the cell periphery or center, respectively (Figures S4C-S4G). As an alternative approach, we first used chemically-induced heterodimerization to connect the N-termini of LOVpep and RAB11, followed by light-dependent recruitment of ePDZb1-tagged motor proteins (Figures S4I, S4J and S5). Using this approach, we observed that upon kinesin recruitment recycling endosomes became enriched near the cell periphery during the illumination interval (Figure S3B), without affecting the distribution of lysosomes or early endosomes (Figure S2C). In addition, recruitment of Myosin-Vb was sufficient to stall recycling endosomes both globally and locally (Figures S4K-S4N). Both CRY-RAB11 and FKBP-RAB11 showed similar distributions as endogenous RAB11, transported transferrin receptors and interacted with the known RAB11 effector, RAB11 family interacting protein 1 (RAB11FIP1) (Figure S6). We chose FKBP-RAB11 for all subsequent experiments, because the greater sensitivity of CRY-PEX to blue light (Figure S4H) easily led to activation during sample handling. It should be noted that, because of the weak

interaction between TagBFP and TagRFP, some light-dependent activation could be observed without addition of rapalog (Figure S5A). Moreover, whereas peroxisomes remained largely immobile at their new location after light-dependent repositioning, the original distribution of recycling endosomes was quickly restored after the light-induced kinesin recruitment was stopped (Figure S3). Thus, kinesin- and dynein-based redistribution and Myosin-Vb-based anchoring of recycling endosomes could be transiently induced with light (Figures S2–S4, Figures S5 and S6), demonstrating that the movement of intrinsically dynamic cargoes can be temporarily amplified or overruled by coupling these cargoes to a specific motor using light.

To test our approach in a more complex and delicate model system, we switched to primary cultures of rat hippocampal neurons. Their polarized morphology and specialized cytoskeletal organization in different compartments, such as axons, dendrites and dendritic spines, should allow transporting cargoes into and out of these compartments by recruiting the appropriate motor proteins. We first examined whether light-induced recruitment of Myosin-Vb was sufficient to drive transport into dendritic spines, as proposed previously (17–20). Indeed, in cells co-expressing PEX–LOV and a fusion of Myosin-Vb with ePDZb1 (MYO–PDZ), $62 \pm 3\%$ of the illuminated spines were targeted with peroxisomes compared to $1 \pm 1\%$ of spines in non-illuminated dendrites (Figures 2G–2J). After the illumination period, the number of peroxisome entries decreased with a half-time of ~ 36 s (Figure 2J). Similarly, RAB11 recycling endosomes could be enriched in specific spines by local illumination (Figures S4O–S4Q), demonstrating that light-controlled transport can be used to manipulate individual dendritic spines.

RAB11 vesicles have been implicated in the control of axon growth, but their local role in the growth cone could not be assessed previously (11,12,21). We therefore used local light-induced recruitment of motor proteins to RAB11 recycling endosomes to test how local dynein-driven removal or kinesin-driven addition of endosomes affects growth cone dynamics (Figures 3A and 3D). Importantly, neither illumination nor addition of the heterodimerizer rapalog (used to link the LOV domain to the N terminus of RAB11) altered growth cone structure or behavior in cells expressing FRB–LOV and PDZ only (Figures S5 and S7). Likewise, in control neurons expressing FKBP–RAB11 together with BICDN–PDZ or KIF–PDZ, but lacking the FRB–LOV protein, exposure to blue light did not affect the rapid filopodial and lamellipodial dynamics or the overall growth of most growth cones. (Figures 3B and 3E). When dynein was coupled to RAB11, a clear decrease in growth cone dynamics and growth was observed (Figures 3C, 3G and S8). By contrast, coupling of kinesin resulted in rapid axon extension in $39 \pm 7\%$ of the growth cones (Figures 3F and 3H). Importantly, when growth cones were not completely collapsed upon dynein-dependent RAB11 depletion, this depletion and the reduced growth cone dynamics could be reversed when cells were no longer exposed to blue light (Figures 3I and 3J). These data demonstrate that growth cone dynamics and axon growth directly depend on RAB11 vesicle functioning near the growth cone, rather than on general RAB11 functions elsewhere in the cell.

Recently, the controlled anchoring and mobilization of mitochondria have emerged as key regulatory events in neurons (8,22–24). Mitochondrial positioning depends on both motor-dependent transport and controlled immobilization by specific docking factors, but the molecular and mechanical interplay between motors and docking factors has remained unclear (22,24). For example, syntaphilin (SNPH) has been proposed to induce anchoring by

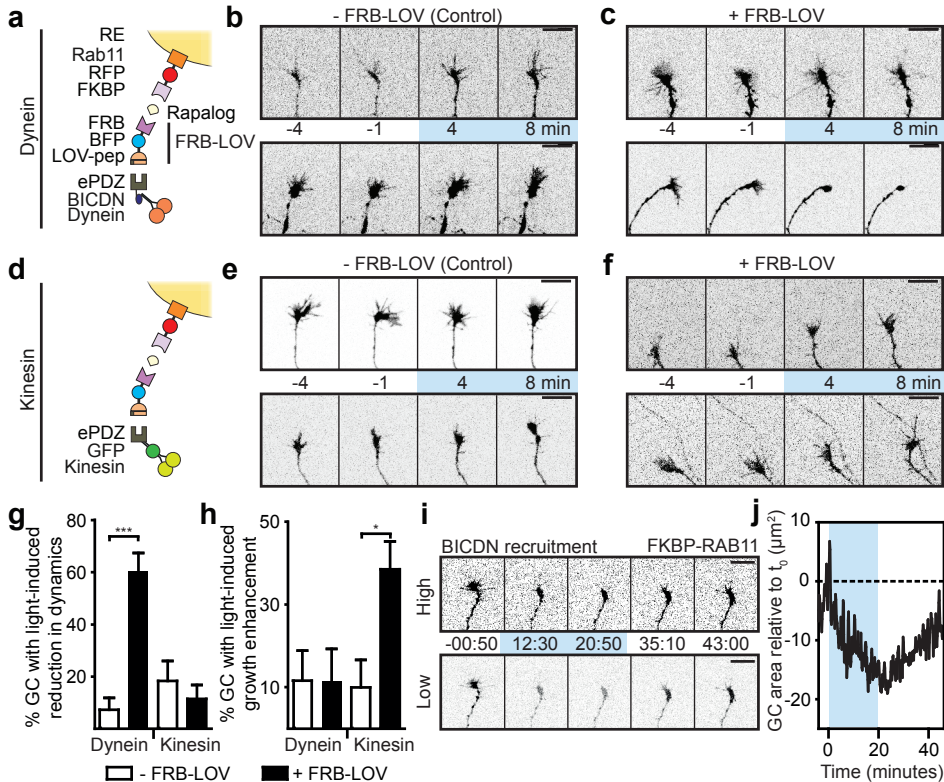


Figure 3 | Motor-based redistribution of recycling endosomes modulates axon outgrowth.

(A, D) Assay and constructs. Rapalog targets FRB–LOV to the Rab11 Nterminus. (B, C, E, F) Growth cone dynamics of neurons expressing FKBP–RAB11 and BICDN–PDZ (B, C) or KIF–PDZ (E, F) without (B, E) or with (C, F) FRB–LOV. (G, H) Light-induced reduction of growth cone dynamics (G) or light-induced growth enhancement (H). Dynein/Kinesin: –FRB–LOV: $n = 21/19$ axons, +FRB–LOV: $n = 25/35$ axons, derived from $n = 5/5$ independent experiments. Mean \pm SEM, * $p < 0.05$, *** $p < 0.0001$, unpaired two-tailed t -test. (I) Same growth cone in low and high contrast illustrating reversibility of reduced FKBP–RAB11 targeting and growth cone dynamics. (J) Area over time for the example shown in I. Scale bars, 10 μm .

crosslinking mitochondria to microtubules and through a direct inactivating interaction with kinesin (25,26), but whether remobilization requires the regulated release of both interactions is not known (23). To test whether recruitment of more motors can overcome anchoring, we used light to recruit KIF–PDZ to axonal mitochondria labelled with TOM–LOV (Figures 4A and 4B) and found that this was sufficient to mobilize most mitochondria in the illuminated region (Figures 4C–4G). Conversely, light-induced recruitment of the N-terminal part of SNPH was sufficient to acutely anchor motile mitochondria, independent of their directionality (Figures 4H–4I). These results demonstrate that regulation of mitochondrial motility and anchoring does not require all-or-nothing switching between the activation and inactivation of specific motors, but instead depends on the balance of forces between active motors and passive anchors. We have established optically-controlled intracellular transport

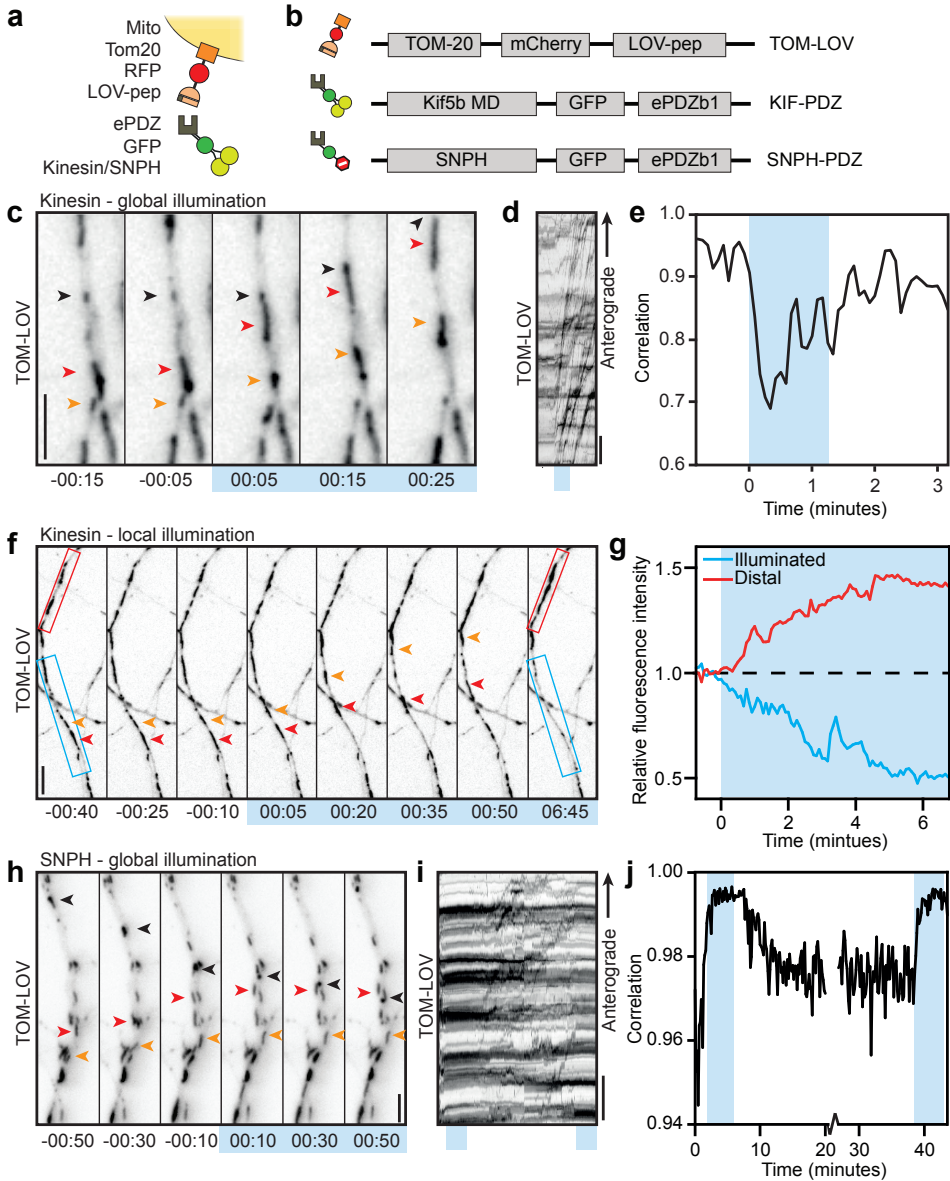


Figure 4 | Altering mitochondrial dynamics through recruitment of motors and anchors.

(A, B) Assay and constructs. (C) Axonal mitochondria before and during KIFPDZ recruitment. Arrowheads track individual mitochondria. (D) Kymograph for axon shown in C, representative for $n = 6$ axons. Blue box marks activation (1 min:15 s). (E) Correlation over time for region shown in C. (F) Axonal mitochondria before and during local illumination (blue box). (G) Relative fluorescence intensity versus time in the illuminated (blue box in F) and the adjacent, distal region (red box in F). (H) Axonal mitochondria before and during SNPH recruitment. Arrowheads track individual mitochondria. (I) Kymograph for axon shown in H, representative for $n = 5$ axons. Blue boxes mark activation (4 min:50 s). (J) Correlation versus time. Scale bars, 5 μ m, except D and I, 10 μ m.

by using light-sensitive heterodimerization to recruit specific cytoskeletal motor proteins to selected cargoes. Our ability to control organelle positioning complements recent work that established optogenetic control over nucleocytoplasmic distribution of proteins (27). We anticipate that this approach will be widely applicable to study how organelle positioning controls cellular functioning, as demonstrated here for the role of recycling endosomes in growth cone dynamics. In addition, it could be used to control cellular processes such as polarization, signaling and outgrowth by depleting or accumulating cargo at specific sites. For example, increased axonal targeting of certain cargoes might promote axon regeneration after injury and provide novel insights into the mechanisms contributing to regeneration failure or success, both in culture and in different animal models (28).

ACKNOWLEDGEMENTS

We are grateful to C. Tucker, T. Inoue, Z.-H. Sheng, G. Banker, R. Prekeris, P. Schätzle and M. Esteves da Silva for sharing reagents and to C. Wierenga and A. Akhmanova for discussions. This research is supported by the Dutch Technology Foundation STW and the Foundation for Fundamental Research on Matter (FOM), which are part of the Netherlands Organisation for Scientific Research (NWO). Additional support came from NWO (NWO-ALW-VICI to C.C.H and NWO-ALWVIDI to L.C.K.) and the European Research Council (ERC starting grant to L.C.K.).

AUTHOR CONTRIBUTIONS

L.C.K. and C.C.H. initiated research. P.B. created reagents. M.A., P.B., C.C.H. and L.C.K. designed experiments. M.A. and P.B. performed experiments. M.A., P.B. and L.C.K. analysed data. M.A., P.B., C.C.H. and L.C.K. wrote the manuscript.

REFERENCES

1. Vale, R. D. (2003) The molecular motor toolbox for intracellular transport. *Cell* 112, 467-480
2. Sheng, Z. H. and Cai, Q. (2012) Mitochondrial transport in neurons: impact on synaptic homeostasis and neurodegeneration. *Nat Rev Neurosci* 13, 77-93
3. Korolchuk, V. I. *et al.* (2011) Lysosomal positioning coordinates cellular nutrient responses. *Nat Cell Biol* 13, 453-460
4. Yadav, S. and Linstedt, A. D. (2011) Golgi positioning. *Cold Spring Harbor perspectives in biology* 3
5. Sadowski, L. *et al.* (2009) Signaling from endosomes: location makes a difference. *Exp Cell Res* 315, 1601-1609
6. Ori-McKenney, K. M. *et al.* (2012) Golgi outposts shape dendrite morphology by functioning as sites of acentrosomal microtubule nucleation in neurons. *Neuron* 76, 921-930.
7. Spillane, M. *et al.* (2013) Mitochondria coordinate sites of axon branching through localized intra-axonal protein synthesis. *Cell reports* 5, 1564-1575
8. Courchet, J. *et al.* (2013) Terminal axon branching is regulated by the LKB1/NUAK1 kinase pathway via presynaptic mitochondrial capture. *Cell* 153, 1510-1525
9. Golachowska, M. R. *et al.* (2010) Recycling endosomes in apical plasma membrane domain formation and epithelial cell polarity. *Trends Cell Biol* 20, 618-626.
10. Higuchi, Y. *et al.* (2014) Early endosome motility spatially organizes polysome distribution. *J Cell Biol* 204, 343-357
11. Eva, R. *et al.* (2012) ARF6 Directs Axon Transport and Traffic of Integrins and Regulates Axon Growth in Adult

- DRG Neurons. *J Neurosci* 32, 1035210364
12. Eva, R. *et al.* (2010) Rab11 and its effector Rab coupling protein contribute to the trafficking of beta 1 integrins during axon growth in adult dorsal root ganglion neurons and PC12 cells. *J Neurosci* 30, 11654-11669
 13. Kennedy, M. J. *et al.* (2010) Rapid blue-light-mediated induction of protein interactions in living cells. *Nat Methods* 7, 973-975
 14. Strickland, D. *et al.* (2012) TULIPs: tunable, light-controlled interacting protein tags for cell biology. *Nat Methods* 9, 379-384
 15. Kapitein, L. C. *et al.* (2010) Probing intracellular motor protein activity using an inducible cargo trafficking assay. *Biophys J* 99, 2143-2152
 16. Kapitein, L. C. *et al.* (2013) Myosin-V opposes microtubule-based cargo transport and drives directional motility on cortical actin. *Curr Biol* 23, 828834
 17. Correia, S. S. *et al.* (2008) Motor protein-dependent transport of AMPA receptors into spines during long-term potentiation. *Nat Neurosci* 11, 457-466
 18. Wagner, W. *et al.* (2011) Myosin-Va transports the endoplasmic reticulum into the dendritic spines of Purkinje neurons. *Nat Cell Biol* 13, 40-48
 19. Wang, Z. *et al.* (2008) Myosin Vb mobilizes recycling endosomes and AMPA receptors for postsynaptic plasticity. *Cell* 135, 535-548
 20. Hammer, J. A., 3rd and Wagner, W. (2013) Functions of class V myosins in neurons. *J Biol Chem* 288, 28428-28434
 21. Bhui, T. and Roy, J. K. (2009) Rab11 is required for embryonic nervous system development in Drosophila. *Cell and tissue research* 335, 349-356
 22. Encalada, S. E. and Goldstein, L. S. (2014) Biophysical challenges to axonal transport: motor-cargo deficiencies and neurodegeneration. *Annual review of biophysics* 43, 141-169
 23. Sheng, Z. H. (2014) Mitochondrial trafficking and anchoring in neurons: New insight and implications. *J Cell Biol* 204, 1087-1098
 24. Sun, T. *et al.* (2013) Motile axonal mitochondria contribute to the variability of presynaptic strength. *Cell reports* 4, 413-419
 25. Chen, Y. and Sheng, Z. H. (2013) Kinesin-1-syntaphilin coupling mediates activity-dependent regulation of axonal mitochondrial transport. *J Cell Biol* 202, 351-364
 26. Kang, J. S. *et al.* (2008) Docking of axonal mitochondria by syntaphilin controls their mobility and affects short-term facilitation. *Cell* 132, 137-148
 27. Niopek, D. *et al.* (2014) Engineering light-inducible nuclear localization signals for precise spatiotemporal control of protein dynamics in living cells. *Nature communications* 5, 4404
 28. Bradke, F. *et al.* (2012) Assembly of a new growth cone after axotomy: the precursor to axon regeneration. *Nat Rev Neurosci* 13, 183-193

SUPPLEMENTAL EXPERIMENTAL PROCEDURES

DNA Constructs

The following constructs have been described: TagRFPT (29) (Gift from R. Tsien), pCIBN(deltaNLS)-pmGFP and pCry2PHR-mCherryN1 (13) (addgene, plasmids #26867 and #26866), Mid(SS/TM)-GFP-LOVpep and ePDZb1-mCherry (14) (addgene, plasmids #34972 and #34981), TOM20-mCherry-GAI (30) (Gift from T. Inoue), HA-Rab11a (31), Kif1a(1-489)-GFP-FRB, kif5b(1-807)-GFP-FRB, MyoVb(1-1090)-GFP-FRB, HA-BicD2(1-594)-FRB and Pex3(1-42)-mRFP (15), pGW2-Pex26 and pGW2-Kif17-GFP-Pex26 (16), GFP-SNPH

(26) (Gift from Z. Sheng), GFP-RCP (32) (Rab11FIP1, gift from R. Prekeris), NPY-GFP (33) and GFPMACF18 (34).

Cloning vectors and fluorescent tags.

The constructs used in this study were cloned in the mammalian expression vectors pGW1-CMV, pGW2-CMV and/or p β actin (15). p β actin-GFP, p β actin-TagRFPt, p β actin-TagBFP and p β actin-iRFP were generated by ligating the fluorescent proteins in the Sall and SpeI site of p β actin.

Tagging motor proteins, adaptors and anchors with CIBN and ePDZb1.

To generate myoVb(1–1090)-GFP-CIBN and myoVb(1–1090)-GFP-ePDZb1, amino acids 1–1090 of myosinVb were cloned in the AscI and EcoRI sites of p β actin-GFP, and either CIBN or ePDZb1 was inserted downstream of GFP using a PCR-based strategy. Similarly, myoVb-iRFP-CIBN was made using the p β actin-iRFP vector backbone. Kif1a(1–383)-GFP-CIBN and Kif1a(1–383)-GFP-ePDZb1 were generated by ligating amino acids 1–383 of mouse KIF1A in the AscI and Sall sites of p β actinGFP. Subsequently, PCR amplified CIBN or ePDZb1 was inserted downstream of GFP. Haemagglutinin (HA)-tagged-BicD2(1–500)-CIBN and BicD2(1–500)-ePDZ were cloned by inserting PCR amplified BicD2(1–500) (referred to as BICDN in the main text) into the p β actin vector backbone. Subsequently, CIBN and ePDZb1 were ligated downstream of BicDN. Kif5b(1–807)-GFP-ePDZb1 was made by inserting PCR amplified kif5b(1–807) into the AscI and BamHI sites of a GFP-ePDZb1 backbone. To create SNPH(45–748)-GFP-ePDZb1, PCR amplified SNPH (forward primer: 5'-agcgctaagcttgccaccatggccatgtccctgcagggaag-3' and reverse primer: 5'gcccttgctcaccatagtcgaccctaccacagccagcagatccac-3') was inserted into a GFP-ePDZb1 backbone using Cold Fusion cloning (System Biosciences).

Tagging peroxisomes, RAB11 vesicles and mitochondria with LOVpep and CRY2PHR.

To generate Pex3-mRFP-LOVpep (PEX-LOV), LOVpep, including a 9-amino-acid linker (GGSGGSGGS), was ligated in the AscI and Sall sites of pGW1Pex3-mRFP. To make TOM20-mCherry-LOVpep, Pex3-mRFP was replaced by TOM20(1–34)-mCherry using the HindIII and AscI sites. To create Cry2PHRtagRFPt-Rab11 and FKBP-tagRFPt-Rab11, Rab11a was introduced in the SpeI and NotI sites of P β actin-tagRFPt. Subsequently, PCR amplified FKBP or Cry2PHR was ligated upstream of tagRFPt. FRB-TagBFP-LOVpep was made by inserting LOVpep, including a 9-amino-acid linker, in the SpeI and NotI sites of p β actin-TagBFP. Subsequently, PCR-amplified FRB was cloned upstream of tagBFP.

Other constructs

pJPA5-TfR-GFP (a gift from Gary Banker) was cloned into β -actin vector. Membrane targeting of GFP was achieved by inserting the 40 most N-terminal residues of the MARCKS protein with an additional palmitoylation site at residue 3 (35) into GW2TagRFPt. To generate mRFP-actin, human cytoplasmic β -actin was cloned from pEGFP-actin (Clontech) in β -actin-mRFP vector

Cell Cultures and Transfection

COS-7 cells were cultured in DMEM/Ham's F10 (1:1) medium containing 10% FCS and 1% penicillin/streptomycin. Then, 2–4 days before transfection, cells were plated on 24-

mm diameter coverslips. Cells were transfected with Fugene6 transfection reagent (Roche) according to the manufacturers protocol and imaged one day after transfection. anchors.

Primary hippocampal cultures were prepared from embryonic day 18 (E18) rat brains (36). Cells were plated on coverslips coated with poly-L-lysine (30 mg ml⁻¹) and laminin (2 mg mml⁻¹) at a density of 75,000 per well. Hippocampal cultures were grown in Neurobasal medium (NB) supplemented with B27, 0.5 mM glutamine, 12.5 mM glutamate, and penicillin plus streptomycin. Hippocampal neurons were transfected 48 h before imaging with Lipofectamine 2000 (Invitrogen). DNA (3.6 µg per well) was mixed with 6.6µl Lipofectamine 2000 in 400 ml NB, incubated for 30 min, and then added to the neurons in NB supplemented with 0.5 mM glutamine at 37°C in 5% CO₂ for 60 min. Next, neurons were washed with NB and transferred to the original medium at 37°C in 5% CO₂ for 2 days. Transport assays targeting dendritic spines were imaged at day-in-vitro (DIV) 20-22 and growth cone or mitochondria assays were imaged at DIV 3-7.

Live Cell Image Acquisition

Time-lapse live-cell imaging of COS-7 cells and hippocampal neurons was performed on a Nikon Eclipse TE2000E (Nikon) equipped with an incubation chamber (Tokai Hit; INUG2-ZILCS-H2) mounted on a motorized stage (Prior) (16). Coverslips (24 mm) were mounted in metal rings, immersed in 0.6 ml Ringer's solution (10 mM Hepes, 155 mM NaCl, 5mM KCl, 1 mM CaCl₂, 1 mM MgCl₂, 2 mM NaH₂PO₄ and 10 mM glucose, pH 7.4) or full medium (RAB11 imaging in COS-7 cells) or conditioned medium (Neuron imaging), and maintained at 37°C and 5% CO₂. Cells were imaged every 5, 10 or 30 seconds for 5-50 minutes using a 40x objective (Plan Fluor, numerical aperture (NA) 1.3, Nikon) and a Coolsnap HQ2 CCD camera (Photometrics). Dense-core vesicles were imaged using a 100x objective (Apo TIRF, 1.49 NA, Nikon) on a Evolve 512 EMCCD camera (Photometrics). A mercury lamp (Osram) and filter wheel containing ET-GFP (49002), ET-DSRed (49005), ET-mCherry (49008) and ET-GFPmCherry (59022) emission filters (all Chroma) were used for excitation and for global activation. For global activation, the GFP excitation filter was used to illuminate the sample for 100-150 ms with every image acquisition during the periods of blue-light exposure. In most experiments, the activation intensity was around 10 W cm⁻² and the total irradiance was about 30 times higher than the minimum irradiance required for full activation (Figure S4H). These settings allowed us to monitor the dynamics of GFP-labeled proteins or growth cones during activation.

For local illumination of specific areas using a 488-nm laser line, a FRAP scanning head was used (FRAP L5 D-CURIE, Curie Institute). Compared to standard FRAP experiments the laser was used at much lower intensities.

Live-cell spinning disk confocal microscopy of growth cones and spines of hippocampal neurons was performed on a Nikon Eclipse-Ti (Nikon) microscope with a Plan Apo VC, 60x, 1.40 NA oil objective (Nikon). The microscope is equipped with a motorized stage (ASI; PZ-2000), a Perfect Focus System (Nikon), an incubation chamber (Tokai Hit; INUG2-ZILCS-H2) and uses MetaMorph 7.7.11 software (Molecular Devices) to control the camera and all motorized parts. Confocal excitation and detection is achieved using 100mW Vortran Stradus 405 nm, 100 mW Cobolt Calypso 491 nm and 100mW Cobolt Jive 561nm lasers and a

Yokogawa spinning disk confocal scanning unit (CSU-X1-A1N-E; Roper Scientific) equipped with a triple-band dichroic mirror (z405/488/568trans-pc; Chroma) and a filter wheel (CSUX1-FW-06P-01; Roper Scientific) containing 4',6-diamidino-2-phenylindole (DAPI; ET-DAPI (49000)), GFP (ET-GFP (49002)) and mCherry (ET-mCherry (49008)) emission filter (all Chroma). Confocal images were acquired with a QuantEM:512 SC EMCCD camera (Photometrics) at a final magnification of 110 nm per pixel, including the additional 2.5× magnification introduced by an additional lens mounted between scanning unit and camera (VM Lens C-2.5X; Nikon). Local activation of photo-heterodimerization was achieved with an ILas FRAP system (Roper Scientific France/ PICT-IBiSA, Institut Curie) and 491nm laser line at low power. To couple FRB-LOV to FKBP-RAB11, rapalog (AP21967) was dissolved to 0.1 mM in ethanol. Then, 20 minutes prior imaging, 0.2 ml of culture medium with rapalog (400 nM) was added to establish a final rapalog concentration of 100 nM.

Image Processing and Analysis

Images of live cells were processed and analyzed using MetaMorph (Molecular Devices), LabVIEW (National Instruments) software and ImageJ (NIH). If not followed by a quantification in a subsequent panel, representative images are representative of 60-90% of the cells studied in the same conditions, with at least five responding cells per condition (except for Figure S4F with three responding cells, because we used the system in Figures S4I and S4J for all subsequent experiments). The exact organelle distributions and dynamics mostly depended on the levels of protein overexpression, which could not be examined before the experiment without triggering heterodimerization. For example, if the motor were poorly expressed, less redistribution was observed. This was most apparent in experiments where three or more constructs were co-expressed, some of which without fluorescent marker that could be used to confirm expression of the motor.

Quantification of redistribution dynamics

Before analysis, cells were masked to exclude contributions from neighboring cells to the analysis. For the color-coded redistribution plots, all images of a time-lapse recording were thresholded at ~5-20 times the standard deviation of the background above the background to yield binary images that were subsequently overlaid nontransparently starting with the final frame (first frame on top) in Figure 1D, and starting with the first frame (last frame on top) in Figure S4D. Each frame was colored using a time-coded gradient that ran from orange to white before and from white to green after blue-light illumination. To quantify the radial redistribution of peroxisomes upon recruitment of (additional) motor proteins, the radius required to include 90% of the total intensity of the cell, $R_{90\%}(t)$, was calculated for each frame as described previously (15).

To quantify changes in the dynamics of peroxisomes or RAB11 vesicles upon recruitment of (additional) motor proteins, we calculated the time-dependent frame-to-frame correlation index $c_r(t)$ (16) by first calculating the integrated intensity of the image obtained by multiplying the frames acquired at t and $t + \Delta t$, that is,

$$\sum_{x=1}^X \sum_{y=1}^Y i(x, y, t) i(x, y, t + \Delta t)$$

in which $i(x,y,t)$ is the intensity at pixel (x,y) of the frame acquired at time t . These values can then be normalized using either the integrated

of the image acquired at t or $t + \Delta t$, i.e.

$$\sum_{x=1}^X \sum_{y=1}^Y i^2(x, y, t)$$

or

$$\sum_{x=1}^X \sum_{y=1}^Y i^2(x, y, t + \Delta t)$$

For our analysis, we used the average result of these two normalizations as our readout, that is,

$$c_{\tau}(t) = \frac{1}{2} \left(\frac{\sum_{x=1}^X \sum_{y=1}^Y i(x, y, t) i(x, y, t + \tau)}{\sum_{x=1}^X \sum_{y=1}^Y i^2(x, y, t)} + \frac{\sum_{x=1}^X \sum_{y=1}^Y i(x, y, t) i(x, y, t + \tau)}{\sum_{x=1}^X \sum_{y=1}^Y i^2(x, y, t + \tau)} \right)$$

$c_{\tau}(t)$ will be 1 if the particles are completely anchored and their positions unchanged after a time τ , whereas $c_{\tau}(t)$ will be 0 if all particles moved to previously unoccupied locations. In practice, $c_{\tau}(t)$ will remain finite even in very dynamic samples, because a subset of particles will move to locations that were occupied by different particles in the first image. In all our analyses, we used frame-to-frame differences. For analyzing the correlation index in small regions (Figures 2D and S4I), measurements were averaged over six adjacent time points.

To determine local changes in fluorescence intensities over time (Figures 1IL), the mean gray value of the first-frame-subtracted recording (Figure 1L), or last-frame-subtracted recording (Figure 1K) was measured, and the maximum was set to 1. Individual peroxisomes or RAB11 vesicle trajectories were obtained using the MTrackJ plugin in ImageJ (37).

Analysis of spine entries

Peroxisomes and RAB11 vesicles were imaged at 1-s intervals, preferably in two dendrites of the same neuron, of which one was illuminated with pulses of 491 nm light directly before the frames indicated. Spine entries during periods of 100 s before, 100 s during and 200 s after illumination were detected manually using the Cell Counter plugin in ImageJ to determine the fraction of cargo-targeted spines and the frame of spine entry. The mean percentage of spines targeted with peroxisomes was compared with a Mann-Whitney test (Figure 2I) and the mean percentages of peroxisome and endosome entries were subjected to a Kruskal-Wallis ANOVA with Dunn's post-hoc test (Figure 2J) or a one-way ANOVA with Bonferroni's post-hoc test (Figure S4P), respectively. The half-time of peroxisome entries into dendritic spines after illumination was estimated by fitting a single exponential function ($R^2 = 0.9942$) through the inverted cumulative histogram of the observed entry events after 491 nm illumination was stopped.

Analysis of axon growth and growth cone area

Axonal growth was manually tracked using the MTrackJ plugin in ImageJ (37). The percentages of growth cones exhibiting light-induced reduction in dynamics or growth enhancements were compared using unpaired two-tailed t-tests (Figures 3G and 3H). In all our experiments, only the RFP channel was available for imaging without triggering photo-heterodimerization before, during and after exposure to blue light. We used this channel to image FKBP-tagRFPt-RAB11 to verify that light-controlled recruitment of BICDN induced the removal of RAB11 endosomes (Figures S8A and S8B). FKBP-RAB11 was enriched at vesicles-like structures, whose dynamics altered upon light-dependent recruitment of BICDN to recruit dynein. In addition, FKBP-RAB11 diffusely filled the axon, which could be used to determine axon morphology and size with precision comparable to a cytoplasmic GFP fill (Figure S8C). We counted the positive pixels in a binarized image obtained by thresholding the median-filtered tagRFPt image, followed by two erosions and closure (38). Because tagRFPt fluorescence of this construct showed a threefold increase in intensity upon 491 nm excitation (Figure S8A), we established a dynamic threshold T that scaled with the maximum intensity of the object, that is, $T = I_{bg} + \sigma_{bg} + 0.02 (I_{max})$, in which I_{bg} and σ_{bg} are the average and standard deviation of the intensity in an area outside the axon, respectively, and I_{max} is the average of the top 2% intensity values above $I_{bg} + \sigma_{bg}$. Using these parameters, changes in area are independent of the changes in intensity upon exposure to blue light or due to dynein-mediated removal of RAB11 vesicles (Figures S8D and S8E).

Relative decreases in growth cone RAB11-FKBP signal were calculated by rescaling all intensity values normalized initially to $t_{-2,30min}$ to the average intensity value of -FRB-LOV control growth cones at t_{8min} (Figure S8A). To calculate changes in growth cone area before blue-light illumination, we compared single growth cone area values averaged over three frames at t_{0min} and t_{-4min} relative to illumination onset (Figure S8G and S8H). Analogously, comparing values at t_{8min} and t_{0min} shows net growth during blue-light illumination (Figures S8I and S8J). All of these results were compared using Mann-Whitney tests (Figures S8B, S8G and S8I). All statistical testing was performed in GraphPad Prism 5 software. No statistical method was used to predetermine sample size.

Immunofluorescence cell stainings, imaging and used antibodies

COS-7 cells (1 day after transfection) or primary hippocampal neurons (2 days after transfection) were either kept in the dark or illuminated for 10 minutes using a blue light-emitting diode mounted in the incubator. Afterwards, cells were fixed at room temperature for 10 minutes with 4% Paraformaldehyde (PFA), 4% sucrose. For detection of EB1, cells were fixed for 5 minutes at -20°C in 100% ice-cold methanol supplemented with 1mM EGTA, followed by 5 minutes post-fixation at room temperature in 4%PFA, 4% sucrose. After fixation, cells were washed three times in PBS and incubated overnight at 4°C in GDB buffer (0.1% BSA, 450 mM NaCl, 0.3% Triton X-100, 16.7 mM phosphate buffer, pH 7.4) containing the primary antibody. The next day, cells were washed three times for 10 minutes in PBS, followed by a 1 hour incubation at room temperature with the secondary antibody in GDB buffer. After washing cells three times 10 minutes in PBS, slides were mounted in Vectashield mounting medium (Vector Laboratories). Images were taken with a Nikon eclipse 80i upright fluorescence microscope and a Coolsnap HQ2 CCD camera (Photometrics), using a 40x oil

objective (Plan Fluor, NA 1.3), 60x oil objective (Plan Apo VC, NA 1.4) or 100x oil objective (Plan Apo VC, NA 1.4).

Antibodies and reagents used: mouse anti-Cytochrome c (6H2.B4, 556432, BD Biosciences), mouse anti-PDI (RL90, MA3-019, affinity BioReagents), Phalloidin-Alexa647 (A22287, Invitrogen), mouse anti-Alpha Tubulin (B-5-1-2, T5168, Sigma), mouse anti-EB1 (610535, BD transduction), mouse anti-Lamp1 (This antibody developed by J.T. August and J.E.K Hildreth, was obtained from the hybridoma bank, created by the NICHD of the NIH and maintained at The University of Iowa, Department of Biology, Iowa City, IA52242), mouse anti-EEA1 (BD transduction), rabbit anti-Rab11 (71-5300, Invitrogen), rabbit anti-Homer-1 (160-002, SySy), Alexa 488-, Alexa 568-, Alexa 647-conjugated secondary antibodies (Invitrogen).

GFP Pull Down and Western Blotting

HEK cells were cultured in DMEM/Ham's F10 (1:1) medium containing 10% FCS and 1% penicillin/streptomycin. Then 1 day after plating, HEK293T cells were transfected using Polyethylenimine (PEI; Polysciences). After 24 hours, GFP beads (GFP-Trap_M, Chromotek) were washed in washing buffer (TBS, 0.5% Triton-X-100 and protease Inhibitor) and incubated for 1 hour in blocking buffer (TBS, 0.5% Triton-X-100, 2% glycerol, 2% chicken egg white). Meanwhile, cells were collected in ice-cold TBS, pelleted and lysed in extraction buffer (TBS 0.5% Triton-X-100, 1x protease inhibitor, phosphatase inhibitor (Roche), 100 μ M GTP γ S, 5mM MgCl₂, pH8.0). Cell lysates were centrifuged for 15 minutes at 4°C at 12.000g, followed by a 1.5-hour incubation of the supernatants with the washed GFP beads, while rotating at 4°C. Beads were collected using a magnetic separator and washed four times. Samples were eluted in SDS sample buffer, boiled for 5 minutes and loaded onto SDS-PAGE gels and blotted on PVDF membranes (Millipore). Blots were blocked in 5% milk in PBST (0.1% Tween in PBS) and incubated overnight at 4°C (primary antibody) or for 1 hour at room temperature (secondary antibody conjugated to horseradish peroxidase) in PBST. Finally, blots were developed using enhanced chemiluminescent Western blotting substrate (Pierce).

Antibodies used: rabbit anti-TagRFPt (ab234, Evrogen), rabbit anti-GFP (ab290, abcam) and anti-rabbit IgG antibody conjugated to horseradish peroxidase (DAKO).

SUPPLEMENTAL REFERENCES

29. Shaner, N. C. et al. (2008) Improving the photostability of bright monomeric orange and red fluorescent proteins. *Nat Methods* 5, 545-551
30. Miyamoto, T. et al. (2012) Rapid and orthogonal logic gating with a gibberellin-induced dimerization system. *Nat Chem Biol* 8, 465-470
31. Hoogenraad, C. C. et al. (2010) Neuron specific Rab4 effector GRASP-1 coordinates membrane specialization and maturation of recycling endosomes. *PLoS Biol* 8, e1000283
32. Peden, A. A. et al. (2004) The RCP-Rab11 complex regulates endocytic protein sorting. *Mol Biol Cell* 15, 3530-3541
33. Schlager, M. A. et al. (2010) Pericentrosomal targeting of Rab6 secretory vesicles by Bicaudal-D-related protein 1 (BICDR-1) regulates neuritogenesis. *EMBO J* 29, 1637-1651
34. Honnappa, S. et al. (2009) An EB1-binding motif acts as a microtubule tip localization signal. *Cell* 138, 366-376

35. De Paola, V. et al. (2003) AMPA receptors regulate dynamic equilibrium of presynaptic terminals in mature hippocampal networks. *Nat Neurosci* 6, 491-500
36. Kapitein, L. C. et al. (2010) Microtubule dynamics in dendritic spines. *Methods Cell Biol* 97, 111-132
37. Meijering, E. et al. (2012) Methods for cell and particle tracking. *Methods in enzymology* 504, 183-200
38. Russ, J. C. (2007) *The image processing handbook*. 5th edn, (CRC/Taylor and Francis)

SUPPLEMENTAL FIGURES

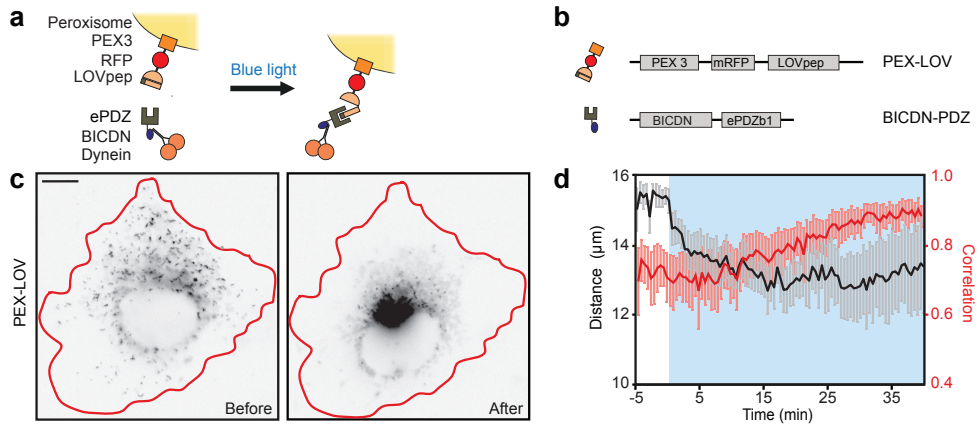
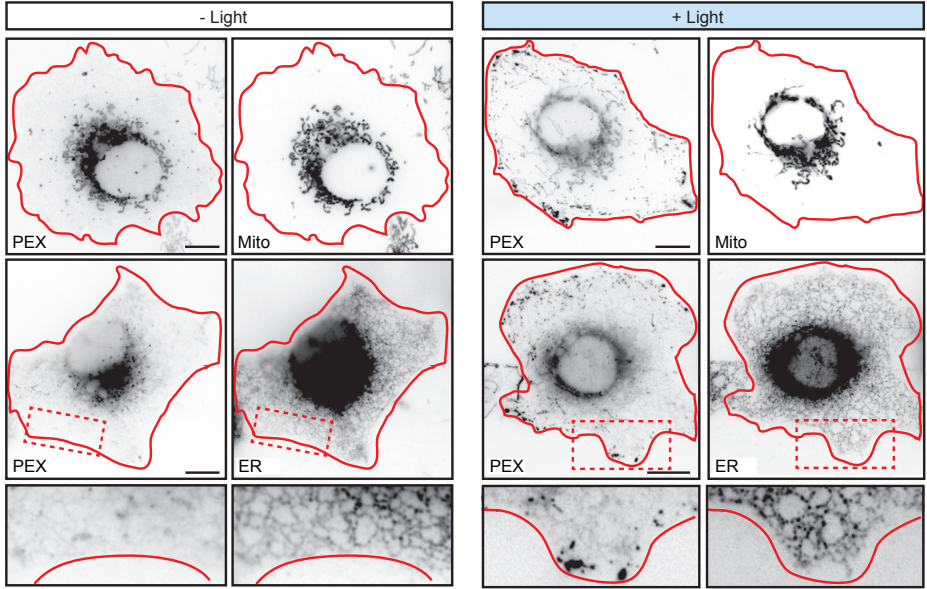


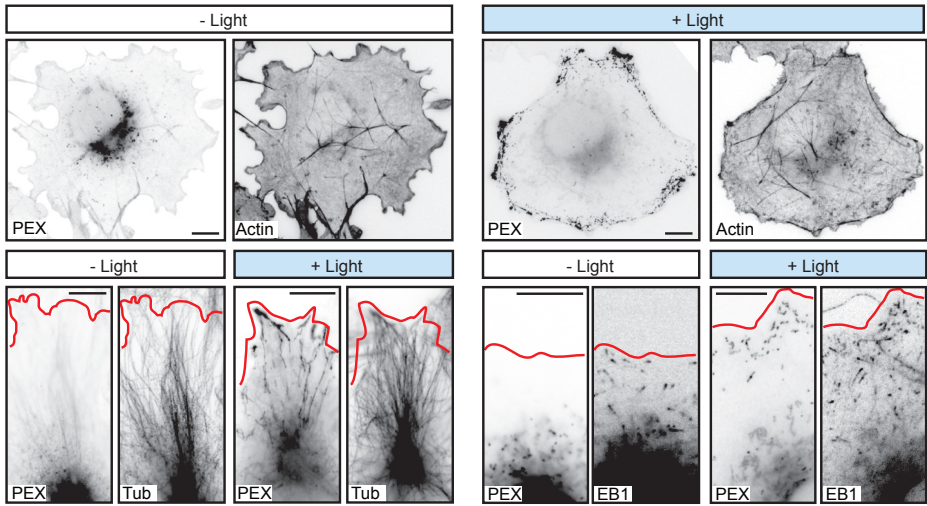
Figure S1 | Optical control of dynein-based cargo motility

(A, B) Assay and constructs. A fusion construct of PEX3, monomeric red fluorescent protein (mRFP) and LOVpep (PEX-LOV) targets peroxisomes. After blue-light illumination, a fusion of the N-terminus of the dynein adaptor BICD2 and ePDZb1 (BICDN-PDZ) is recruited to peroxisomes. **(C)** Peroxisome distribution in a COS-7 cell expressing PEX-LOV and BICDN-PDZ before and during light-induced recruitment of dynein (inverted contrast). Red lines indicate cell outline. Scale bar, 10 μ m. **(D)** Black: Time trace of the $R_{90\%}$ (radius of circle enclosing 90% of cellular fluorescence; see Experimental Procedures) in cells expressing PEX-LOV and BICDN-PDZ ($n = 5$ cells). Red: correlation index (frame-to-frame differences in the peroxisome recordings; see Experimental Procedures) of the same cells. Blue-light illumination is indicated in blue; mean \pm SEM.

a



b



c

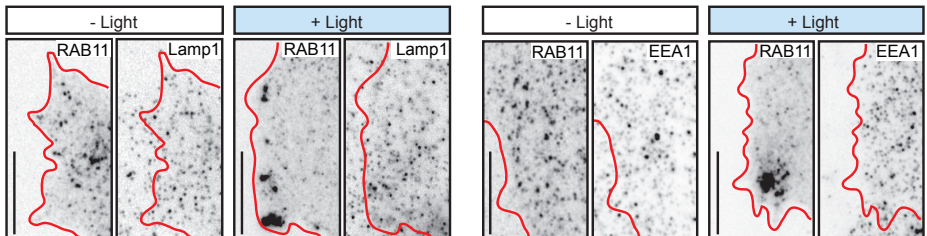


Figure S2 | Light-induced organelle redistribution is organelle-specific and does not affect the cytoskeleton.

(A) Images of fixed cells expressing PEX-LOV and KIF-PDZ, showing the distribution of peroxisomes and mitochondria (anti-cytochrome-c), or peroxisomes and the endoplasmic reticulum (anti-protein disulfide isomerase (PDI)) in the absence (left) or presence (right) of blue light. **(B)** Images of fixed cells expressing PEX-LOV and KIF-PDZ, showing the distribution of peroxisomes and phalloidin, α -tubulin or EB1 staining in the absence or presence of blue light. **(C)** Images of fixed cells expressing FKBP-RAB11, FRB-LOV and KIF-PDZ, showing the distribution of RAB11 recycling endosomes together with lysosomes (anti-Lamp1) or early endosomes (anti-EEA1) in the absence or presence of blue light. Red lines indicate cell outline. Scale bars, 10 μ m.

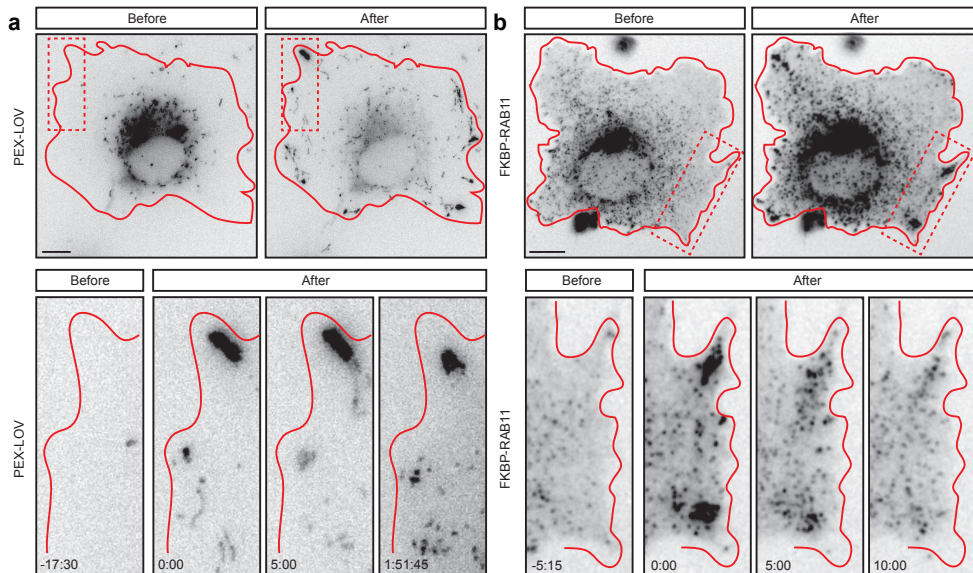


Figure S3 | After light-induced organelle displacement, peroxisomes remain at their newly obtained position whereas the distribution of recycling endosomes quickly reverses back to normal.

(A) Peroxisome distribution before and after exposure to blue light in cells expressing PEX-LOV and KIF-PDZ. Blue-light illumination was terminated at $t_{0:00}$. **(B)** Distribution of RAB11 recycling endosomes before and after exposure to blue light in cells expressing FKBP-RAB11, FRB-LOV and KIF-PDZ. Blue light was turned off at $t_{0:00}$. Red lines indicate cell outline. Scale bars, 10 μ m.

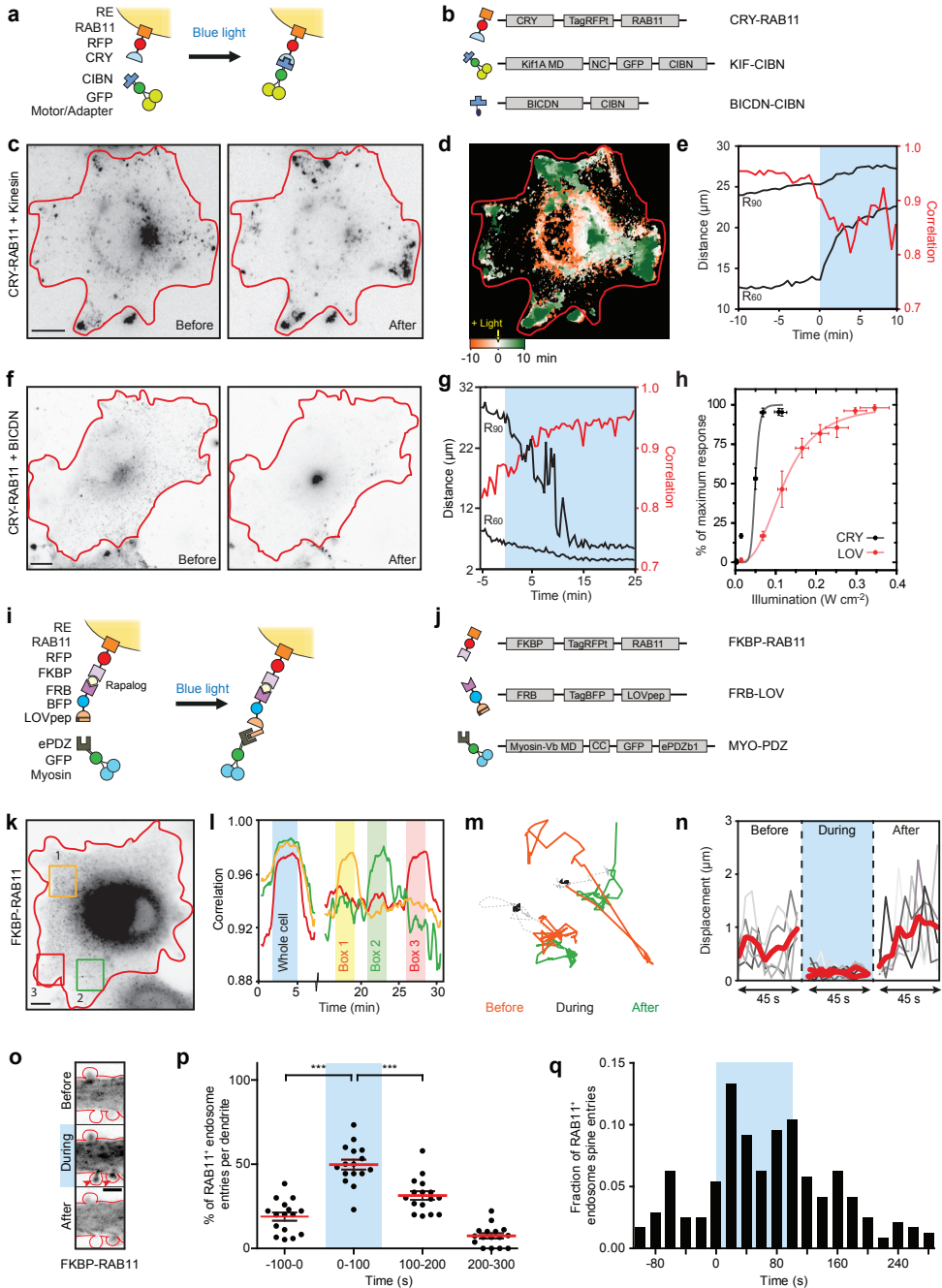


Figure S4 | Spatiotemporal control of recycling endosome distribution and dynamics.

(A, B) Assay and constructs: A fusion construct of CRY2PHR, tagRFpT and RAB11, (CRY-RAB11) targets RAB11 recycling endosomes. After blue-light illumination, a fusion of truncated KIF1A, GFP and CIBN (KIF-CIBN) or a fusion of truncated BICDN, GFP and CIBN (BICDN-CIBN) is recruited to RAB11 recycling endosomes. (C) RAB11 vesicle distribution before and after light-induced recruitment of

KIF1A (inverted contrast). Red lines indicate cell outline. Scale bar, 10 μ m. **(D)** Overlay of sequential binarized images from the recording in C, color-coded by time as indicated. Orange marks the initial distribution of RAB11 vesicles, whereas green marks regions targeted after exposure to blue light. **(E)** Time trace of the $R_{60\%}$ and $R_{90\%}$ (black) and the correlation index (red) of the cell shown in C and D. Blue box marks blue-light illumination. **(F)** RAB11 distribution in a cell expressing CRY-RAB11, and BICDN-CIBN before and after blue-light illumination (inverted contrast). Red lines indicate cell outline. Scale bar, 10 μ m. **(G)** Time trace of the $R_{60\%}$ and $R_{90\%}$ (black) and correlation index for the cell shown in F. **(H)** Irradiance response curve for cells transfected with CRY-PEX and KIF-CIBN (red), or PEX-LOV plus KIF-PDZ (black). To exclude activation failure due to poorly expressed motors, the number of cells reacting at each concentration was divided by the number of cells responding to subsequent high irradiance ($\sim 1.3 \text{ W cm}^{-2}$). Three biological replicates. Cells per intensity (for increasing intensities): 28, 21, 22, 20, 24, 22 and 20 for CRY, 30, 28, 33, 31, 28, 33, 33, 32 and 26 for LOV. Error bars depict SEM; three biological replicates. Solid line shows fit to

$$R = \frac{100 \cdot I^n}{(I_0^n + I^n)}$$

with R the response, I the illumination intensity, I_0 the intensity at which the response is 50%, and n the Hill coefficient. For CRY-PEX and PEX-LOV, I_0 is 0.05 and 0.12 W cm^{-2} , respectively. **(I, J)**, Assay and constructs: A fusion construct of FKBP, tagRFpT and RAB11, (FKBP-RAB11) targets RAB11 recycling endosomes. Rapalog addition couples FKBP to FRB, leading to recruitment of the FRB, tagBFP and LOVpep fusion protein (FRB-LOV). Upon blue-light illumination a fusion of truncated Myosin-Vb, GFP and ePDZb1 (MYO-PDZ) is recruited to RAB11 vesicles. **(K)** RAB11 distribution in a cell expressing FKBP-RAB11, FRB-LOV, and MYO-PDZ before sequential blue-light illumination of the regions marked with numbered boxes (inverted contrast). Scale bar is 10 μ m. **(L)** Time traces of the correlation index in the areas shown in K. Blue box marks whole-cell exposure to blue light, whereas colored boxes indicate local illumination. **(M)** Example trajectories of two RAB11 recycling endosomes before, during and after recruitment of Myosin-Vb, as indicated. Data was acquired with 1 s intervals. For each period 40 seconds are shown. **(N)** Frame-to-frame displacements of RAB11 recycling endosomes before, during and after light-induced recruitment of Myosin-Vb (5 s interval). Thick lines show the average of five tracks in shades of gray. **(O)** FKBP-RAB11 distribution (inverted contrast) in a dendrite and dendritic spines before, during and after blue-light illumination. Images are maximum projections spanning 60 s. Red lines indicate cell outline, arrowheads mark spines targeted with recycling endosomes during blue-light illumination. Scale bar, 2 μ m. **(P)** Percentage of recycling endosome spine entry events per dendrite before, during and after illumination in bins of 100 s. Blue box indicates blue-light illuminated interval, $n = 16$ dendrites in three independent experiments. Red bar denotes mean \pm SEM, *** $p < 0.0001$, one-way ANOVA, Bonferroni's post-hoc test. **(Q)** Histogram of fraction of all ($n = 237$) recycling endosome spine entries in bins of 20 s. Blue box indicate blue-light illuminated interval.

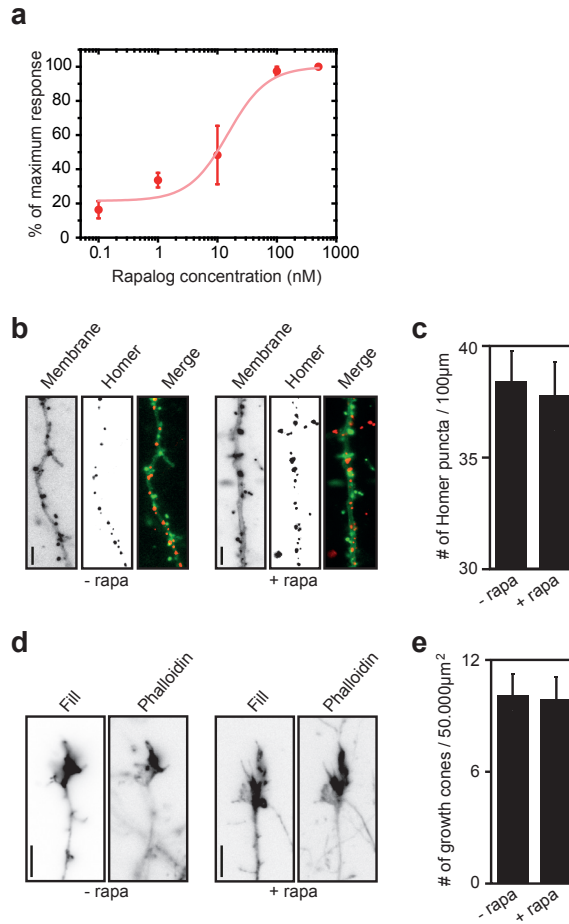


Figure S5 | Rapalogs in the nanomolar range is sufficient to recruit FRB–LOV to FKBP–RAB11 and does not affect the number of spines or growth cones in hippocampal neurons.

(A) Response curve of RAB11 recycling endosome relocalization in cells expressing FKBP–RAB11, FRB–LOV, and KIF–PDZ exposed to blue light in relation to rapalog concentration. To exclude activation failure due to poorly expressed motors, the number of cells reacting at each concentration was divided by the number of cells responding to subsequent high rapalog concentration (1 μM). Solid line shows fit to $R = (R_{\min} I_0^n + 100 I^n) / (I_0^n + I^n)$, with R the response, c the rapalog concentration, c_0 the concentration at which the response is 50%, n the Hill coefficient, and R_{\min} the response at 0 mM rapalog. R_{\min} is 22% and c_0 is 15 nM. $n = 30$ (0.1 nM), 37 (1 nM), 30 (10 nM), 28 (100 nM) and 28 (500 nM) responsive cells from three independent experiments. Error bars depict SEM. **(B)** Hippocampal neurons transfected with membrane-GFP incubated for 2.5 h in the presence or absence of 100 nM rapalog, co-stained with the post-synaptic marker Homer. **(C)** Quantification of the number of Homer puncta per 100 μm dendrite length in the presence or absence of 100 nM rapalog. ($n = 13$ neurons per condition). Error bars depict SEM. **(D)** Hippocampal neurons transfected with GFP incubated for 2.5 h in the presence or absence of 100 nM rapalog, co-stained with phalloidin. **(E)** Quantification of the number of growth cones per 50,000 μm² in the presence or absence of 100 nM rapalog, co-stained with phalloidin. $n = 19$. Scale bars, 5 μm. Error bars depict SEM.

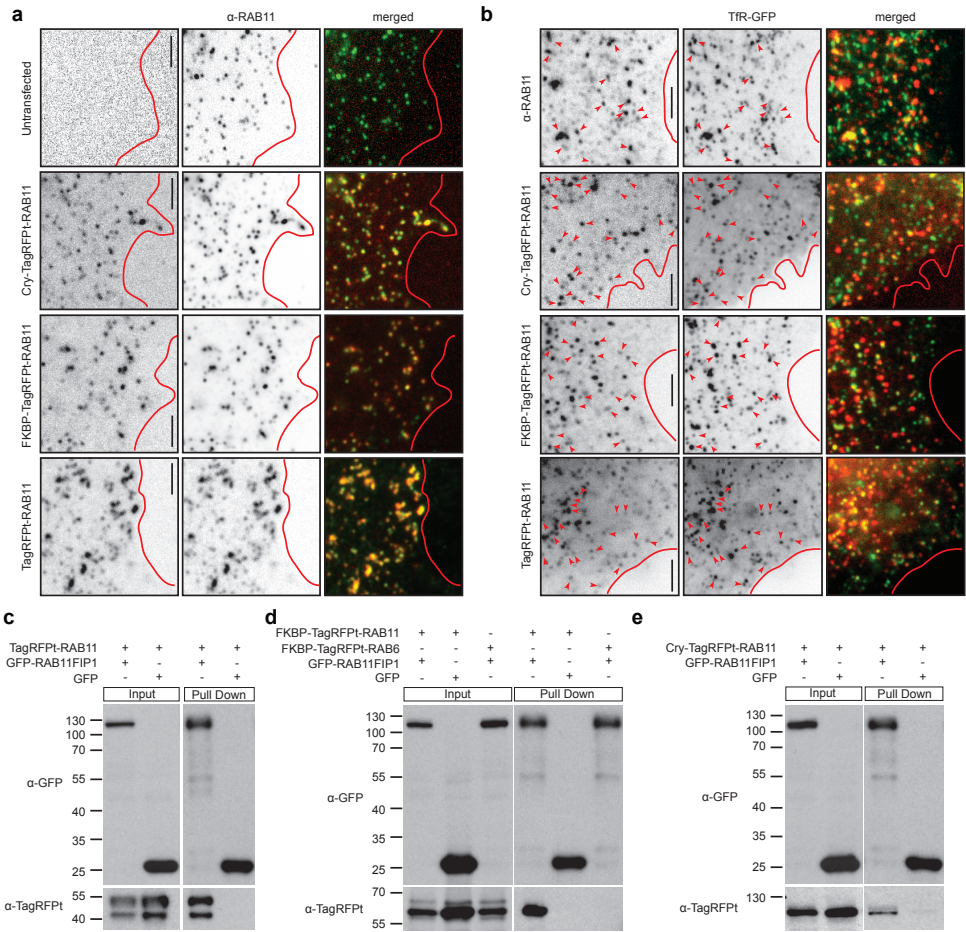


Figure S6 | RAB11 fusion constructs are recognized by the RAB11 antibody, partially co-localize with transferrin receptors and interact with Rab11FIP1.

(A) Images of untransfected cells or cells transfected with CRY-RAB11, FKBP-RAB11 or TagRFpL-RAB11, co-stained with anti-RAB11 antibody (Inverted contrast). Red lines indicate cell outline. Scale bar, 2.5 μ m. **(B)** Images of cells transfected with TfR-GFP only, or co-transfected with CRY-RAB11, FKBP-RAB11 or TagRFpL-RAB11 (Inverted contrast). Red lines indicate cell outline. Scale bar, 2.5 μ m. **(C-E)** GFP pull-down assays with lysates of HEK cells expressing GFP or GFP-RAB11FIP1 together with TagRFpL-RAB11 (C), FKBP-RAB11 or FKBP-TagRFpL-RAB6 (D) or CRY-RAB11 (E) were analyzed by Western blotting using antibodies against TagRFpL and GFP.

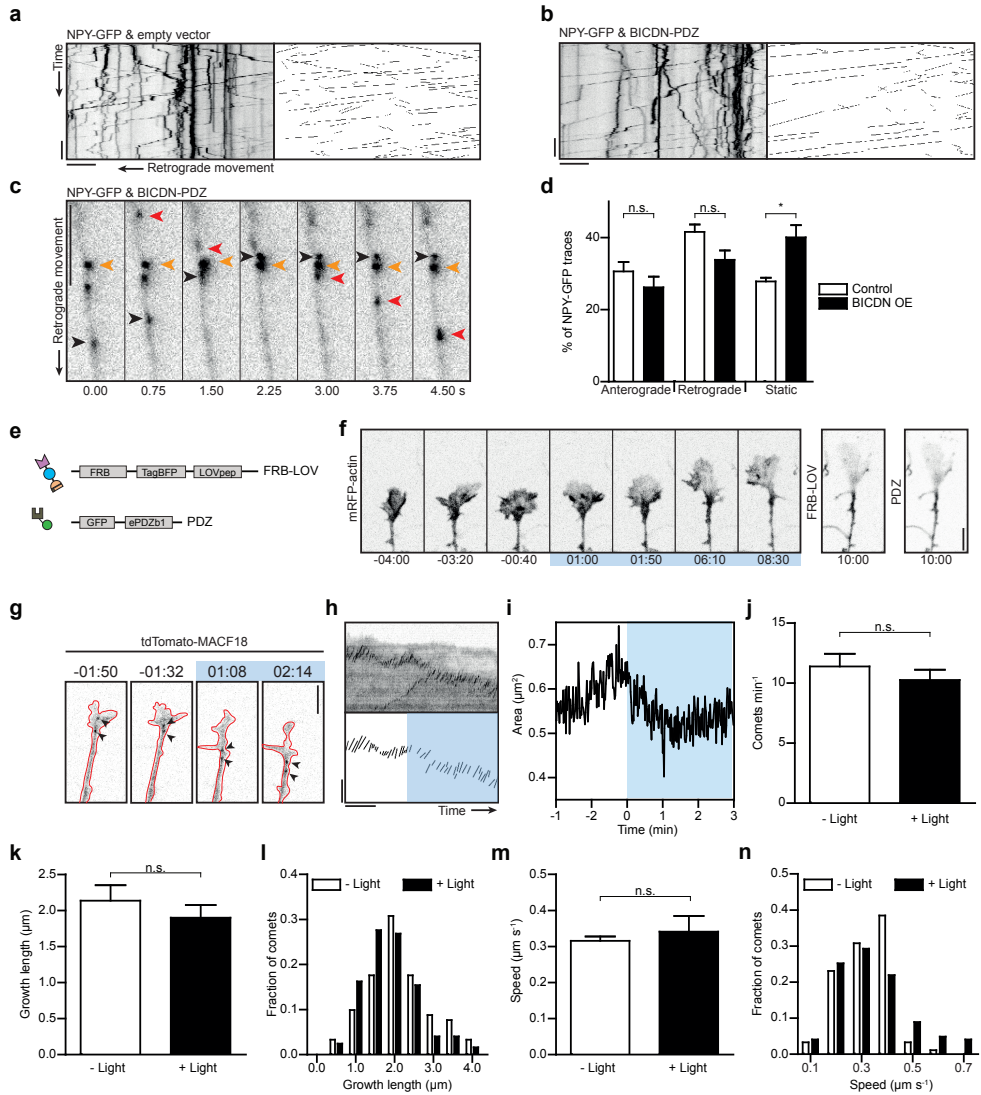


Figure S7 | BICDN overexpression does not significantly inhibit dynein-based transport and the growth cone cytoskeleton is not affected by light-induced recruitment of BICDN to recycling endosomes.

(A, B) Left: kymograph of dense-core vesicles motility in an axon expressing neuropeptide Y (NPY) fused to GFP (NPY-GFP) and empty vector (A) or BICDN-PDZ (B) (inverted contrast), representative of $n = 5$ and $n = 10$ axons, respectively. Right: corresponding binary image of traces used for further analysis of anterograde and retrograde movements. Scale bars, 5 μm and 10 s. (C) Position of dense-core vesicles along an axon expressing NPY-GFP and BICDN-PDZ. Single colored arrowheads point to the same vesicle, highlighting retrograde (red), anterograde (black) and non-moving (orange) vesicles. Scale bar, 5 μm. (D) Quantification of the percentage of static, anterograde and retrograde moving vesicles from kymographs shown in A and B in axons with ($n = 10$) or without ($n = 5$) BICDN-PDZ overexpression. Graph shows mean ± SEM, * $p < 0.05$, one-way ANOVA and Bonferroni's multiple comparison test. (E) A fusion of FRB, tagBFP and LOVpep (FRB-LOV) and a fusion of GFP and ePDZb1

(PDZ) were expressed in neurons. After blue-light illumination, LOVpep undergoes a conformational change, allowing binding of PDZ to FRB-LOV. **(F)** Actin dynamics in growth cones co-expressing mRFP-actin along with the constructs shown in E, in response to light-induced heterodimerization of FRB-LOV and PDZ, representative of $n = 5$ growth cones. The blue box indicates the interval of blue-light illumination. Scale bar, $5\mu\text{m}$. **(G)** Imaging of microtubule (MT) plus-ends using tdTomato-MACF18 shows the dynamics of microtubule plus-ends in growth cones before and during blue-light illumination in neurons co-expressing FKBP-RAB11, FRB-LOV and BICDN-PDZ. Red line indicates cell outline, arrowheads point at plus-ends. Scale bar, $5\mu\text{m}$. **(H)** Kymograph of MACF18 comets of the growth cone shown in G and binarized traces used for analysis, representative of $n = 4$ growth cones. Blue box indicates blue-light illumination interval. Scale bars, $5\mu\text{m}$ and 1 min. **(I)** Area measurement of growth cone shown in G before and during blue-light illumination. **(J)** Quantification of the number of MACF18 comets per minute in growth cones before and during blue-light illumination ($n = 4$ neurons). Graph shows mean \pm SEM. Paired two-tailed t -test, $n = 4$ cells. **(K)** Quantification of the growth length of MACF18 comets in growth cones before and during blue-light illumination ($n = 4$ neurons). Graph shows mean \pm SEM. Paired two-tailed t -test, $n = 4$ cells. **(L)** Distribution of fraction of MACF18 comets per growth length in bins of $0.5\mu\text{m}$ ($n = 214$ traces). **(M)** Quantification of the growth speed of MACF18 comets in growth cones before and during blue-light illumination ($n = 4$ neurons). Graph shows mean \pm SEM. Paired two-tailed t -test, $n = 4$ cells. **(N)** Distribution of fraction of MACF18 comets per growth speed in bins of $0.1\mu\text{m s}^{-1}$ ($n = 214$ traces).

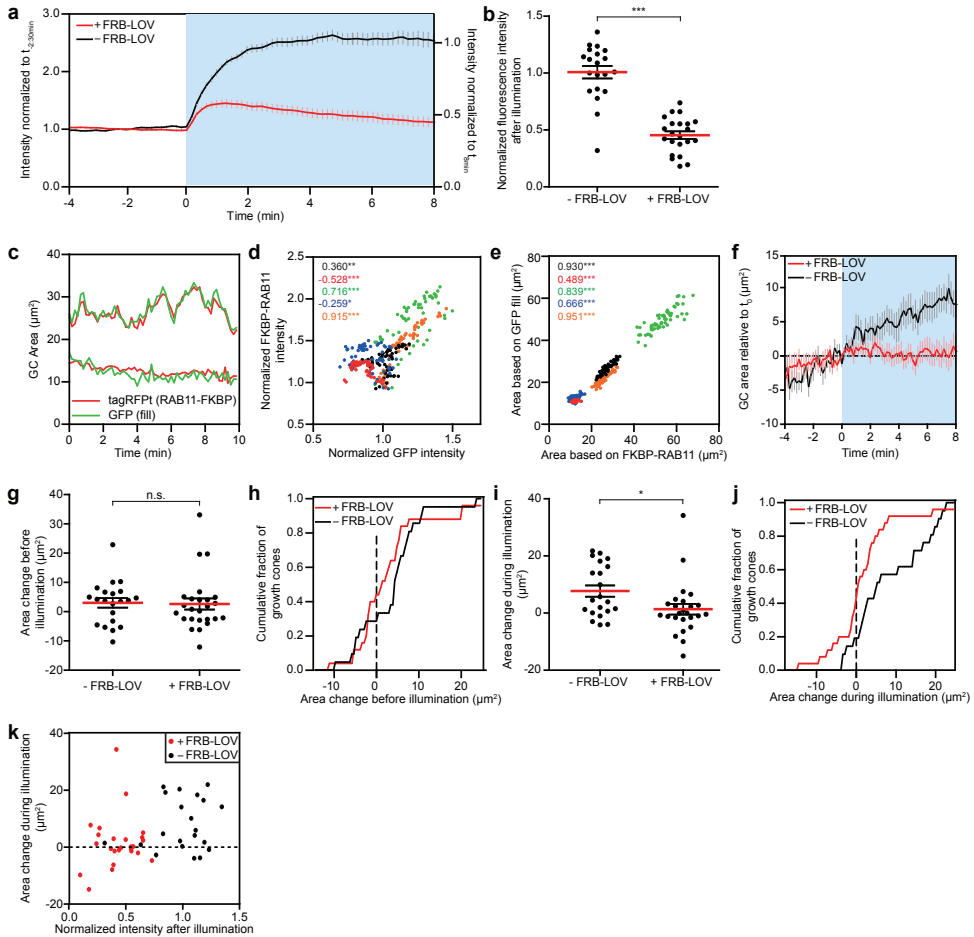


Figure S8 | Intensity rescaling and accurate growth cone area measurements based on RAB11 fluorescence.

(A) Mean intensity of growth cone FKBP–RAB11 fluorescence from neurons expressing BICDN–PDZ in the absence (black, $n = 21$) or in the presence (red, $n = 25$) of FRB–LOV normalized to the intensity before ($t_{-2:30min}$) (left axis) and rescaled relatively to the intensity of -LOV growth cones at t_{8min} (right axis). Blue box indicates blue-light illuminated interval. Graph shows mean \pm SEM. (B) Quantification of FKBP–RAB11 fluorescence intensity in the same neurons as shown in A after 8 minutes of blue-light illumination, normalized to the average fluorescence at t_{8min} in control neurons. Graph shows mean \pm SEM, *** $p < 0.0001$, Mann-Whitney test. (C) Area measurements of two representative growth cones from neurons expressing FKBP–RAB11, FRB–LOV, BICDN–PDZ and soluble GFP over time. Representative of five growth cones (shown in D and E). (D) Normalized tagRFPT–RAB11 intensity of five growth cones as in C, plotted against their normalized GFP intensity. Intensity values are averaged over the first five frames per growth cone. Pearson correlation coefficient (r) for each growth cone is indicated in top left corner. Same color indicates measurements of the same growth cone. (E) FKBP–RAB11-based area measurements plotted against GFP-based area measurements of the same growth cones as in D. Pearson correlation coefficient (r) for each growth cone is indicated in top left corner. Same color indicates measurements of the same growth cone.

(F) Traces of growth cone area measurements based on FKBP-RAB11 signal in the absence ($n = 25$, red trace) and presence ($n = 21$, black trace) of FRB-LOV in growth cones before and during blue-light illumination (See Experimental Procedures). Graph shows mean \pm SEM. Blue box indicates blue light-exposed interval. **(G)** Quantification of the area increase in the absence and presence of FRB-LOV in growth cones during blue-light illumination (-4 to 0 min). Values per growth cone are averaged over three frames. Graph shows mean \pm SEM. $p = 0.4145$ (n.s. not significant), Mann-Whitney test. **(H)** Cumulative histogram showing the fraction of growth cones with area shrinkage or growth (left or right of dashed line, respectively) before blue-light illumination (-4 to 0 min). Values per growth cone are averaged over three frames. **(I)** Quantification of the area change of -FRB-LOV and +FRB-LOV growth cones during blue-light illumination (0 to 8 min). Values per growth cone are averaged over three frames. Graph shows mean \pm SEM, * $p = 0.0206$, Mann-Whitney test. **(J)** Cumulative histogram showing the fraction of growth cones with area shrinkage or growth (left or right of dashed line, respectively) during blue-light illumination (0-8 min). Values per growth cone are averaged over three frames. **(K)** Scatter plot showing net growth during blue-light illumination and normalized fluorescence intensity after blue-light illumination per +FRB-LOV (red) or -FRB-LOV (black) growth cone.



A Phytochrome-Derived Photoswitch for Intracellular Transport

Max Adrian, Rein I. Hoogstraaten, Jelmer Willems and Lukas C. Kapitein

Cell Biology, Faculty of Science, Utrecht University, 3584 CH Utrecht, The Netherlands.

Manuscript submitted

ABSTRACT

Studying the regulation and functions of subcellular organelle positioning has been challenging due to a lack of tools to manipulate the positioning of specific organelles within cells. Recently, blue-light dependent dimerization of selected organelles with specific motor proteins has been demonstrated as a powerful approach to position organelles within living cells at will. The phytochrome B protein-protein interaction with its interacting factors has been shown to function as a photoswitch, dimerizing under red light and dissociating under far-red light. Here we engineer phytochrome domains into optogenetic organelle-motor heterodimers. This system allows to reversibly recruit motors to organelles with unprecedented spatiotemporal control as demonstrated by a combination of live cell imaging and pattern illumination. Precise optogenetic control of organelle motility and positioning will contribute to a better understanding of the spatial biology of cells.

RESULTS & DISCUSSION

In many cell types the proper subcellular positioning of organelles is crucial for correct functioning and also determines their inheritance in daughter cells after cell division (1, 2). Even in cells with a less defined cellular architecture, many organelles rely on contacts with other organelles for functions like metabolism, lipid transfer and signaling (3–6). Despite this importance, studying the role of organelle positioning has until recently been difficult for the lack of adequate tools to position organelles at will in living cells (1). We have previously shown that cellular cargoes such as organelles can be positioned in living cells by chemically induced recruitment of constitutively active motor proteins (7). Recently, we and others have extended this toolbox by making this heterodimerization light-inducible (8, 9), allowing to control organelle positioning with subcellular precision or *in vivo* (10).

In these light-inducible approaches, dimerization of LOV domains (11) or cryptochromes (12) is induced by blue light. Alternatively, UV light can be used to uncage a chemical dimerizer, but only at the expense of spatial precision and repeated reversibility (13). Nevertheless, also using blue light-sensitive domains severely limits the design of live imaging experiments, because GFP-tagged proteins cannot be imaged without activation of the dimerization system. In addition, these dimerization systems rely on their intrinsic dissociation kinetics for unbinding of the motors after returning to dark conditions. Even though binding affinities and rates of these systems have been optimized to suit a variety of applications (11, 14, 15), a direct ‘off-switch’ that actively dissociates motors from their cargoes should enable more precise positioning.

Light-inducible dimerization domains in phytochromes from *Arabidopsis thaliana* have been shown to behave as bidirectional photoswitches (16). The amino-terminal domain of phytochrome B (PhyB) can be switched from a red light-absorbing Pr state to a far-red light-absorbing Pfr state with red light in the presence of the co-factor phycocyanobilin (PCB). In the Pfr state, PhyB interacts with Phytochrome Interacting Factors (PIF) (17) and importantly, remains bound until illuminated with far-red light, which reverts PhyB into its Pr state and thereby dissociates from PIF rapidly (16). This photoswitchable system has so far been used to regulate gene transcription in yeast, mammalian cells and *in vivo* in zebrafish (18–20) or to engineer light-sensitive signal cascades (16, 21). Here, we develop organelle positioning

assays using phytochrome-derived dimerization domains to establish switch-like control over organelle movement on sub-cellular scale with high temporal resolution using red and far-red light.

To couple motor domains to organelles, we engineered fusion constructs of PhyB(1-908) and GFP-labeled organelle markers and fused PIF6(1-100) to previously characterized motor domains of kinesin and dynein motors (7, 9). Light-induced dimerization should then induce transport of the target cargo to the cell periphery or the microtubule organizing center (MTOC), respectively (Figure 1A). First this system was tested in fixed cells that were globally exposed to red light for 30 minutes prior to fixation. Recycling endosomes tagged with Phy-Rab11 were spread throughout the cytoplasm and partly enriched in the perinuclear region in control conditions. In the presence of kinesin-1 derived Kif5-PIF and PCB, repositioning of recycling endosomes could be induced with red light illumination in all cells imaged (Figure 1B, D). Moreover, to test the universality of this system, we repeated the experiment with the motor domain of Kif1a, a member of the kinesin-3 family. Recruitment of Kif1-PIF to recycling endosomes also induced their robust repositioning to the cell periphery in 96% of the cells (Supporting Information Figure S1). Similarly, by recruiting BICD-PIF to recycling endosomes, dynein-mediated transport to the MTOC was induced and recycling endosomes heavily accumulated at the MTOC in 74% of cells (Figure 1C, E).

In addition, we performed the same kinesin recruitment assays with peroxisomes labelled with Phy-Pex. Both coupling of kinesin-1 or kinesin-3 motor domains resulted in efficient repositioning of peroxisomes to the cell periphery after illumination with red light in 96% and 88% of cells imaged, respectively (Supporting Information Figure S2). Together these results demonstrate that our strategy to reposition cellular organelles by recruiting motor proteins using phytochrome-derived dimerization domains can efficiently be used for different combinations of organelles and motors.

To further optimize organelle tagging and to reduce the construct size of the fusion protein, a shorter amino-terminal truncation of PhyB (20) was tested. However, already in the absence of light, significant repositioning of endosomes to the periphery was observed after addition of PCB in 70% and 44% of cells expressing Phy(1-650)-Rab11 and Kif5-PIF or Kif1-PIF, respectively. Moreover, the coupling was irreversible under far-red light (Supporting Information Figure S3). Such irreversible hyperactivity of short amino-terminal truncations has also been reported previously (16, 22) and we therefore abandoned this approach.

To directly assess repositioning dynamics, we next carried out live cell imaging experiments. Since exposure of PhyB to low levels of ambient light may already activate PIF binding (22), addition of PCB was delayed until briefly before start of illumination. This allowed better handling of samples and prevented unintentional premature activation. Yet, we consistently noticed that the blue light used to excite GFP was already sufficient to activate recycling endosome repositioning in our assays. Therefore, we tested the reactivity of recycling endosome repositioning in a fixed experiment in which cells were either not illuminated or illuminated with far-red, red, green or blue light before fixation (Figure 2A). Indeed, exposure to blue light resulted in repositioning of recycling endosomes to the cell periphery with similar efficiency as red light illumination in 87% and 90% of cells, respectively. Similarly, 51% of the cells illuminated with green light showed endosome accumulations at the cell

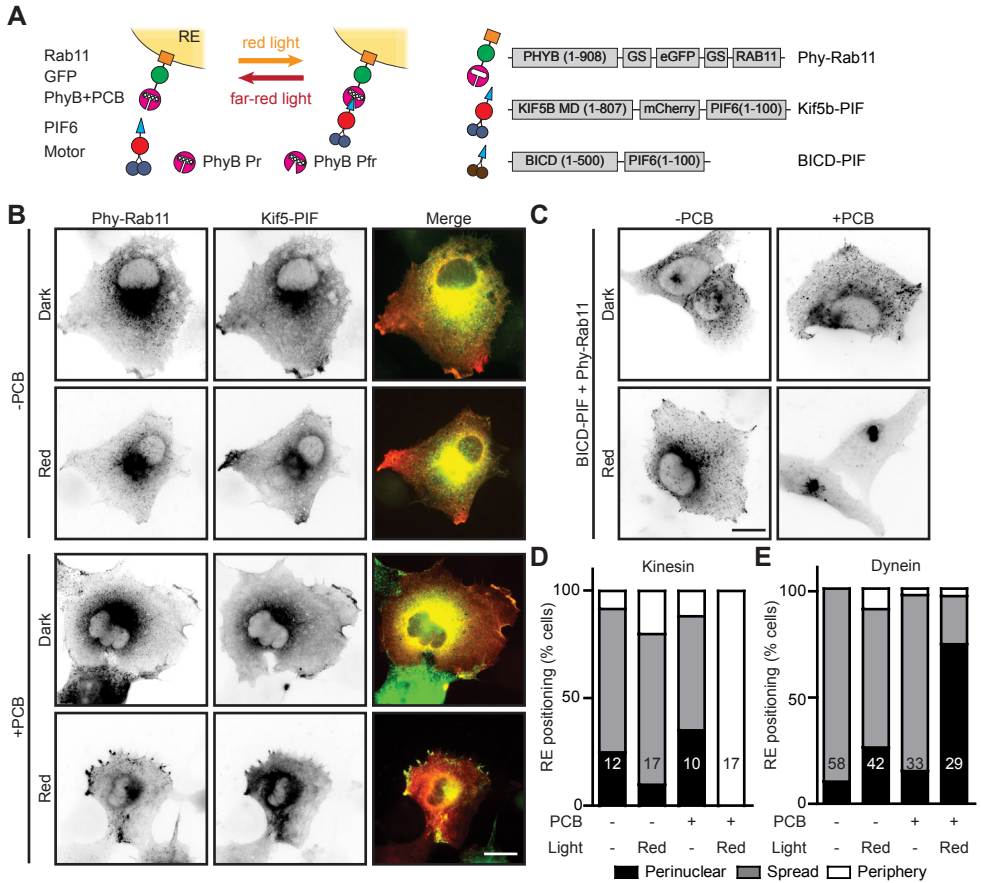


Figure 1 | Repositioning of recycling endosomes using light-induced phytochrome-based dimerization with motor proteins.

(A) Assay and constructs. Recycling endosomes were tagged with fluorescently-labelled Rab11 fused to PhyB(1-908) (Phy-Rab11). Upon exposure to red light, PhyB changes conformation from the Pr to the Pfr state, allowing it to bind PIF6 which is coupled to Kif5b(1-807)-mCherry (Kif5-PIF) or the dynein adaptor BICD(1-500) (BICD-PIF). (B) Distribution of recycling endosomes tagged with Phy-Rab11 in cells expressing Kif5b-PIF with or without PCB incubated either in the dark or under red light for 30 minutes. (C) Distribution of recycling endosomes tagged with Phy-Rab11 in cells expressing (color-less) BICD-PIF with or without incubation of PCB either in the dark or under red light for 30 minutes. (D, E) Quantification of manually scored Phy-Rab11 localization of experiments shown in (B) and (C), respectively. Numbers in bars indicate *n* cells analyzed for each condition. Scale bars are 20µm.

periphery, indicating that this motor recruitment assay is very sensitive to activation by light of the entire visible spectrum (Figure 2B). As expected, the relative radial distribution of recycling endosomes in far-red light illuminated cells was smallest, with 90% of endosomal fluorescence located in 9µm distance from the cell center, compared to 14µm, 18µm, 27µm and 35µm for dark, green, blue and red illuminated cells of similar size, respectively (Figure

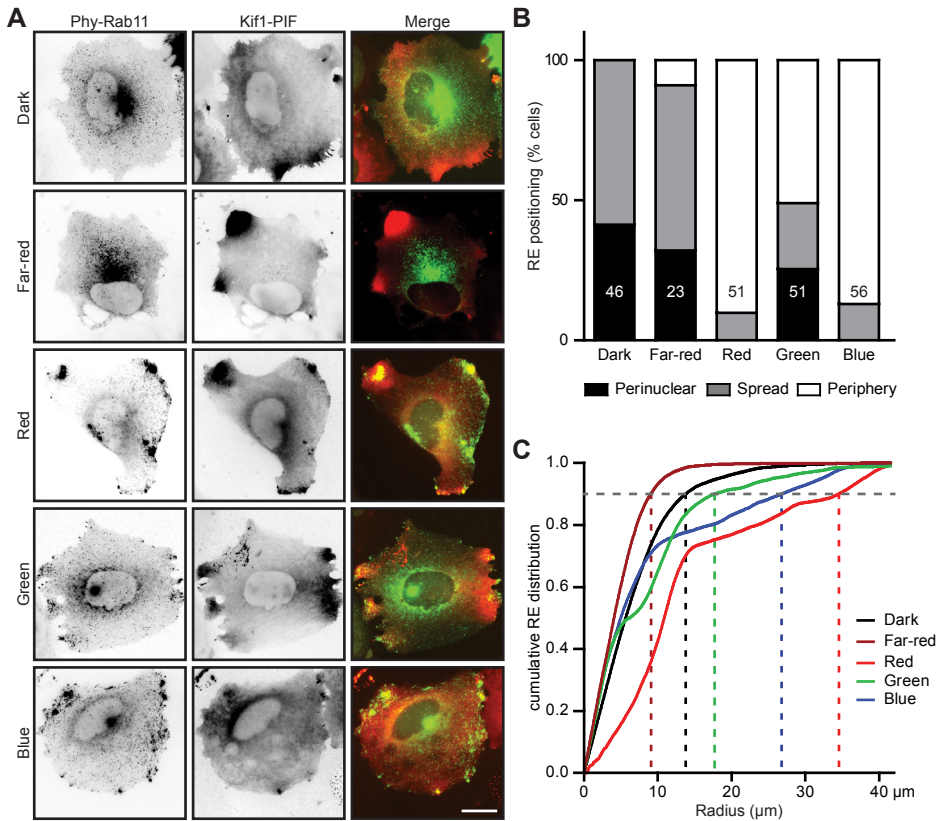


Figure 2 | PhyB-PIF interaction is sensitive to a range of visible wavelengths and requires far-red illumination to dissociate.

(A) Distribution of recycling endosomes tagged with Phy-Rab11 in cells expressing Kif1-PIF incubated with PCB either in the dark or under indicated colored light for 30 minutes. (B) Quantification of manually scored Phy-Rab11 localization of experiments shown in (A). Numbers in bars indicate n cells analyzed for each condition. (C) Cumulative measurements of Phy-Rab11 signal measured radially from the cell center to the periphery for cells shown in (A). Intersection with horizontal grey line indicates radius encompassing 90% of all Phy-Rab11 signal. Scale bar is 20μm.

2C). Thus, while organelle repositioning is not exclusively activated by red light, it can be prevented by far-red illumination, suggesting that the system may still be used for effective on/off photoswitching of organelle motility.

During subsequent live-imaging experiments, cells were exposed to far-red light before the start of the acquisition or whenever motors should be dissociated from recycling endosomes (Figure 3A). During illumination with 625nm light repositioning of recycling endosomes to the cell periphery could be followed (Figure 3B, Movie 1) and quantified (Figure 3C-E). The increase in peripheral Phy-Rab11 fluorescence intensity was accompanied by a simultaneous loss of intensity in the perinuclear region of the cell (Figure 3C). The frame-to-frame correlation index, a measure for repositioning activity in a region (7, 9), indicates that motility

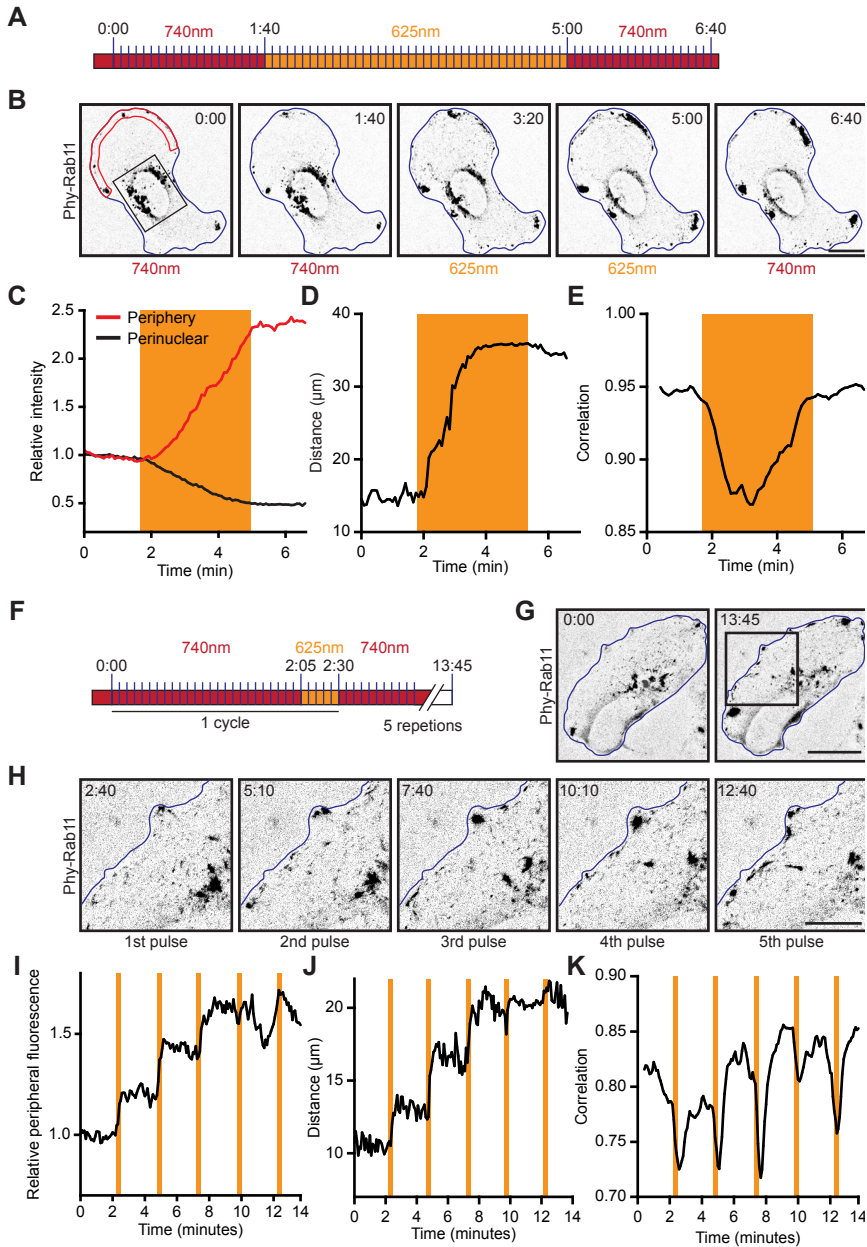


Figure 3 | Live-cell imaging demonstrates photo-switch behavior of phytochrome-based organelle repositioning.

(A) Schematic representation of light exposure during live-cell imaging experiment. Between each blue light exposure for GFP imaging (at 5s intervals), cells were illuminated with pulses of 740nm or 625nm LEDs. (B) Recycling endosomes imaged before, during and after dimerization of Phy-Rab11 with Kif1-PIF. Scale bar is 30 μm . See also Movie 1. (C-E) Analysis of Phy-Rab11 localization over time during the experiment shown in (B). (C) Measurements of fluorescence intensity in the perinuclear region (black) and at the cell periphery (red) indicated in (B). (D) Displacement expressed as the

radius of the circle surrounding 80% of the PhyB-Rab11 signal. (E) Frame-to-frame correlation (from 0 to 1) indicating motility of Phy-Rab11. (F) Schematic representation of light exposure during live-cell imaging experiment as in (A). Note that 5 cycles of alternating 740/625nm illumination were carried out. (G) Recycling endosomes imaged at the beginning and end of the experiment shown in (F). See also Movie 2. (H) Close-up on the region indicated in (G) showing Phy-Rab11 localization before illumination and after each 625nm illumination. Scale bar is 15 μ m. (I-K) Analysis of Phy-Rab11 localization over time during the experiment shown in (F-H). (I) Measurements of fluorescence intensity at the cell periphery. (J) Displacement expressed as the radius of the circle surrounding 50% of the PhyB-Rab11 signal. (K) Frame-to-frame correlation (from 0 to 1) indicating motility of Phy-Rab11. Blue lines indicate cell outlines, all times given in min:s. Red boxes indicate 740nm illumination, orange boxes indicate 625nm illumination. For clarity red boxes indicating 740nm illumination are not shown in quantifications.

of recycling endosomes increases nearly instantly after onset of 625nm illumination (Figure 3E). The peripheral intensity and displacement radius (Figure 3C, D) of recycling endosomes increase shortly after as endosomes move towards the cell periphery. The correlation and the displacement radius level already during the 625nm illumination window as endosomes gradually accumulate at the cell periphery, while the increase in peripheral Phy-Rab11 fluorescence intensity only stops after cells are illuminated with 740nm light. These results demonstrate that organelle positioning can be temporally controlled by exposing cells to sequential illumination with red and far-red light.

Next, we further studied the switch-like dynamics of the phytochrome system by quickly cycling between 'on' and 'off' states (16). For this, the illumination scheme was adjusted to cycle between short 625nm light pulses for 5 consecutive frames, to activate organelle repositioning briefly, and 25 frames of 740nm light, to dissociate motors from recycling endosomes (Figure 3F). While overall relocation of recycling endosomes to the cell periphery was observed in this assay (Figure 3G, H, Movie 2), increased motility of recycling endosomes was confined to periods of 625nm illumination and stopped within seconds after inactivation (Figure 2I-L, Movie 2). These results show that the PhyB-PIF dimerization can be used as a photoswitch to increase temporal precision of organelle repositioning.

In addition to increased temporal resolution when using the phytochrome system, patterned illumination with either 625 or 740nm should allow for local activation/deactivation of organelle repositioning at subcellular resolution. To test this, we actively dissociated motors from recycling endosomes with global 740nm illumination, while a smaller region of the cell was illuminated with 625nm to locally induce organelle repositioning (Figure 4A). Peripheral accumulation of recycling endosomes was observed at the 625nm illuminated part of the cell, whereas the 740nm illumination prevented repositioning elsewhere or after 625nm illumination was terminated (Figure 4B, C, Movie 3). To test whether organelle repositioning induced with 625nm illumination could also locally be stopped using 740nm light, we adjusted the illumination scheme to illuminate a subcellular region with 740nm after prior global activation of repositioning with 625nm light (Figure 4D). Recycling endosomes initially started moving towards the cell periphery, but were prevented from reaching the cell periphery in 740nm illuminated areas (Figure 4E, F, Movie 4). This local inactivation of organelle repositioning could further be quantified by correlation analysis, showing decreased

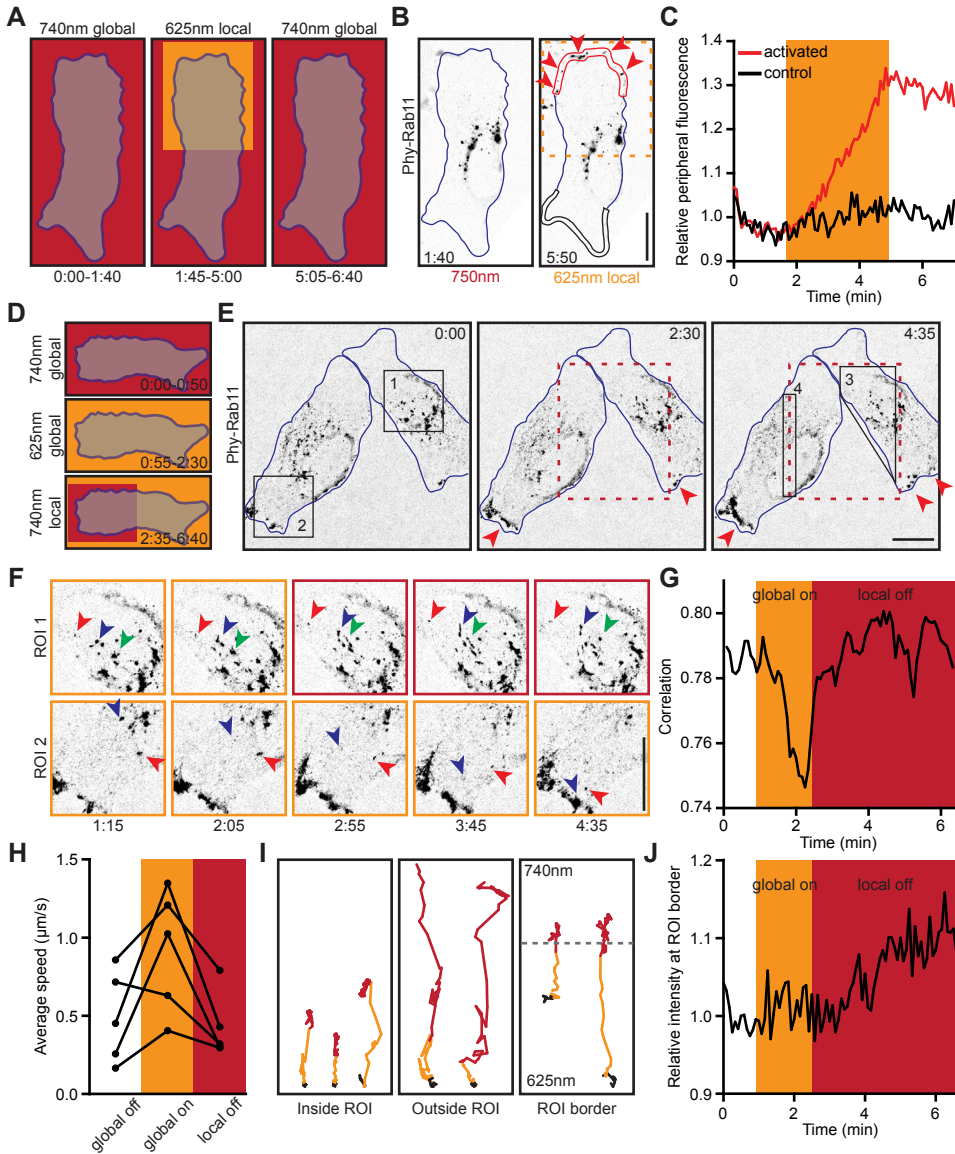


FIGURE 4 Local illumination with patterns of red/far-red light allows spatial control over organelle positioning.

(A) Schematic representation of light exposure during live-cell imaging experiment. After global illumination with 740nm light for 20 frames, a small area is illuminated with 625nm light for 40 frames, followed by global 740nm light to dissociate all motors. Illuminations were interspersed with GFP imaging excitation light every 5s. (B) Recycling endosome localization before and after local dimerization to Kif1-PIF with 625nm light in region indicated with orange dashed box. See also Movie 3. (C) Quantification of peripheral Phy-Rab11 at 625nm illuminated region (red) and control region (black) as indicated in (B). (D) Schematic representation of light exposure during live-cell imaging experiment. After global activation with 625nm light for 20 frames, a small area

is illuminated with 740nm light for 50 frames to locally dissociate motors. **(E)** Recycling endosome localization during local dissociation of Phy-Rab11 from Kif5-PIF as outlined in (D). Red dashed box indicates 750nm illuminated area. See also Movie 4. **(F)** Zooms of regions 1 and 2 shown in (E). Colored arrowheads highlight position of the same recycling endosomes in consecutive frames. Color of image border indicates wavelength of local illumination. **(G)** Frame-to-frame correlation (from 0 to 1) indicating motility of Phy-Rab11 in region 3 shown in (E). **(H)** Average speed of individual recycling endosomes in locally 740nm illuminated area (red dashes in (E)). **(I)** Trajectories of recycling endosomes inside, outside or on the border of locally deactivated area. Trajectories are shown in black during initial global 740nm illumination (frame 1-10), orange during global 625nm illumination (frames 11-30) and red during local 740nm illumination (frames 31-80). Note that these time intervals are not equally long. **(J)** Relative fluorescence intensity along the border of local 740nm illuminated area (region 4 in (E)), normalized to average intensity before global 625nm illumination. Blue lines indicate cell outlines. Orange and red boxes indicate 625nm and 740nm illumination, respectively. For clarity red boxes indicating global 740nm illumination are not shown. Scale bars are 30 μ m.

motility in a 740nm illuminated area (Figure 4G). In addition, measuring the average speed of recycling endosomes in this area showed that the 625nm-induced increase was reversed after local deactivation with far-red light (Figure 4H). Single trajectories from recycling endosomes show that endosome motility in 740nm illuminated areas rapidly decreased while endosomes outside this region showed continuous motility. Interestingly, endosomes crossing into the 740nm illuminated area also quickly stopped moving (Figure 4I) and accumulated on the border of this region (Figure 4J). Thus, locally patterned illuminations allows repositioning or retaining of organelles within subcellular areas with high precision.

In conclusion, we demonstrate that phytochrome-derived motor-cargo switches allow fast and actively reversible coupling of organelles and motor proteins. This interaction could be spatiotemporally controlled by exposing regions of interest to red and far-red light to induce or reverse binding, respectively. The main advantage over blue light-inducible recruitment of motors to organelles lies in the fast and active reversibility of the phytochrome system with a separate wavelength (16). Even though we found that phytochromes are sensitive to a broad spectrum, including blue light, far-red illumination actively dissociates PhyB-PIF interactions during live imaging of GFP-labelled structures. In addition, combining phytochromes and blue light-sensitive systems in parallel should allow for orthogonal control of positioning of two organelles similar to previously demonstrated gene expression assays (23).

Dependence on PCB as a cofactor could be considered a limiting factor for this system, because it is not expressed in animal cells. However, for our purposes, this dependence enabled us to easily handle transfected cells in ambient light conditions before the start of the experiments, because addition of purified PCB to the cell medium for 1h was sufficient. In other model systems, particularly *in vivo*, this may prove more challenging. However, injection of PCB into zebrafish embryos has been reported (19) and cultured cells have also been engineered to metabolize abundant biliverdin into PCB (24) to overcome this limitation. Recently, a photo-switchable dimerization system has been reported that uses biliverdin in its chromophore and is activated by far-red light (25). This system may thus overcome the requirement of exogenous compounds and the broad activation spectrum reported here, but its photoswitch

NIS software (Nikon). For live cell imaging, cells were transfected with Eugene6 (Promega) and imaged 16-24h later after incubation with 15 μ m PCB for at least 1 hour in fresh culture medium at 37°C and 5% CO₂. Cells were imaged with a 40x (Plan Fluor, NA 1.3, Nikon) oil-immersion objective on a Nikon Ti inverted microscope equipped with a sample incubator (Tokai-Hit), a mercury lamp (Osram), ET-GFP (49002), ET-mCherry (49008) filter cubes and a Coolsnap HQ2 CCD camera (Photometrics), controlled with μ Manager 1.4 software.

Illumination Schemes

For fixed experiments, transfected cells were incubated in the dark or in red, blue or green light using either a custom array of RGB-LEDs (~10 μ W), custom far-red LEDs (~200 μ W) or a commercial color adjustable LED light (~20 μ W, LivingColors 70019, Philips) for 30min.

For live cell imaging cells were illuminated with >725nm light prior to acquisition using the halogen transmission light path and a 725 cut-on colored glass filter (FSQ-RG9, Newport) at ~5mW on the specimen. To illuminate the cells during acquisition we used a Polygon 2000 digital mirror device equipped with 625nm and 740nm LEDs (all Mightex) that exposed ROIs between imaging frames as indicated with 625nm or 740nm light with up to 72.38mWcm⁻² and 33.22mWcm⁻² at the backfocal plane, respectively. Light exposure was synchronized with camera frames using camera-evoked TTL triggers. For global illumination blue excitation light pulses for GFP imaging (200ms) were interspersed with 4.5s of 625nm or 740nm light pulses at 10% and 100% of maximal LED power, respectively. For local activation of PhyB-PIF dimerization, after each GFP excitation, the activation ROI was illuminated with 2% 625nm LED power for 500ms followed by a 3.8s exposure of the surrounding inactivation area with 100% 740nm LED power. To locally dissociate PhyB-PIF dimers, a ROI was illuminated with 100% 740nm LED power for 3.8s, after illuminating the remainder of the cell with 2% 625nm LED power for 500ms to keep it activated between excitation pulses. It is important to note that without far-red illumination between imaging excitations, PhyB will be activated by the light required to image eGFP.

Analysis of Endosome Distribution

Most analyses of acquired images were performed with FIJI software and resulting graphs were plotted with Graphpad Prism 5. To quantify the effect of organelle repositioning in fixed cell experiments, organelle localization in cells of at least 2 coverslips were categorized as perinuclear enriched, evenly spread throughout the cytoplasm or clearly enriched at the cell periphery. The number of cells (*n*) is shown for each experiment. To quantify the efficiency of organelle repositioning in response to illumination with different wavelengths, we quantified the cumulative signal of thresholded (top 8% of signal) Phy-Rab11 measured along radial ROIs from the center to the periphery of the cell relative to the sum of all signal measured. The intercept of the resulting curve with $y=0.9$ indicated the radius of a circle surrounding 90% of all organelles.

To quantify peripheral organelle enrichments over time in live cell experiments, fluorescence intensity relative to the average of the first 10 imaging frames (baseline before induction of dimerization) was plotted as measured in background subtracted (rolling ball radius of 20px) ROIs located as indicated. Further measures of organelle motility and repositioning

(correlation index, tracking and displacement measures) were done as described previously (7, 9).

ACKNOWLEDGEMENTS

This work is supported by the Netherlands Organisation for Scientific Research (NWO) (NWO-ALW-VIDI to L.C.K.), the Dutch Technology Foundation STW and the Foundation for Fundamental Research on Matter (FOM), which are part of the NWO, and the European Research Council (ERC Starting Grant to L.C.K.).

AUTHOR CONTRIBUTIONS

M.A., R.I.H. and J.W. performed experiments. M.A. analyzed and interpreted the data. L.C.K. supervised the study. M.A. and L.C.K. wrote the manuscript.

REFERENCES

1. van Bergeijk, P., C.C. Hoogenraad, and L.C. Kapitein. 2016. Right Time, Right Place: Probing the Functions of Organelle Positioning. *Trends Cell Biol.* 26: 121–34.
2. Jongsma, M.L.M., I. Berlin, and J. Neefjes. 2015. On the move: organelle dynamics during mitosis. *Trends Cell Biol.* 25: 112–24.
3. Prinz, W.A. 2014. Bridging the gap: membrane contact sites in signaling, metabolism, and organelle dynamics. *J. Cell Biol.* 205: 759–69.
4. Helle, S.C.J., G. Kanfer, K. Kolar, A. Lang, A.H. Michel, and B. Kornmann. 2013. Organization and function of membrane contact sites. *Biochim. Biophys. Acta - Mol. Cell Res.* 1833: 2526–2541.
5. Schrader, M., L.F. Godinho, J.L. Costello, and M. Islinger. 2015. The different facets of organelle interplay—an overview of organelle interactions. *Front. Cell Dev. Biol.* 3: 56.
6. Rambold, A.S., S. Cohen, and J. Lippincott-Schwartz. 2015. Fatty acid trafficking in starved cells: Regulation by lipid droplet lipolysis, autophagy, and mitochondrial fusion dynamics. *Dev. Cell.* 32: 678–692.
7. Kapitein, L.C., M. a Schlager, W. a van der Zwan, P.S. Wulf, N. Keijzer, and C.C. Hoogenraad. 2010. Probing intracellular motor protein activity using an inducible cargo trafficking assay. *Biophys. J.* 99: 2143–52.
8. Duan, L., D. Che, K. Zhang, Q. Ong, S. Guo, and B. Cui. 2015. Optogenetic Control of Molecular Motors and Organelle Distributions in Cells. *Chem. Biol.* 22: 1–12.
9. Bergeijk, P. Van, M. Adrian, C.C. Hoogenraad, and L.C. Kapitein. 2015. Optogenetic control of organelle transport and positioning. *Nature.* 518: 111–114.
10. Harterink, M., P. van Bergeijk, C. Allier, B. de Haan, S. van den Heuvel, C.C. Hoogenraad, and L.C. Kapitein. 2016. Light-controlled intracellular transport in *Caenorhabditis elegans*. *Curr. Biol.* 26: R153–4.
11. Strickland, D., Y. Lin, E. Wagner, C.M. Hope, J. Zayner, C. Antoniou, T.R. Sosnick, E.L. Weiss, and M. Glotzer. 2012. TULIPs: tunable, light-controlled interacting protein tags for cell biology. *Nat. Methods.* 9: 379–84.
12. Kennedy, M.J., R.M. Hughes, L. a Peteya, J.W. Schwartz, M.D. Ehlers, and C.L. Tucker. 2010. Rapid blue-light-mediated induction of protein interactions in living cells. *Nat. Methods.* 7: 973–5.
13. Ballister, E.R., S. Ayloo, D.M. Chenoweth, M. a Lampson, and E.L.F. Holzbaur. 2015. Optogenetic control of organelle transport using a photocaged chemical inducer of dimerization. *Curr. Biol.* 25: R407–R408.
14. Guntas, G., R. a Hallett, S.P. Zimmerman, T. Williams, H. Yumerefendi, J.E. Bear, and B. Kuhlman. 2015. Engineering an improved light-induced dimer (iLID) for controlling the localization and activity of signaling proteins. *Proc. Natl. Acad. Sci.* 112: 112–117.
15. Zimmerman, S.P., R.A. Hallett, A.M. Bourke, J.E. Bear, M.J. Kennedy, and B. Kuhlman. 2016. Tuning the Binding Affinities and Reversion Kinetics of a Light Inducible Dimer Allows Control of Transmembrane

- Protein Localization. *Biochemistry*. 55: 5264–5271.
16. Levskaya, A., O.D. Weiner, W. a Lim, and C. a Voigt. 2009. Spatiotemporal control of cell signalling using a light-switchable protein interaction. *Nature*. 461: 997–1001.
 17. Ni, M., J.M. Tepperman, and P.H. Quail. 1999. Binding of phytochrome B to its nuclear signalling partner PIF3 is reversibly induced by light. *Nature*. 400: 781–4.
 18. Shimizu-Sato, S., E. Huq, J.M. Tepperman, and P.H. Quail. 2002. A light-switchable gene promoter system. *Nat. Biotechnol.* 20: 1041–4.
 19. Beyer, H.M., S. Juillot, K. Herbst, S.L. Samodelov, K. Müller, W.W. Schamel, W. Römer, E. Schäfer, F. Nagy, U. Strähle, W. Weber, and M.D. Zurbriggen. 2015. Red Light-Regulated Reversible Nuclear Localization of Proteins in Mammalian Cells and Zebrafish. *ACS Synth. Biol.* 4: 951–958.
 20. Müller, K., R. Engesser, S. Metzger, S. Schulz, M.M. Kämpf, M. Busacker, T. Steinberg, P. Tomakidi, M. Ehrbar, F. Nagy, J. Timmer, M.D. Zurbriggen, and W. Weber. 2013. A red/far-red light-responsive bi-stable toggle switch to control gene expression in mammalian cells. *Nucleic Acids Res.* 41: e77.
 21. Toettcher, J.E., O.D. Weiner, and W. a Lim. 2013. Using optogenetics to interrogate the dynamic control of signal transmission by the ras/erk module. *Cell*. 155: 1422–34.
 22. Pathak, G.P., D. Strickland, J.D. Vrana, and C.L. Tucker. 2014. Benchmarking of optical dimerizer systems. *ACS Synth. Biol.* 3: 832–8.
 23. Müller, K., R. Engesser, J. Timmer, M.D. Zurbriggen, and W. Weber. 2014. Orthogonal optogenetic triple-gene control in Mammalian cells. *ACS Synth. Biol.* 3: 796–801.
 24. Müller, K., R. Engesser, J. Timmer, F. Nagy, M.D. Zurbriggen, and W. Weber. 2013. Synthesis of phycocyanobilin in mammalian cells. *Chem. Commun. (Camb)*. 49: 8970–2.
 25. Kaberniuk, A.A., A.A. Shemetov, and V. V Verkhusha. 2016. A bacterial phytochrome-based optogenetic system controllable with near-infrared light. *Nat. Methods*. 13: 591–597.

SUPPLEMENTAL MOVIES

Movie 1 | This video corresponds to Figure 3B. Repositioning of Phy-Rab11 with Kif1-PIF during global 625nm illumination. Total time: 6 minutes and 35 seconds. Acquired with 5 seconds between frames. 50x sped up. (h.264, AVI, 5.9 Mb). Scale bar is 15µm.

Movie 2 | This video corresponds to Figure 3G. Repositioning of Phy-Rab11 with Kif1-PIF during short pulses of global 625nm illumination. Total time: 13 minutes and 40 seconds. Acquired with 5 seconds between frames. 50x sped up. (h.264, AVI, 7.6 Mb). Scale bar is 15µm.

Movie 3 | This video corresponds to Figure 4A. Repositioning of Phy-Rab11 with Kif1-PIF during local 625nm illumination. Total time: 6 minutes and 35 seconds. Acquired with 5 seconds between frames. 50x sped up. (h.264, AVI, 4.1 Mb). Scale bar is 15µm. Box indicates 625nm illuminated area.

Movie 4 | This video corresponds to Figure 4E. Local deactivation of Phy-Rab11 repositioning with Kif5-PIF during local 740nm illumination. Total time: 6 minutes and 35 seconds. Acquired with 5 seconds between frames. 50x sped up. (h.264, AVI, 7.0 Mb). Scale bar is 15µm. Box indicates 740nm illuminated area.

SUPPLEMENTAL FIGURES

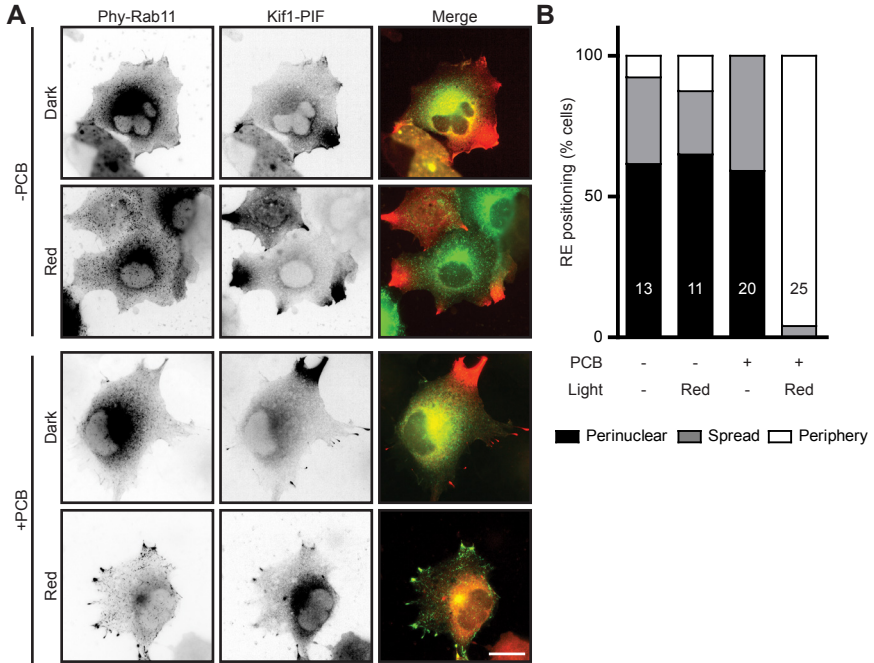


Figure S1 | Repositioning of recycling endosomes with kinesin-3 Kif1a.

(A) Distribution of recycling endosomes tagged with Phy-Rab11 in cells expressing Kif1a(1-383)-PIF6 (Kif1-PIF) with or without PCB incubated either in the dark or under red light for 30 minutes. (B) Quantification of manually scored Phy-Rab11 localization of experiment shown in (A). Numbers in bars indicate *n* cells analyzed for each condition. Scale bar is 20µm.

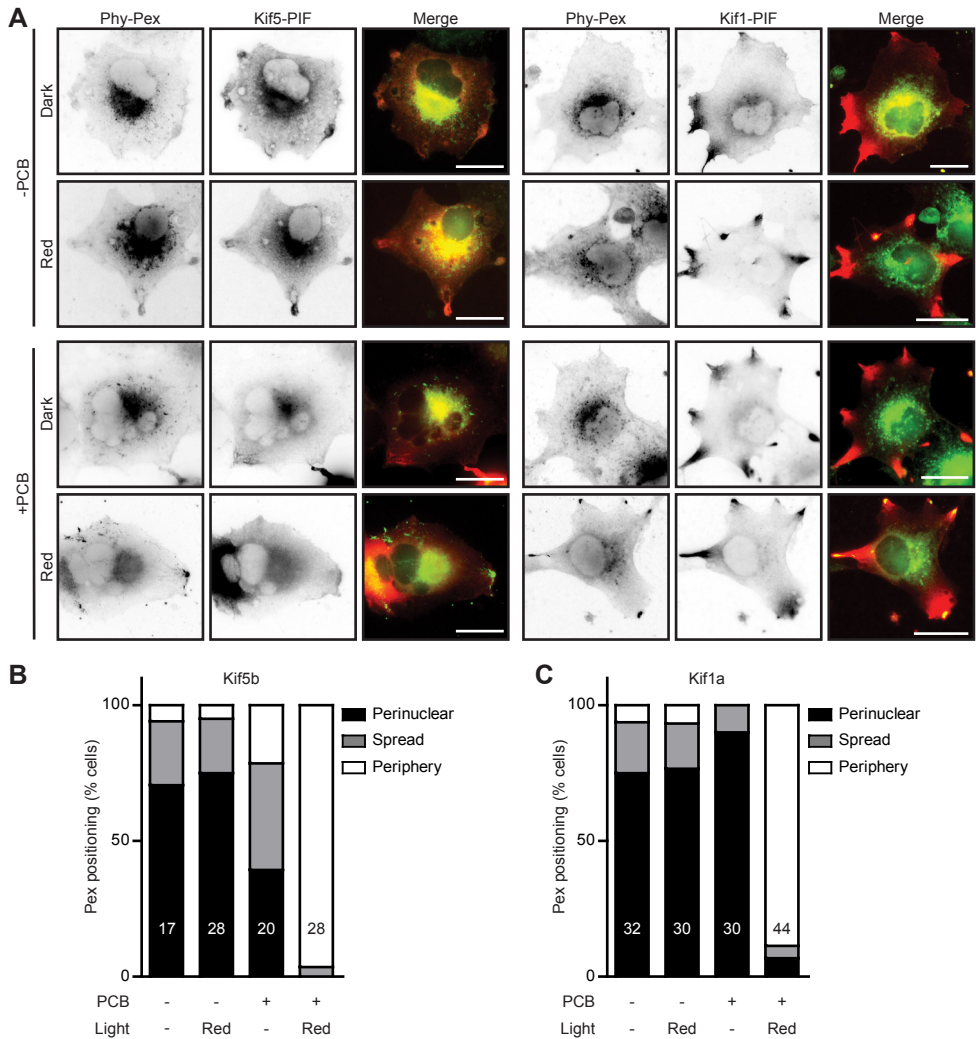


Figure S2 | Repositioning of peroxisomes with kinesin-1 or kinesin-3.

(A) Distribution of peroxisomes tagged with PhyB(1-908)-eGFP-Pex26(246-305)(Phy-Pex) in cells expressing Kif5-PIF (left) or Kif1-PIF (right) with or without PCB incubated either in the dark or under red light for 30 minutes. (B, C) Quantification of manually scored Phy-Pex localization of experiment shown in (A) for cells expressing Kif5-PIF (B) and Kif1-PIF (C). Numbers in bars indicate *n* cells analyzed for each condition. Scale bars are 20 μm.

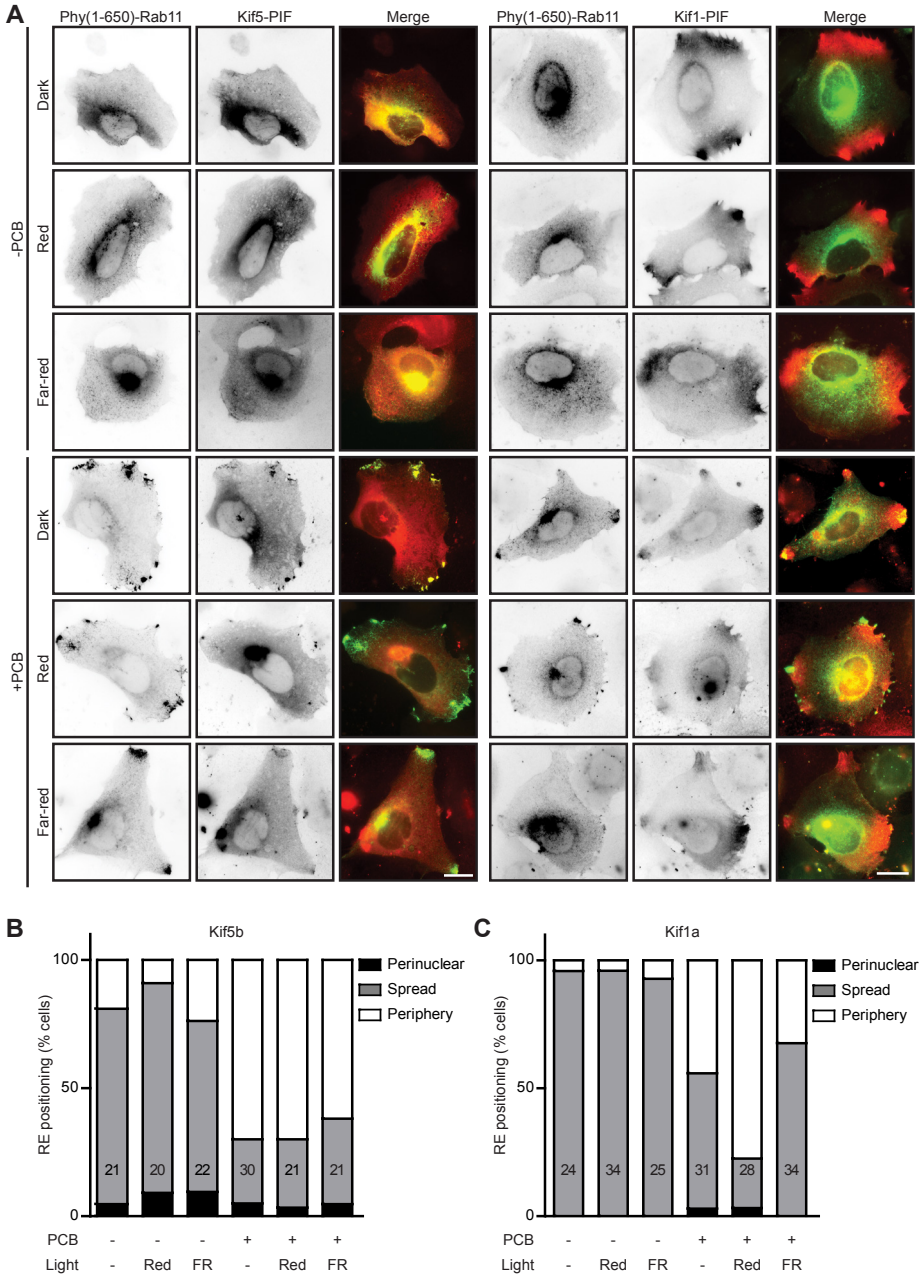


Figure S3 | Amino-terminal truncation of PhyB results in hyperactivation of PIF binding.

(A) Distribution of recycling endosomes tagged with PhyB(1-650)-eGFP-Rab11 (Phy(1-650)-Rab11) in cells expressing Kif5-PIF (left) or Kif1-PIF (right) with or without PCB incubated either in the dark or under red or far-red light for 30 minutes. **(B, C)** Quantification of manually scored Phy-Rab11 localization of experiment shown in (A) for cells expressing Kif5-PIF (B) and Kif1-PIF (C). Numbers in bars indicate *n* cells analyzed for each condition. Scale bars are 20µm.



General Discussion

Max Adrian

Division of Cell Biology, Faculty of Science, Utrecht University, Utrecht, The Netherlands.

GENERAL DISCUSSION

The research described in this thesis ranges from studying glutamate receptor dynamics in the membrane of dendritic spines to controlling positioning of recycling endosomes with different optogenetic systems. While these research projects may appear unrelated at first sight, all the work included in this thesis centres around one main question:

How does the spatial organization of a cell support its functioning?

We studied the role of passive and active transport in the spatial organization of the cell and we developed tools to probe the role of organelle positioning in cellular processes. In this general discussion, I will summarize the key findings, put them into a broader scientific perspective and suggest new avenues for further research.

CELLULAR COMPARTMENTALIZATION IN NEURONS

The first part of this thesis focuses on the spatial compartmentalization in neurons. In **Chapter 2**, we reviewed dendritic spines as compartments that can coordinate electrical and biochemical input by regulating their spread along the dendrite. Particularly the spine neck plays a role in restricting crosstalk of molecules in the spine head and the dendritic shaft (1, 2). Based on this knowledge, in **Chapter 3** we tested the hypothesis that spine morphology regulates the membrane-bound diffusion timescales.

Next to studying the dynamics of membrane proteins in dendritic spines, we also investigated how cargoes are delivered to neuronal compartments using active transport mechanisms. The supply routes of glutamate receptors in dendrites have been a longstanding point of discussion in the literature (3). In **Chapter 4**, live microscopy reveals the dynamics of the recycling endosomes in dendrites that transport and supply glutamate receptors to dendritic spines. Moreover, inducible removal of recycling endosomes from dendritic spines rapidly changed strength and composition of the post-synapse. Furthermore in **Chapter 5**, we demonstrate that in the growth cone, recycling endosomes are required for a different function, axonal outgrowth.

Dendritic spines: Morphology regulates membrane-bound diffusion

To unravel the impact of spine morphology on membrane-bound diffusion, we measured spine morphology using nanoscopy and compared diffusion time constants yielded either from particle simulations on these morphologies or from experimental measurements using photoconversion. We found that spine morphology indeed sets the lower bound for diffusion time scales in this system, but that the neck diameter in itself is not a good predictor. This result seemed counter-intuitive at first, as the numerical simulations showed a relation between neck width and the diffusion time constant (2). However, in these simulations all other shape parameters were kept constant. In our measurements, we were limited to actual spine morphologies and changes in other parameters are confounding the effect of the neck width on diffusion. Moreover, we found a surprising correlation, albeit weak, between head width and neck width in our dataset that earlier super-resolution studies did not report (1). This correlation may explain why we do not see strong effects on the diffusion time for

different neck widths. The decrease of the diffusion time induced by a smaller neck width may be compensated by the increase in diffusion time resulting from a smaller head. This led us to define a shape factor that reduces the dimensionality of spine morphology. Using this approach, we showed that many spines exhibit membrane-bound diffusion time scales close to the values predicted by particle simulations on spines with a comparable morphology.

However, a substantial group of spines showed slower diffusion than predicted, indicating that other mechanisms restrict membrane diffusion even more than spine morphology. Such mechanisms may include membrane microdomains, corralling effects of the underlying cytoskeleton or the crowding effects of other membrane proteins in dendritic spines (4–6). Interestingly, also specific proteins may affect membrane-bound diffusion in spines. The septin family of proteins has important roles in the development of dendrites and spine maturation. Septins were found to form complexes at the plasma membrane, often located at the base of dendritic spines (7). In another context, it has been shown that these complexes are ring shaped and promote *f*-actin bundling (8, 9). Septin7 accumulations in the spine neck have been shown to specifically reduce diffusion rates of transmembrane and inner-leaflet associated proteins in dendritic spines (10). Although our probe was developed to minimally interact with the post-synaptic density and other interactors of glutamate receptors, it will likely be affected by such non-selective diffusion barriers. It would be valuable to expand our set of measurements by measuring diffusion times of different membrane probes, which are either anchored in the inner or outer membrane leaflet or contain one or multiple transmembrane domains, to gain further insights of the specificity of these barriers.

There are two technical aspects that could be further improved in our study of membrane-bound diffusion in spines: First, to calculate the surface area of the spine, we assume in our study that spines are symmetrical as we use rotationally invariant functions to describe their morphology. Of course in reality spines are not symmetrical and our morphologies are just approximations. Our current imaging setup precluded PALM acquisitions in 3D. However, with the advent of fast 3D single molecule localization microscopy, new techniques allow to reconstruct the actual surface morphology of spines. It would be very interesting to run particle simulations on a large dataset of realistic 3D spine morphologies to refine our predictions. However, particle simulations on such asymmetrical shapes will also require additional computational power.

Second, complimentary to our bulk-diffusion measurements using photoconversion, tracking single molecules in dendritic spines can reveal more local patterns of membrane-bound diffusion. Tracking fluorescent dyes incorporated into the plasma membrane at high resolution has already shown that diffusion speeds are lower in spine necks compared to spine heads (11). Different variations of this technique have also been applied to study the lateral diffusion of glutamate receptors (12). However, in many cases the analysis of the resulting tracks is reduced to a two-dimensional plane, which does not reflect the curved three dimensional morphology of dendritic spines (13, 14). Therefore it would be very beneficial to develop 3D particle tracking of PALM/PAINT acquisitions to study membrane-bound diffusion in dendritic spines. Together these technical improvements will allow for an even more faithful characterization of membrane-bound diffusion in dendritic spines and reveal the effects of local morphologies.

Studying the effect membrane curvature on diffusion also has applications outside of dendritic spines. Membrane curvature may regulate diffusion of membrane bound proteins in a variety of cellular processes. The tubes of recycling endosomes or endocytic zones, for example, are curved membrane domains in which certain molecules need to be enriched for sorting or internalization, respectively. Also in the vesicles leaving the Golgi apparatus or the ER, specific cargoes need to be accumulated. It is therefore conceivable that similar to dendritic spines, curved membranes elsewhere in the cell influence membrane-bound diffusion into these compartments e.g. by retaining receptor molecules. There are numerous ways in which curvature of membranes is generated and sensed in the cell so that clustering of proteins or abscission of vesicles may be correctly coordinated (15). The combination of nanoscopic morphology and diffusion speed measurements will certainly also allow studying these processes in the future.

Active transport of glutamate receptor in recycling endosomes along dendrites

We next investigated active transport mechanisms of glutamate receptors in dendrites in **Chapter 4**. In particular, we studied the dynamics of recycling endosomes in dendritic spines and explored their contribution to the delivery of glutamate receptors to the post-synapse. Interestingly, endosomal transport is highly dynamic and many recycling endosomes are moving long distances using microtubules as tracks. Entries into spines were shown to be dependent on actin-based transport, but occasional entries along microtubules were observed too.

Imaging recycling endosome fusions with the plasma membrane along the dendrite, we could also demonstrate that about 30% of exocytic events from recycling endosomes take place in spines, indicating that spine localization of these endosomes is important. This was further investigated with experiments, in which we removed recycling endosomes from dendritic spines by acutely linking them to the motor protein transporting cargo back to the dendritic shaft. Endosome removal resulted in lower levels of glutamate receptors at synapses and smaller postsynaptic densities.

With this study, we could demonstrate that intracellular pools of glutamate receptors in the spine head are necessary to keep the concentration of receptors in the plasma membrane constant. On the other hand, removal of these pools from spine heads did not impact the electrophysiological behaviour of the cell. One interpretation of these observations is that the lower levels of surface glutamate receptors are still sufficient for signal transmission in the PSD and that lateral diffusion of receptors is sufficient. It would be interesting to challenge neurons with such a decreased pool of glutamate receptors in the plasma membrane to assess their functionality over longer time periods or after stimulation. LTP-induced recycling of glutamate receptors increases endocytosis (16) and may therefore require higher reserve pools in the plasma membrane to maintain or increase synaptic strength.

Previous studies suggested that lateral diffusion is responsible for 70-90% of receptors inserted into the synapse after potentiation (17). Taken together with our observation that removal of endosomes from spines resulted in a loss of 10-20% of surface receptors, this could explain why we did not observe effects on the electrical properties of these cells. While exocytosis of recycling endosomes is an efficient way to amplify the number of glutamate receptors

available to the synapse (2), it currently seems that the place of release along the dendrite is not crucial to maintain proper neuronal functioning.

Since there is increasing evidence that synapses receive clustered inputs that often correlate with positioning along a dendritic branch (18), it would be exciting to study the range of intracellular transport in recycling endosomes. It was previously reported that stimulation of a dendritic spine can trigger exocytosis of glutamate receptors along several micrometres of the dendritic shaft in response to diffusing signalling proteins (17). Interestingly, in contrast to earlier assumptions that recycling endosomes in dendrites are rather static structures at the base of dendritic spines (19), we found a substantial pool of highly dynamic recycling endosomes carrying glutamate receptors along dendrites. By keeping intracellular receptor pools restricted within a dendritic branch, the dynamic transport within a synaptic cluster could support a cluster-wide response. Live-imaging studies could help to determine the range of vesicular transport and the likelihood of reversals at branch points in order to substantiate this hypothesis. It would also be interesting to study whether mobile and immobile recycling endosomes have different functions in the dendrite.

In our study, we show that recycling endosomes enter dendritic spines mostly via myosin-mediated transport and that kinesin-driven transport only occurs occasionally under steady-state conditions. Others have shown that upon stimulation microtubule targeting of dendritic spines increases (20, 21) and that this correlated with increased trafficking of certain cargoes (22). Moreover, increasing levels of PSD-95 after stimulation of spines were shown to be dependent on such transient microtubule entries (23). In contrast, we saw a reduction of PSD-95 in spines after removing recycling endosomes with myosin VI. The exact interplay of actin and microtubule based transport into dendritic spines thus remains unresolved. Further studies should examine whether the relative importance of cytoskeletal fibres in active transport of glutamate receptors also changes under different physiological or developmental conditions.

Recycling endosomes: Versatile compartments

As discussed above, the dynamics of recycling endosomes and their correct positioning in spines are important for maintaining synaptic architecture. Interestingly, recycling endosomes also have other functions in the neuron. We showed in **Chapter 5** that recycling endosomes are required at growth cones for proper filopodial dynamics and axonal outgrowth. Unfortunately, our assay did not allow us to tease out whether this effect is due to a lack of lipids to expand the plasma membrane, a lack of receptors to sense the environment or the absence of a signalling platform of internalized receptors. Yet locally enriching or removing these endosomes is a much more subtle approach than knocking out components of this pathway, as that interferes with other local functions.

It is likely that recycling endosomes at the growth cone are not only supplying membrane but have functions in supplying receptors to the plasma membrane. It has been shown that Rab11-positive recycling endosome traffic TrkA and β 1 integrin receptors in the axon (24, 25). Next to supplying extra receptors that may amplify the biochemical cascades that drive axon growth, recycling endosomes may also be actively involved in this signalling cascade. The uptake of activated receptors into recycling endosomes has been suggested as a mechanism

to spread signals from the plasma membrane into other cellular regions through signalling endosomes (26). Especially in neurons that rely on protein synthesis or transcription regulation in the distant soma, such retrograde signals could be essential (27). Indeed the presence of signalling endosomes at the growth cone is essential for growth cone motility and outgrowth (28). Identifying the exact signal cascades and their targets in different cellular compartments will be an exciting target for further research.

While it is apparent that organelles like recycling endosomes can have multiple functions within a neuron, it is still unclear how the cell can distinguish these functions. We have been studying Rab11-positive recycling endosomes in dendrites and axons. Clearly, there must be a sorting mechanism that restricts those endosomes carrying glutamate receptors to the dendritic compartment while other factors need to be sorted into the axon. The regulation of this mechanism does not rely on Rab11 as it is expressed in both compartments. It would be interesting to further study this decision-making process and its underlying mechanism. One possibility might be that subpopulations of recycling endosomes recruit different Rab11 effector proteins. Two downstream effectors Rab11-FIP2 bind myosin V (29). Alternatively, adapter proteins like AP-1 have been shown to sort somatodendritic cargo through recruitment of kinesin-1 and 3 motors (30–32). Also it is known that glutamate receptors bind GRIP adaptor proteins that regulate their transport into dendrites (33). It will be a future challenge to identify more of these sorting mechanisms and to unravel their importance in neuronal trafficking processes.

EXPANDING THE OPTOGENETIC TOOLBOX FOR CELL BIOLOGY

The increasing amount of tools that optogenetics is offering to cell biologists opens new opportunities to manipulate cellular processes with high precision. In **Chapter 5**, we developed an optogenetic assay to induce transport of organelles in cells. Subsequently, we extended this toolbox with a second generation of photo-switchable domains to increase the accuracy with which we can position organelles in living cells in **Chapter 6**. In this section, I highlight some of the research questions in cell biology that optogenetics can be applied to and discuss an application we have recently developed in our lab. Also the current technical limitations and innovations to further broaden optogenetic applications are discussed here.

Optogenetic tools for cell biologists

Over the last years, research labs studying a wide range of cell biological topics have adopted optogenetic strategies to manipulate the processes they investigate. One of the first studies used light-sensitive modules to study actin polymerization by using a photo-caged actin polymerizing enzyme whose activity was made light-dependent (34). From these pioneering applications, the research community has now moved forward to produce general optogenetic strategies that can be more easily employed to study a variety of cellular functions.

Using different optogenetic tags, many cellular processes have been put under light control, for example cellular morphology and migration during development (35), inositol metabolism (36), protein secretion (37), protein degradation (38), acidification of lysosomes (39) and release of synaptic vesicles (40). Also optical control of transcription and editing of epigenetic marks have been implemented (41). Protein clustering, either to inhibit their function or

to study protein aggregation underlying different pathologies, has also been made light-inducible using oligomerization of Cry2 mutants (42, 43). Recently, this approach has been further developed to induce phase transitions in the cytoplasm by inducible aggregation of soluble peptides containing intrinsic disordered regions from known pathological aggregates (44). This assay enabled the team to identify the concentration thresholds for aggregation and to study the reversibility of aggregated peptides.

Many of these applications make use of the inducible dimerization properties of the light-sensitive domains. Using light-sensitive dimerization domains, any two proteins of choice can be linked together at high spatio-temporal precision. On the one hand, this allows optogenetic assays to interfere with endogenous dimerization processes that are abundant molecular process in cells. Many receptors rely on dimerization to transduce signals from the environment to the cytoplasm and many downstream reactions rely on protein-protein interactions. It is therefore not surprising that several signalling cascades that rely on upstream receptor dimerization have been engineered to react to light (45). Applications of spatiotemporally controlling receptor signalling are numerous. For example Raf signalling has been successfully controlled to modulate anti-tumour immunology (46) or spatiotemporal Erk signalling has been studied during the embryonic development of the fly (47). On the other hand, optogenetically-controlled dimerization can also be used to force exogenous interactions within the cell. LOVTRAP, a optogenetic assay that inhibits protein activity with light, uses this light-induced re-localisation to sequester proteins away from their site of activity, e.g. to mitochondria, to prevent them from interacting with their endogenous targets (48).

Another strategy to use light-sensitive domains in cell biological applications is to exploit the conformational change to regulate protein activity. The LOV domain undergoes a conformational change by unfolding its J α -helix upon illumination with blue light (49). Through controlled protein engineering, this change in protein folding can be used to cage protein activity in the dark and release this inactivation during illumination (50). Further development of this approach has now led to a more general approach to control protein function with light. Through computational analysis of any type of protein, loops can be identified on the protein's surface that allow introduction of a LOV domain without interfering with the proteins function in the dark condition. Upon the light-induced conformational change, extrinsic disorder of the protein's structure is induced, rendering the protein temporarily dysfunctional (51). Another approach to use conformational change to control protein activity is to introduce caged kinase inhibiting peptides into cells. By releasing the steric interactions of the LOV domain with the peptide with blue light, the peptide can bind the kinase and thereby inhibit its function temporarily without changing the expression level of the kinase of interest (52).

Through the continuous development of optogenetic modules, cell biologists now have the tools to control a large amount of cellular processes with light. Especially the rational development of protein domains that can be inserted with relative ease this field should expand quickly as the technical groundwork and characterization of the optogenetic systems has been done. It will be interesting to test the boundaries of possible applications and also evaluate their possibilities *in vivo*, e.g. to test tissue responses to acute dysregulation of cellular signalling in cancer models or to study the roles of spatiotemporal signalling in development.

Applications for organelle positioning assays

In **Chapter 5**, we controlled positioning of peroxisomes, recycling endosomes and mitochondria in unpolarised cells and neurons using optogenetics. In our assay, we couple specific motor domains to cargoes of our choice to determine the function of organelle positioning. These assays require detailed knowledge on the behaviour of the motor domains used in order to predict the direction and kinetics of the re-localisation process (53). Knowing the directionality of these motor domains, we could specifically enrich organelles in certain cellular regions. This approach may be further exploited to manipulate positioning of other organelles or in different contexts. On the one hand, this assay could be used to mislocalise organelles or proteins into non-endogenous compartments in order to understand their local function and to study their effect on processes as neuronal polarization. Open questions are, for example, the requirement of mitochondria for axonal branching and regeneration or the function of lysosomal retrograde transport in axons (54–56). On the other hand, one can also study organelle interactions, by acutely preventing organelle contact through re-localisation to opposite positions. As a first step into this direction, we recently tested re-localising different organelles including lysosomes, the Golgi apparatus and the endoplasmic reticulum (ER). While dispersion of the Golgi stacks and re-localisation of lysosomes to the cell periphery was successful, moving the large tubular network of the ER out of a cellular region was difficult. Finding good protein anchors in each organelle membrane is key to successfully re-localise any organelle.

UNDERSTANDING THE ROLE OF APICAL RECYCLING ENDOSOMES IN MVID

In order to further study the impact of recycling endosome positioning, we decided to investigate the apical recycling compartment in epithelial cells (57). In healthy polarized epithelial cells of the intestine, recycling endosomes localize sub-apically in the terminal web below the brush border consisting of densely packed microvilli. Loss of Rab11 results in a failure to properly polarize the cell and failure to establish microvilli (58). Interestingly, mislocalisation of Rab11 has a similar effect and patients of microvillus inclusion disease (MVID) show exactly this phenotype (Figure 1a) (59). The microvilli defect can be explained by the inability of patient cells to sustain an apical signalling cascade that normally results in phosphorylation of apical Ezrin (60). This could be due to the absence of the kinase Mst4 that localises to apically anchored recycling endosomes (61, 62). Moreover, these patients also show large inclusions of microvilli in the cytoplasm, indicating that the cells are not incapable of making microvilli but do so at the wrong site. Genetic studies showed that most MVID patients have mutations in the MYO5B gene (63). This strongly suggests that the incorrect localisation of recycling endosomes and failure to accumulate them at the apical membrane is due to their defective transport (Figure 1b). We hypothesized that correcting the positioning of recycling endosomes to the apical membrane should rescue microvillus formation in a model of the MVID phenotype.

To test this, we first established a model into which we can introduce our light-inducible motor-binding assays. We chose caco-2 cells because they quickly polarize *in vitro* and form spheroids with an apical lumen if cultured in a 3D matrix. We stably overexpress dTomato-

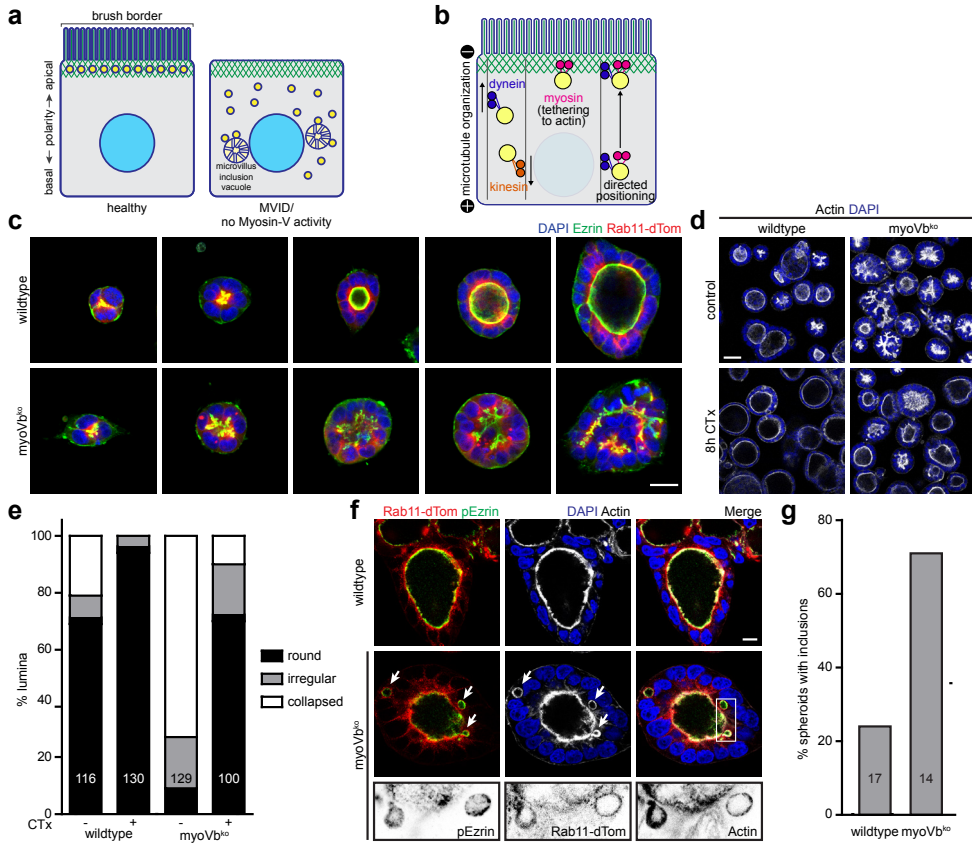


Figure 1 | Knock-out of MyoVb in 3D caco-2 cultures as a model for MVID.

(a) Schematic illustration of healthy and MVID phenotype in enterocytes. Yellow circles indicate recycling endosomes and green lines indicate actin fibres. Note that MVID cells lack apical recycling endosome enrichment and brush border but instead show cytoplasmic microvillus inclusions. **(b)** Working model of active transport routes of recycling endosomes in epithelial cells. **(c)** Wildtype and *myoVb^{ko}* caco-2 cells grown as spheroids in matrigel showing increasing stages of maturation. Cells express Rab11-dTom to visualize recycling endosomes (red) and are stained for the apical marker Ezrin (green). Scale bar is 50µm. **(d)** Wildtype and *myoVb^{ko}* spheroids stained with phalloidin (white) and DAPI (blue) to visualize lumen formation with or without addition of cholera toxin. Scale bar is 50µm. **(e)** Quantification of percentage of spheroids showing a single lumen in experiment shown in (d). n (cells) is indicated for each condition. **(f)** Localization of recycling endosomes (red), phosphorylated ezrin (green) and actin (white) in 4-day old wildtype or *myoVb^{ko}* spheroids. Arrows point at microvillus inclusions. Lower panel shows zoomed single channel images of region indicated with white box. Scale bar is 10µm. **(g)** Quantification of percentage of spheroids showing (pEzrin⁺) microvillus inclusions after 4 days in 3D culture.

Rab11 to follow recycling endosomes in control and *myoVb* knockout cell lines, a model of MVID (64). Indeed *myoVb^{ko}* cells do not form a proper lumen, even if stimulated with cholera toxin to boost lumen formation (Figure 1c-e). Also, we observed large inclusions

expressing apical markers and enriched with actin and recycling endosomes at their membrane similar to microvillus inclusions in MVID patients (Figure 1f,g). Thus, we are able to mimic the MVID phenotype using 3D cultures of caco-2 cell spheroids.

Next, we introduced our light-inducible organelle positioning system into these cells following a similar strategy as in **Chapter 5** (Figure 2a). Previously, we used the TULIP system to recruit motor domains to organelles. While it performed very well, one disadvantage is the incompatibility of carboxy-terminal fusions with the LOVpep domain. One way to overcome this is the use of improved light-inducible dimer (iLID) domains. iLIDs are based on the same LOV domain as TULIPs but the ePDZ binding peptide at the carboxy-terminus was replaced with a *ssrA* peptide that, if illuminated with blue light, interacts with a *sspB* domain. Otherwise this system performs similarly to the TULIP domains used previously (65) (Figure 2a).

Since apical recycling endosomes usually induce phosphorylation of ezrin at the apical membrane, we measured ezrin phosphorylation at the basal membrane as a readout for defective polarization. We show that expression of *mvoVb-sspB* reduced the MVID phenotype in *myoVb^{KO}* cells. Illumination with blue light for 16h further reduced basal pEzrin levels in *myoVb^{KO}* cells (Figure 2c,d). Next, we followed recruitment of recycling endosomes to the apical membrane with live microscopy. Strikingly, we did not see any gross defect in iLID-dTomato-Rab11 localization at the start of the experiment. Neither did illumination recruit additional iLID-dTomato-Rab11 to the apical membrane although *MyoVb-sspB* correctly localized to the apical membrane (Figure 2e-g). These results suggest that the iLID system used here is constitutively active and therefore rescued the phenotype already in absence of light.

Thus, at present we were not able to inducibly reposition recycling endosomes with light in *myoVb^{KO}* cells due to a too high dark-state affinity of the iLID(nano)-tagged motor. Interestingly, expression of this motor domain rescued the MVID phenotype already before illumination. This suggests that repositioning recycling endosomes is sufficient to rescue the MVID phenotype and that our approach should be successful if the light-inducible domains were exchanged. At the same time as we performed these experiments, a novel iLID variant with lower affinity called iLID(micro) was published (66). Using this domain with lower affinity should indeed make our assay light-inducible, alternatively these experiments could also be performed with chemical hetero-dimerization using rapalog at the expense of reversibility and spatiotemporal control. Once confirmed in caco2 *myoVb^{KO}* cells, it will also be very interesting to introduce this system into patient derived iPS cells or organoids to study the effect of restoration of recycling endosome positioning in diseased cells.

IMPROVING OPTOGENETIC ASSAYS AND APPLICATIONS

When planning to use optogenetics for any project, it is crucial to select the right assay with the best suited dimerization modules. It is very important to test dimerizers with different affinities for each application to exclude artefacts from dark activation or insufficient binding, as we have seen above. The binding and on/off kinetics of LOV-based systems have been characterized in detail (65–67). Also the phytochromes were well studied before they have been employed for sophisticated signalling assays (68–70). This basic research is important for

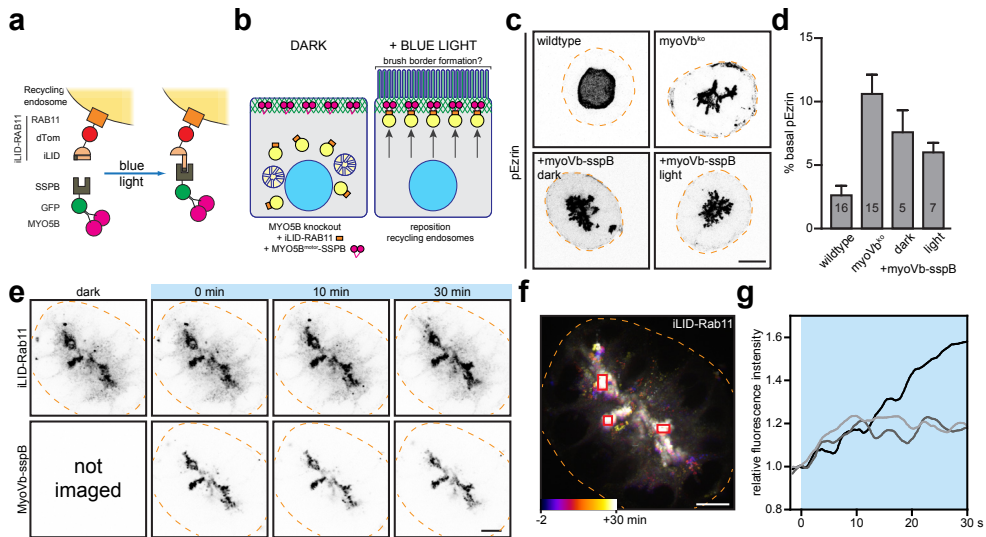


Figure 2 | Optogenetic repositioning of recycling endosomes in MVID spheroids.

(a) Assay: Recycling endosomes are tagged with a fusion protein of iLID, dTomato and Rab11. Illumination with blue light induces a conformational change in iLID exposing an SsrA peptide that can bind to sspB. This binding results in recruitment of sspB-GFP-tagged myosin-Vb motor domain to the recycling endosome. **(b)** Schematic representation of experimental strategy. In *myoVb*^{ko} cells, coupling of *myoVb* motor domains to recycling endosomes by light-induced heterodimerization detailed in (a) should result in repositioning of recycling endosomes to the subapical actin-dense region. This assay shows whether repositioning of recycling endosomes to the apical membrane is sufficient to induce brush border formation and/or clearance of microvillus inclusions. **(c)** Localisation of phosphorylated Ezrin in wildtype, *myoVb*^{ko} and *myoVb*^{ko} spheroids expressing the light-inducible system shown in (a) before and after blue-light illumination. Scale bar is 10µm. **(d)** Quantification of the percentage of mis-localized phosphorylated Ezrin at the basal membrane (indicated with orange dashes in (c)). n (spheroids) is indicated per condition. **(e)** Images of time-lapse experiment of *myoVb*^{ko} spheroids expressing iLID-dTomato-Rab11 and MyoVb-GFP-sspB before and during illumination with blue light. Scale bar is 10µm. Dashed orange lines indicate spheroid outline. Note that the GFP-tagged *myoVb*-sspB cannot be imaged in the dark condition. **(f)** Colour-coded sum projection of iLID-Rab11 of time-lapse shown in (e). Dashed lines indicate spheroids outline, Scale bar is 10µm. Note that immobile structures appear as white. **(g)** Quantification of relative fluorescence intensity in 3 apical regions marked with red boxes in (f). Blue box indicates blue light illumination.

choosing the correct optogenetic tools for any given application. In our organelle repositioning assays in **Chapter 5**, we noticed that the relatively fast off-kinetics of the LOV system were still insufficient to precisely predict the site of organelle accumulation. Since kinesin motors have an average speed of 1µm/s, the organelles will be transported further than just the edge of the locally induced region of interest and even often reached the cell cortex, because the dark-state inactivation times were in the range of tens of seconds. In addition, when developing novel assays, more factors than the sensitivity and reversion times of the light-sensitive domains are important (45). For transport assays, for example, it was important that the light-induced

interaction of the two domains is strong enough to withstand forces exerted by the molecular motors attached to them. General benchmarking of the dimerization systems is therefore difficult. Rather, testing these tools systematically for individual assays, as already described for transcription in yeast (71), will help other scientist to decide which tools to use.

Next to improving the optogenetic protein domains, also other aspects of the assays can be further improved. Our current strategies to introduce light-sensitive domains still rely on overexpression. Overexpressing proteins or protein fragments may interfere with physiological protein levels or act as dominant negatives. Genome editing could solve this problem by fusing the light-sensitive domains directly onto the endogenous proteins (72). Especially tightly regulated signalling proteins as the Rab GTPases are better studied by endogenous tagging (73).

Fusing light-sensitive domains to proteins may furthermore impact their function. While this principle was exploited in photo-caging enzymes (34), for most applications it may interfere with the cellular response even in the absence of light stimuli. One alternative to directly tagging organelles with light-sensitive domains lies in tagging them with a small peptide that links them to the light-sensitive domain in a second step. This approach can have two advantages. First, the endogenous system will only become light-sensitive once the domain is recruited. Second, adding an adapter may overcome restrictions in fusing light-sensitive domains to the carboxy- or amino-terminus of a protein of interest. For example, in **Chapter 5** we tagged Rab11 with and FKBP domain on its amino-terminus. This was necessary because only amino-terminal fusions are tolerated on Rab11 but the LOV peptide can only be fused on a carboxy-terminus. While we used the rapalog system to inducibly recruit the LOV domain to Rab11, an interesting alternative would be the use of constitutive, covalent binding, e.g. with the Spy catcher system (74).

Applying optogenetic assays *in vivo* is currently still challenging. Our lab demonstrated that light-inducible repositioning of organelles is feasible in neurons of *C. elegans* (75) and others have applied membrane recruitment assays in zebrafish and *Drosophila* using phytochromes and iLIDs, respectively (76, 47). We expect more reports applying optogenetic tools *in vivo* to follow, but so far the penetration of light into tissue has been an important bottleneck. Blue light-sensitive systems are difficult to activate in deeper tissues due to poor penetrance of shorter wavelength due to scattering. In addition, higher light intensities will induce more phototoxic damage. Therefore, red-shifted light-sensing domains are favourable *in vivo*. On the other hand, red light-inducible phytochromes require phycocyanobilin (PCB) as a co-factor. This biliverdin derivative is not produced in most mammalian cells and has to be supplied into the system, e.g. by injection (76). Alternatively, cells could be reprogrammed to synthesise PCB themselves through overexpression of two enzymes in its metabolic pathway (77). This is however not a trivial solution, especially in model organisms. A more practical solution to this problem may lie in a novel pair of light-inducible dimers that are sensitive to far-red light. Bacterial phytochromes do not require addition of PCB as they use abundant biliverdin as a co-factor. This pair of photo-switchable dimerization domains based on bacterial phytochromes is activated by far-red light with wavelengths >750nm and inactivated by illumination with red light (78). An additional advantage of this system over plant phytochromes may lie in the activation with 750nm light. While PhyB is activated by a wide range of wavelengths, overlapping with the spectra used for live-cell imaging, bacterial

phytochromes should not be affected by unintended activation during imaging. While this approach seems promising, it remains to be seen how these domains behave in live-imaging setups; whether the inactivation is efficient and whether the rather bulky domains do not disrupt endogenous functions of targeted proteins.

CONCLUDING REMARKS

Studying transport mechanisms in cells is important to understand the dynamics of cellular biology. The constant turnover of proteins and adaptation to cues from the environment is a challenging and complex task for every cell. It is fascinating to study the mix of passive transport by diffusion and the highly regulated active transport by motor proteins that together achieve homeostasis. Especially in highly compartmentalized cells, it is crucial that organelles and proteins reach their destination in order to carry out complex cellular functions. Therefore, it is important to study how the interaction of different transport mechanisms works, both in models of healthy and pathological conditions. Efforts to pinpoint the defects in protein transport underlying neurodegenerative diseases will greatly benefit from a thorough understanding of the basic principles of cellular transport and compartmentalization. Moreover, this knowledge is certainly required when designing side-effect-free medications.

In order to answer the ever more specific questions of cell biology, not only in the field of cytoskeletal transport, having adequate tools becomes the key advantage to carry out successful experiments. Optogenetics already allows precise spatiotemporal manipulations within a cell. Over the coming years this toolbox will certainly further expand and become a standard tool for cell biologists. This work by multidisciplinary researchers developing modular optogenetic protein domains should soon overcome current technical limitations in view of orthogonality and combination with multi-chromatic live-cell imaging. Also, having these novel tools at hand will lead to creative biological questions that we could not address directly before. Indeed, a bright future awaits cell biology (79).

REFERENCES

1. Tønnesen, J., G. Katona, B. Rózsa, and U.V. Nägerl. 2014. Spine neck plasticity regulates compartmentalization of synapses. *Nat. Neurosci.* 17: 678–685.
2. Kusters, R., L.C. Kapitein, C.C. Hoogenraad, and C. Storm. 2013. Shape-Induced Asymmetric Diffusion in Dendritic Spines Allows Efficient Synaptic AMPA Receptor Trapping. *Biophys. J.* 105: 2743–2750.
3. Opazo, P., and D. Choquet. 2011. A three-step model for the synaptic recruitment of AMPA receptors. *Mol. Cell. Neurosci.* 46: 1–8.
4. Kusumi, A., C. Nakada, K. Ritchie, K. Murase, K. Suzuki, H. Murakoshi, R.S. Kasai, J. Kondo, and T. Fujiwara. 2005. Paradigm shift of the plasma membrane concept from the two-dimensional continuum fluid to the partitioned fluid: high-speed single-molecule tracking of membrane molecules. *Annu. Rev. Biophys. Biomol. Struct.* 34: 351–378.
5. Santamaria, F., J. Gonzalez, G.J. Augustine, and S. Raghavachari. 2010. Quantifying the effects of elastic collisions and non-covalent binding on glutamate receptor trafficking in the post-synaptic density. *PLoS Comput. Biol.* 6: e1000780.
6. Li, T.P., Y. Song, H.D. MacGillavry, T.A. Blanpied, and S. Raghavachari. 2016. Protein Crowding within the Postsynaptic Density Can Impede the Escape of Membrane Proteins. *J. Neurosci.* 36: 4276–95.
7. Tada, T., A. Simonetta, M. Batteredon, M. Kinoshita, D. Edbauer, and M. Sheng. 2007. Role of Septin cytoskeleton in spine morphogenesis and dendrite development in neurons. *Curr. Biol.* 17: 1752–8.

8. Mavrikakis, M., Y. Azou-Gros, F.-C. Tsai, J. Alvarado, A. Bertin, F. Iv, A. Kress, S. Brasselet, G.H. Koenderink, and T. Lecuit. 2014. Septins promote F-actin ring formation by crosslinking actin filaments into curved bundles. *Nat. Cell Biol.* 16: 322–334.
9. Xie, Y., J.P. Vessey, A. Konecna, R. Dahm, P. Macchi, and M. a Kiebler. 2007. The GTP-binding protein Septin 7 is critical for dendrite branching and dendritic-spine morphology. *Curr. Biol.* 17: 1746–51.
10. Ewers, H., T. Tada, J.D. Petersen, B. Racz, M. Sheng, and D. Choquet. 2014. A Septin-Dependent Diffusion Barrier at Dendritic Spine Necks. *PLoS One.* 9: e113916.
11. Shim, S.-H., C. Xia, G. Zhong, H.P. Babcock, J.C. Vaughan, B. Huang, X. Wang, C. Xu, G.-Q. Bi, and X. Zhuang. 2012. Super-resolution fluorescence imaging of organelles in live cells with photoswitchable membrane probes. *Proc. Natl. Acad. Sci.* 109: 13978–13983.
12. Ehlers, M.D., M. Heine, L. Groc, M. Lee, and D. Choquet. 2007. Diffusional trapping of GluR1 AMPA receptors by input-specific synaptic activity. *Neuron.* 54: 447–60.
13. Kusters, R., and C. Storm. 2014. Impact of morphology on diffusive dynamics on curved surfaces. *Phys. Rev. E.* 89: 32723.
14. Oswald, F., E. L M Bank, Y.J.M. Bollen, and E.J.G. Peterman. 2014. Imaging and quantification of transmembrane protein diffusion in living bacteria. *Phys. Chem. Chem. Phys.* 16: 12625–34.
15. McMahon, H.T., and J.L. Gallop. 2005. Membrane curvature and mechanisms of dynamic cell membrane remodelling. *Nature.* 438: 590–6.
16. Lu, J., T.D. Helton, T.A. Blanpied, B. Rácz, T.M. Newpher, R.J. Weinberg, and M.D. Ehlers. 2007. Postsynaptic positioning of endocytic zones and AMPA receptor cycling by physical coupling of dynamin-3 to Homer. *Neuron.* 55: 874–89.
17. Patterson, M. a, E.M. Szatmari, and R. Yasuda. 2010. AMPA receptors are exocytosed in stimulated spines and adjacent dendrites in a Ras-ERK-dependent manner during long-term potentiation. *Proc. Natl. Acad. Sci. U. S. A.* 107: 15951–6.
18. van Bommel, B., and M. Mikhaylova. 2016. Talking to the neighbours: the molecular and physiological mechanisms of clustered synaptic plasticity. *Neurosci. Biobehav. Rev.* 71: 352–361.
19. Park, M., J.M. Salgado, L. Ostroff, T.D. Helton, C.G. Robinson, K.M. Harris, and M.D. Ehlers. 2006. Plasticity-induced growth of dendritic spines by exocytic trafficking from recycling endosomes. *Neuron.* 52: 817–30.
20. Hu, X., C. Viesselmann, S. Nam, E. Merriam, and E.W. Dent. 2008. Activity-dependent dynamic microtubule invasion of dendritic spines. *J. Neurosci.* 28: 13094–13105.
21. Jaworski, J., L.C. Kapitein, S.M. Gouveia, B.R. Dortland, P.S. Wulf, I. Grigoriev, P. Camera, S. a Spangler, P. Di Stefano, J. Demmers, H. Krugers, P. Defilippi, A. Akhmanova, and C.C. Hoogenraad. 2009. Dynamic microtubules regulate dendritic spine morphology and synaptic plasticity. *Neuron.* 61: 85–100.
22. McVicker, D.P., A.M. Awe, K.E. Richters, R.L. Wilson, D.A. Cowdrey, X. Hu, E.R. Chapman, and E.W. Dent. 2016. Transport of a kinesin-cargo pair along microtubules into dendritic spines undergoing synaptic plasticity. *Nat. Commun.* 7: 12741.
23. Hu, X., L. Ballo, L. Pietila, C. Viesselmann, J. Ballweg, D. Lombard, M. Stevenson, E. Merriam, and E.W. Dent. 2011. BDNF-Induced Increase of PSD-95 in Dendritic Spines Requires Dynamic Microtubule Invasions. *J. Neurosci.* 31: 15597–15603.
24. Eva, R., E. Dassie, P.T. Caswell, G. Dick, C. french-Constant, J.C. Norman, and J.W. Fawcett. 2010. Rab11 and its effector Rab coupling protein contribute to the trafficking of beta 1 integrins during axon growth in adult dorsal root ganglion neurons and PC12 cells. *J. Neurosci.* 30: 11654–69.
25. Ascaño, M., A. Richmond, P. Borden, and R. Kuruvilla. 2009. Axonal targeting of Trk receptors via transcytosis regulates sensitivity to neurotrophin responses. *J. Neurosci.* 29: 11674–85.
26. Howe, C.L., and W.C. Mobley. 2004. Signaling endosome hypothesis: A cellular mechanism for long distance communication. *J. Neurobiol.* 58: 207–16.
27. Ibáñez, C.F. 2007. Message in a bottle: long-range retrograde signaling in the nervous system. *Trends Cell*

- Biol. 17: 519–28.
28. Steketee, M.B., S.N. Moysidis, X.-L. Jin, J.E. Weinstein, W. Pita-Thomas, H.B. Raju, S. Iqbal, and J.L. Goldberg. 2011. Nanoparticle-mediated signaling endosome localization regulates growth cone motility and neurite growth. *Proc. Natl. Acad. Sci. U. S. A.* 108: 19042–7.
 29. Wang, Z., J.G. Edwards, N. Riley, D.W. Provance, R. Karcher, X.-D. Li, I.G. Davison, M. Ikebe, J. a Mercer, J. a Kauer, and M.D. Ehlers. 2008. Myosin Vb mobilizes recycling endosomes and AMPA receptors for postsynaptic plasticity. *Cell.* 135: 535–48.
 30. Schmidt, M.R., T. Maritzen, V. Kukhtina, V.A. Higman, L. Doglio, N.N. Barak, H. Strauss, H. Oschkinat, C.G. Dotti, and V. Haucke. 2009. Regulation of endosomal membrane traffic by a Gadkin/AP-1/kinesin KIF5 complex. *Proc. Natl. Acad. Sci.* 106: 15344–9.
 31. Nakagawa, T., M. Setou, D.-H. Seog, K. Ogasawara, N. Dohmae, K. Takio, and N. Hirokawa. 2000. A Novel Motor, KIF13A, Transports Mannose-6-Phosphate Receptor to Plasma Membrane through Direct Interaction with AP-1 Complex. *Cell.* 103: 569–581.
 32. Fariás, G.G., L. Cuitino, X. Guo, X. Ren, M. Jarnik, R. Mattera, and J.S. Bonifacino. 2012. Signal-Mediated, AP-1/Clathrin-Dependent Sorting of Transmembrane Receptors to the Somatodendritic Domain of Hippocampal Neurons. *Neuron.* 75: 810–823.
 33. Hoogenraad, C.C., A.D. Milstein, I.M. Ethell, M. Henkemeyer, and M. Sheng. 2005. GRIP1 controls dendrite morphogenesis by regulating EphB receptor trafficking. *Nat. Neurosci.* 8: 906–15.
 34. Wu, Y.I., D. Frey, O.I. Lungu, A. Jaehrig, I. Schlichting, B. Kuhlman, and K.M. Hahn. 2009. A genetically encoded photoactivatable Rac controls the motility of living cells. *Nature.* 461: 104–8.
 35. Guglielmi, G., H.J. Falk, and S. De Renzis. 2016. Optogenetic Control of Protein Function: From Intracellular Processes to Tissue Morphogenesis. *Futur. Cell Biol.* 4: 864–874.
 36. Idevall-Hagren, O., E.J. Dickson, B. Hille, D.K. Toomre, and P. De Camilli. 2012. Optogenetic control of phosphoinositide metabolism. *Proc. Natl. Acad. Sci. U. S. A.* 109: E2316–23.
 37. Chen, D., E.S. Gibson, and M.J. Kennedy. 2013. A light-triggered protein secretion system. *J. Cell Biol.* 201: 631–40.
 38. Renicke, C., D. Schuster, S. Usherenko, L.O. Essen, and C. Taxis. 2013. A LOV2 domain-based optogenetic tool to control protein degradation and cellular function. *Chem. Biol.* 20: 619–626.
 39. Rost, B.R., F. Schneider, M.K. Grauel, C. Wozny, C. G Bentz, A. Blessing, T. Rosenmund, T.J. Jentsch, D. Schmitz, P. Hegemann, and C. Rosenmund. 2015. Optogenetic acidification of synaptic vesicles and lysosomes. *Nat. Neurosci.* 18: 1845–52.
 40. Lin, J.Y., S.B. Sann, K. Zhou, S. Nabavi, C.D. Proulx, R. Malinow, Y. Jin, and R.Y. Tsien. 2013. Optogenetic inhibition of synaptic release with chromophore-assisted light inactivation (CALI). *Neuron.* 79: 241–253.
 41. Konermann, S., M.D. Brigham, A.E. Trevino, P.D. Hsu, M. Heidenreich, L. Cong, R.J. Platt, D. a Scott, G.M. Church, and F. Zhang. 2013. Optical control of mammalian endogenous transcription and epigenetic states. *Nature.* 500: 472–6.
 42. Taslimi, A., J.D. Vrana, D. Chen, S. Borinskaya, B.J. Mayer, M.J. Kennedy, and C.L. Tucker. 2014. An optimized optogenetic clustering tool for probing protein interaction and function. *Nat. Commun.* 5: 4925.
 43. Bugaj, L.J., A.T. Choksi, C.K. Mesuda, R.S. Kane, and D. V Schaffer. 2013. Optogenetic protein clustering and signaling activation in mammalian cells. *Nat. Methods.* 10: 249–252.
 44. Shin, Y., J. Berry, N. Pannucci, M.P. Haataja, J.E. Toettcher, and C.P. Brangwynne. 2016. Spatiotemporal Control of Intracellular Phase Transitions Using Light-Activated optoDroplets. *Cell.* 168: in press.
 45. Tischer, D., and O.D. Weiner. 2014. Illuminating cell signalling with optogenetic tools. *Nat. Rev. Mol. Cell Biol.* 15: 551–558.
 46. Tan, P., L. He, G. Han, and Y. Zhou. 2016. Optogenetic Immunomodulation: Shedding Light on Antitumor Immunity. *Trends Biotechnol.* : in press.
 47. Johnson, H.E., Y. Goyal, N.L. Pannucci, T. Schüpbach, S.Y. Shvartsman, and J.E. Toettcher. 2017. The

- Spatiotemporal Limits of Developmental Erk Signaling. *Dev. Cell.* 40: 185–192.
48. Wang, H., M. Vilela, A. Winkler, M. Tarnawski, I. Schlichting, H. Yumerefendi, B. Kuhlman, R. Liu, G. Danuser, and K.M. Hahn. 2016. LOVTRAP: an optogenetic system for photoinduced protein dissociation. *Nat. Methods.* 13: 755–8.
 49. Swartz, T.E., P.J. Wenzel, S.B. Corchnoy, W.R. Briggs, and R.A. Bogomolni. 2002. Vibration spectroscopy reveals light-induced chromophore and protein structural changes in the LOV2 domain of the plant blue-light receptor phototropin 1. *Biochemistry.* 41: 7183–7189.
 50. Lungu, O.I., R. a. Hallett, E.J. Choi, M.J. Aiken, K.M. Hahn, and B. Kuhlman. 2012. Designing Photoswitchable Peptides Using the AsLOV2 Domain. *Chem. Biol.* 19: 507–517.
 51. Dagliyan, O., M. Tarnawski, P. Chu, D. Shirvanyants, I. Schlichting, N. V. Dokholyan, and K.M. Hahn. 2016. Engineering extrinsic disorder to control protein activity in living cells. *Science.* 354: 1441–1444.
 52. Yi, J.J., H. Wang, M. Vilela, G. Danuser, and K.M. Hahn. 2014. Manipulation of Endogenous Kinase Activity in Living Cells Using Photoswitchable Inhibitory Peptides. *ACS Synth. Biol.* 3: 788–795.
 53. Lipka, J., L.C. Kapitein, J. Jaworski, and C.C. Hoogenraad. 2016. Microtubule-binding protein doublecortin-like kinase 1 (DCLK1) guides kinesin-3-mediated cargo transport to dendrites. *EMBO J.* 35: 302–318.
 54. Pu, J., C.M. Guardia, T. Keren-Kaplan, and J.S. Bonifacino. 2016. Mechanisms and functions of lysosome positioning. *J. Cell Sci.* 129: 4329–4339.
 55. Spillane, M., A. Ketschek, T.T. Merianda, J.L. Twiss, and G. Gallo. 2013. Mitochondria coordinate sites of axon branching through localized intra-axonal protein synthesis. *Cell Rep.* 5: 1564–75.
 56. Zhou, B., P. Yu, M.Y. Lin, T. Sun, Y. Chen, and Z.H. Sheng. 2016. Facilitation of axon regeneration by enhancing mitochondrial transport and rescuing energy deficits. *J. Cell Biol.* 214: 103–119.
 57. Goldenring, J.R. 2015. Recycling endosomes. *Curr. Opin. Cell Biol.* 35: 117–122.
 58. Bryant, D.M., A. Datta, A.E. Rodríguez-Fraticelli, J. Peränen, F. Martín-Belmonte, and K.E. Mostov. 2010. A molecular network for de novo generation of the apical surface and lumen. *Nat. Cell Biol.* 12: 1035–45.
 59. Golachowska, M.R., D. Hoekstra, and S.C.D. van IJendoorn. 2010. Recycling endosomes in apical plasma membrane domain formation and epithelial cell polarity. *Trends Cell Biol.* 20: 618–26.
 60. Dhekne, H.S., N.-H. Hsiao, P. Roelofs, M. Kumari, C.L. Slim, E.H.H.M. Rings, and S.C.D. van IJendoorn. 2014. Myosin Vb and Rab11a regulate phosphorylation of ezrin in enterocytes. *J. Cell Sci.* 127: 1007–17.
 61. Gloerich, M., J.P. ten Klooster, M.J. Vliem, T. Koorman, F.J. Zwartkruis, H. Clevers, and J.L. Bos. 2012. Rap2A links intestinal cell polarity to brush border formation. *Nat. Cell Biol.* 14: 793–801.
 62. Vogel, G.F., K.M.C. Klee, A.R. Janecke, T. Müller, M.W. Hess, and L.A. Huber. 2015. Cargo-selective apical exocytosis in epithelial cells is conducted by Myo5B, Slp4a, Vamp7, and Syntaxin 3. *J. Cell Biol.* 211: 587–604.
 63. Thoeni, C.E., G.F. Vogel, I. Tancevski, S. Geley, S. Lechner, K. Pfaller, M.W. Hess, T. Müller, A.R. Janecke, Y. Avitzur, A. Muise, E. Cutz, and L. a. Huber. 2014. Microvillus Inclusion Disease: Loss of Myosin Vb Disrupts Intracellular Traffic and Cell Polarity. *Traffic.* 15: 22–42.
 64. Cartón-García, F., A.W. Overeem, R. Nieto, S. Bazzocco, H. Dopeso, I. Macaya, J. Bilic, S. Landolfi, J. Hernandez-Losa, S. Schwartz, S. Ramon y Cajal, S.C.D. van IJendoorn, and D. Arango. 2015. Myo5b knockout mice as a model of microvillus inclusion disease. *Sci. Rep.* 5: 12312.
 65. Guntas, G., R. a. Hallett, S.P. Zimmerman, T. Williams, H. Yumerefendi, J.E. Bear, and B. Kuhlman. 2015. Engineering an improved light-induced dimer (iLID) for controlling the localization and activity of signaling proteins. *Proc. Natl. Acad. Sci.* 112: 112–117.
 66. Zimmerman, S.P., R.A. Hallett, A.M. Bourke, J.E. Bear, M.J. Kennedy, and B. Kuhlman. 2016. Tuning the Binding Affinities and Reversion Kinetics of a Light Inducible Dimer Allows Control of Transmembrane Protein Localization. *Biochemistry.* 55: 5264–5271.
 67. Strickland, D., Y. Lin, E. Wagner, C.M. Hope, J. Zayner, C. Antoniou, T.R. Sosnick, E.L. Weiss, and M. Glotzer. 2012. TULIPs: tunable, light-controlled interacting protein tags for cell biology. *Nat. Methods.* 9: 379–84.

68. Levskaya, A., O.D. Weiner, W. a Lim, and C. a Voigt. 2009. Spatiotemporal control of cell signalling using a light-switchable protein interaction. *Nature*. 461: 997–1001.
69. Toettcher, J.E., O.D. Weiner, and W. a Lim. 2013. Using optogenetics to interrogate the dynamic control of signal transmission by the ras/erk module. *Cell*. 155: 1422–34.
70. Toettcher, J.E., D. Gong, W. Lim, and O.D. Weiner. 2011. Light-based feedback for controlling intracellular signaling dynamics. *Nat. Methods*. 8: 837–839.
71. Pathak, G.P., D. Strickland, J.D. Vrana, and C.L. Tucker. 2014. Benchmarking of optical dimerizer systems. *ACS Synth. Biol*. 3: 832–8.
72. Cong, L., F.A. Ran, D. Cox, S. Lin, R. Barretto, N. Habib, P.D. Hsu, X. Wu, W. Jiang, L.A. Marraffini, and F. Zhang. 2013. Multiplex genome engineering using CRISPR/Cas systems. *Science*. 339: 819–23.
73. Dunst, S., T. Kazimiers, F. von Zadow, H. Jambor, A. Sagner, B. Brankatschk, A. Mahmoud, S. Spann, P. Tomancak, S. Eaton, and M. Brankatschk. 2015. Endogenously Tagged Rab Proteins: A Resource to Study Membrane Trafficking in *Drosophila*. *Dev. Cell*. 33: 351–365.
74. Li, L., J.O. Fierer, T.A. Rapoport, and M. Howarth. 2014. Structural analysis and optimization of the covalent association between SpyCatcher and a peptide tag. *J. Mol. Biol*. 426: 309–317.
75. Harterink, M., P. van Bergeijk, C. Allier, B. de Haan, S. van den Heuvel, C.C. Hoogenraad, and L.C. Kapitein. 2016. Light-controlled intracellular transport in *Caenorhabditis elegans*. *Curr. Biol*. 26: R153–4.
76. Beyer, H.M., S. Juillot, K. Herbst, S.L. Samodelov, K. Müller, W.W. Schamel, W. Römer, E. Schäfer, F. Nagy, U. Strähle, W. Weber, and M.D. Zurbriggen. 2015. Red Light-Regulated Reversible Nuclear Localization of Proteins in Mammalian Cells and Zebrafish. *ACS Synth. Biol*. 4: 951–958.
77. Müller, K., R. Engesser, J. Timmer, F. Nagy, M.D. Zurbriggen, and W. Weber. 2013. Synthesis of phycocyanobilin in mammalian cells. *Chem. Commun. (Camb)*. 49: 8970–2.
78. Kaberniuk, A.A., A.A. Shemetov, and V. V Verkhusha. 2016. A bacterial phytochrome-based optogenetic system controllable with near-infrared light. *Nat. Methods*. 13: 591–597.
79. Perez, F. 2015. Cell biology: Organelles under light control. *Nature*. 518: 41–42.





Addendum

Summary

Nederlandse Samenvatting

Zusammenfassung in deutscher Sprache

Curriculum Vitae

List of Publications

Acknowledgements

LAYMAN'S SUMMARY

Cells are complex building blocks of our bodies. Many processes have to be coordinated within a cell at any given time to carry out basic household and cell-type specific functions. Therefore, cells contain specialised compartments, over which the biochemical reactions can be distributed efficiently. These compartments are called cellular organelles. Examples of organelles are the plasma membrane, the nucleus (containing the genetic information), endosomes (transport vesicles) and mitochondria (energy production) amongst many others. In order to carry out their functions, these organelles need to be positioned at specific cellular locations. For instance, mitochondria are often found at locations where a lot of energy is consumed. Since cells are dynamic and can adapt to signals from their environment, also the positioning of organelles needs to be constantly regulated. In addition, many organelles need to interact, for example to exchange proteins, and therefore need to be positioned closely to one another. Next to organelles, also many proteins are subjected to sorting mechanisms that ensure their correct positioning within the cell.

Positioning and sorting of organelles and proteins is especially crucial for polarized cells like neurons. Neurons extend two types of protrusions from their cell body: Several dendrites and a single axon (see Chapter 1 Figure 2). Dendrites receive and process the signals from upstream neurons and the axon in turn sends signals on to the next neurons. Different proteins are required for either of these tasks. Receptor proteins that are stimulated by incoming signals need to be transported into dendrites and inserted into synapses. Synapses are the contact sites between two neurons and they are typically found in small protrusions called dendritic spines. The axon on the other hand needs to be supplied with neurotransmitters that can be released to excite downstream synapses. During development, the axon needs to grow towards its target region in order to build a correct neuronal circuit. The growth cone at the tip of the axon therefore not only needs to extend forward, but also decides where to turn by sensing its environment with specialized receptors. Thus, it is crucial that each cellular domain receives the necessary proteins and that these proteins reach their site of action in order for the cell to carry out its function.

To position proteins and organelles, cells can rely on two transport mechanisms: Passive diffusion and active transport with motor proteins. Simple diffusion of proteins through the cytoplasm or membranes allows proteins to slowly disperse in crowded environments eventually leading to an even distribution. In chapters 2 and 3, we studied the diffusion of membrane proteins (for instance glutamate receptors) through the plasma membrane in dendritic spines. Here, we focused on the influence of the three-dimensional shape of dendritic spines on the diffusion dynamics of glutamate receptors. Therefore, we measured the spine shape with near nanometer-precision and used computer models to predict the diffusion dynamics in each spine. Comparing these models to actual measurements of the membrane-bound diffusion showed that the spine shape often limits the speed with which proteins can move out of dendritic spines. However, in some cases additional mechanisms can further slow down receptor diffusion.

In chapter 4, we focused on the active transport mechanism that uses motor proteins to carry organelles or proteins along the fibres of the cytoskeleton. Before glutamate receptors can diffuse through the plasma membrane, they need to be transported into dendrites in

vesicles called recycling endosomes. We showed that recycling endosomes are predominantly transported along microtubules into dendrites. There, they can either fuse with the plasma membrane, thereby releasing the receptors into the membrane, or use different fibres called actin filaments to enter dendritic spines. We demonstrated that the pool of recycling endosomes in dendritic spines is important to maintain synaptic strength, because acutely removing them from dendritic spines resulted in smaller synapses with fewer glutamate receptors.

In order to better study the role of organelle and protein localisation within cells, we developed new tools to manipulate their positioning in chapters 5 and 6. For this, we used light-sensitive protein-tags, that were originally found in plants, and that react to specific wavelengths of light by binding to one another. By fusing these protein tags to organelles and motor proteins of our choice, we could induce the recruitment of motor proteins to the organelles by illuminating the cells with light. This resulted in transport of the organelles in the desired direction with high spatial and temporal control, as illumination can be restricted to subcellular regions and repeatedly be switched on and off. We used this approach to show that recycling endosomes are required locally in the growth cone for axonal outgrowth. Moreover, we are currently using these systems to understand the role of recycling endosomes in microvillus inclusion disease, a condition in which patients cannot absorb nutrients in their intestines.

In summary, the research described in this thesis aims to uncover the role of spatial organization in cellular functions. We studied both passive and active transport routes and developed novel techniques that allow manipulating cellular transport with high accuracy. Understanding the principles of spatial cell organisation and manipulating intracellular transport will contribute to a thorough understanding of cellular physiology, which is key to identifying defects underlying diseases.

NEDERLANDSE SAMENVATTING

Cellen zijn de complexe bouwstenen van ons lichaam. Een groot aantal processen moet binnen een cel gecoördineerd worden, zodat de cel zowel huishoudelijke functies als specifieke functies per celtype kan voltooien. Daarom bevatten cellen een aantal compartimenten waarover de biochemische reacties efficiënt worden verdeeld. Deze compartimenten noemen we organellen, bijvoorbeeld het celmembraan, de celkern (bevat de genetische informatie), endosomen (transportblaasjes) en mitochondriën (energiecentrales) en vele anderen. Om hun functies uit te kunnen voeren moeten deze organellen op bepaalde plekken binnen een cel terecht komen. Zo zijn mitochondriën vaak in gebieden te vinden waar veel energie nodig is. Omdat cellen erg dynamisch zijn en op signalen van buitenaf reageren, moet ook de positionering van organellen aanpasbaar zijn. Verder hebben veel organellen contact met andere organellen nodig om stoffen uit te wisselen, daarom moeten zij vlak bij elkaar liggen. Niet alleen de positie van organellen is belangrijk, maar ook eiwitten worden op verschillende manieren binnen de cel gesorteerd en bereiken zo de plek waar ze hun taak kunnen volbrengen.

De juiste positionering van organellen en eiwitten is vooral belangrijk in gepolariseerde cellen, bijvoorbeeld neuronen (zenuwcellen). Neuronen hebben twee soorten uitlopers: meerdere dendrieten en één axon (zie Hoofdstuk 1 Fig 2). Dendrieten ontvangen signalen van vooruitgaande neuronen en het axon stuurt vervolgens signalen naar de volgende cellen. Er zijn verschillende eiwitten nodig om signalen te ontvangen of te versturen. Receptor eiwitten, die door inkomende signalen geprikkeld worden, moeten in de dendrieten terecht komen en daar in synapsen worden opgenomen. Synapsen zijn de contact punten tussen twee neuronen en zij bevinden zich meestal in kleine zijtakken van de dendriet, genoemd dendritic spines. Daarnaast moeten neurotransmitters naar het axon gebracht worden zodat ze vanuit daar op de volgende synapsen kunnen worden vrijgelaten. Tijdens zijn ontwikkeling moet het axon de juiste connecties met andere neuronen en weefsels maken. De groeikegel aan het uiteinde heeft daarom receptoren nodig waarmee hij zijn omgeving kan voelen om zo de juiste kant op te groeien. Het is dus uiterst belangrijk dat elk cellulair domein de juiste eiwitten ontvangt en dat deze eiwitten vervolgens op de juiste plek in actie komen om alle taken van de cel uit te kunnen voeren.

Om eiwitten en organellen te positioneren, hebben cellen twee manieren van transport tot hun beschikking: Passieve diffusie en actief transport met motoreiwitten. Diffusie door het cytoplasma of door celmembranen zorgt voor een gelijkmatige verdeling van de eiwitten. In hoofdstukken 2 en 3 bekeken wij de diffusie van membraaneiwitten (zoals glutamaatreceptoren) in dendritic spines. Wij waren vooral geïnteresseerd hoe de driedimensionale vorm van zo'n dendritic spine de snelheid van de diffusie beïnvloedt. Daarom hebben wij de morfologie van dendritic spines met bijna nanometer-precisie gemeten en vervolgens computermodellen gebruikt om de dynamiek van membraan diffusie te simuleren in elke spine. Als we deze voorspellingen met metingen van de diffusiesnelheid in dezelfde spines vergelijken, zien wij dat de vorm van de spine de diffusie snelheid veelal beperkt, maar dat ook andere factoren deze dynamiek nog verder beperken.

In hoofdstuk 4 bestudeerden wij het actieve transportmechanisme dat gebruik maakt van motor eiwitten om organellen of eiwitten langs het cytoskelet te transporteren. Voordat glutamaatreceptoren in de celmembraan terecht komen, moeten ze in transportblaasjes

naar de dendrietten vervoerd worden. Wij lieten zien, dat dit transport vooral langs het netwerk van microtubuli plaatsvindt. In de dendriet kunnen de transportblaasjes ofwel met de plasmamembraan fuseren, en zo de receptoren in de membraan vrijlaten, danwel langs actinevezels in dendritic spines terecht komen. Deze tweede pool van transportblaasjes in dendritic spines is belangrijk voor de sterkte van de synaps, want toen wij ze uit de spines weghaalden werden de synapsen kleiner en bevatten minder glutamaat receptoren.

Om de functies van organel- en eiwitpositionering in cellen beter te kunnen bestuderen, hebben wij in hoofdstukken 5 en 6 nieuwe technologieën ontwikkeld om hun lokalisatie te manipuleren. Daarvoor gebruiken wij lichtgevoelige eiwitdomeinen die oorspronkelijk in planten zijn ontdekt en op bepaalde golflengtes van licht reageren en vervolgens aan elkaar binden. Door deze eiwitdomeinen op organellen en motoreiwitten naar onze keuze te zetten, kunnen wij motoreiwitten naar organellen brengen door de cel te belichten. Dit brengt ons in staat om organellen in een bepaalde richting binnen de cel te verplaatsen. Omdat de belichting snel aan en uit kan, en omdat we ook alleen kleine regio's van een cel kunnen belichten, hebben wij een nauwkeurig systeem tot onze beschikking om transport binnen de cel aan te sturen. Wij hebben deze proeven gebruikt om te demonstreren dat bepaalde transportblaasjes lokaal in een groeikegel van het axon aanwezig moeten zijn om deze te laten groeien. Verder zijn wij op dit moment bezig om hiermee de rol van transportblaasjes te onderzoeken in een ziekte waarmee patiënten geen voedingsstoffen in hun darmen kunnen opnemen.

Het doel van dit proefschrift was de functie van de ruimtelijke organisatie van cellen in kaart te brengen. Wij hebben onderzoek gedaan naar zowel passief als actief transport en nieuwe technieken ontwikkeld waarmee wij intracellulair transport nauwkeurig kunnen manipuleren. Door de spatiële organisatie van cellen te bestuderen en cellulair transport te manipuleren, zullen wij in toekomst de fysiologie van de cel beter kunnen begrijpen en zo de onderliggende defecten bij bepaalde ziektes kunnen aanwijzen.

ZUSAMMENFASSUNG IN DEUTSCHER SPRACHE

Zellen sind die komplexen Bausteine unserer Körper. Viele Prozesse müssen in allen Zellen zu jeder Zeit koordiniert werden, um sowohl Haushalts- als auch Zelltyp-spezifische Funktionen auszuführen. Darum gibt es in Zellen spezialisierte Abteilungen, über die die biochemischen Reaktionen effizient verteilt werden. Diese Abteilungen werden Organellen genannt und Beispiele sind die Zellmembran, der Zellkern (enthält die genetische Information), Endosomen (Transportvesikel) und Mitochondrien (Energiezentralen). Um ihre Funktionen zu erfüllen, müssen diese Organellen an bestimmten Orten in der Zelle positioniert werden. So sind beispielsweise Mitochondrien an Stellen zu finden, die viel Energie benötigen. Da Zellen sehr dynamisch sind und auf Einflüsse aus ihrer Umgebung reagieren, muss auch die Positionierung der Organellen anpassbar sein. Zusätzlich müssen einige Organellen auch miteinander in Kontakt kommen, zum Beispiel um Stoffe auszutauschen, und müssen daher nah zueinander positioniert werden. Des Weiteren müssen auch Proteine in der Zelle sortiert und an ihre Einsatzplätze transportiert werden.

Die Positionierung von Organellen und Proteinen ist im besonderen Maße für polarisierte Zellen sehr wichtig. Nervenzellen, auch Neuronen genannt, sind polarisierte Zellen, von deren Zellkörper zwei Arten von Ausläufern ausgehen: meist mehrere Dendriten und ein einzelnes Axon (siehe Kapitel 1 Fig 2). Dendriten empfangen und verarbeiten Signale, die das Neuron von vorherigen Zellen erhält, und das Axon sendet wiederum Signale an die folgenden Zellen. Natürlich sind für diese zwei Prozesse verschiedene Proteine notwendig: Rezeptorproteine, die die eingehenden Reize in zelluläre Signale umwandeln, müssen in die Dendriten gelangen um dort in Synapsen eingebaut zu werden. Synapsen sind die Kontaktpunkte zwischen zwei Neuronen und sind in Dendriten meist in kleinen Ausstülpungen zu finden, die dendritischer Dorn oder Dornfortsatz genannt werden. Andererseits müssen Neurotransmitter in das Axon gebracht werden, sodass sie von dort aus auf folgende Zellen ausgeschüttet werden können. In der Entwicklungsphase des Axons werden spezielle Rezeptoren im Wachstumskegel am äußersten Ende des Axons benötigt, um dort Wachstum und Richtung des Axons zu regulieren. Es ist also ersichtlich, dass jede zelluläre Domäne die richtigen Organellen und Proteine erhalten muss um ihre Aufgaben erfüllen zu können.

Um Proteine und Organellen zu befördern, gibt es zwei Transportmechanismen in Zellen: passive Diffusion und aktiver Transport mit Motorproteinen. Einfache Diffusion ermöglicht es Proteinen, sich durch das Zellplasma oder in der Zellmembran zu bewegen, um letztendlich gleichmäßig verteilt zu werden. In Kapitel 2 und 3 haben wir die Diffusion von Membranproteinen (z.B. Glutamatrezeptoren) in dendritischen Dornen untersucht. Dabei konzentrierten wir uns auf den Effekt der dreidimensionalen Morphologie der Dornen auf die Diffusionsdynamik. Zu diesem Zweck haben wir die Dornen mit nahezu Nanometer-Präzision vermessen, um danach die Dynamik von membrangebundener Diffusion mit Computermodellen für jeden Dorn zu simulieren. Ein Vergleich dieser Simulationen mit experimentellen Messungen der Diffusionsgeschwindigkeit zeigte, dass die Dornmorphologie die Diffusionsgeschwindigkeit begrenzt. Jedoch war die gemessene Geschwindigkeit in einigen Dornen weitaus langsamer als erwartet, was auf weitere Mechanismen hinweist, die diesen Prozess beeinflussen.

In Kapitel 4 wendeten wir uns dem aktiven Transport mit Motorproteinen zu, der für

die Positionierung von Organellen entlang des Zellskeletts verantwortlich ist. Bevor Glutamatrezeptoren nämlich in der Membran diffundieren können, müssen sie mittels Vesikeln, so genannten Recycling Endosomen, in Dendriten gelangen. Wir zeigten, dass diese Endosomen hauptsächlich Mikrotubuli Filamente als Gleise für ihren Transport benutzen. Einmal in Dendriten, können die Endosomen mit der Zellmembran verschmelzen und so die Rezeptoren auf die Zellmembran gelangen lassen, oder sie können entlang anderer Filamente, dem Actinskelett, in dendritische Dornen gelangen. Ein Vorrat an Endosomen in dendritischen Dornen ist wichtig, um die Stabilität der Synapse zu gewährleisten. Wenn wir diese Endosomen nämlich kurzzeitig aus den Dornen entfernten, wurden die Synapsen kleiner und enthielten weniger Rezeptoren.

Um die Bedeutung der Positionierung verschiedener Organellen in Zellen besser untersuchen zu können, haben wir in Kapiteln 5 und 6 neue Methoden dazu entwickelt. Wir verwendeten lichtempfindliche Proteine, die ursprünglich in Pflanzen entdeckt wurden. Sobald Licht einer spezifischen Wellenlänge diese Proteine aktiviert, binden sie an Partnerproteine. Wir platzierten diese Proteinpaare auf Organellen und Motorproteine unserer Wahl und konnten sie so kontrolliert aneinander binden lassen. Auf diese Weise können wir Organellen in beliebige Richtungen innerhalb der Zelle bewegen. Da die Belichtung schnell ein- und ausgeschaltet werden kann und wir sehr genau die belichtete Fläche regulieren können, haben wir eine sehr genaue Kontrolle über diesen künstlichen Transportvorgang. Wir haben diese Technik angewendet, um zu zeigen, dass Endosomen im Wachstumskegel des Axons lokal das Wachstum regulieren. Außerdem erforschen wir hiermit momentan die Rolle von Endosompositionierung in einer Krankheit, die es Patienten nicht ermöglicht, Nährstoffe in ihren Darmzellen aufzunehmen.

Das Ziel dieser Doktorarbeit lag in der Erforschung der räumlichen Organisation des Zellinneren. Dazu haben wir sowohl passive als auch aktive Transportmechanismen untersucht und neue Methoden geschaffen, mit denen wir intrazellulären Transport manipulieren können. Dieses Wissen und unsere technischen Fortschritte ermöglichen es uns, die Physiologie der Zelle besser zu verstehen, und werden uns in der Zukunft dabei helfen, Defekte, die bei diversen Krankheiten auftreten, auf zellulärem Niveau zu identifizieren.

CURRICULUM VITAE

Max Adrian was born on 29 June 1987 in Aachen, Germany. After graduating from high-school (Einhard Gymnasium Aachen) in 2006 and completing his national service, he started studying at University College Utrecht in 2007. In this liberal arts college, he completed tracks in life & medical sciences, chemistry and law and obtained his BSc in Science *magna cum laude* in 2010. He continued his studies at Utrecht University with a Master's in biomedical sciences within the Cancer Genomics and Developmental Biology programme. For this degree he carried out an internship in the lab of Prof Geert Kops, then at the Molecular Cancer Research division of the University Medical Center Utrecht, focusing on the molecular aspects of mitotic checkpoint signalling. For a second internship with Prof Stefan Schulte-Merker at the Hubrecht Institute, he studied a novel gene involved in lymphangiogenesis of zebrafish. His MSc thesis on the dynamics of glutamate receptor transport in neurons, written under supervision of Dr Lukas Kapitein, introduced him to neuronal cell biology. Following his graduation *cum laude* in 2012, Max joined the Kapitein lab in the Division of Cell Biology of Utrecht University to study protein and organelle transport with advanced live-cell microscopy techniques and to develop optogenetic assays as a PhD candidate. The results of this research are described in this thesis. In spring 2017 Max continues his research career as a postdoctoral research fellow in the neuroscience department of Genentech in South San Francisco, California in the lab of Prof Casper Hoogenraad.

LIST OF PUBLICATIONS

M. Adrian, R. Kusters, C.J. Wierenga, C. Storm, C.C. Hoogenraad, and L.C. Kapitein. 2014. Barriers in the brain: resolving dendritic spine morphology and compartmentalization. *Front. Neuroanat.* 8: 142.

P. van Bergeijk*, **M. Adrian***, C.C. Hoogenraad, and L.C. Kapitein. 2015. Optogenetic control of organelle transport and positioning. *Nature.* 518: 111–114.

M. Esteves da Silva, **M. Adrian**, P. Schätzle, J. Lipka, T. Watanabe, S. Cho, K. Futai, C.J. Wierenga, L.C. Kapitein, and C.C. Hoogenraad. 2015. Positioning of AMPA Receptor-Containing Endosomes Regulates Synapse Architecture. *Cell Rep.* 13: 933–943.

T. Kärpanen, Y. Padberg, S.A. van de Pavert, C. Dierkes, N. Morooka, J. Peterson-Maduro, G. van de Hoek, **M. Adrian**, N. Mochizuki, K. Sekiguchi, F. Kiefer, D. Schulte, and S. Schulte-Merker. 2017. An Evolutionarily Conserved Role for Polydom/Svep1 During Lymphatic Vessel Formation. *Circ. Res.* *In press.*

M. Adrian, W. Nijenhuis, R.I. Hoogstraaten, J. Willems, and L.C. Kapitein. 2017. A Phytochrome-Derived Photoswitch for Intracellular Transport. *Submitted.*

M. Adrian, R. Kusters, C. Storm, C.C. Hoogenraad, L.C. Kapitein. 2017. Probing the Interplay between Dendritic Spine Morphology and Membrane-Bound Diffusion. *Submitted*

* equal contribution

DANKWOORD

I postponed writing this very last part of my thesis for a while, because writing it means that I am about to definitely finish my PhD. Looking back at the past 4.5 years, I have had the honour of getting to know a wonderful group of people through my work in the cell biology lab. With them I have not only shared an interest in science, but I have also built friendships that are very dear to me. I hope that leaving the lab at de Uithof will not mean leaving behind those friends, even as we each move on to new adventures ahead.

First of all, I would like to thank my supervisors and promotor: Lukas and Casper. I still vividly remember taking the Light Microscopy course at the end of my Master's and meeting **Lukas** for the first time. The energy and passion with which you explained us the principles of phase contrast, darkfield, brightfield, DIC and many other microscopes on the first day was breath-taking. So was the speed with which you managed to fill the chalkboard with innumerable drawings of light paths, intensity curves and Jablonski diagrams. The drawings kept coming also during the many meetings we had on my research projects all throughout my time in the lab. Your fascination for the cytoskeleton and cellular transport mechanisms is sheer endless – just like your creativity to come up with experiments to study them. I would like to thank you for getting me involved in so many great projects during my time in the lab (even though I rejected your proposal to work on autophagy, I have actually come to change my mind and I don't think anymore that autophagy is that boring) and giving me the freedom to develop and try so many techniques along the way. I really enjoyed working with you and I nearly always left your office very motivated after I got stuck on a project. Ending my work in your lab with a lecture in your microscopy course was a nice moment coming around full circle. I wish you all the best for the future and hope that many more lab members will be able to carry out a fraction of your ideas in the future – I would love to stay in the loop and hear about it.

Casper, I first met you around the same time as I took Lukas's microscopy course, when I interviewed for a PhD position in the cell biology department. From that very first meeting on I have enjoyed talking to you and learning from your vast experience and knowledge. Even though I struggled at times to prepare enough slides with data every month to entertain you and the rest of the monthly meeting group for an hour, I very much appreciated the feedback and great atmosphere in these meetings. It was also in those meetings that Lukas and you found leads for projects in my data that I was using to illustrate that the experiments did not work... Your ability to focus on details and simultaneously stay on top of what is going on in an ever-expanding department is remarkable. I am impressed how the department has developed and grown under your leadership these last years and I hope that this friendly and open spirit will continue to make the 5th floor a great place to do science. I was both surprised and very proud when you asked me to join you at Genentech last fall and I am extremely excited to continue working with you in California.

I would also like to thank the other group leaders of the department. **Anna**, your expertise on the cytoskeleton is immense, and paired with your instinct for thorough experimental setups, this makes you a very valuable advisor in our department. No piece of data (good or bad) seems to ever slip your memory and I have learned a lot through our discussions and your feedback during seminars. I also enjoyed the discussions on Friday evenings, when

you joined us over a beer to discuss life as a scientist or interesting new developments in cell biology. I wish you all the best and that the +TIPs may forever grow in your lab. **Paul**, even though you do not remember my short bachelor's research project, you were the first "real-life" PI I met. We had many nice conversations during lunch and I hope I could convince you that not all liberal arts graduates are full of hot air. Good luck with all your collaborations and research on the nanobodies! **Corette**, thank you for trying to teach us cell biologists a bit of real neuroscience. Your input during the monthly meetings has helped to shape the Rab11 story and my spine papers. I wish you all the best and hope that many more boutons will find their way under your two (or three) photon microscope. **Esther**, I always enjoyed our conversations, in the lab or at the terraces of Ledig Erf. Even though you started swapping your bench for the lecture hall during the years, you were always involved in the lab. I wish you all best and lots of strength to soon return to the Kruyt! Be prepared, Lukas now has many more meetings in the office, better bring some extra batteries for the noise-cancelling headphones. And new to this list, **Harold**: During my MSc thesis, I learned a lot from your papers on receptor motility in synapses and suddenly you joined the lab. Your arrival meant over hours for the STORM microscope and in very little time you managed to start up Team Harold. Thanks for your feedback during our work discussions and all the best in your new role as PI. I hope the receptors will blink extra bright for you. A bit further down the corridor, **Sander**, **Mike** and **Inge** keep track of the developmental biologists. Thank you for the discussions during the Monday meetings and the great atmosphere during shared borrels and the lab outings. All the best and good luck with that recent expansion of the lab. Last but not least, the 5th floor would not be the same without **Fons**. Thank you for letting me try out my teaching skills on your students. Unfortunately, I never had the privilege to follow one of your courses myself, but I'm glad to know that the coming generations of students will still enjoy your passionate teaching with your recorded lectures. Enjoy your retirement; greetings to the hills of Zuid-Limburg.

Also outside our university, I would like to thank some outstanding scientists that I had the pleasure to meet and work with. My PhD position was part of a FOM-programme, called Barriers in the Brain, that was a cooperation of several labs. **Kees Storm** and **Rémy Kusters** from TU Eindhoven, it was a pleasure to be introduced to the world of biophysics and particle simulations. I am happy that the spine shape manuscript and the review paper worked out so nicely. Also I'd like to thank the other members, **Thomas Schmidt** and **Wim Pomp** from Leiden University and **Erwin Peterman** and **Vandana Singh Kushwaha** from the VU Amsterdam for the nice meetings and feedback. Lastly, I would like to thank the **FOM Foundation** for the courses and administrative and financial support.

Another collaborator I would like to mention here is **Sven van Ijzendoorn** from UMC Groningen. Your advice and protocols for growing spheroids of caco-2 cells greatly helped me to set up this system in our lab. Although the myoVb-project was not finished at the time I wrote this thesis, I hope that this project will result in a nice publication soon.

I would also like to thank the remaining members of my reading committee, **Judith Klumperman** and **Jeroen Pasterkamp**, for assessing my thesis and giving me the opportunity to defend my work.

Also, it is time to say goodbye to the great colleagues that made office and bench-life so

much fun. I joined office O.502 already when I wrote my Master's thesis (back then we still had free spots in the offices...) and Bas, Catia and Marleen had just moved in a few months earlier. **Bas**, it is always a lot of fun having you around. I enjoyed taking apart (and trying to put together again) microscopes and computer with you and I learned a lot about optics and super resolution imaging from you. Although it was not always easy to initiate conversations with you when your earplugs blasted hardstyle mixes, your humour entertained our office and you were always up for a chat. I hope we will still catch a few State of Trance festivals, together with Sam and Eugene, and I wish you good luck with your new job. **Marleen**, queen of antibodies and the only real doctor of the lab. You were always open to discuss science, help out with staining protocols or just have a chat. I will miss our conversations and I wish you all the best for the future. **Cátia**, the high-energy master slicer and queen of boutons: Always running between the microscope, slice culture and computer. I admire the patience with which you quantified what felt like millions of synapses; I already got tired just watching you. At the same time you always had a story to share and, together with Marleen, burst out in songs at random intervals. I already miss the loudest and weirdest sneezes mixed into loud 90s music blasting from youtube through your earplugs. Later on, **Anaël** joined the office and it turned out that his dancing skills, ranging from penguin-rave to riding on Wilco's back (I got a great photo of that), nicely fitted in. I hope you will be able to untangle all microtubules in dendrites soon. All of us have left or are about to leave the office soon. I couldn't have wished for a better surrounding to work in and I hope to keep in touch with all of you! Keeping up the fun in this office will be a challenge for **Eliana**, **Desiree** and **Mithila**, but I'm sure you'll do fine. Best of luck with your projects!

I'd also like to thank the rest of the Kapitein lab for an amazing time. First of all of course **Petra**: I remember being very confused by your project when I joined the lab. All those different kinesins that move (or not) around the cell. But shortly after, Lukas asked to "quickly help out" with the optogenetics, once you had the system finally working. It was great working with you, learning the motor assays and preparing the manuscript, even if it took a little longer than we thought at first. It was an honour to be your paranimf. I wish you good luck in Boston and hope to see you soon again. **Eugene**, none of the lab's data would ever get analysed without you. I learned a lot from you and appreciated your quick help with all the questions you answered. Your curiosity about biology and knowledge of math, physics and programming make up a great combination and result in spot-on feedback during work-discussions. Next to that, I enjoyed the parties and borrels we had inside and outside the lab. I hope you will still enjoy many karaoke parties and I'll be following even from far by reading your tweets! **Marina**, your giggles are not echoing down the hallways anymore but I haven't forgotten the good times we had in the lab and outside. It was great seeing your own new lab in Hamburg and I wish you lots of success over there. Don't forget to take some holidays now and then so that your paraglider doesn't get dusty! **Roderick**, man of a thousand projects, you have been around for quite some time since you started as a master's student in the lab. Your perseverance has already paid off in great successes and I'm sure you'll continue producing great assays. Nonetheless you were also a loyal member of the Friday borrels that I'll miss very much. Good luck! **Anne**, you took on a completely new field of research in our lab after some very preliminary data from Lukas and me. But by now the project has picked up great and I'm sure it will end in a nice story. Also you always actively participated in our social activities and I hope you'll enjoy the rest of your PhD. **Chiung-Yi**, your work on the rotating motors fascinated me from the beginning. I wish you good luck with it! **Wilco**, after teaching me

everything there is to know about western blots and immunofluorescence as my supervisor during my first lab internship, you suddenly applied as a postdoc to our lab. You are a great teacher and I appreciated your patience when I once again looked for bands of interacting proteins on a blot even though I denatured the proteins... You also led by example when it comes to work/party balance. I still remember the great parties in the Stratenum (yes, also looking at you, Mattie!). It was fun working with you again, even though the caco project turned out far more complex than we first thought. Thank you for now quickly fitting in the revision experiments for the phytochrome paper! I wish you all the best for the future.

Although officially belonging to Lukas's lab, I also felt very much at home in Casper's lab, where I kept my bench as the last outpost after the rest moved to the back of the corridor. **Phebe**, you keep all the labs running and are invaluable for everyone working in the department. You not only make sure the beer stock doesn't run out but you also often join our parties and I will miss you. Good luck keeping the lab tidy! **Marta**, you showed me how to image recycling endosomes in the first weeks of my PhD. It was fun to work with you on the Rab11 paper and sharing the monthly meeting with Casper. I wish you all the best for the future! **Phil**, you also competed with us for Casper's time during those meetings. Your feedback and ideas have greatly helped my experiments and I always enjoyed working with you. I hope you enjoy your new job in Switzerland! **Sam**! Next to inventing the axon initial segment, you had time for many parties and we were an awesome team both mixing and drinking cocktails, as there is ample evidence in the photo records... I will miss you as my party-buddy in California and I hope you will come over to visit. **Martin**, you are bridging the different labs of the 5th floor like no other and your broad interest and knowledge are very helpful in many discussions. You also showed me that life as a post-doc can be very enjoyable and I gladly think back at the many lab-outings and borrels that we had together. Also to you all the best! **Josta**, the mastermind behind pretty much all lab activities. You worked on more projects than I can count and always kept your focus while at the same time taking time for all the fun things outside the lab, very impressive! I'm sad you're not joining us in California, but I know that you made the right decision. **Feline** seems to be Josta's successor in terms of activity organization. It's great to see your enthusiasm for science and I hope your stem cells will continue to behave well, so that you have time to throw that cocktail party you promised us. **Sybren** you joined the lab very enthusiastically and you are a loyal fellow of the Friday borrel, make sure to sometimes drag the group to town and keep up the spirit. **Joanna**, I learned a lot from you about motor proteins and admire your patience to test all of them in PEX assays. I am looking forward to working with you in San Francisco along with **Amélie, Elena and Olga**. Good luck with finishing your projects, I'll make sure to find some nice places in the Bay Area before your arrival. **Lena**, it was nice working with you on the FOM project and organizing the meetings for it. Good luck with all those beautiful slices! **Bart**, you always have a joke or pun ready and I enjoyed the lunch breaks with you. **Inês**, our centrosome specialist, I hope you will soon figure out the mysteries of augmin complexes. I enjoyed the nice lunch breaks with you. **Mariella**, it was always a great talking to you. I hope you are enjoying the world of science communication. **Kah Wai**, good luck with the new job and your son! **Gabi**, good luck with the mitochondria and keep up the nice blog on figure design. **Riccardo**, all the best with finishing up your projects always caught up between 5th and 6th floor. **Diudonné**, thank you for all those neuron cultures and figuring out how to keep them yeast free. I'd love to join another yeast-free-party. **Marijn**, I'm sure you're enjoying Berlin, thank you for letting Sam and me turn your place into a cocktail bar. It was a lot of fun! **Robert**, I took up the challenge to get R

more popular in the lab. All the best in Rotterdam, both at the Erasmus and with your family! **Laura**, all the best for the future. **Yujie and Xingxiu**, good luck with your projects!

Further I'd like to thank the rest of the Cell Biology division and our colleagues from Developmental Biology for the many nice activities and discussions along the way. **Ilya**, master of the microscopes. Thank you for teaching me so much about microscopes and helping out when I needed to reconfigure our setups. Keep up the good work and all the best! **Amol**, good luck finishing your project and I hope we'll still find an opportunity to fly together. **Ivar**, thanks for your help on the 3D cultures. It was great to see your project together with **Ben** (good luck in France!) turn out so cool. Congratulations and all the best for the future! **Hai-Yin**, good luck with your project, I am amazed by your patience to perform your tricky experiments and your dedication to quickly return to the lab after your accident! **Maud**, thanks for the many nice talks and advice on 3D cultures. **Andrea**, I learned a lot about vesicular transport from you and admire your knowledge and drive to do great science. See you in San Francisco. **Helma, Qingyang, Dennis, Jingchao, Ruddi, Ankit, Kai, Chao, Bram, Raimond, York and Peter-Jan**, thank you for all the nice moments of the past years, I wish you all the best! Also all the best to **Sofia, René, Jarno and Rachid**, thanks for your help along the way!

Greetings also to the “worm people” down the corridor. **Lars and Thijs**, I enjoyed all the borrels and parties with you, many of which Lars co-organized. **Suzanne, Suzan, Vincent, Selma and Ruben**, all the best for the future!

During my PhD, I had the honour of working with three students that did their research internships in our lab and under my daily supervision. While each of you had individual strengths, I am very proud of what you have achieved and how you have developed as scientists during these internships. **Niek**, even if the MR receptors haven't turned into a great story, thank you for your hard work! **Rein**, you have greatly contributed to the Phytochrome paper (not only by losing the old PCB stock) and laid the groundwork for this project. **Jelmer**, fuelled by your interest in cell biology you have not only developed a big toolbox for repositioning even more organelles but you also helped out on pressing experiments with the Phytochromes. I'd like to thank all of you once again and I wish you all the best for the future.

Back when I was a student there were a few key people that paved the way for me getting interested in cell biology and ultimately starting a PhD. I would like to thank **Bas Defize** and **Fred Wiegant** for their excellent courses and support during my Bachelor's education. Later, during my lab rotations I had the privilege of working in two fantastic research groups. **Geert**, in your lab I could for the first time try to apply my biology knowledge in the lab and I learned a lot about mitosis. I really enjoyed being treated as a part of the lab and that I could even set up a side-project. This experience had a great impact on my choice to later start a PhD. Thank you for your support and guidance at that stage. Then I joined **Stefan's** lab where I enjoyed working with zebrafish and could learn more microscopy skills. **Terhi**, thank you so much for teaching me all those assays, from injecting tiny one-cell embryos to genotyping, imaging and cloning the candidate gene. I am still deeply impressed by your patience and precision in the lab. I very much enjoyed working with you and wish you all the best in Norway!

Besides spending a good part of your life in the lab, a PhD project should also teach you to

balance your life in your free time. I have an amazing group of friends both in the Netherlands and Germany that regularly helped me to forget about experiments for a weekend and I enjoyed every trip to Aachen, Berlin, Bonn, London, Hamburg, Bordeaux, Brussels, Dublin, Slovenia, the French Alps, München, and Roundwood. Thank you for keeping me sane over the past years and I wish you all the best. I hope we'll stay in contact despite the big time difference with California and you are always very welcome to come visit.

Without the continuous support of my family, I would probably never have started this PhD. Liebe **Ruth**, lieber **Hans**, solange ich denken kann, habt ihr immer alles daran getan um Coco und mir alles zu ermöglichen, was wir uns in den Kopf setzen. Eure Unterstützung und Großzügigkeit hätte nicht größer sein können und ich weiß, dass ich euch Vieles zu verdanken habe. Auch wenn ihr nicht allen Einzelheiten meiner Forschung folgen könnt, habe ich mich immer gefreut zu sehen, wie sehr es euch interessiert und ihr auf dem Laufendem bleiben wollt. Ich habe die vielen Wochenenden in Aachen bei Euch sehr genossen um auch in den hektischsten Zeiten kurz zur Ruhe zu kommen und den Bücherstapel (obwohl brav mitgenommen) links liegen zu lassen. Nun verschlägt mich die Forschung, auf die ihr so stolz seid, gerade nach Kalifornien. Ich hoffe, dass wir trotz der Distanz weiterhin viel miteinander sprechen und ich freue mich schon auf die Besuche in Aachen und euch in San Francisco zu empfangen. Vielen Dank für alles! Liebe **Coco**, dass es letztendlich Biologie für uns beide im Studium wurde, ist schön, auch weiß ich nichts über Vogelgesang oder Spinnen die Marienkäfer essen um Ameisen von ihren Eiern fernzuhalten. Ich wünsche dir viel Erfolg zum Abschluss deines Masters und hoffe, dass du eine tolle nächste Herausforderung findest, die dich glücklich macht. Ich freue mich schon dich und Nils nochmal in Hamburg zu besuchen, auch wenn es nun doch länger dauern wird. Jetzt bist du näher an Aachen dran als ich und musst du die Alten unterhalten. Bleib wie du bist und lass uns mal öfter skypen!

Jasmijn, we have just been through the quite turbulent finishing phase of our PhDs. Four years ago when we started with our projects nearly simultaneously, we could not have imagined what life as a PhD student would be like. I could not have wished for a better girlfriend – and now wife – at my side. Together, we have overcome all obstacles, motivated each other and celebrated our successes. Now, we will end this chapter with defending our theses in the same week! I cannot wait for our next adventure to begin in California. You are the kindest and friendliest person I know and I cannot express how lucky I feel to be with you. I love you.

Hora Est!

